RUPRECHT-KARLS-UNIVERSITÄT HEIDELBERG

Federica Mantegazzini

Development and characterisation of high-resolution metallic magnetic calorimeter arrays for the ECHo neutrino mass experiment

Dissertation

July 2021

KIRCHHOFF-INSTITUT FÜR PHYSIK

Dissertation

submitted to the

Combined Faculties of the Natural Sciences and Mathematics

of the Ruperto-Carola-University of Heidelberg, Germany

for the degree of

Doctor of Natural Sciences

Put forward by

M.Sc. Federica Mantegazzini

from Robecco sul Naviglio (Milano, Italy)

Oral examination: 7 July 2021

Development and characterisation of high-resolution metallic magnetic calorimeter arrays for the ECHo neutrino mass experiment

Referees: JProf. Dr. Loredana Gastaldo
Prof. Dr. Hans-Christian Schultz-Coulon

Abstract

This work is focused on the development of cryogenic metallic magnetic calorimeter detectors with implanted ^{163}Ho source for the ECHo (Electron Capture in ^{163}Ho) experiment for the determination of the effective electron neutrino mass by studying the ^{163}Ho electron capture spectrum. The detector prototype fabricated for the first experimental phase, ECHo-1k, has been fully characterised, in terms of thermodynamic properties, detector response, energy resolution and ^{163}Ho activity per detector pixel. The specific heat per holmium ion in silver has been determined, comparing the response of detector pixels with and without implanted ^{163}Ho. This accurate measurement indicates a lower value of the ^{163}Ho half-life with respect to the value reported in literature. Two implanted ECHo-1k detector chips have been operated in parallel in a dilution refrigerator which has been equipped with a 64-channel read-out chain. A high-statistics measurement with more than 10^8 ^{163}Ho electron capture events has been performed and the analysis of the resulting spectrum will allow to reach a sensitivity below 20 eV on the effective electron neutrino mass. Based on the outcomes of the ECHo-1k experimental phase, a novel detector design has been conceived in order to achieve the detector performance required for the succeeding experimental phase, ECHo-100k. The new ECHo-100k detector has been successfully fabricated and fully characterised, showing an improved detector response and an excellent energy resolution that reaches 3 eV FWHM, matching the designed value. The results obtained in this thesis set the starting point of the ECHo-100k experiment.

Entwicklung und Charakterisierung hochauflösender Detektorarrays basierend auf metallischen magnetischen Kalorimetern für das ECHo-Neutrinomassen-Experiment

In der vorliegenden Arbeit wird die Entwicklung kryogener metallischer magnetischer Kalorimeter besprochen, die eine implantierte ^{163}Ho-Quelle aufweisen und mit deren Hilfe - im Rahmen des ECHo-Experiments (Electron Capture in ^{163}Ho) zur Bestimmung der effektiven Elektron-Neutrinomasse - das ^{163}Ho-Elektroneneinfangspektrum untersucht werden soll. Der Detektorprototyp, der für die erste experimentelle Phase ECHo-1k produziert wurde, wurde vollständig charakterisiert in Bezug auf thermodynamische Eigenschaften, Detektorantwort, Energieauflösung und ^{163}Ho-Aktivität pro Detektorpixel. Die spezifische Wärme pro Holmiumion in Silber wurde durch den Vergleich der Detektorantwort von Detektorpixeln mit und ohne implantiertes ^{163}Ho bestimmt. Diese hochpräzise Messung deutet auf eine gegenüber dem Literaturwert reduzierte Halbwertszeit von ^{163}Ho hin. Zwei implantierte ECHo-1k-Detektorchips wurden zeitgleich in einem Verdünnungskryostaten, der mit einer 64-kanaligen Auslesekette ausgestattet ist, eingesetzt. Eine umfangreiche Messung mit mehr als 10^8 ^{163}Ho-Elektroneneinfangereignissen wurde durchgeführt; die Analyse des resultierenden Spektrums wird eine Sensitivität gegenüber der effektiven Eletron-Neutrinomasse von unter 20 eV aufweisen. Basierend auf den Ergebnissen der experimentellen Phase ECHo-1k wurde ein neues Detektordesign entworfen um die Anforderungen der nächsten experimentellen Phase ECHo-100k zu erreichen. Der neue ECHo-100k-Detektor wurde hergestellt und vollständig charakterisiert; er weist eine verbesserte Detektorantwort und eine exzellente Energieauflösung von bis zu 3 eV FWHM auf, was dem Designwert entspricht. Die Ergebnisse der vorliegenden Arbeit stellen den Anfang des ECHo-100k-Experiments dar.

Contents

1. Introduction

'Neutrinos', Maurice Goldhaber once stated, 'are remarkable particles: they induce courage in theoreticians and perseverance in experimenters'.

It is undeniable, on the other hand, that neutrinos endlessly fuel debates among physicists, starting from the first decades of the XX century, when neutrinos have not been discovered yet. At that time, investigations pioneered by Lise Meitner and Otto Hahn suggested that electrons emitted in beta-decay emerged with discrete energies. In these experiments, the electrons were bent according to their energy by means of a spectrometer and then detected with a photographic plate positioned after a movable slit. However, when James Chadwick measured electrons from a beta-decay using a point counter instead of a photographic plate, he found out that the energy of the electrons varies continuously, with peaks only at few energies. Furthermore, he was able to explain why the detection through the photographic plate could give rise to the discrete lines, as that method was too sensitive to small changes of intensity, mistaking them as energy peaks in the spectrum. After the First World War the debate on the nature of the beta-decay spectrum continued, with arguments in favor of the hypothesis of a continuous energy spectrum and, on the other side, defending the idea of discrete lines.

According to Meitner's hypothesis, the electrons should always start with the same monochromatic energy and then lose certain amounts in subsidiary processes, interacting with atoms and nuclei, and therefore giving rise to many energy peaks in the spectrum. In this case, the total electron energy must equal the maximum at the end of the spectrum. In the year 1927 the experiment conducted by Charles Drummond Ellis and William Wooster at Cambridge put an end to the controversy measuring the total electron energy in a single decay process exploiting a calorimetric approach, i.e. with the electron source surrounded by the detector. The result of the integral measurement was an energy equal to the average energy of the spectrum, demonstrating that the electrons start with a range of energies. In other words, the beta spectrum is ultimately continuous.

This was not the end of the story, rather the beginning, since a new problem arose. Assuming that the electron shares the decay energy with the nucleus, we are dealing with a two-body process which should always yield electrons with the same energy - provided that energy and momentum are conserved. Even a physicist like Niels Bohr was willing to sacrifice the fundamental laws of energy and momentum conservation to solve the puzzle of the nature of the beta-decay spectrum. Wolfgang Pauli, for his part, suggested that an undetectable neutral third particle was involved in the

process as 'desperate remedy' to retain energy and momentum conservation. This is the particle that later on Enrico Fermi called neutrino - the 'little neutral one'.

Even if Pauli's idea dates back to the year 1930, making neutrinos one of the 'oldest' particles of the Standard Model, the experimental discovery took place only in the middle of the fifties, when Clyde L. Cowan and Frederick Reines exploited the inverse beta-decay process as detection channel for fission neutrinos created in a nuclear power plant. Pauli himself soon realised that his particle would be difficult to detect. This concern was confirmed by Hans Bethe and Rudolf Peierls who in 1934 calculated an interaction cross section of less than $10^{-44}\,\mathrm{cm}^2$, suggesting that 'there is no practically possible way of observing the neutrino'.

The small cross sections of the interaction with matter is one of the properties that make neutrinos 'special' particles in the Standard Model. This property derives from the fact that neutrinos' only possible electroweak interactions are charged-current and neutral-current, exchanging the heavy virtual $\mathrm{W}^{\pm}$ and Z^0 bosons.

A second - and more mysterious - property that distinguishes neutrinos is the littleness of their mass. As a matter of fact, neutrino masses are at least six order of magnitude smaller than the masses of leptons and quarks. This tiny mass, which cannot be explained in the framework of the Standard Model, makes neutrinos one of the most interesting particles, opening the horizon to physics beyond the Standard Model. On the other hand, this minute mass leads to great challenges from the experimental point of view in order to achieve its determination. Currently, three different approaches are pursued to reach this goal: indirect neutrino mass determination via cosmological observables, search for neutrinoless double-beta decay and direct measurement based on kinematics of beta or electron capture processes. While the first two methods are model-dependent and therefore the outcome would rely on the accuracy of the underlying theories, the last one is a completely model-independent approach, exclusively based on energy-momentum conservation. Here, the impact of a non-zero neutrino mass consists of the reduction of the end-point energy with respect to the Q-value by the value of the effective neutrino mass. In order to detect these effects and to exploit them to determine the effective neutrino mass, a very precise measurement of a high-statistics spectrum is necessary. From the experimental point of view, the requirements to reach this precision are extremely challenging. Nevertheless, many experiments are currently pushing the limits of the state-of-the-art detector technology to accomplish this mission, showing the 'perseverance' mentioned in Goldhaber's quote.

One of these experiments is the Electron Capture in ^{163}Ho experiment, ECHo, which is based on the study of the ^{163}Ho electron capture spectrum. The work discussed in this thesis has been carried on within the ECHo experiment and its focus is on the development and characterisation of suitable cryogenic detectors for the determina-

tion of the electron neutrino mass. In chapter 2 a general overview on the physics of massive neutrinos is presented, with particular attention to the different experimental methods aiming for the neutrino mass determination. Chapter 3 is dedicated to the description of the ECHo experiment. The goal of this experiment is the determination of the effective electron neutrino mass which can be achieved through the analysis of a high energy resolution calorimetrically measured ^{163}Ho spectrum. The detector technology is based on metallic magnetic calorimeters (MMCs) operated at millikelvin temperature, which can reach excellent energy resolution. The working principle and the most relevant properties of such cryogenic detectors are presented in chapter 4. The first phase of the ECHo experiment, ECHo-1k, has been dedicated to the development and characterisation of the first MMC array prototypes, allowing for the measurement of a high-statistics ^{163}Ho spectrum with more than 10^8 electron capture events. Chapter 5 contains the results of this first phase, which have paved the way for the preparation of the current phase of the experiment, ECHo-100k, which has just begun. The ECHo-1k detector has been exploited to investigate the specific heat of ^{163}Ho implanted in silver - which has an important influence on the detector response - leading to an unexpected result and suggesting a redefinition of the ^{163}Ho half-life with respect to the value currently reported in literature, as described in chapter 6. In order to satisfy the requirements of the ECHo-100k experimental phase, a new optimised detector has been developed in the context of this work, showing substantially improved performances. The ECHo-100k detector design, fabrication and characterisation is presented in chapter 7. Finally, a summary of the work is given in chapter 8.

2. Massive neutrinos

Neutrinos are massless fermions, according to the Standard Model. However, the experimental evidence of neutrino oscillations ultimately proves that neutrinos are massive particles. The determination of the neutrino mass is one of the most stringent questions in the field of particle physics as well as one of the principal goals of the program of current and future researches in neutrino physics.
Different methodologies can be implemented to achieve this aim, ranging from cosmological methods based on the description of how matter is distributed in the Universe to searches for neutrinoless double-beta decay and investigations of the effect of finite neutrino masses in low energy electron capture and beta-decay processes. In the following the basic formalism of neutrino oscillations is presented, with the main intent of showing why this crucial discovery - worth the Nobel Price in 2015 - implies the massive nature of neutrinos. Afterwards, the diverse experimental ways currently implemented for the determination of the neutrino masses are reviewed, emphasising the difference of the experimental observables, the advantages on one hand and the challenges on the other hand of each approach.

2.1 Neutrino oscillations

Neutrinos are neutral fermions that interact only via weak force and gravity. Weak interactions create neutrinos in one of the three leptonic flavors: electron neutrinos (ν_e), muon neutrinos (ν_μ), or tau neutrinos (ν_τ), in association with the corresponding charged lepton.

Neutrinos are one of the most abundant particles in the universe. For instance fusion reactions in the core of the Sun produce a large flux of neutrinos, mainly via the proton-proton reaction:

$$4p \rightarrow^4 \mathrm{He} + 2e^+ + 2\nu_e \tag{2.1}$$

releasing 26.73 MeV of energy, some of which is taken by the neutrinos.

The proton-proton reaction is divided in many branches. About 86% of all solar neutrinos are produced from the main proton-proton reaction (PP1), which involves the emission of electron neutrinos with an energy up to 400 keV:

$$p + p \rightarrow d + e^+ + \nu_e \,. \tag{2.2}$$

Several other production mechanisms contribute to the emission of electron neutrinos from the Sun, with energies up to 18 MeV. Because of the small cross section in the interaction with ordinary matter, essentially all neutrinos emitted by the Sun reach Earth and can in principle be detected.

The expected flux of solar neutrinos on Earth can be predicted with great confidence by the Standard Solar Model and it is about $7 \times 10^{10}\,\mathrm{cm}^{-2}\mathrm{s}^{-1}$ [Gru05]. The first attempt to measure the flux of neutrinos from the Sun was the Homestake experiment performed by Raymond Davis and collaborators in the late sixties. A chlorine-based detector was used, exploiting the radiochemical process $\nu_e + {}^{37}\mathrm{Cl} \rightarrow e^- + {}^{37}\mathrm{Ar}$, which, however, limited the threshold energy to 0.814 MeV. For this reason the experiment could detect only higher energy neutrinos from side chains in the solar fusion. As a result, a clear deficit with respect to the well predictable expected flux was found [Cle98], giving origin to the so called "solar neutrino problem".

Various subsequent experiments confirmed the deficit, including GALLEX [Ham99], GNO [Alt05], SAGE [Abd09] and Super-Kamiokande [Abe11]. While the first three experiments exploited gallium-based radiochemical detectors and are therefore characterised by a very low energy threshold that allows the detection of pp neutrinos, the Super-Kamiokande experiment is based on water-Cherenkov detectors with a higher threshold. Thus, the observed neutrino deficit is independent of the energy range. In particular, the GALLEX experiment first observed the PP1 neutrinos, measuring a shortfall of neutrinos: the data read 76.4 ± 8 solar neutrino units, representing about 55% of the predicted rate. The first attempts to solve the solar neutrino problem assumed mistakes in the Standard Solar Model, i.e. overestimation of temperature and pressure in the core of the Sun.
The most quoted explanation involves neutrino flavour oscillations. The name "neutrino oscillations" refers to a quantum phenomenon wherein neutrinos created with a certain leptonic flavour are later measured with a different leptonic flavour. As the change of flavour is periodic with the travelling distance divided by the neutrino energy, this effect is addressed as neutrino oscillations. After the discovery of this phenomenon in 1998 by the Super-Kamiokande collaboration [Fuk98], in 2001 the SNO experiment was able to demonstrate that neutrino oscillations are responsible for the observed solar neutrino deficit [Ahm02].

SNO was the first experiment that was able to detect all three neutrino flavours with enough sensitivity, using 1000 tons of heavy water as target material. The solar neutrinos could be detected through three channels:

- Charged current (CC) interaction, sensitive only to electron neutrinos. In this interaction a neutrino converts the neutron in a deuterium nucleus d to a proton p: $\nu_e + d \rightarrow p + p + e^-$.

- Elastic scattering (ES) interaction, sensitive to all neutrino flavours, but with higher cross-section for electron neutrinos. In this interaction a neutrino collides with an atomic electron e and imparts some of its energy to it: $\nu_x + e^- \rightarrow \nu_x + e^-$.

- Neutral current (NC) interaction, equally sensitive to all neutrino flavours. In this interaction a neutrino dissociates the deuterium nucleus d, breaking it into its constituents, neutron n and proton p: $\nu_x + d \rightarrow p + n + \nu_x$.

While the total measured flux in the flavour-independent NC channel was consistent with the expectations based on the solar models, a strong evidence of a non-electron neutrino component in the solar flux was found by comparing the fluxes detected in the different channels [Ahm02]. In other words, it was proofed that a certain fraction of solar neutrinos created with an electronic flavour are detected on Earth with another flavour, confirming the existence of the neutrino oscillations phenomenon.

The concept of neutrino oscillations was initially introduced in 1957 by Bruno Pontecorvo, who proposed that neutrino-antineutrino transitions can occur in analogy with neutral kaon mixing. This concept was then developed by Maki, Nakagawa and Sakata to set up the quantitative theory of neutrino flavour oscillations, which was further elaborated by Pontecorvo in 1967 - eleven years before the first observation of the solar neutrino deficit [Pon68].

The quantum mechanical formalism of neutrino oscillations is based on the following main assumption: the three[1] orthogonal weakly-interacting neutrino flavour eigenstates ν_α with $\alpha = e, \mu, \tau$ are not identical to the orthogonal mass eigenstates ν_i with $i = 1, 2, 3$, but they are related through a unitary matrix U. Therefore, a neutrino with flavour α created in a weak interaction process involving a charged (anti)lepton $l_\alpha^{-(+)}$ is described by the flavour state as a superposition of the mass eigenstates [Giu07]:

$$|\nu_\alpha\rangle = \sum_i U_{\alpha i}^* \, |\nu_i\rangle \ . \tag{2.3}$$

The U matrix represents the so called Pontecorvo-Maki-Nakagawa-Sakata (PMNS) matrix, in analogy with the CKM matrix describing the quark mixing.

The flavour state $|\nu_\alpha(t)\rangle$ describes a neutrino created with a definite flavour α at time $t = 0$. For simplicity, in the following natural units are used, i.e. $\hbar = c = 1$, as

[1] Several models take into account the existence of sterile neutrinos and therefore a larger number of eigenstates. The theory can be generalised assuming n states and mass eigenstates, where n is arbitrarily large and includes three active states which interact via W and Z bosons.

well as in the rest of this work. Using the Schrödinger equation to describe the time evolution of this state and using the inverse of equation 2.3, we obtain:

$$|\nu_\alpha(t)\rangle = \sum_i U^*_{\alpha i} e^{-\mathrm{i}E_i t} |\nu_i\rangle = \sum_{\beta=e,\mu,\tau} \left(\sum_i U^*_{\alpha i} e^{-\mathrm{i}E_i t} U_{\beta i} \right) |\nu_\beta\rangle \tag{2.4}$$

where E_i is the corresponding energy eigenvalue.

The superposition of massive neutrino states $|\nu_\alpha(t)\rangle$, which is the pure flavour state given by equation 2.3 at $t = 0$, becomes a superposition of different flavour states at $t > 0$.

The transition probability from the state $|\nu_\alpha\rangle$ to the state $|\nu_\beta\rangle$ can be calculated as:

$$\begin{aligned} P(\alpha \to \beta) &= |\, \langle \nu_\beta | \nu_\alpha(t) \rangle \,|^2 \\ &= \sum_{i,j} U^*_{\alpha i} U_{\beta i} U_{\alpha j} U^*_{\beta j} e^{-\mathrm{i}(E_i - E_j)t} \,. \end{aligned} \tag{2.5}$$

In the ultrarelativistic limit, in which $p_i >> m_i$ and $p_i \approx E$, the neutrino energy becomes:

$$E_i = \sqrt{m_i^2 + p_i^2} \sim p_i + \frac{m_i^2}{2p_i} \sim E + \frac{m_i^2}{2E} \tag{2.6}$$

where E is the total neutrino energy. Therefore it is possible to approximate:

$$E_i - E_j \sim \frac{\Delta m^2_{ij}}{2E} \tag{2.7}$$

where Δm^2_{ij} is the squared-mass difference: $\Delta m^2_{ij} = m_i^2 - m_j^2$.

In neutrino oscillation experiments the time t is not measured, but the distance L between the source and the detector is known. Since ultrarelativistic neutrinos propagate almost at the speed of light, it is possible to state that $t = L$. Using this approximation and equation 2.7, the transition probability in equation 2.5 becomes:

$$P(\alpha \to \beta) = \sum_{i,j} U^*_{\alpha i} U_{\beta i} U_{\alpha j} U^*_{\beta j} \exp\left(-\mathrm{i} \frac{\Delta m^2_{ij} L}{2E} \right) . \tag{2.8}$$

This expression shows that the source-detector distance L and the neutrino energy E are the quantities depending on the experiment which determine the phases of the neutrino oscillations. The amplitude of the oscillations is specified only by the

elements of the mixing matrix U, which are constants of nature. It is clear that the experimental confirmation of neutrino oscillations implies massive neutrinos. However, oscillation measurements yield precise information only on the values of the squared-mass differences, but not on the absolute values of neutrino masses.

The oscillation data can be fitted in terms of the squared mass differences: the solar mass splitting $\Delta m^2_{21} = 7.42^{+0.21}_{-0.20} \times 10^{-5}\,\mathrm{eV}^2$ and the atmospheric mass splitting $\Delta m^2_{31} = 2.517^{+0.026}_{-0.028} \times 10^{-3}\,\mathrm{eV}^2$ [Est20] [NuF]. Matter effects fix the sign of the solar mass splitting, $\Delta m^2_{21} > 0$[2], while the atmospheric mass splitting is measured only via neutrino oscillations in vacuum, which depend only on its absolute value, leaving its sign unknown. As a results, two ordering schemes are possible: the *normal ordering* (NO) with $\Delta m^2_{31} > 0$ or the *inverted ordering* (IO) with $\Delta m^2_{31} < 0$. From the known mass splittings resulting from neutrino oscillation experiments, we can state that at least two neutrino masses are larger than $\sqrt{\Delta m^2_{21}} \sim 8\,\mathrm{meV}$ and at least one of them is larger than $\sqrt{\Delta m^2_{31}} \sim 50\,\mathrm{meV}$. Therefore, it is possible to extract a lower limit on the sum of the three neutrino masses $\sum m_\nu = \sum_{i=1}^{3} m_i$, where m_1 (m_3) is the lightest neutrino mass in the normal (inverted) ordering. From the best-fit values for the neutrino mass splittings, it results that $\sum m_\nu \lesssim 0.06\,\mathrm{eV}$ in normal ordering or $\sum m_\nu \lesssim 0.10\,\mathrm{eV}$ in inverted ordering [DS18].

2.2 Neutrino mass determination

The knowledge of the neutrino mass scale is crucial both for Particle Physics and Cosmology and it is an essential ingredient to understand the neutrino mass generation mechanism. Since the measurements of neutrino oscillations are sensitive only to the squared-mass difference, different approaches are necessary in order to gain information on the absolute neutrino mass values. Currently, various experiments are being performed or planned to investigate the neutrino mass and they can be classified in three main categories that can access different experimental observables:

1. Cosmological observations, probing the limit on the sum of the masses of all mass eigenstates $m_\nu = \sum_i m_{\nu_i}$;
2. Search for neutrinoless double-beta decay ($0\nu\beta\beta$), setting limits on the so called Majorana neutrino mass $m_{\beta\beta} = |\sum_i U^2_{ei} m_{\nu_i}|$;
3. Direct measurements based on energy-momentum conservation in low energy beta or electron capture decays, sensitive to the effective (anti-) neutrino mass squared $m^2_{\nu_\alpha} = \sum_i |U^2_{\alpha i}| m^2_{\nu_i}$.

The first two techniques are powerful but indirect tools to probe the absolute neutrino mass scale. They rely on specific theoretical models and therefore their outcome is

strongly model-dependent. On the other hand, the third method is solely based on the kinematics of the evaluated process and therefore it is essentially model-independent.
In the following the experimental methods currently pursued for the determination of the neutrino mass are shortly reviewed. Particular emphasis is given to the direct approach based on the kinematics of the electron capture decay in ^{163}Ho, which is used in the context of this work.

2.2.1 Cosmology

At present, the strongest upper limit on the sum of neutrino masses is from cosmological observations [Agh20]:

$$\sum_i m_{\nu_i} < 0.12\,\mathrm{eV}\,. \tag{2.9}$$

Massive neutrinos leave unique imprints on cosmological observables throughout the history of our universe. Neutrino masses in the sub-eV to eV range significantly alter the expansion evolution near the epoch of matter-radiation equality. On the other side, neutrino free-streaming affects the growth of structures at late times. Observational probes currently used to detect these signatures include cosmic microwave background (CMB) anisotropies and the distribution of matter in the universe, the so called large scale structure (LSS) [Won11].

The main signature of neutrino masses in the CMB is connected to the so called early integrated Sachs-Wolfe (ISW) effect. Shortly before the photon decoupling, occuring at a temperature of $T \sim 0.26\,\mathrm{eV}$, is the epoch of matter-radiation equality, with a temperature of $T \sim 1\,\mathrm{eV}$. Since the transition from radiation to matter domination happens so close in time to the epoch of photon decoupling, the photon energy is locally influenced by gravitational potentials. This leads to a nontrivial evolution of the photon geodesics, the imprint of which today is preserved in the CMB anisotropies. This is the early ISW effect. If the absolute neutrino mass is in the order of 1 eV, the transition from fully relativistic to nonrelativistic relic neutrinos happened at $T \sim 1\,\mathrm{eV}$, thereby contributing to the early ISW effect. Thus, the size of the CMB temperature anisotropy, especially at the first acoustic peak, brings information on the neutrino mass scale and it allows to set a constraint from the CMB alone.

The large scale structure (LSS) is influenced by two different phenomena. The first one is the ISW effect during photon decoupling in the transition from radiation to matter domination, as described above. The second one is the neutrino free streaming. Neutrinos are created with a large thermal velocity, which makes them

difficult to trap into potential wells up to a characteristic free streaming length l_{fs} which depends on their mass. On smaller scales, with $l < l_{\mathrm{fs}}$, the neutrinos are captured and their gravitational influence suppress the formation of anisotropies, affecting the large-scale matter distribution. Various types of surveys of the LSS are available. The most powerful one is based on galaxy redshift measurements, which provide three dimensional galaxy catalogues. Recently the Lyman-α forest probe has gained considerable attention. Essentially, it consists of absorption features in intergalactic low density gases along the line of sight to a distant quasar.

Future nearly all-sky spectroscopic galaxy surveys, as planned for example with the ESA Euclid mission [Rac16], will investigate the cosmological neutrino background at high statistical significance, providing important insights into neutrino properties, including the neutrino mass scale.

2.2.2 Neutrinoless double-beta decay

Double-beta decay ($2\nu\beta\beta$) is a very rare process foreseen by the Standard Model and experimentally observed for several nuclides. It consists of two simultaneous beta-decays in the same nucleus with the emission of two electrons and two electron antineutrinos with energies typically up to 1 - 3 MeV. On the other hand, the neutrinoless double-beta decay ($0\nu\beta\beta$) is an hypothetical nuclear transition which is not allowed in the Standard Model and it violates lepton number conservation [Giu12]. In this case the antineutrino emitted at one vertex is absorbed at the other vertex as a neutrino, essentially exchanging a virtual neutrino, as shown in figure 2.1.

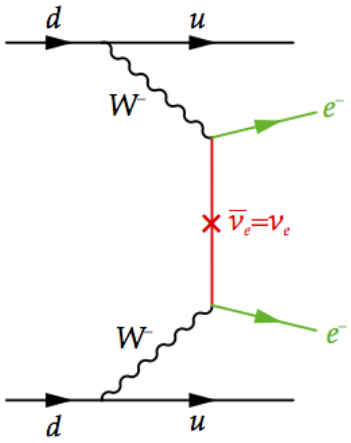

Figure 2.1: Feynman diagram of the neutrinoless double-beta decay. The exchange of a virtual neutrino is marked in red, while the two electrons in the final state are marked in green.

The $0\nu\beta\beta$ decay exists only if the neutrino is a Majorana particle, i.e. if it is identical to its own antiparticle. In this case, the observable nuclear decay would be:

$$(A, Z) \rightarrow (A, Z + 2) + 2e^{-} . \tag{2.10}$$

Similar transitions could occur through the emission of a pair of positrons, double electron capture or electron capture together with single emission of a positron, with a nuclear transition from (A, Z) to $(A, Z-2)$. The observation of any of these variations would definitively demonstrate that the lepton number is not conserved - opening a new scenario where Leptogenesis could be the explanation for the Baryon Asymmetry of the Universe - and it would show that neutrinos are Majorana particles, providing information on the absolute neutrino mass.

The decay rate $\Gamma^{0\nu}$ of the process can be calculated as[2]:

$$\Gamma^{0\nu} = \frac{1}{T^{0\nu}_{1/2}} \propto G^{0\nu}(Q, Z) \cdot |M^{0\nu}|^2 \cdot |m_{\beta\beta}|^2 \tag{2.11}$$

where $T^{0\nu}_{1/2}$ is the half-life, $G^{0\nu}$ represents the phase-space term, which depends on the Q-value of the decay and on the atomic number Z, $|M^{0\nu}|$ is the nuclear matrix element and $m_{\beta\beta}$ is the so called effective Majorana mass:

$$m_{\beta\beta} = \left| \sum_i U^2_{ei} m_{\nu_i} \right| = \left| \sum_i |U^2_{ei}| m_{\nu_i} e^{\mathrm{i}\alpha_i} \right| \tag{2.12}$$

where two complex phases $\alpha_{1,2}$, called Majorana phases, are present.

The largest uncertainty in this calculation is given by the estimation of the nuclear matrix elements - which relies on sophisticated theoretical nuclear models - and by the completely unknown phases.

From equation 2.11 it is clear that the experimental measurement of the $0\nu\beta\beta$ decay rate can be used as a tool to investigate the absolute neutrino mass and the mass ordering. The effective Majorana mass term $m_{\beta\beta}$ contains the three neutrino mass eigenvalues m_{ν_i} and the elements of the first row of the mixing matrix U_{ei}, which include the CP-violating Majorana phases $\alpha_{1,2}$, as shown in equation 2.12. It is worth to note that the existence of these phases in the coherent sum over the mass eigenvalues m_{ν_i} could possibly lead to an effective Majorana mass that is smaller than the effective electron neutrino mass or even to a cancellation of it.

[2]Here we assume that the exchange of a light Majorana neutrino is the mechanism leading to neutrinoless double beta decay.

The experimental search for the $0\nu\beta\beta$ process is based on the detection of the two emitted electrons and on the very precise measurement of the sum of their kinetic energy. Since the nuclear recoil is typically negligible, the sum of the electrons energy must be equal to the Q-value of the transition. Therefore, the experimental signature is a monochromatic peak at the Q-value in the measured spectrum, on top of the continuous double-beta component ($2\nu\beta\beta$).

The sensitivity $S^{0\nu}$ of an experiment searching for $0\nu\beta\beta$ is usually defined as the minimum half-life compatible with the background fluctuations at a given confidence level [Bro19]. In the limit of zero-background, i.e. when the background level is so low that the expected number of background events in the ROI smaller than one, the sensitivity is given by the expression:

$$S^{0\nu}_{0\mathrm{bkg}} = \log(2) \cdot \epsilon \cdot \frac{x\eta N_{\mathrm{A}}}{\mathscr{M}_A} \frac{MT}{n_{\mathrm{B}}} \tag{2.13}$$

where ϵ is the detection efficiency, x is the stoichiometric multiplicity of the compound containing the $\beta\beta$ candidate, η is the $\beta\beta$ candidate isotopic abundance, N_A is the Avogadro number, $\mathscr{M}_A$ is the compound molecular mass, M is the detector mass, T is the measuring time, n_B is the maximum number of counts compatible with no observed counts at a given C.L. (in the assumption of Poisson statistics) and log denotes the natural logarithm.

The expression in 2.13 clearly shows the role of the basic experimental parameters. Increasing the measuring time and the detector mass as well as improving the detector efficiency have a direct impact on the sensitivity of the experiment.

In nature we find 69 $\beta\beta$-unstable nuclides candidates [Tre02]. However, only a small subset is of any practical interest for the investigation of $0\nu\beta\beta$. In fact, the choice of a suitable isotope is dictated by the following requirements:

- high Q-value, i.e. preferably above 2.6 MeV, which on one side increases the phase-space factor and therefore the decay probability and on the other side corresponds to a lower beta-gamma natural radioactive background;
- high detector energy and time resolutions in order to reduce the background counts from the $2\nu\beta\beta$ decay channel;
- large natural isotopic abundance or, alternatively, a feasible enrichment;
- compatibility with the detection techniques.

Each of these conditions implies often contradictory constraints and therefore a compromise solution is usually unavoidable. Consequently, the list of isotopes commonly taken into consideration is: ^{48}Ca, ^{76}Ge, ^{82}Se, ^{96}Zr, ^{100}Mo, ^{116}Cd, ^{130}Te, ^{136}Xe

and ^{150}Nd [Giu12]. All these nuclides have been studied and employed in different searches.

The isotope ^{136}Xe isotope is exploited by three collaborations for the search of $0\nu\beta\beta$: EXO-200, KamLand-Zen and NEXT. EXO-200 uses xenon both as source and detector for the two emitted electrons. The EXO-200 detector consists of a cylindrical time projection chamber (TPC) filled with liquefied xenon enriched in the isotope ^{136}Xe, where the depositions of energy produce both ionisation and scintillation signals. EXO-200 was able to set a lower limit on the half-life of $0\nu\beta\beta$: $T_{1/2}^{0\nu\beta\beta}(^{136}\text{Xe}) > 1.8 \times 10^{25}\,\text{yr}$ (90% C.L.), corresponding to an effective Majorana mass of less than $147 - 398\,\text{meV}$ [Alb18].
KamLAND-Zen uses 13 tons of enriched xenon as a source, contained in a nylon balloon that is surrounded by a liquid scintillator outer balloon of 13 meters diameter. The lower limit on the $0\nu\beta\beta$ decay half-life that could be reached so far by the KamLAND-Zen collaboration is $T_{1/2}^{0\nu\beta\beta}(^{136}\text{Xe}) > 1.07 \times 10^{26}\,\text{yr}$ (90% C.L.), corresponding to upper limits on the effective Majorana neutrino mass in the range $61 - 165\,\text{meV}$ [Gan16]. The upgrade project KamLAND-Zen 800 has started in 2019.
Finally, the NEXT experiment makes use of high-pressure gaseous xenon time projection chambers (HPXe) with electroluminescent amplification of the signal. The ability to reconstruct the trajectory of the two electrons emitted in the decays is a unique feature of the HPXe, which contributes to the suppression of backgrounds. Currently calibration runs are being performed to demonstrate the energy resolution and tracking capabilities of the detector [Sim20].
In future also the DARWIN experiment developed to search for dark matter interactions in a 40 tons liquid xenon target with dual-phase TPCs will have the possibility to reach high sensitivity in the search of $0\nu\beta\beta$ decay [Aal16].

The isotope ^{76}Ge is the choice of the GERDA collaboration, which has searched for $0\nu\beta\beta$ with bare germanium detectors surrounded by liquid argon, which serves as high-purity shielding against products of radioactive decays as well as active veto and provides cooling for the germanium diodes. Also GERDA has not observed any signal, deriving a lower half-life limit of $T_{1/2}^{0\nu\beta\beta}(^{76}\text{Ge}) > 1.8 \times 10^{26}\,\text{yr}$ (90% C.L.) and therefore a limit on the effective Majorana neutrino mass of $79 - 180\,\text{meV}$ [Ago20].
Another ^{76}Ge-based experiment is planned by the MAJORANA collaboration, which is currently constructing the Majorana Demonstrator, based on germanium crystals and P-Type Point-Contact (PPC) detectors [Alv19]. The developments in terms of background suppression, energy resolution and sensitivity achieved by GERDA and MAJORANA are opening the way to LEGEND, a next generation germanium-based experiment with sensitivity to half-lives of $10^{27}\,\text{yr}$ and beyond [Abg17].

A different approach has been pursued by the CUORE collaboration, which employs low-temperature macrobolometers to search for $0\nu\beta\beta$ in ^{130}Te. ^{130}Te features high

natural abundance and sufficiently large Q-value. The CUORE detector consists of 988 TeO_2 crystals operated at millikelvin temperature, each having a mass of 750 g, equipped with a thermistor to record thermal signals and a heater for thermal gain stabilisation. Combining the CUORE results with those of two earlier experiments, Cuoricino and CUORE-0, a limit of $T_{1/2}^{0\nu\beta\beta}(^{130}\text{Te}) > 1.5 \times 10^{25}\,\text{yr}$ (90% C.L.) was set, which in terms of effective Majorana neutrino mass it translates into a limit of $110 - 520\,\text{meV}$ [Ald18].

The main parameters and results of the mentioned experiments are summarised in table 2.1.

Experiment	Isotope	M / kmol	$L(T_{1/2})$ / yr	$m_{\beta\beta}$ / meV	Ref.
EXO-200	^{136}Xe	1.0	1.8×10^{25}	$< 147 - 398$	[Alb18]
KamLAND-Zen	^{136}Xe	270	10.7×10^{25}	$< 61 - 165$	[Gan16]
GERDA	^{76}Ge	0.41	18×10^{25}	$< 79 - 180$	[Ago20]
CUORE	^{130}Te	1.59	1.5×10^{25}	$< 162 - 757$	[Ald18]

Table 2.1: Summary of the results of the main experiments searching for neutrinoless double-beta decay. For each experiment the used isotope, the detector mass M, the achieved limit on the half-life of the $0\nu\beta\beta$ process, $L(T_{1/2})$, the limit on the Majorana mass $m_{\beta\beta}$ and the corresponding reference are reported.

Many other experiments are currently being planned or under construction, like the AMoRE experiment using molybdenum crystals and metallic magnetic calorimeter (MMC) detectors [Par16] and SuperNEMO, the successor of NEMO-3, based on a tracker-calorimeter architecture with a thin layer of the isotope under investigation sandwiched between trackers and surrounded by calorimetry [Wat17].

2.2.3 Direct neutrino mass determination

The direct neutrino mass determination is based purely on kinematics without any further assumption and it is sensitive to the effective neutrino mass squared $m(\nu_\alpha)^2$, where α is the neutrino flavour. In principle there are two possible methods: time-of-flight measurements and precision investigations of weak decays. The first ones require very long baselines and therefore particularly strong sources, like a core-collapse supernova. The neutrino signal from the supernova SN1987A recorded in 1987 by the Kamiokande detector, for example, allowed to set an upper bound on the electron neutrino mass $m_{\nu_e} \leq 12\,\text{eV}$ [DA87]. Unfortunately, supernova explosions are rare events and they are still not described by the current astrophysical models. As a result, the most sensitive model-independent approach to determine the neutrino mass is based on kinematics of weak decays and more explicitly on the investigations of β or electron capture processes. Here the neutrino is not directly observed, but

the other decay products, which share the available decay energy with the neutrino[3], can be precisely measured. Since the minimum energy required to create a neutrino corresponds to its mass, the maximum energy in the measured spectrum is reduced by that amount and therefore the spectrum is distort in the vicinity of the end-point. The experimentally accessible observable is the effective electron neutrino and antineutrino mass:

$$m_{\nu_e} = \sqrt{\sum_i |U_{ei}^2| m_{\nu_i}^2} \text{ and } m_{\bar{\nu}_e} = \sqrt{\sum_i |U_{ei}^2| m_{\bar{\nu}_i}^2}\,. \tag{2.14}$$

In contrast with the effective Majorana neutrino mass $m_{\beta\beta}$, this sum averages over all neutrino mass eigenstates m_{ν_i} ($m_{\bar{\nu}_i}$) contributing to the electron (anti-) neutrino and no phases of the mixing matrix are left.

Kinematics of beta decay

In the case of β decay, a neutron in the nucleus decays to a proton by emitting an electron e and an electron antineutrino $\bar{\nu}_e$, leading to a nuclear decay of the type:

$$(A, Z) \rightarrow (A, Z+1) + e^- + \bar{\nu}_e\,. \tag{2.15}$$

The energy spectrum of the emitted electron can be calculated using the Fermi's golden rule and in the limit of small neutrino masses it can be written as function of the effective electron antineutrino mass $m_{\bar{\nu}_i} = \sum_i |U_{ei}|^2 m_{\bar{\nu}_i}^2$:

$$\begin{aligned} \frac{dN}{dE_e} = {} & \frac{G_F^2 \cos\Theta_C{}^2}{2\pi^3} |M_{\text{had}}|^2 F(E_e, Z+1) \\ & \cdot p_e \cdot (Q_\beta - E_e)^2 \sqrt{1 - \frac{m_{\bar{\nu}_e}^2}{(Q_\beta - E_e)^2}} \end{aligned} \tag{2.16}$$

where G_F is the Fermi coupling constant, Θ_C is the Cabibbo angle, $|M_{had}|^2$ is the nuclear matrix element, F is the Fermi function, accounting for the Coulomb interaction between electron and daughter atom, p_e and E_e are respectively the electron momentum and energy and Q_β is the Q-value of the decay.

From equation 2.16 it is evident that the effect of a non-zero effective mass is prominent when $(Q_\beta - E_e)^2 \approx m_{\bar{\nu}_e}^2$, i.e. at the end-point of the spectrum.

[3]The nucleus recoil is negligible.

Tritium The classical isotope that has been used for the neutrino mass determination via analysis of the β-decay spectrum is tritium (^{3}H), which decays to helium-3:

$$^3_1\mathrm{H} \rightarrow ^3_2\mathrm{He}^{1+} + e^- + \bar{\nu}_e \,. \tag{2.17}$$

The short half-life of 12.3 years and the relative low Q-value of 18.6 keV make tritium an attractive nuclide for this kind of measurements, since these properties maximise the total decay rate per amount of isotope and the relative fraction of events in the ROI, respectively [Dre13] [Mer13]. In particular, the relative number of events in the end-point region scales with Q_β^{-3}.

The current best limit on the effective electron antineutrino mass has been achieved by the Karlsruhe Tritium Neutrino (KATRIN) experiment, improving the previous result by almost a factor of two [Ake19]:

$$m_{\bar{\nu}_e} < 1.1\,\mathrm{eV}\,(90\%\ \mathrm{C.L.})\,. \tag{2.18}$$

This upper limit is derived from a fit of the integrated electron spectrum over a narrow interval around the end-point, resulting in an effective neutrino mass square value of $(-1.0^{+0.9}_{-1.1})\,\mathrm{eV}^2$.

The KATRIN experiment [Ake21] combines a windowless gaseous molecular tritium source (WGTS) with a spectrometer based on the principle of magnetic adiabatic collimation with electrostatic filtering (MAC-E-filter). The technology is optimised to improve energy resolution and statistics and to reduce the systematic uncertainties. Tritium molecules of high isotopic purity are injected through capillaries into the WGTS and diffuse to both the ends of the WGTS, reaching a stable decay rate of 10^{11} decays/s. The β-electrons that are emitted in the forward beam direction are adiabatically guided to the spectrometer by a magnetic field with position-dependent intensity and direction, to maximise the fraction of electrons that can be led to the spectrometer. The flow of tritium is reduced via differential and cryogenic pumping to avoid tritium-related background in the spectrometer section. A tunable electrostatic potential is created in the middle of the spectrometer, where the electrons have momentum parallel to the direction of motion and to the electric field. Only those electrons with enough kinetic energy are transmitted, while the remaining ones are reflected. The high-energy transmitted electrons finally reach the focal-plane detector where they are counted. By varying the filter potential and counting the transmitted electrons for each setting, the integral tritium spectrum can be determined. KATRIN is designed to reach a 5σ discovery level of $m(\bar{\nu}_e) = 350\,\mathrm{meV}$ and a 90% upper limit of $m(\bar{\nu}_e) = 200\,\mathrm{meV}$.

Another experiment employing tritium is Project 8, which is currently exploring a

new technique based on the measurement of the coherent cyclotron radiation emitted by the β-electrons in a static magnetic field [Mon09]. The cyclotron frequency ω depends on the electron charge q and mass m_e, on the magnetic field B and, most important, on the electron kinetic energy E:

$$\omega = \frac{\omega_0}{\gamma} = \frac{qB}{m_e + E}\,. \tag{2.19}$$

The corresponding radiation emitted by the electron motion carries the information of the electron kinetic energy. The detection of the electron radiation can be used as an innovative tool to perform a nondestructive spectroscopic measurement called Cyclotron Radiation Emission Spectroscopy (CRES). The technical realisation of this approach consists of a magnetic trap inside of a wave guide, the size of which matches the frequency band of interest, which in turn depends on the magnetic field. The radiated power scales with B^2 and $\sin^2\theta$, where θ is the angle between the electron momentum vector and the magnetic field direction. Therefore, strong magnetic fields as well as large angles are favourable. For an electron with an energy of about 18.6 keV, near the tritium end-point, in a magnetic field of 1 T at a pitch angle of 90°, approximately 1.2 fW is radiated. The energy resolution of this technique can be improved by reducing the pitch angle spread and the magnetic field inhomogeneity. Preliminary sensitivity studies show that one year of data taking with a density of 10^{11} molecules/cm^3 and a sensitive volume of 10 m^3 could bring the experiment to a sensitivity of $m(\nu_e) \approx 100$ meV (90% C.L.). Using an atomic tritium source of 10^{12} atoms/cm^3 and a sensitive volume of 100 m^3 a sensitivity of $m(\nu_e) \approx 40$ meV could in principle be obtained [Asn13].

Kinematics of electron capture

An electron capture (EC) process happens when an inner atomic electron is captured by the nucleus. Consequently, a nuclear proton is transformed to a neutron emitting an electron neutrino. The nuclear transition can be written as:

$$(A, Z) + e^- \rightarrow (A, Z-1) + \nu_e\,. \tag{2.20}$$

The hole in the atomic shell that is left by the captured electron can be filled by an outer-shell electron, emitting an X-ray with an energy equal to the difference between the energy of the atomic shell and the one of the electron. This process is called radiative transition. Alternatively, the available energy after the filling of the hole is used to emit a weaker bound electron. This process is non-radiative and it is called "Auger effect". In the particular case when the hole and the filling electron belong to the same atomic shell the process is renamed "Coster-Kronig transition".

After an EC decay, the daughter atom is left in an excited state and, in order to reach its ground state, a series of transitions take place, involving the emission of X-rays and electrons. The available energy, given by the Q-value of the decay, is shared between the neutrino, the excitations of the resulting ^{163}Dy atom and the nuclear recoil:

$$Q_{\mathrm{EC}} = E_\nu + E_{\mathrm{EC}} + E_{\mathrm{r}} \tag{2.21}$$

where E_ν is the total neutrino energy, given by the sum of its kinetic energy and rest mass: $E_\nu = \sqrt{p_\nu^2 + m_\nu^2}$, E_{EC} indicates the electronic de-excitations and E_{r} is the nucleus recoil energy.

Hence, the de-excitation energy spectrum is affected at the end-point by the non-zero neutrino mass, in a similar fashion as described in the case of β-decays. To obtain information on the neutrino mass, the EC de-excitation energy spectrum must be precisely measured. In order to overcome the lack of precise knowledge on the branching ratios of the different decay channels, a calorimetric measurement where the source is included inside the detector is favourable. This calorimetric approach was first introduced in 1982 for the isotope ^{163}Ho [DR82].

In first approximation, the EC differential decay rate can be written as:

$$\begin{aligned}\frac{d\Gamma}{dE_{\mathrm{EC}}} = \mathscr{C} &\left\{ (Q_{\mathrm{EC}} - E_{\mathrm{EC}})^2 \sqrt{1 - \frac{m_{\nu_e}^2}{(Q_{\mathrm{EC}} - E_{\mathrm{EC}})^2}} \right\} \\ &\cdot \sum_{\mathrm{H}} \phi_{\mathrm{H}}^2(0) B_{\mathrm{H}} \frac{\Gamma_{\mathrm{H}}}{2\pi} \frac{1}{(E_{\mathrm{EC}} - E_{\mathrm{H}})^2 + \Gamma_{\mathrm{H}}^2/4}\end{aligned} \tag{2.22}$$

where $\mathscr{C}$ is a constant that contains the squares of the nuclear matrix element and the Fermi coupling strength, followed by the phase-space term for the neutrino, equal to $E_\nu \cdot p_\nu$, in curly brackets. Here, Q_{EC} is the Q-value of the EC transition, E_{EC} is the decay energy and m_{ν_e} is the effective electron neutrino mass. The third part of the formula consists in a sum of Lorentzian functions, describing the series of peaks corresponding to the captured electrons at the electronic levels H. Each peak is centred at the energy E_{H} and its width is described by Γ_{H}. The relative amplitudes depend on the value of the electron wave function at the nucleus, $\phi_{\mathrm{H}}(0)$, and on the exchange and overlap corrections, B_{H}. As in the case of β-decay, the impact of the neutrino mass on the spectrum becomes larger at the end-point.

The basic nuclear process reported in the expression 2.20, mediated by the weak force, is the same than in the β-decay. However, in the case of EC the particle in the final state is an electron neutrino instead of an electron antineutrino. Therefore,

the study of the kinematics of EC is a powerful tool which plays a complementary role with respect to tritium-based techniques.

Holmium-163 The best candidate for neutrino mass determination by means of EC spectroscopy is the isotope ^{163}Ho, which is the nuclide used in the ECHo experiment. In fact, ^{163}Ho is characterised by two desirable properties that enhance the statistics in the ROI:

- the smallest Q-value among the nuclides that undergo EC: $Q_{\mathrm{EC}} = 2.833(30_{\mathrm{stat}})(15_{\mathrm{sys}})\,\mathrm{keV}$ [Eli15];
- a resonance at $E_{\mathrm{H}} \approx 2.04\,\mathrm{keV}$, rather close to the Q-value.

Both these features increase the relative number of events in the ROI, which obviously depends on the maximum energy in the spectrum and on the shape of the spectrum in the end-point region. Furthermore, it is favourable from a pure experimental point of view. Typically, the detector energy resolution scales with the energy input and therefore a low Q-value will intrinsically improve the detector performance. Furthermore, the absolute count rate increases with a larger Q-value, possibly leading to issues like pile-up events that cannot be resolved.

In contrast to the β-spectrum, the shape of the EC spectrum described in 2.22 is affected by the discrete nature of the electron shells and therefore it is characterised by a series of energy peaks, which can be used for the detector calibration. The decay rate is largely enhanced close to the central energies of the resonances E_{H}. In the case of ^{163}Ho, the MI resonance peak, corresponding to the capture of 3s electrons, is centred at the energy $E_{\mathrm{MI}} \approx 2.04\,\mathrm{keV}$ and therefore relatively close to the end-point. As a result, the number of events in the ROI is dominated by the MI tail.

The decay scheme for ^{163}Ho is the following:

$$\begin{aligned} {}^{163}_{67}\mathrm{Ho}_{96} &\rightarrow {}^{163}_{66}\mathrm{Dy}^{*}_{97} + \nu_e \\ &\rightarrow {}^{163}_{66}\mathrm{Dy}_{97} + E_{\mathrm{EC}} \end{aligned} \tag{2.23}$$

for which the half-life reported in literature is 4570 y [Bai83] [Kaw88].

In the ^{163}Ho atom there are 67 protons, 96 neutrons and 67 electrons, of which 20 electrons (the ones in the s and $\mathrm{p}_{1/2}$ shells) have a substantial overlap with the nucleus and therefore directly contribute to the EC amplitude. Because of the low Q-value, only electrons from the 3s shell or higher can be captured. The angular momentum selection rules do not allow the capture of electrons with total angular momentum

$j \geq 3/2$ at leading orders. As a result, seven major resonances are present[4]: MI to PI (for capture events from the 3s to the 6s shells) and MII to OII (for capture events from the $3p_{1/2}$ to the $5p_{1/2}$ shells)[5], as visible in figure 2.2a.

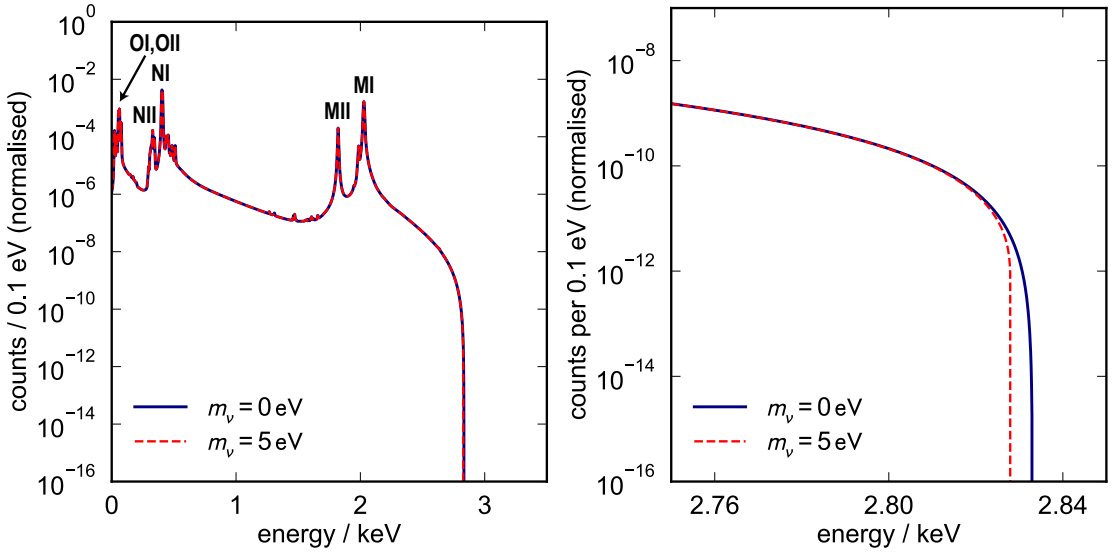

(a) **(b)**

Figure 2.2: The calorimetric EC spectrum of ^{163}Ho calculated for neutrinos with zero mass (solid blue line) and a mass of 5 eV (dashed red line), including second-order effects [Bra20]. In **(a)** the all energy range is shown, while in **(b)** a zoom in the end-point region is shown, where the distortion due to the non-zero neutrino mass is prominent.

Since the electrons in the ^{163}Ho atom are not behaving as independent entities and they are subject to Coulomb forces, all electrons react when one of them is captured. Thus, the simplified expression in 2.22 is only a first approximation of the spectrum shape. Several additional shake-up and shake-off processes are present, in which an outer second electron is excited to an unoccupied bound level or to the continuum, respectively. These transitions give rise to satellite structures that have been experimentally observed aside the main resonances [Gas17]. Important efforts are currently carried on at a theoretical level to reach a precise quantitative understanding of the ^{163}Ho EC spectrum [Bra18] [Bra20], as further discussed in section 3.2.1.

Currently, two main experiments are aiming for the determination of the effective electron neutrino mass using ^{163}Ho: HOLMES [Alp15] and ECHo[6]. Both the experi-

[4]Here we assume a decay of a neutral atom.

[5]The spectroscopic notation (K, L, M, ...) for atomic levels will be use in the following.

[6]A third experiment, NuMECS [Cro16], after a promising starting has been interrupted for funding reasons.

ments make use of cryogenic microcalorimeters with embedded ^{163}Ho. The HOLMES experiment plans to use Transition Edge Sensors (TES) arrays, each pixel containing an ^{163}Ho activity of about 300 Bq, for a total of 1000 detectors [Alp15]. In contrast, the ECHo experiment employs metallic magnetic calorimeter (MMC) array, aiming to an activity of 10 Bq per pixel and a final total number of detectors of 12000 for the presently planned phase. The different strategies are driven by different priorities. HOLMES gives more weight to the need for statistics, paying the price of a higher unresolved pile-up fraction, which contributes to the background level, as discussed in section 3.1. An unresolved pile-up event occurs when two or more events occur in a detector within a time that is shorted than the detector time resolution and therefore they cannot be resolved. This causes a background event with an energy equal to the sum of the energies of the single events. ECHo sets as main requirement a limited ^{163}Ho activity per detector in order to keep the unresolved pile-up fraction under control, at the cost of an increased number of detectors to be operated in parallel, and to guarantee best conditions for the operation of MMCs in terms of minimised detector heat capacity and limited count rate.

The current best limit on the effective electron neutrino mass has been recently achieved by the ECHo collaboration [Vel19b]:

$$m(\nu_e) \leq 150\,\text{eV}\,(95\%\ \text{C.L.})\,. \tag{2.24}$$

improving after more than thirty years the limit of 225 eV (95% C.L.) from the measurement by P.T. Springer et al. based only the radiative component - i.e. internal bremmsstrahlung (IBEC) - of the ^{163}Ho EC spectrum [Spr87]. In this experiment the holmium source consisted of about 3.3×10^{17} atoms for a total activity of about 1 MBq. The source was prepared as $^{163}HoF_3$ compound and vacuum-evaporated on a stainless steel substrate placed in front of a 30 mm^2 Si(Li) detector with an energy resolution of 137 eV. The effect of the neutrino mass was inferred by fitting the M_1O_2 and M_1N_2 X-ray transitions, taking into account the detection efficiency and response and the background level as well as the interference component from lower energetic X-rays.

3. The ECHo experiment

The investigation of the absolute scale of neutrino masses can open new doors towards physics beyond the Standard Model. The Electron Capture in ^{163}Ho - ECHo - experiment aims to reach sub-eV sensitivity on the effective electron neutrino mass analysing the calorimetric electron capture (EC) spectrum of ^{163}Ho, therefore ensuring a purely kinematics-based and model-independent approach.

In order to reach this arduous goal, several aspects must be taken into account, starting from the choice of the detector technology. The detectors must guarantee high energy resolution and fast response as well as a quantum efficiency close to 100%. A large number of detectors with implanted ^{163}Ho need to be operate in parallel to reach high statistics. As a matter of fact, to achieve a calorimetrical measurement of the EC spectrum, the ^{163}Ho ions must be completely surrounded by the detector and thus a dedicated ^{163}Ho implantation process needs to be developed and engineered. Besides the hardware preparation, also a dedicated analysis strategy needs to be developed to reconstruct the EC spectrum and to investigate the end-point region in order to gain information on the effective electron neutrino mass. For that, both a reliable theoretical description of the ^{163}Ho EC spectrum and a precise measurement of the corresponding Q-value represent crucial ingredients. Furthermore, the background sources need to be identified and reduced. The final experimental results must be compared with a theoretical background model, tailored to the ECHo experiment. The following sections are dedicated to the detailed discussion of each of these aspects.

The ECHo schedule currently foresees two phases: a small scale experiment, ECHo-1k, to reach a sensitivity below 20 eV on the electron neutrino mass and a medium scale experiment, ECHo-100k, which will lower the sensitivity below 3 eV. The modular approach of the ECHo experiment will also allow to further scale up to additional phases with higher exposures.

The ECHo collaboration started the first experimental phase, ECHo-1k, in 2015. The main goal of ECHo-1k was to develop and characterise a suitable detector chip prototype with embedded ^{163}Ho and to operate it collecting at least 10^8 EC events. With this statistics the designed sensitivity can be reached, allowing to set a new limit on the effective electron neutrino mass and improving the current best limit [Vel19b] by about one order of magnitude. The complete characterisation of the ECHo-1k detector chip as well as the high-statistics measurement campaign represent the first part of the work discussed in this thesis. The ECHo-1k data acquisition was completed in May 2020 and the data analysis is currently on-going. The results

obtained during the ECHo-1k phase have been adopted as basis to optimise the detector design and layout in order to meet the more demanding requirements for the next phase, ECHo-100k. The development, design, fabrication and characterisation of the ECHo-100k detector represent the second part of this work.

3.1 Detector technology

The choice of the detector technology is a crucial point to be considered to build a competitive experiment for the determination of the neutrino mass. In a calorimetric measurement, each EC event is detected singularly and the corresponding energy is estimated from the detector response. In the case of a cryogenic calorimeter, the detector signal consists of a pulse described by its rise time, which defines the detector time resolution, its decay time and its amplitude, which is proportional to the energy deposition. Overall, the instrumental response function can be typically described by a Gaussian function characterised by its full-width at half maximum (FWHM), which corresponds to the energy resolution of the detector. In the following, the influence of the detector parameters on the final sensitivity of the experiment is discussed.

The finite time resolution leads to the presence of an intrinsic background component in the measured spectrum, namely the unresolved pile-up. An unresolved pile-up event occurs when multiple individual decays happen within the time resolution of the detector, i.e. within a time interval that is shorter than the rise time. The resulting detector response is a signal with an amplitude corresponding to the sum of the energies of the individual decays and it cannot be easily tagged as pile-up. The fraction of events giving unresolved pile-up f_{pu} in the case of two events coincidence can be estimated in first approximation as:

$$f_{\mathrm{pu}} = a \cdot \tau_{\mathrm{r}} \tag{3.1}$$

where a is the ^{163}Ho activity and τ_{r} is the time resolution of the detector.

Assuming an unresolved pile-up fraction with a multiplicity of two (i.e. only two events overlap within the rise time), the pile-up spectrum is given by the auto-convolution of the ^{163}Ho spectrum itself. The measured spectrum is the sum of the single event spectrum and the pile-up spectrum. As the background source caused by unresolved pile-up cannot be eliminated, it must be suppressed limiting the source activity and favouring fast detectors with a short rise time. Metallic magnetic calorimeters (MMCs) have demonstrated an intrinsic rise time shorter than 100 ns [Pie12] which makes them the fastest low temperature microcalorimeters presently available for energy ranges up to few keV. This is one of the reasons that justifies the choice of MMCs as detector technology for the ECHo experiment.

In order to keep the unresolved pile-up fraction below 10^{-5}, the activity per detector must be lower than tens of Bq. The threshold value $f_{\mathrm{pu}} < 10^{-5}$ is defined as maximum allowed background level and it constraints the allowed rate of background from material radioactivity to be below the pile-up spectrum in the region of interest. Since a total activity of the order of MBq is required for the final phase of the ECHo experiment, the number of single detector pixels to be operated in parallel is in the order of 10^5, considering an activity of 10 Bq per pixel. A multiplexed read-out scheme able to reduce the total number of read-out channels and to preserve the performances of the single detector pixels is essential for the ECHo experiment. Thus, the compatibility of the detector technology with the multiplexing system is a substantial requirement. For MMC detectors a microwave SQUID multiplexing system (μMUXing) can be adopted and it is currently under development [Weg18b] [San19]. The basic concept of μMUXing is presented in section 3.1.3.

The final analysis of the measured ^{163}Ho EC spectrum to extract information on the electron neutrino mass relies on an accurate experimental spectral shape. For this reason, the definition of the energy scale and the precise determination of the energy of each event play decisive roles.
The energy scale is calculated with a calibration function that depends on the physics of the detector. Uncertainties in the calibration function lead to uncertainties in the position of the end-point of the spectrum, which in turn result in systematic errors in the analysis for the determination of the neutrino mass. For MMCs an almost ideal linear calibration function for energies up to 10 keV was demonstrated, with deviations below 1% that can be well described by the thermodynamical model of the detector [Sik20].
The precision in the estimation of the energy of each event represents the energy resolution of the detector, which is defined as the full width at half maximum of the Gaussian detector response. A poor energy resolution would lead to a smearing of the measured spectrum and it would deteriorate the ability to distinguish ^{163}Ho from background events. An energy resolution of few eV is required to sufficiently resolve the spectral shape. With MMCs developed for X-ray spectroscopy an energy resolution of 1.6 eV FWHM at 5.9 keV [Kem18] has been achieved, which is comparable with the best values presently reached by any kind of cryogenic detector at this energy scale.

In summary, the four detector properties that have a major influence on the final sensitivity of the experiment are the following:

1. time resolution, defined by the rise time;
2. compatibility with a multiplexed read-out system to reach sufficient statistics;
3. definition of the energy scale, resulting from the detector calibration function;

4. energy resolution of the detector.

Therefore, MMCs appear to be the best detector candidates for the ECHo experiment. The basic working concept of MMCs is presented in the following.

3.1.1 Working principle of metallic magnetic calorimeters

The general idea of microcalorimetry is based on the usage of an absorber, whose temperature is monitored with a sensitive thermometer. According to the first law of thermodynamics, the energy E of the particle that is absorbed is converted to a temperature change δT:

$$\delta T \approx \frac{E}{C} \tag{3.2}$$

where C denotes the total heat capacity of the detector.

In first order, C can be considered independent from the temperature, as the increase of temperature ΔT is small if compared to the operational temperature of the detector. Assuming a detector heat capacity in the order of picojoules, $C \approx 1\,\mathrm{pJ}$, an energy input $E = 3\,\mathrm{keV}$ leads to an increase of temperature $\Delta T \approx 0.5\,\mathrm{mK}$, while the operational temperature is in the order of $10 - 20\,\mathrm{mK}$.

In the case of MMCs, the temperature information is extracted from the change of magnetisation of a paramagnetic sensor sitting in a static magnetic field. In order to make MMCs suitable for the ECHo experiment, two specific features have been introduced, namely the enclosure of the ^{163}Ho source in the detector and a microwave SQUID multiplexing read-out. These two aspects are discussed in section 3.1.2 and in section 3.1.3, respectively.

For typical applications, a MMC detector consists of an absorber, in which the energy of the particle is converted to heat, and a paramagnetic sensor sitting in a constant weak magnetic field, which acts as thermometer and measures that energy. These two components are in strong thermal contact with each other, but they have a rather weak coupling to a thermal reservoir. The absorption of energy in the microcalorimeter leads to an increase in temperature and a decrease in magnetisation of the sensor. The change of magnetisation δM that follows an absorption of energy E is given by the simple relation [Fle05]:

$$\delta M = \frac{\partial M}{\partial T}\delta T = \frac{\partial M}{\partial T}\frac{\delta E}{C}\,. \tag{3.3}$$

.

In order to measure the magnetisation signal δM, the sensor is placed in a superconducting pick-up coil coupled with a sensitive Superconducting Quantum Interference Device (SQUID) magnetometer that reads out the corresponding change of magnetic flux: $\delta\Phi \propto \delta M$. Figure 3.1 shows a simple scheme of the different parts that compose the detector.

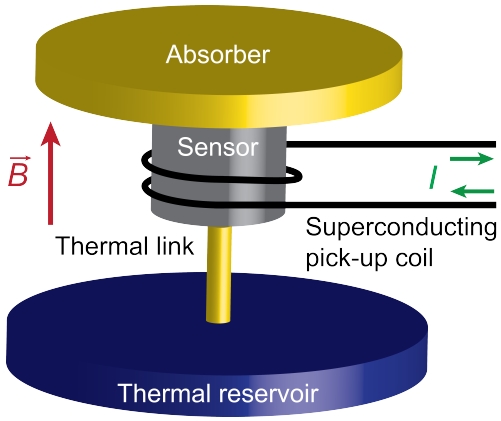

Figure 3.1: Schematic drawing of the different parts of a MMC detector. The weak magnetic field **B** is marked in red and the current signal in the superconducting pick-up coil is marked in green.

According to equation 3.3, the total heat capacity of the detector C should be minimised in order to gain signal size. Thus, small volumes and low working temperatures are favourable. Indeed, MMCs are typically operated at low temperatures, $T < 50\,\mathrm{mK}$, and the detector size is in the order of hundreds of micrometers for the detection of energies up to 20 keV. Additionally, the slope of the magnetisation response as function of temperature $\partial M/\partial T$ plays a role in the signal size.

Several aspects distinguish MMCs from other microcalorimeters. In contrast to calorimeters based on resistive sensors, where the signal is based upon a transport property, the response of MMCs is defined by near equilibrium thermodynamic properties of the sensor. Hence, it is possible to describe the physics of MMCs with remarkable fidelity. Moreover, MMCs are non-dissipative devices and no galvanic contact to the calorimeter itself is necessary to read out the sensor.
A detailed description of the single detector components and the theoretical background on MMCs is included in chapter 4.

3.1.2 Implantation of the ^{163}Ho source

In order to acquire a calorimetric spectrum, the ^{163}Ho source needs to be embedded inside the microcalorimeters, ensuring a 4π geometry and high quantum efficiency. For that, high-purity ^{163}Ho must be produced and implanted into the detectors.

Production and isolation of ^{163}Ho

^{163}Ho is an artificial, long-lived isotope, which decays only via EC. The ^{163}Ho half-life currently reported in literature is $\tau_{1/2} = 4570\,\mathrm{y}$ [Bai83] [Kaw88]. The production of high-purity ^{163}Ho, free from any long-lived radioactive contamination, is a prerequisite for the ECHo experiment.

^{163}Ho can be produced following two different pathways: charged-particle irradiation at accelerator facilities or neutron activation in a nuclear reactor, both leading to the inevitable co-production of significant amounts of unwanted radionuclides, especially in the second case. Chemical separation schemes based on ion-chromatography [Kor88] and isolation techniques [Moc15] can be applied to obtain ultrapure ^{163}Ho. However, the presence of the metastable isotope $^{166\mathrm{m}}$Ho with a half-life of 1200 y [Fal65] represents an issue in calorimetric measurements and it cannot be eliminated with chemical approaches. Thus, a final electromagnetic isotope separation step is always necessary to produce radiochemically ultrapure ^{163}Ho.

The advantages of the reactor-based production are the larger cross sections and the possibility to irradiate multiple samples simultaneously. As consequences, large amounts of ^{163}Ho can be produced comparatively quickly and the access to a reactor facility for irradiation time is comparatively easier.
The ^{163}Ho for the ECHo experiment is produced via thermal neutron activation of ^{162}Er, leading to ^{163}Er that subsequently decays to ^{163}Ho via EC with a half-life of 75 min. Two enriched ^{162}Er targets of 6.7 mg and 30 mg, respectively, have been irradiated in the high-flux reactor at the Institut Laue-Langevin (ILL) in Grenoble, France. The Er targets are prepurified prior irradiation to limit the production of undesired byproducts and to minimise the formation of $^{166\mathrm{m}}$Ho [Dor18]. After irradiation, the Er targets are chemically processed to isolate holmium samples. Different holmium samples are characterised using Inductively-Coupled-Plasma Mass Spectrometry (ICP-MS), Resonant Ionisation Mass Spectrometry (RIMS) techniques and Neutron activation analysis (NAA) to determine the amount of byproducts.

Two Ho samples have been produced with an estimated amount of ^{163}Ho of $(3.6 \pm 0.2) \times 10^{16}$ atoms and $(1.2 \pm 0.2) \times 10^{18}$ atoms, respectively. The desired product nuclide ^{163}Ho is the main component in both the Ho samples, with the exception of large amounts of stable sodium. The isobaric Dy-isotope ^{163}Dy contributes a share of only (0.08 ± 0.01) % and (0.10 ± 0.02) % to the 163 u isobar for the two samples, respectively, which represents an insignificant amount [Dor18]. The atom ratios of $^{166\mathrm{m}}$Ho:^{163}Ho varies for individual samples and reaches values $< 4 \cdot 10^{-4}$ in the sample with higher concentration, thus requiring a further suppression. This can be achieved by applying magnetic isotope separation during the implantation procedure, as described in the following.

Ionisation, separation and implantation of ^{163}Ho

In order to efficiently enclose high-purity ^{163}Ho in the ECHo detectors, the processes of ionisation, isotope separation and implantation have been optimised at the magnetic mass separator RISIKO (Johannes Gutenberg University, Mainz) shown in figure 3.2 [KT19a].

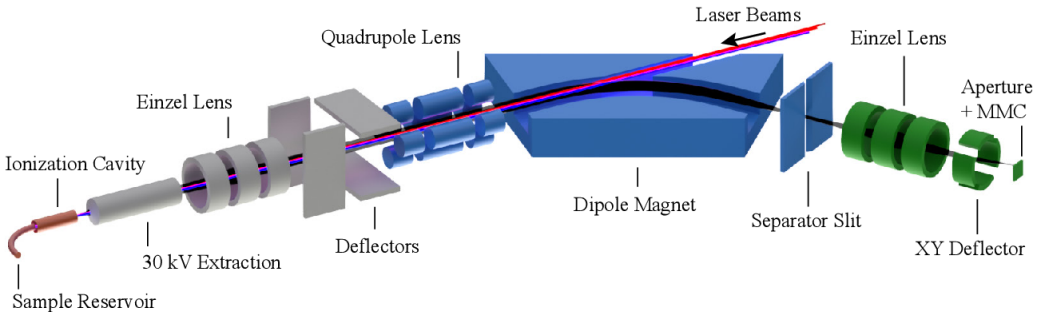

Figure 3.2: Schematic overview of the RISIKO mass separator. The laser beams are used to ionise the Ho sample, from which the 30 keV is extracted and guided trough the magnetic mass separation system towards the implantation in the MMC detectors [KT19a].

For the resonant ionisation of Ho, two lasers of the Mainz titanium-sapphire laser system [Rot11] are used in a Z-shaped resonator geometry, exploiting the intra-cavity frequency doubling technique [Son15] to reach an output power of about 500 mW and an high-quality beam profile. A new two-step blue-blue resonant laser ionisation scheme has been developed, ensuring full optical saturation and therefore enhancing the ionisation efficiency, which is estimated to be about 69% [KT19a].
The beam is accelerated using a 30 kV extraction potential and undergoes mass separation in a 60° double-focusing sector field magnet with a mass resolution of $m/\Delta m \geq 400$. At the magnet focal plane, the desired mass is separated from its neighbours by a slit. It has been shown that the contaminants with mass 166 u and higher, including the dangerous ^{166m}Ho, are suppressed to $\leq 1.4(6) \times 10^{-5}$ of the amount before the magnet, while ^{165}Ho is reduced to $1.0(5) \times 10^{-4}$ of the initial amount.

As it will be described in the next chapter, MMC detectors designed for the ECHo experiment feature a planar geometry with a size in the order of hundred of micrometers and they are microfabricated on silicon wafers. The area of a single detector chip, typically containing an array of 64 MMC pixels, is about 5 mm × 10 mm, depending on the specific design. In order to perform a single-chip implantation process, the detector chip is protected with a layer of photoresist and in the centre of each MMC pixel a reduced area is left uncovered to be implanted. The surface of the chip as well as the chip support are covered with a conductive gold layer which is connected

inside a Faraday cup to measure the ion current and to prevent possible charging up. A reduced aperture is placed in the flight path of the ^{163}Ho ions and mounted in a rotatable XY positioner that allows for an accurate adjustment. A dedicated Einzel lens and an electrostatic XY deflector are installed between the separation slit and the implantation region to improve the geometrical implantation efficiency. The ion beam density profile has been analysed in dependence of the ion current. The beam shape and dimensions remain almost constant within the range between 3 nA and 210 nA, reaching an implantation efficiency of about 20% [KT19a].

3.1.3 Read-out technology

The change of magnetisation of the MMC sensor that follows the deposition of energy in the detector is translated into a change of flux in a pick-up coil. In order to convert the flux signal into a voltage (or current) signal, Superconducting Quantum Interference Devices (SQUIDs) are used [Cla04]. Along with their large bandwidth, their almost quantum limited noise performance and their intrinsic compatibility with operational temperatures in the millikelvin range, SQUIDs are well suited for the read-out of MMC detectors. Typically, the input coil of a current-sensing SQUID is connected to the pick-up coil of the MMC detector, forming a superconducting flux transformer which transduces the change of magnetisation of the MMC sensor into a change of flux in the SQUID loop [Fle05] [Fle09].
The general working principle of a dc-SQUID as well as the coupling between detector and SQUID current sensor are described in more detail in section 4.3.4.

Single-channel read-out

A typical read-out configuration that improves the noise performances and provides sufficiently large system bandwidth to resolve the fast MMC rise time is the two-stage SQUID set-up [Cla04]. The scheme of a two-stage dc-SQUID configuration is depicted in figure 3.3. The signal from the MMC detector is coupled to a front-end dc-SQUID, the output of which is coupled to the input of a second-stage SQUID array (i.e. $\sim$ 16 dc-SQUIDs in series) that serves as low noise amplifier [Kem15].

In the two-stage set-up the front-end SQUID is operated in voltage bias mode by choosing the load resistor R_{g} much smaller than the dynamical resistance R_{dyn} of the front-end SQUID, to decrease the power dissipation on the SQUID chip and, in turn, on the detector chip. The second-stage amplifier SQUID array is operated in current bias mode. As a result, the change of magnetic flux Φ_{S} penetrating the front-end SQUID loop is converted into an output current which runs through the input coil of the amplifier SQUID, thus creating a change of magnetic flux in the

SQUID array.
The flux gain G_Φ is expressed by:

$$G_\Phi = \frac{M_{\mathrm{iA}}}{M_{\mathrm{dyn}} + R_{\mathrm{g}}/V_\Phi} \,. \tag{3.4}$$

Here, M_{iA} represents the mutual inductance between the amplifier SQUIDs and the corresponding input coil, V_Φ is the flux-to-voltage transfer coefficient of the front-end SQUID and $M_{\mathrm{dyn}} = R_{\mathrm{dyn}}/V_\Phi$ is the intrinsic current sensitivity of the front-end SQUID.

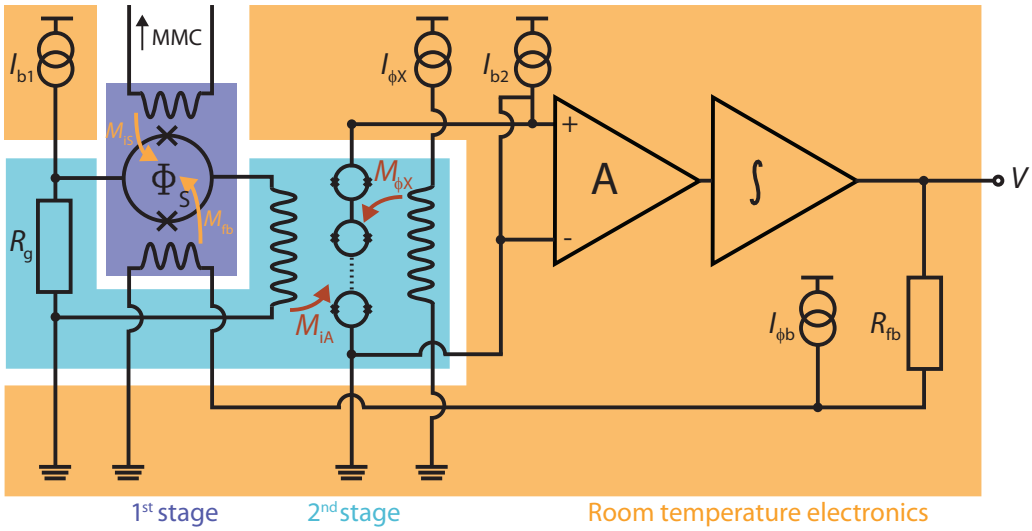

Figure 3.3: Schematic circuit of a two-stage SQUID configuration, where the first stage is marked in violet, the second stage is marked in blue and the room temperature electronics is marked in orange.

The output voltage of the second stage is amplified using a low-noise amplifier at room temperature and then fed into a voltage integrator, as shown in figure 3.3. The output voltage V_{out} is converted into a feedback current via the feedback resistor R_{fb}. The feedback current runs through a feedback coil coupled to the front-end SQUID with a mutual inductance M_{fb}. In this way, a negative flux feedback signal is created, which compensates the initial change of flux in the front-end SQUID. This flux-locked loop (FLL) feedback mechanism linearises the SQUID response, keeping the front-end SQUID at a constant working point [Cla04].

The hardware implementation of a two-stage SQUID set-up requires front-end SQUIDs and amplifier SQUIDs at the millikelvin stage as well as room-temperature feedback electronics and ten electrical wires to be routed from room-temperature to the SQUID cryogenic set-up. More details on the single-channel read-out chain for the ECHo-1k experiment are given in section 5.2.

Multiplexed read-out

The planned number of detectors for the future phases of the ECHo experiment is in the order of 10^5. Scaling up the single-channel read-out scheme is unfeasible, as the number of feedback electronics and electrical wires scales linearly with the number of detectors. As a matter of fact, this scenario would lead to intolerable power load to the cryogenic platform as well as to unaffordable costs. The solution to read out simultaneously a high number of detectors reducing the wiring is a multiplexing approach. Currently a dedicated microwave SQUID multiplexing technique (μMUXing) is under development [Weg18a] [Weg18b] [San19]. The multiplexed read-out scheme is shown in figure 3.4.

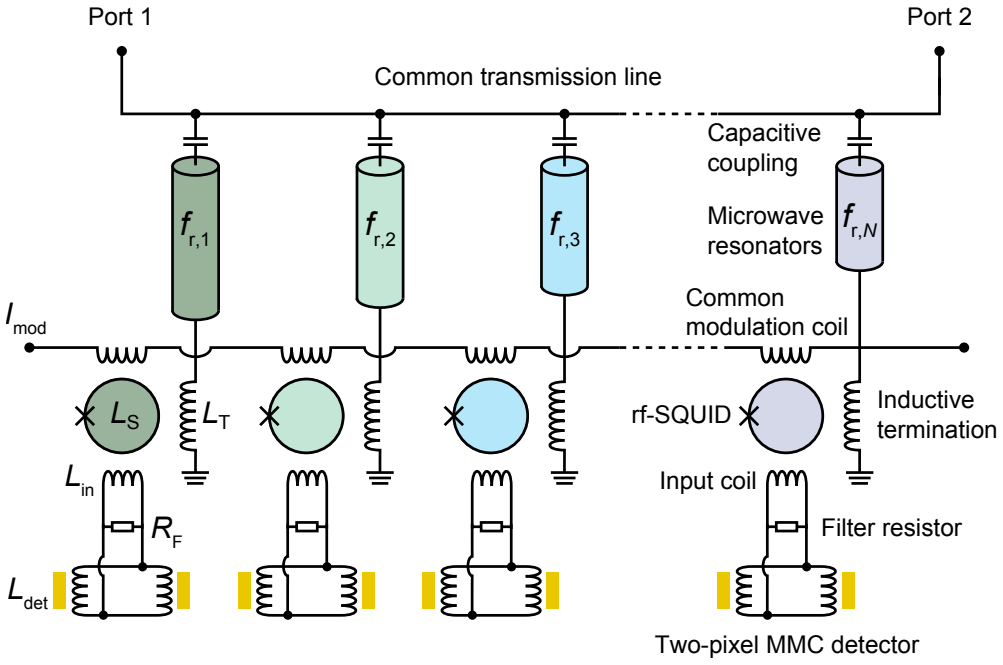

Figure 3.4: Schematic circuit diagram of the microwave SQUID multiplexer (μMUX). Each detector channel consists of two MMC pixels (yellow boxes) with the corresponding pick-up coil.

Each MMC channel is inductively coupled to a non-hysteretic rf-SQUID whose inductance changes as a function of the penetrating flux. The rf-SQUID is inductively coupled to a microwave-resonator with a unique resonance frequency. When an event occurs in the detector, the corresponding change of flux causes a change of inductance in the rf-SQUID which in turn modifies the resonance frequency of the resonator. All the resonators are capacitively coupled to a common transmission line.
A software-defined radio system (SDR) [San19] creates a frequency comb to monitor the transmitted amplitude and phase of each μMUX channel via a flux-ramp

modulation technique [Mat12] and from that the detector signals are reconstructed. This requires only one cryogenic high electron mobility transistor (HEMT) amplifier and two coaxial cables routed from room temperature to the μMUX chip. The total number of detectors that can be read out simultaneously is mainly limited by the available bandwidth and the level of tolerable crosstalk. Assuming a bandwidth of 4 GHz for each HEMT amplifier and requiring a frequency spacing of 10 MHz, about 400 detector channels, i.e. 800 MMC pixels, can be read out by each μMUX set-up.

3.2 Theoretical description of the ^{163}Ho spectrum

In the ^{163}Ho atom 67 electrons are present and 20 of them belong to the s and $p_{1/2}$ shells, exhibiting a significant overlap with the nucleus and thus having a finite probability to be captured. Considering the available energy for the decay and the angular momentum selection rules, electrons can be captured only from the 3s, $3p_{1/2}$, 4s, $4p_{1/2}$, 5s, $5p_{1/2}$ and 6s shells. Besides these seven main resonances, additional satellites appear in the measured ^{163}Ho EC spectrum [Gas17]. In order to interpret these structures and thus to reduce systematic uncertainties related to an inadequate description of the spectrum close to the end-point, a deeper understanding of the electronic relaxation after EC is required. A quantitative theoretical model of the ^{163}Ho EC spectrum is currently being developed through *ab initio* calculations, based on the theory of core level spectroscopy [Bra18] [Vel19b] [Bra20].

3.2.1 *Ab initio* calculation of the ^{163}Ho spectrum

The standard approach to calculate the ^{163}Ho EC transition probability, i.e. the ^{163}Ho EC energy spectrum, is to apply Fermi's goldern rule:

$$\frac{\mathrm{d}\Gamma}{\mathrm{d}\omega} \propto \sum_{\Psi_{\mathrm{Dy}^*+\nu}} |\langle \Psi_{\mathrm{Dy}^*+\nu}| \, T \, |\Psi_{\mathrm{Ho}}\rangle|^2 \, \delta(E_{\mathrm{Ho}}, E_{\mathrm{Dy}^*} + E_\nu) \, . \tag{3.5}$$

Here, Ψ_{Ho} is the many-body ground state of the ^{163}Ho atom (including electrons and nucleus), $\Psi_{\mathrm{Dy}^*+\nu}$ is one of the many excited states of Dy with one additional electron neutrino. The respective energies of the listed states are E_{Ho} and $E_{\mathrm{Dy}^*} + E_\nu$. Finally, T is defined as the transition operator which removes an electron from the ^{163}Ho atom and transforms a proton from the nucleus to a neutron, simultaneously creating an electron neutrino.

Considering the neutrino-matter interaction as negligible, the wave function $\Psi_{\mathrm{Dy}^*+\nu}$ can be factorised as a product of the nuclear wave function, the electronic wave function and the neutrino wave function. The transition operator T can be similarly

expanded. In this way, it is possible to sum explicitly over all neutrino momentum states and to write the following expression [Bra18]:

$$\frac{\mathrm{d}\Gamma}{\mathrm{d}E_{\mathrm{EC}}} \propto \sum_{\Psi^{e^-}_{\mathrm{Dy}^*}} \left| \left\langle \psi^{e^-}_{\mathrm{Dy}^*} \right| T_{e^-} \left| \psi^{e^-}_{\mathrm{Ho}} \right\rangle \right|^2 \times \delta(E_{\mathrm{EC}} - E_{\mathrm{Dy}^*} + E_{\mathrm{Dy}})(Q_{\mathrm{EC}} - E_{\mathrm{EC}}) \sqrt{(Q_{\mathrm{EC}} - E_{\mathrm{EC}})^2 - m_\nu^2} \tag{3.6}$$

where $Q_{\mathrm{EC}} = E_{\mathrm{Ho}} - E_{\mathrm{Dy}}$ is the difference between the Ho and Dy atomic ground states and $E_{\mathrm{EC}} = Q_{\mathrm{EC}} - E_\nu$ is the energy of the excited Dy atom.

The application of equation 3.6 involves the sum over all the possible excited states of the Dy atom, which are in principle infinite, each carrying an infinitesimally small contribution to the spectrum. Therefore, the sum of the Dy excited states cannot be considered as a feasible approach. A numerically more convenient solution can be implemented using the Green's function formalism in the Lehmann representation, which describes the time evolution of the state created after an EC event through a Fourier transformation [Bra18]. In this framework, the challenge is reduced to provide an accurate description of the atomic ground state of ^{163}Ho and to model the time evolution of the wave function after an EC event. Several second-order effects come into play at this point, which affect the resulting spectrum. In the following paragraphs the relaxation processes that are included in the *ab initio* calculation of the spectrum are listed and the corresponding effects on the ^{163}Ho EC spectrum are shortly overviewed [Bra18] [Vel19b] [Bra20].

Spectrum with no relaxation processes When an electron is captured from a ns or $n\mathrm{p}_{1/2}$ shell of the ^{163}Ho atom, a core hole is created in the corresponding orbital. If the wave function was frozen into this state, the resulting spectrum would contain separate lines corresponding to the orbitals from which the electron was removed. In this simplified scenario, the ^{163}Ho EC spectrum is described by the neutrino phase-space term multiplied by the sum of the Lorentzian resonances, as discussed in section 2.2.3 and reported in equation 2.22.

Spectrum accounting for modified nuclear and core hole potentials An additional relaxation process that modifies the simple model presented above is caused by the change of nuclear and core hole potentials when an electron is captured and a proton is transformed into a neutron. Due to the spherical shape of the nuclear potential and the conservation of angular momentum, scattering of the holes can occur in orbitals with the same angular momentum but different principle quantum number, i.e. from ns to ms and from $n\mathrm{p}_{1/2}$ to $m\mathrm{p}_{1/2}$. The overall influence on the

EC ^{163}Ho spectrum consists of a relatively modest shift of the major peaks of up to 3 eV.

Spectrum accounting for inter-core relaxation due to Coulomb repulsion A further relaxation channel includes scattering between core shells with different angular momentum as an effect of Coulomb interaction. In this process a hole moves to a different excitation energy level. The angular momentum of all electrons together is conserved, but this does not apply to the angular momentum of a single electron. As a result, $p_{3/2}$ electrons can scatter into $p_{1/2}$ holes and d electrons can scatter into s holes, transferring their angular momentum to 4f electrons in the valence shell. These relaxation processes lead to core holes in shells from which EC is not directly possible. Hence, the corresponding effect on the EC ^{163}Ho spectrum is the appearance of additional peaks at the excitation energies of the $3p_{3/2}$, 3d, $4p_{3/2}$ and 4d orbitals. The amplitudes of these peaks depend on the Coulomb interaction and on the energy difference between the states that participate in the scattering process and they result smaller than the amplitudes of the main lines.

Spectrum accounting for relaxation into all locally bound states The next level of relaxation accounts for changes in the number of core holes and valence electrons, due to Coulomb interaction. This occurs if a core electron deexcites filling the hole created after the EC event and transferring energy to another core electron, which scatters into the valence shell. Specifically, in this so called Auger decay, two electrons are moved from any of the occupied shells (i.e. 1s-6s, 2p-5p, 3d-4d shells) to the 4f orbital and the ns or $np_{1/2}$ orbitals, respectively. In the final state, the atom is left with two core holes. The corresponding scattering amplitude depends on the Coulomb repulsion, which is maximised when the overlap between the involved orbitals is large. As a result, the following Auger states with two core holes and an additional electron in the 4f shell are most significant[1]: $4p4d4f^{12}$, $3d4d4f^{12}$ and $3d3d4f^{12}$. This level of the theoretical model describes the shoulders of the 3s (MI) and 4s (NI) and additional peaks emerge in the region between the $3p_{1/2}$ (MII) and 4s (NI) lines as well as on the left flanks of the 3s (MI) and $3p_{1/2}$ (MII) lines. Due to Coulomb repulsion, the peaks are split into multiplets. The major result of this calculation is the ability to reproduce the structures above the 4s (NI) line and the split width of the $4p_{1/2}$ (NII), which have been experimentally observed. The calculated spectrum including relaxation into all locally bound states is shown in figure 3.5.

[1]Here the following notation is used: $n_1l_1n_2l_24f^k$, where $n_1l_1n_2l_2$ indicate the two core hole states and $4f^k$ indicates the additional electron in the valence shell.

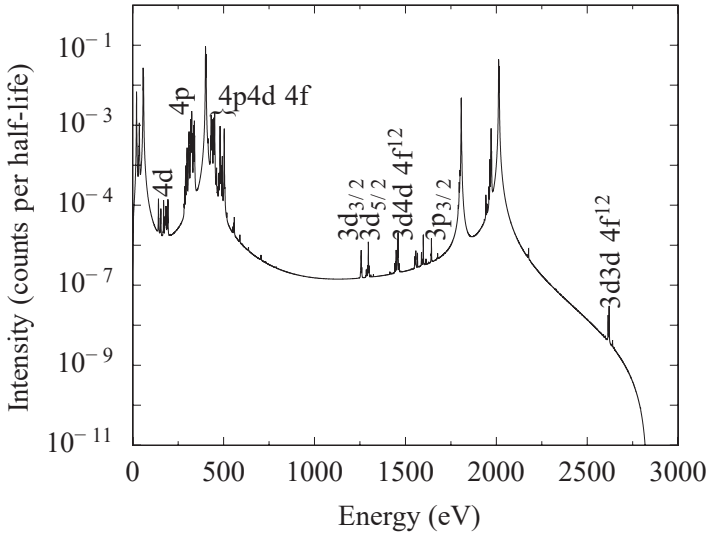

Figure 3.5: Theoretical spectrum including relaxation into all locally bound states, calculated with a Lorentzian linewidth of 1 eV to reveal the contributions of the different excited states. The labels indicate which shells host holes and if an additional electron is present in the 4f shell. Figure reproduced from [Bra18].

Spectrum accounting for relaxation into unbound states When a core electron is captured by the nucleus, the resulting modified Coulomb interaction in the atomic shells cannot only lead to electrons scattering into previously unoccupied orbitals, but also to electrons scattering into unbound orbitals. In this last case, an electron scatters from an occupied orbital into the previously created core hole, gaining energy that is transferred to a second electron, which scatters from an occupied orbital into the continuum. This process is known as the Auger-Meitner decay. For example, states with energy just above the 4s (NI) line can be reached by capturing a 4p electron followed by an Auger-Meitner decay transferring a 4s electron to the 4p shell and emitting a 4f valence electron into the vacuum. These channels open at energy slightly above the binding energy of the 4s shell. Overall, the resulting effect on the spectrum is an asymmetric Mahan line-shape broadening of the local atomic multiplets, which significantly improves the agreement between theory and experiment [Vel19b] [Bra20]. Figure 3.6 shows a comparison between the *ab initio* theory of the EC ^{163}Ho spectrum with a Lorentzian broadening and with a Mahan broadening and the experimental data.

The demonstrated presence of high-energy tails for the main resonances, including the MI line, increases the expected fraction of events in the end-point region of the spectrum, where the non-zero neutrino mass leaves the major imprint. The current theoretical description [Vel19b] [Bra20] shows an increase of the count rate in the

region between 2.6 keV and 2.838 keV of about a factor of two with respect to the simplest theoretical model (equation 2.22), allowing to reach the target sensitivity with half of the exposure. Furthermore, this level of the theoretical description shows how the spectral shape close to the end-point becomes to a very high degree of accuracy linear on a logarithmic scale [Bra20]. The deviation from a straight line in the region of the Q-value is related to the effective neutrino mass, allowing for a relatively simple approach of the analysis for the determination of the effective electron neutrino mass.

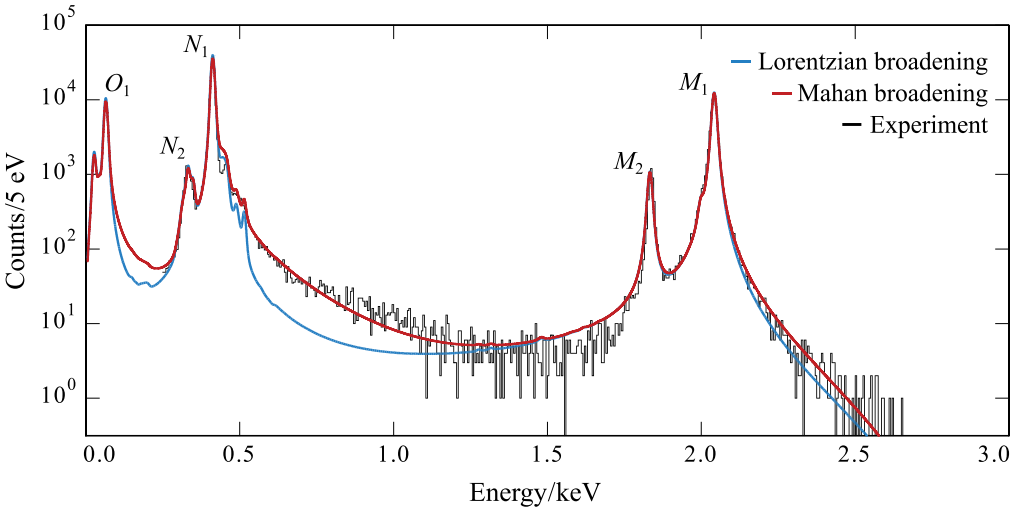

Figure 3.6: Measured EC ^{163}Ho spectrum (black) compared to the theoretical calculation broadened using a Lorentzian line-shape (blue) and a Mahan line-shape (red). In both cases a further Gaussian broadening to account for the detector resolution is added. Figure reproduced from [Vel19b].

3.3 Q-value determination

The precise knowledge of the Q_{EC}-value of the EC decay of ^{163}Ho is a crucial requirement for the success of the ECHo experiment and it has been set as one of the first goals of the ECHo collaboration. The results obtained in the past with indirect measurements carried out by several independent experiments showed a discrepancy of few hundred eV, scattering from $Q_{\mathrm{EC}} \approx 2.5$ keV to $Q_{\mathrm{EC}} \approx 2.9$ keV. In particular, the results obtained with cryogenic microcalorimetry [Gat97] [Ran12] exceeded the recommended Q_{EC}-value of 2.555(16) keV of the Atomic-Mass Evaluation AME2012[2] [Wan12]. Figure 3.7 shows an overview of the results obtained in different measurements of Q_{EC}.

[2]The AME2012 recommended Q_{EC}-value has been obtained by averaging only proportional counter data and storage-ring measurements.

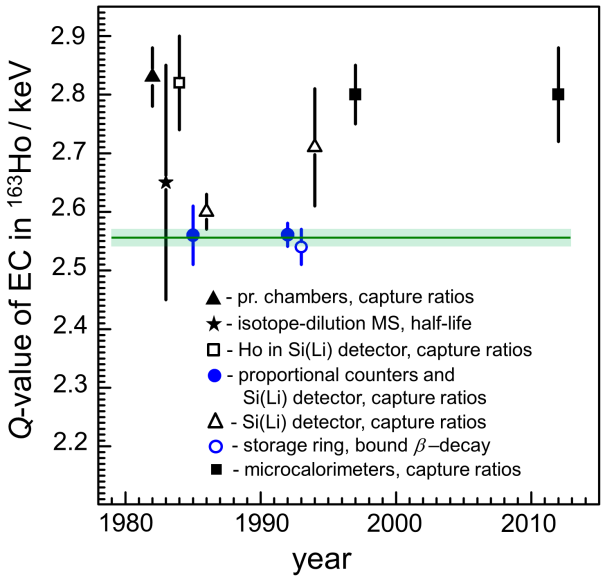

Figure 3.7: Overview of the scattered results obtained by different groups in the measurement of Q_{EC}. Different markers indicate different experimental methods. The green line and the shaded band correspond to the recommended Q_{EC}-value and its uncertainty [Wan12], obtained by averaging only the blue data points in the plot. Figure reproduced from [Eli15].

In order to solve the controversy, a direct method was required, measuring the mass difference of the initial and final states of the EC decay, namely the difference between the mass of the daughter atom ^{163}Ho and the mass of the mother atom ^{163}Dy:

$$Q_{\mathrm{EC}} = m_{\mathrm{Ho}} - m_{\mathrm{Dy}} = m_{\mathrm{Dy}} \left(\frac{m_{\mathrm{Ho}}}{m_{\mathrm{Dy}}} - 1 \right) . \tag{3.7}$$

Hence, an accurate measurement of Q_{EC} reduces to a high-precision measurement of the ratio of the two masses $m_{\mathrm{Ho}}/m_{\mathrm{Dy}}$, as the absolute mass of ^{163}Dy is well known [Wan12].

An uncertainty of a few ten eV on the Q_{EC}-value is sufficient for the ECHo experiment to enable a sensitivity below 10 eV on the effective electron neutrino mass. For the future phases of ECHo, which aims to reach sub-eV sensitivity, the uncertainty on Q_{EC} must be approximately 1 eV. Currently, the only technique providing the required accuracy is high-precision Penning-trap mass spectrometry (PTMS) [Bla13]. In a Penning trap the free cyclotron frequency f_{C} of a nuclide ion of charge q in a strong magnetic field B is measured and the nuclide mass m can be determined using the relation:

$$f_{\mathrm{C}} = \frac{1}{2\pi}\frac{q}{m}B\,. \tag{3.8}$$

The magnetic field must be homogeneous and the ion must be confined in a well defined volume for some seconds to allow for the precise measurement of the cyclotron frequency. This configuration is achieved with a Penning trap set-up, i.e. superimposing a static three-dimensional quadrupole electric field on the magnetic field and thus creating a potential well along the magnetic field lines [Bro86]. Because of the presence of the electrostatic field, the motion of the ion in a Penning trap is not described by a simple cyclotron motion with frequency f_{c}, but a combination of three independent harmonic eigenmotions, two circular motions, commonly referred to as magnetron $(-)$ and reduced cyclotron motion $(+)$, and an axial motion (z). According to [Bro81], the following relation is valid for Penning trap systems with small imperfections in the alignment of the electronic and magnetic field:

$$f_{\mathrm{c}}^2 = f_+^2 + f_-^2 + f_z^2\,. \tag{3.9}$$

On the level of few parts in 10^{10} a simpler relation between the frequencies of the circular motions f_- and f_+ and the pure cyclotron frequency f_{c} holds:

$$f_{\mathrm{c}} = f_+ + f_-\,. \tag{3.10}$$

The ratio of the free cyclotron frequencies of two ions with the same charge state measured in the same magnetic field is equal to the ratio of their masses.

Presently, the most precise determination of the Q_{EC}-value has been achieved in 2015 by the ECHo collaboration [Eli15] with the Penning-trap mass spectrometer SHIPTRAP, located at the GSI-Helmholtz centre in Darmstadt [Blo07]. Singly-charged ions of ^{163}Ho and ^{163}Dy were produced by laser irradiation of the corresponding Ho and Dy samples. The production of the Ho sample is described in section 3.1.2. It is worth mentioning that the purity requirements on the sample for the PTMS measurement differ from the ones for the detector implantation, as in the first case the presence of ions of mass numbers other than 163 will generally not reach the measurement trap, while contamination with ^{163}Dy can lead to systematic uncertainties in the PTMS measurements and needs to be under control. The ^{163}Ho$^+$ and ^{163}Dy$^+$ ions were transferred into a preparation trap for cooling and separation of undesired impurities via the mass-selective buffer gas cooling technique [Sav91] and further transferred into a measurement trap for the measurement of the cyclotron frequency f_{c}. The determination of f_{c} relies on equation 3.10 and it exploits the novel Phase-Imaging Ion-Cyclotron Resonance (PI-ICR) technique, based on the measurements of the phases of the radial ion motions in the trap after a given period

of excitation-free propagation. This approach extends the achievable precision to a level of few parts in 10^{10} [Eli13b] [Eli13a].

From the final frequency ratio of the two ions $R = 1.00000007867(20_{\text{stat}})(10_{\text{sys}})$, the resulting mass difference is:

$$\Delta m = Q_{\text{EC}} = 2.833(30_{\text{stat}})(15_{\text{sys}})\,\text{keV}\,. \tag{3.11}$$

This result deviates by more than seven sigma experimental uncertainty from the recommended value of the Atomic-Mass Evaluation AME2012 [Wan12], but it perfectly agrees with microcalorimetric measurements [Gat97] [Ran12]. The new recommended value of the Atomic-Mass Evaluation AME2016 for the Q_{EC}-value of ^{163}Ho is 2.834 keV [Wan17].

The ultimate goal of the ECHo collaboration - the determination of the neutrino mass on a sub-eV level - requires an unprecedentedly high precision of 1 eV in the measurement of the Q_{EC}-value. For that, the Penning trap mass spectrometer PENTATRAP is currently being developed at the Max-Planck Institute for Nuclear Physics, Heidelberg. PENTATRAP will feature five identical cylindrical Penning traps to provide the possibility of flexible measurement schemes and fast exchanges of ions between the traps. The aim of PENTATRAP is to reach an accuracy of $< 10^{-11}$ in the measurements of mass ratios of highly charged ions [Rou12].

3.4 Background studies

The information on the effective electron neutrino mass in the ^{163}Ho EC spectrum lies mainly in the end-point, where only a very small fraction of EC events fall. About 5×10^{-10} events are expected within the last 10 eV before the Q-value. The exiguity of signal in the region of interest does not allow a simple subtraction of the expected background from the observed number of events. It is necessary to suppress the single background sources so that the sum of them is maintained below the level of the signal rate.

The potential background sources for the ECHo experiment can be classified in the following categories:

1. unresolved pile-up;
2. bulk contaminations of the detectors;
3. environmental radioactivity;
4. cosmic radiation.

For most of the background sources, such as cosmic radiation, γ and α particles, the hit of the primary radiation on the detector typically leads to relatively high-energy signals which do not interfere with the end-point region of interest around $Q_{\mathrm{EC}} \approx 2.8\,\mathrm{keV}$. Nonetheless, a partial deposition of energy in the interaction with the detector or the creation of secondary radiation with lower energy can create background events that would lead to artificial structures in the ^{163}Ho spectrum, possibly within the region of interest. Similarly, X-rays and low energy electrons emitted in atomic de-excitations following radioactive decays of unstable nuclides represent a potential source of background. In order to investigate and quantify these background sources, the usage of Montecarlo simulations is the most effective approach. In the following the different background sources are shortly discussed [Gas17] [Goe20].

Unresolved pile-up As discussed in section 3.1, unresolved pile-up events represent an irreducible source of background, which can be kept under control by guaranteeing a sufficiently fast response of the detectors and by tuning accordingly the ^{163}Ho activity per detector pixel. The unresolved pile-up level defines the allowed total background level from other sources. The sensitivity goals of the ECHo-1k and ECHo-100k phases presented at the begining of the chapter are defined assuming a total background level below $10^{-5}\,\mathrm{counts/eV/det/day}$.

Bulk contaminations The background represented by bulk contaminations in the detectors is expected to be dominated by co-implanted radioisotopes. In particular, the metastable β^-/γ-emitter isotope $^{166\mathrm{m}}$Ho poses potential issues, due to its long-life of 1200 y [Fal65]. The adopted strategies to guarantee the production and implantation of radiochemically ultrapure ^{163}Ho samples have been already reviewed in section 3.1.2.

Environmental radioactivity Radioactive contaminants are inevitably present in the raw materials of the experimental set-up. Moreover, the contamination level may further increase during the storage and the assembly of the parts, due to cosmogenic activation and exposure to radon contaminated air and dust particles. Thus, radiopure components are selected and the materials used for the set-up assembly will undergo a dedicated screening using low background gamma spectrometry. The information from the screening as well as from dedicated background analysis based on muon-veto measurements will be used to determine the background model.

Cosmic radiation Cosmogenic muons as well as the hadronic part of cosmic rays and the corresponding cascades of secondary particles contribute to the background. The ECHo-1k and ECHo-100k experiments are performed above ground and therefore the cosmic radiation is not suppressed. The corresponding background signals can be tagged by synchronising the signal of the detectors with the output signals of a active muon veto or by using pulse shape discrimination techniques. In order to investigate both these strategies, dedicated measurements have been performed during the ECHo-1k phase, using a specifically designed scintillator-based muon veto system [Goe20]. From a preliminary analysis, the implementation of pulse shape discrimination seems to lead to promising results in the identification of background events.

4. Metallic magnetic calorimeters

Metallic magnetic calorimeters (MMCs) are cryogenic microcalorimeters operated at millikelvin temperature, whose operation principle is based on a paramagnetic temperature sensor. The sensor magnetisation changes when the detector temperature increases, giving rise to a signal.

MMCs are composed of an energy absorber, optimised in size and material to have high absorption efficiency for the physics case of the particular experiment, a paramagnetic temperature sensor in a constant magnetic field which is thermally tightly connected to the absorber and finally a weak thermal link to a thermal bath, which defines the idle temperature of the detector. A superconducting coil, well magnetically coupled to the sensor, is used both for providing the constant magnetic field thanks to a persistent current and as a pick-up coil for the detection of the magnetisation change in the sensor following a change of temperature of the detector.

As previously discussed in section 3.1.1, the fast response as well as the outstanding energy resolution and the reliable calibration make MMCs the best choice as detector technology for the ECHo experiment. Besides the use for the calorimetric measurement of the EC ^{163}Ho for the determination of the effective electron neutrino mass, applications of MMCs range from high resolution X-ray spectroscopy of highly charged heavy ions [Hen15] to rare events searches, as neutrinoless double beta decay [Ale19], as well as investigations on molecular fragmentation in interaction with electron beams [Gam16].

The general working principle of MMCs has already been introduced in section 3.1.1. The essential sub-components of the detector are addressed in more detail in the following sections 4.1 and 4.2. Thermodynamic models that well describe the properties of the detector are presented and the conditions to optimise the detector performances are discussed. The detector geometry and the coupling between the detector and the SQUID-based read-out are illustrated in section 4.3. The final detector response and the achievable energy resolution are derived in section 4.4. Finally, since the detector development for the ECHo experiment requires to embed the ^{163}Ho source inside the MMC absorber, the related expected effects on the detector performances are discussed in section 4.5.

4.1 Particle absorber

In principle, a microcalorimeter could be functional without the need of an absorber, as the energetic particle could be stopped directly by the sensor. However, this strategy substantially limits the optimisation of the detector, preventing to flexibly adapt geometry, active area and material to the particular application. Employing a separate element which is dedicated to the absorption of the energy is, therefore, a preferable approach. The absorber needs to guarantee sufficient stopping power but small heat capacity, not to spoil the detector response, according to equation 3.3. Furthermore, the absorber must exhibit good thermalisation properties to ensure a fast and complete thermalisation after the particle energy is deposited. Finally, the layout and the material of the absorber should be compatible with the microfabrication processes used to fabricate the detector.

4.1.1 Absorber material

The absorber material is chosen according to the particular application and to the energy range of the particles to be detected. A good thermalisation behaviour requires a high thermal conductivity, which is given by the presence of conduction electrons and thus it comes along with a dominant electronic contribution to the specific heat at low temperatures. In general, the specific heat c of a material consists of two contributions, the electronic contribution c_e and the phononic contribution c_ph:

$$c = c_\mathrm{e} + c_\mathrm{ph} = \gamma T + \beta T^3 \tag{4.1}$$

with proportionality constants β and γ (the Sommerfeld coefficient). In case the absorber material is a dielectric, only the phononic contribution is left in 4.1.

For this reason, dielectrics are attractive candidates as absorber materials due to the small heat capacity at low temperatures, but they are characterised by relatively long recombination times. The fraction of charge that is trapped in lattice defects differ from one event to another. These statistical fluctuations have a negative impact on the resolution [McC93]. Superconductors at temperatures below their critical temperature share the same convenient property of dielectric material, as the Cooper pairs add a negligible contribution to the specific heat. The downside is a not yet well understood thermalisation behaviour, probably due to the creation of quasiparticles with long recombination times [Cos93]. Therefore, for detection of low energetic particles, the best choice is to employ normal metals as absorber materials. In contrast to dielectrics and superconductors, normal metals are free of metastable states and their good thermal conductivity ensures a fast thermalisation. The price

to pay, however, is the presence of conduction electrons, which bring a contribution to the specific heat, $c_e \propto T$, that at low temperatures $T \to 0$ dominates over the phononic contribution, $c_{ph} \propto T^3$. For the detection of particle in the high energy range or for application requiring large masses, dielectric absorbers may be preferred.

The absorber material used for the fabrication of MMC arrays for the ECHo experiment is gold. Along with its very high stopping power and the its suitability for microlithography techniques, gold is a very attractive candidate not only for ECHo detectors, but for many other applications [Hen15] [Gam16].

Thermalisation mechanisms in gold absorbers If an X-ray photon is stopped by a gold absorber, the primary resulting interaction mechanism is the generation of an energetic electron via photoelectric effect. The energy of the electron rapidly decreases due to electron-electron scattering and after about 0.1 ps the mean energy of the electrons is reduced to 0.1 eV. This energy is further reduced by generating high-frequency phonons, which interact with the conduction electrons and, thus, thermalise. Eventually the phononic and electronic systems reach a thermal equilibrium. Most of the energy is returned into the electronic system, being characterised by a larger heat capacity at low temperature. The complete thermalisation within the full absorber volume occurs via thermal diffusion. The corresponding time scale depends mainly on the absorber geometry. Considering an absorber with an area of $250\,\mu m \times 250\,\mu m$ and a thickness of $5\,\mu m$ made of pure gold with a resistance ratio of $R_{300\,K}/R_{4\,K} \approx 3$, the thermalisation time is estimated to be about $0.1\,\mu s$ [Fle05].

The thermalisation process following the deposition of energy in the absorber can be impaired by the loss of athermal phonons. This issue occurs if phonons are able to escape the absorber, pass through the sensor and be thermalised only in the detector substrate. As a consequence, part of the particle energy would not be detected. Low-energy tails in the energy spectra acquired with MMCs have been observed and attributed to this effect [Fle09]. In order to reduce the probability of loss of athermal phonons, the contact area between sensor and absorber must be reduced, for instance introducing stem structures between the sensor and the absorber, as described in detail in section 5.1.1.

4.2 Temperature sensor

The distinctive feature of MMCs, if compared to other microcalorimetry techniques, is the magnetic nature of the detection mechanism. The paramagnetic sensor converts the increase of temperature following the energy deposition into a change of magnetisation, according to equation 3.3. The magnetic response of the sensor defines the sensitivity of the detector. The choice of the paramagnetic material is discussed in the next section and the fundamental thermodynamic properties of the sensor, namely the specific heat and the temperature-dependent magnetisation, are derived in section 4.2.2. Finally, the sensor response and the related influence of nuclear spins are analysed in sections 4.2.3 and 4.2.4.

4.2.1 Sensor material

As in the case of the absorber, the choice of the sensor material is the result of a compromise, since different and in part conflicting requirements have to be taken into account. The priority demands for application in particle detection are high sensitivity and fast thermalisation time.

Considering the sensitivity, cerium magnesium nitrate (CMN) has been considered an attractive candidate for the operation in the temperature range of few millikelvin and it has been investigated at the early stages of development of MMC detectors. The contribution to the heat capacity from interacting magnetic moments is comparably small, despite the high spin concentration. However, the main disadvantage of dielectric materials, including CMN, is the extremely weak coupling between the spin system and the phononic system at low temperatures. The corresponding relaxation times are in the order of seconds. Thus, employing dielectric as sensor material critically slow down the detector response to values that are unacceptable for applications in particle detection [Uml92].

A solution to this problem consists in embedding the magnetic ions in metallic host materials [Ban93]. In this case, a fast thermalisation is guaranteed by the rapid energy exchange between the conduction electrons and the localised spins. Time constants well below 1 µs are easily obtained. The drawbacks that come along with the usage of metallic materials are the additional contribution to the heat capacity and the indirect exchange interaction between the localised spins (RKKY[1] interaction), both due to the conduction electrons. The RKKY interaction leads to a further increase of the heat capacity and a reduction of the temperature dependence of the magnetisation. Thus, rare-earth elements are preferred, as the RKKY interaction is comparably small.

[1] Ruderman-Kittel-Kasuya-Yosida.

The MMC detectors fabricated and operated in the framework of this work feature a sensor made of dilute erbium ions embedded in silver (Ag:Er). The typical concentration is several hundred ppm. At this low concentration level, erbium atoms replace silver atoms at regular fcc lattice sites, donating three electrons to the conduction band. The resulting Er^{3+} ions have the electron configuration $[Kr]4d^{10}4f^{11}5s^25p^6$, with a partially filled 4f orbital, which leads to the paramagnetic behaviour. The influence of the crystal field is suppressed due to the small radius of the 4f shell, which is surrounded and shielded by the much larger 5s and 5p shells [Fle05]. Hence, the magnetic moment $\boldsymbol{\mu}$ can be calculated assuming **LS** coupling as [Ens05]:

$$\begin{aligned} \boldsymbol{\mu} &= g\mu_\mathrm{B}\mathbf{J} \\ &= \left(1 + \frac{J(J+1) + S(S+1) - L(L+1)}{2J(J+1)}\right)\mu_\mathrm{B}\mathbf{J} \end{aligned} \tag{4.2}$$

where μ_B denotes the Bohr magneton. According to Hund's rules, $S = 3/2$, $L = 6$ and $J = S + L = 15/2$. The resulting Landé factor is $g = 6/5$.

This description holds for temperatures above 100 K [Wil69], but at lower temperatures the crystal field effects are not any longer negligible. The sixteen-fold degenerate ground state is split into multiplets, the lowest of which is separated from the next one by $\Delta E/k_\mathrm{B} \approx 25\,\mathrm{K}$ [Hah92]. Hence, at sufficiently low temperatures and assuming a small external magnetic field, the behaviour of erbium in silver can be described as a two-level system with effective spin $\tilde{S} = 1/2$ and effective Landé factor $\tilde{g} = 34/5$ [Fle05]. At temperature below 50 mK, the exchange interaction between magnetic moments becomes more significant, decreasing the dependence on temperature of the magnetic susceptibility [Fle05]. Finally, at temperature below 0.9 mK a transition to spin glass state is observed [Fle00].

4.2.2 Thermodynamic properties

The thermodynamic properties that determine the performance of MMC detectors are the heat capacity and the magnetisation. As discussed in the previous section, the sensor can be considered as an ensemble of non-interacting magnetic moments, in first approximation. In order to provide a precise quantitative analysis, however, the indirect exchange interaction between the spins needs to be included in the calculation.

Model with non-interacting magnetic moments

Let us first consider the sensor as a system of N non-interacting spins in a volume V. At low temperature ($T \approx 10 - 100\,\mathrm{mK}$) only the ground state of the crystal-field is occupied and, in the presence of an external magnetic field B, the system acts as a two-level system with Zeeman energy splitting $E_\mathrm{Z} = \tilde{g}\mu_\mathrm{B}B$.

The **heat capacity** C_s of such a system is given by the Schottky expression [Ens05]:

$$C_\mathrm{s} = Nk_\mathrm{B}\left(\frac{E_\mathrm{Z}}{k_\mathrm{B}T}\right)^2 \frac{e^{E_\mathrm{Z}/k_\mathrm{B}T}}{(e^{E_\mathrm{Z}/k_\mathrm{B}T}+1)^2} \tag{4.3}$$

.

The resulting curve exhibits a maximum when the thermal energy $k_\mathrm{B}T \approx E/2$, as visible in the graphic in figure 4.1a, where the reduced heat capacity $C_\mathrm{s}/Nk_\mathrm{B}$ is plotted against the reduced temperature $k_\mathrm{B}T/E_\mathrm{Z}$. In the limit $T \to 0$, the heat capacity drops exponentially as $C_\mathrm{s} \propto e^{-E_\mathrm{Z}/k_\mathrm{B}T}$, while in the limit $T \to \infty$ the heat capacity the heat capacity decreases as $C_\mathrm{s} \propto B^2/T^2$.

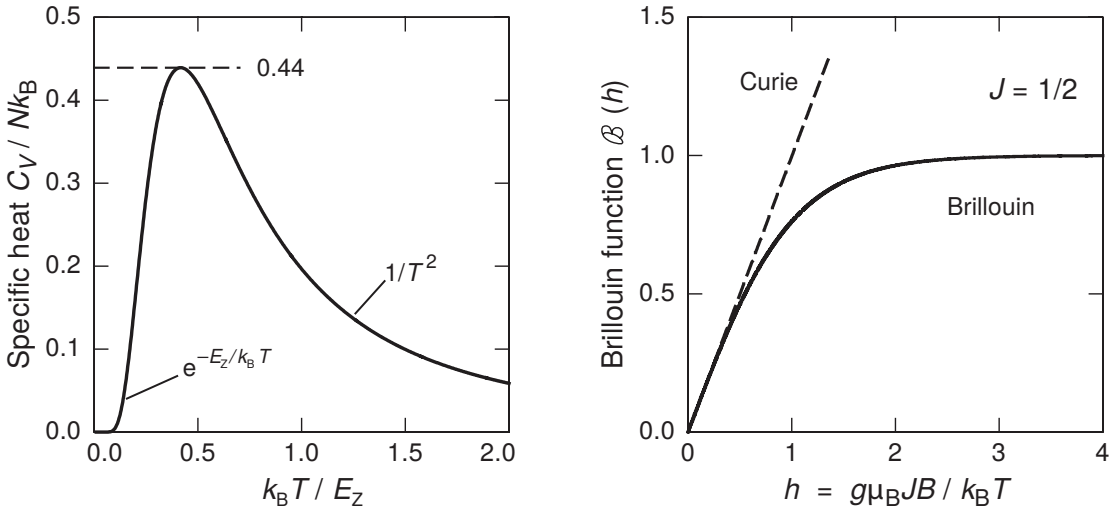

Figure 4.1: Reduced specific heat **(a)** and reduced magnetisation **(b)** of a system of N non-interacting magnetic moments. Plots reproduced from [Ens00].

The corresponding **magnetisation** is given by:

$$M = \frac{N}{V}\tilde{g}\tilde{S}\mu_\mathrm{B}\boldsymbol{\mathcal{B}}_{\tilde{\mathrm{S}}}(h) \tag{4.4}$$

where $h = \tilde{g}\tilde{S}\mu_\mathrm{B}/(k_\mathrm{B}T)$ reflects the ratio between magnetic and thermal energy and $\boldsymbol{\mathcal{B}}_{\tilde{\mathrm{S}}}(h)$ is the Brillouin function, which for $\tilde{S} = 1/2$ is $\boldsymbol{\mathcal{B}}_{\tilde{\mathrm{S}}=1/2}(h) = \tanh(h)$ [Ens05].

In the low temperature limit $h \to \infty$, all moments are aligned in the field direction and only the ground state is occupied, resulting in $\boldsymbol{\mathcal{B}}_{\tilde{\mathrm{S}}} = 1$. In the high temperature limit $h \to 0$, $\boldsymbol{\mathcal{B}}_{\tilde{\mathrm{S}}}(h)$ can be approximated by the first linear term h of the Taylor expansion, resulting in a $1/T$ dependence of the magnetisation, known as Curie law, $M \propto B/T$. The reduced magnetisation $MV/N\tilde{g}\mu_{\mathrm{B}}$ is plotted against the inverse of the reduced temperature in figure 4.1b.

Model with interacting magnetic moments

The results derived in the previous section, assuming a system of non-interacting spins, describe in a qualitative way the thermodynamic properties of the paramagnetic sensor. A more precise picture must include the interactions between the magnetic moments, which results in two effects [Fle05]:

(i) **Dipole-dipole interaction**, which can be expressed in terms of the effective spins of the two dipoles $\tilde{\mathbf{S}}_i$ and $\tilde{\mathbf{S}}_j$:

$$\mathcal{H}_{ij}^{\mathrm{dd}} = \Gamma_{\mathrm{dd}} \frac{\tilde{\mathbf{S}}_i \cdot \tilde{\mathbf{S}}_j - 3(\tilde{\mathbf{S}}_i \cdot \hat{r}_{ij})(\tilde{\mathbf{S}}_j \cdot \hat{r}_{ij})}{(2k_{\mathrm{F}} r_{ij})^3} \tag{4.5}$$

where $\hat{r}_{ij}$ is the unit vector between the two magnetic moments and k_{F} is the Fermi wave vector of the conduction electroncs of the host material and $\Gamma_{\mathrm{dd}} = (\mu_0/4\pi)(\tilde{g}\mu_B)^2(2k_{\mathrm{F}})^3$.

(ii) **RKKY interaction**, which, under the assumption that the mean free path of the conduction electrons is larger than the mean distance between the localised erbium ions, is described by:

$$\mathcal{H}_{ij}^{\mathrm{RKKY}} = \Gamma_{\mathrm{RKKY}} (\tilde{\mathbf{S}}_i \cdot \tilde{\mathbf{S}}_j) F(2k_{\mathrm{F}} r_{ij}) \tag{4.6}$$

with the Kittel function $F(x) = 1/x^3(\cos x - \sin x/x)$ and the amplitude Γ_{RKKY} given by:

$$\Gamma_{\mathrm{RKKY}} = \mathcal{J}^2 \frac{4V_0 m_{\mathrm{e}}^* k_{\mathrm{F}}^4}{\hbar^2 (2\pi)^3} \frac{\tilde{g}^2 (g_J - 1)^2}{g_J^2} \,. \tag{4.7}$$

Here, $\mathcal{J}$ denotes the coupling energy between the localised magnetic moments and the conduction electrons, V_0 is the volume of the elementary cell and m_{e}^* is the effective mass of the conduction electrons.

Both the dipole-dipole interaction and the RKKY interaction scale with $1/r^3$ and therefore their relative strength is typically expressed with a parameter defined as $\alpha = \Gamma_{\mathrm{RKKY}}/\Gamma_{\mathrm{dd}}$.

In order to include the effects of the interaction between magnetic moments, numerical calculations are required. The numerically most convenient way is to use simulations based on mean-field approximation [Wal77], which however neglect the dipole-dipole interaction.
A more exact approach is to diagonalise the Hamiltonian for a cluster of randomly distributed spins in the metal lattice and to repeat this procedure for a large number of configurations. Heat capacity and magnetisation are finally obtained by averaging. In [Fle03] and [Ens00] this approach is implemented for Au:Er with an Er^{3+} concentration of 300 ppm. The resulting magnetisation and heat capacity are reported in figure 4.2, showing a good agreement to the experimental data.

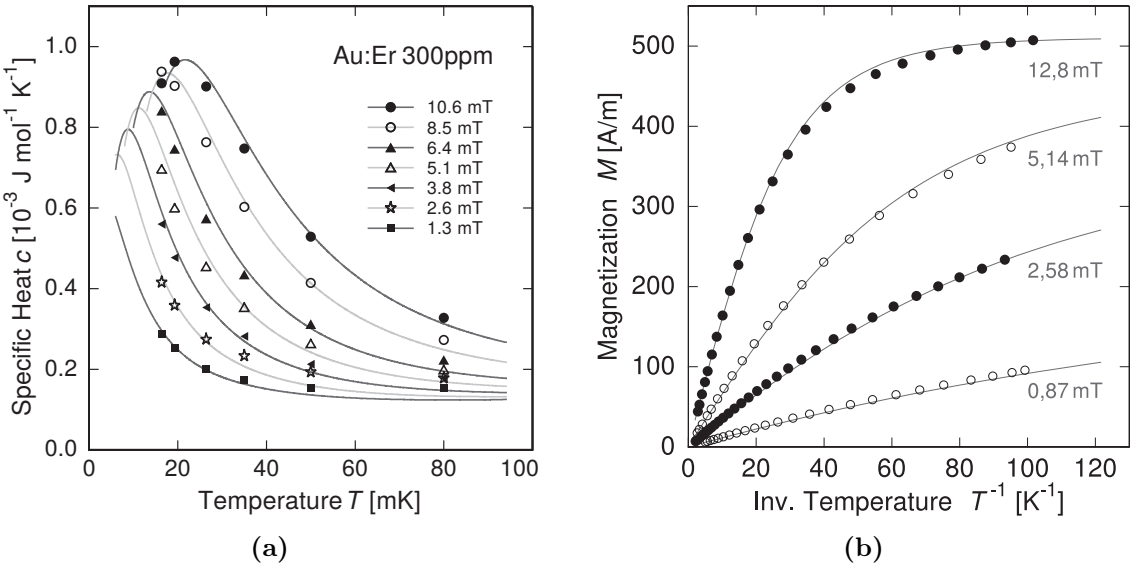

Figure 4.2: Specific heat **(a)** and magnetisation **(b)** of Au:Er with a concentration of 300 ppm as a function of the inverse temperature for different magnetic fields. The experimental data are shown with symbols and the simulations are shown with solid lines. Plots reproduced from [Fle03].

The comparison of the results of these simulations to the simple model with non-interacting magnetic moments reveal the effects of the spin interaction. The maximum value of the specific heat is reduced, while the Schottky peak is wider and the specific heat at high temperatures increases. The magnetisation curve exhibits saturation effects already at higher temperatures if compared to the non-interacting spin case, yielding to a decrease of the temperature dependence of the magnetisation. Overall, calculations based on averaging over spin clusters provides a quantitative

agreement with the data, demonstrating that the thermodynamic properties of erbium diluted in noble metals can be described with confidence. The same numerical approach is exploited to obtain the simulations for Ag:Er sensors used in the detector characterisation presented in chapters 5 and 7.

4.2.3 Sensor response

In order to design a competitive microcalorimeter for particle detection, two main aspects of the sensor performance need to be considered, namely the response time and the signal amplitude.

The **response time** of the sensor depends on the physics that leads to the formation of the signal. In section 4.1.1 the thermalisation mechanisms inside the absorber after an energy deposition are described. As next step, the heat flows from the absorber into the sensor. The corresponding time scale substantially depends on the thermal connection between sensor and absorber. In order to ensure a fast thermalisation of the sensor, the absorber material must be a metal or a semi-metal and the sensor needs to be connected to the absorber in such a way that the conduction electrons carry the heat across the interface. If the contact is sufficiently effective, no degradation of the response time of the detector due to the interface between the two components is observed. In some physics application, the rise time can be artificially slowed down by creating a bottleneck in the contact between sensor and absorber. Finally, the energy carried by the electrons is shared with the magnetic moments generating the sensor signal. Thus, as already pointed out, a strong electron-spin coupling is an essential property of the sensor and this is the main reason to prefer metallic paramagnetics, as Ag:Er and Au:Er, over dielectric materials. The time scale of this process depends on the electron-spin relaxation time $\tau_{\mathrm{K}} = K/T$, where T is the temperature and $K = 7 \times 10^{-9}\,\mathrm{sK}$ is the Korringa constant [Ens00]. In the case of Au:Er, the resulting spin-electron relaxation time is less than $10^{-7}\,\mathrm{s}$ at 50 mK [Fle05].

The **amplitude of the signal** produced by the sensor corresponds to the change of magnetisation that follows an energy input, as reported in equation 3.3. If the sensor is modelled as an ensamble of N non-interacting magnetic moments with a heat capacity C_{s} in a volume V and in a magnetic field B, the number of spins that are flipped by an energy change δE_{s} in the system is:

$$N_{\mathrm{f}} = \frac{\delta E_{\mathrm{s}}}{E_{\mathrm{Z}}} = \frac{\delta E_{\mathrm{s}}}{\tilde{g}\mu_{\mathrm{B}}B} = \frac{C_{\mathrm{s}}\delta T}{\tilde{g}\mu_{\mathrm{B}}B} \tag{4.8}$$

where $E_{\mathrm{Z}} = \tilde{g}\mu_{\mathrm{B}}B$ is the energy splitting of the Zeeman system, which is in the order of few μeV, and $\delta T = \delta E_{\mathrm{s}}/C_{\mathrm{s}}$ is the change of temperature that causes the energy

input δE_s.

The subsequent change of magnetisation δM is given by [Ens05]:

$$\delta M = -\frac{N_\mathrm{f}\tilde{g}\mu_\mathrm{B}}{V} = -\frac{C_\mathrm{s}\delta T}{VB} = \frac{\partial M}{\partial T}\delta T \tag{4.9}$$

where $\partial M/\partial T$ represents the dependence of the magnetisation of the sensor upon the temperature and it is linked to the heat capacity of the sensor C_s. Inserting equation 3.2 and defining the total heat capacity of the detector, C, as the sum of the heat capacity of the spin system of the sensor, C_s, the heat capacity of the electronic system of sensor and absorber, C_e and the heat capacity of the phononic system of sensor and absorber, C_ph, the change of magnetisation can be written as:

$$\delta M \approx -\frac{1}{V} \cdot \frac{C_\mathrm{s}(B,T)}{C_\mathrm{s}(B,T) + C_\mathrm{e}(T) + C_\mathrm{ph}(T) + C_\mathrm{s}} \cdot \frac{E}{B}\,. \tag{4.10}$$

Assuming $k_\mathrm{B}T/E_\mathrm{Z} > 1$, which implies small magnetic field and high enough temperature, the heat capacity of the sensor increases as $C_\mathrm{s} \propto B^2$, according to equation 4.3. In this limit the electronic heat capacity C_e is dominating and therefore, using equation 4.10, the magnetisation signal is linearly proportional to the magnetic field, $\delta M \propto B$.
For a given temperature, the maximum of the signal amplitude is reached if $C_\mathrm{s}(B) = C_\mathrm{e} + C_\mathrm{ph}$. The useful conclusion for the detector optimisation is that matching the heat capacity of the spin system with the heat capacity of the electronic and phononic system is recommended.
If the magnetic field increases, C_s becomes larger until is dominating over the other heat capacity components, $C_\mathrm{s} \gg C_\mathrm{e} + C_\mathrm{ph}$. In this case, according to equation 4.10, the magnetisation signal is inversely proportional to the magnetic field, $\delta M \propto 1/B$. In the limit of large magnetic fields, the complete energy input is transferred to the spin system and it is used to flip the magnetic moments in the sensor. As a result, the amplitude of the magnetisation signal is substantially independent of the temperature. In terms of detector optimisation, this last case leads to a comparably small signal which is independent on the detector temperature. Despite the drawback of a decreased signal, this scenario could be convenient to reduce the negative influence of temperature fluctuations of the cryostat.

4.2.4 Influence of nuclear spins

The presence of nuclear spins in the sensor can potentially affect the detector performance. Both the erbium ions and the metallic host atoms can feature a non-zero nuclear spin and a nuclear quadrupole moment.

The **erbium** isotope ^{167}Er exhibit a nuclear spin $I = 7/2$, which generates a nuclear magnetic moment and, therefore, hyperfine interaction with the 4f electrons. The magnetisation as well as the heat capacity are influenced by the hyperfine splitting, as discussed in [Fle00]. In the temperature and magnetic field range of interest for the operation of MMCs, the heat capacity is enhanced and the magnetisation is reduced. The second effect is connected to the first one, as the energy input into the extra heat capacity system does not contribute in the flipping of the magnetic moments, thus reducing the magnetisation signal in the sensor. In order to optimise the sensitivity of the sensor it is required to reduce as much as possible the amount of ^{167}Er in the fabrication of the sensor. The sensor of the MMC detectors used and developed in the context of this work is fabricated using erbium samples enriched in ^{168}Er, which is characterised by zero nuclear spin.

The host materials typically used for the fabrication of MMC sensors are gold and silver. The only naturally abundant isotope of **gold** is ^{197}Au, with a nuclear spin $I = 3/2$, a large nuclear electric quadrupole moment of 0.55 b [Pow74]. In pure gold, the cubic symmetry of the electric field leads to degenerate nuclear energy levels. Thus, no contribution of the nuclear spins to the specific heat is expected in this case. When gold nuclei are in the vicinity of an Er^{3+} ion, however, the charge distribution is changed and the lattice is deformed. The resulting electric field gradient can split the nuclear levels, leading to an additional heat capacity [Her00]. The signal of MMCs with Au:Er sensor exhibit an additional fast decay component with a time constant in the range between 0.2 ms and 1 ms, depending on the magnetic field. This effect has been attributed to the nuclear quadrupole moment of gold [Ens00].

An alternative choice is to employ **silver** instead of gold as metallic host material. The naturally abundant isotopes ^{107}Ag and ^{109}Ag are characterised by a nuclear spin $I = 1/2$ and no nuclear quadrupole moment. In this case, the drawback is the stronger RKKY interaction with the parameter α in the range between $\alpha \approx 6.4$ and $\alpha \approx 15$ [Bur08]. The enhanced interaction between the magnetic moments leads to two negative effects that reduce the detector response. One side the specific heat of the magnetic moments is larger for typical working temperatures of MMCs, above 20 mK. On the other side, the magnetisation signal M and its temperature dependence $\partial M/\partial T$ are reduced. Nevertheless, silver represents a promising candidate as host material thanks to the absence of quadrupole moments, the strongly reduced hyperfine splitting and the marginal nuclear heat capacity. Silver is used as sensor host material in the detectors that have been developed and characterised in this work.

4.3 Detector geometry and sensor read-out

The magnetic response of the sensor to an energy input δE, corresponding to an increase of temperature $\delta T = \delta E/C_\mathrm{s}$ can be written in terms of a change of magnetic moment $\delta m = \delta M \cdot V$, using equation 4.9:

$$\delta m = C_\mathrm{s}\frac{\delta T}{B} = \frac{\delta E}{B}\,. \tag{4.11}$$

Here, we neglect any other contribution to the detector heat capacity a part from the one of the spins, C_s, and we use a model of non-interacting spins.
If this spin system is placed inside a circular loop of wire of radius r, the change of flux $\delta\Phi$ resulting from the change of magnetic moment δm is given by:

$$\delta\Phi = \mu_0\frac{G}{r}\delta m \tag{4.12}$$

where G is a dimensionless factor which describes the geometry of the spins within the loop.

If we include in the model also the heat capacity of the absorber and the non-spin heat capacity of the sensor, defining the sum of the two as C', the fraction of the energy released in the calorimeter that reaches the spin system is $\beta \coloneqq C_\mathrm{s}/(C_\mathrm{s} + C')$. Thus, equation 4.12 becomes:

$$\delta\Phi = \mu_0\frac{G}{r}\frac{C_\mathrm{s}}{C_\mathrm{s} + C'}\frac{\delta E}{B}\,. \tag{4.13}$$

As already anticipated in the section 4.2.3, in the limit of small magnetic fields, such that $E_\mathrm{Z} \ll k_\mathrm{B}T$ and $C_\mathrm{s} \propto B^2$, the flux signal $\delta\Phi$ increases linearly with the magnetic field B in the low-field region and the maximum signal is reached if $C_\mathrm{s}(B) = C'$. The combination of equation 4.11 and equation 4.13, together with this last observation, sets three major points for the geometrical implementation of the detector:

(i) The sensor must be placed as close as possible to the wire of the magnetometer, as the coupling decreases with the distance between them.

(ii) The magnetic field B must be minimised to increase the magnetic signal δm.

(iii) The spin heat capacity of the sensor should match with the sum of the remaining heat capacity contributions to maximise the detector signal.

4.3.1 Planar gradiometric geometry

The simplest approach to read out the sensor of a MMC detector is to place it directly inside the loop of a SQUID magnetometer. However, this layout requires an external coil to produce the magnetic field that is needed to align the magnetic moments of the sensor. The resulting dipole field scales with $1/r^3$, leading to potentially large crosstalk between neighbouring detectors. Thus, scaling up this configuration to fabricate large detector arrays is problematic.

A more convenient strategy consists in fabricating two parallel planar meander-shaped pick-up coils equipped with planar sensors on top [Fle09]. The two pick-up coils are connected in parallel and inductively coupled to the input coil of a SQUID current sensor, forming a first-order gradiometer. The detector and the SQUID do not need to share the same substrate and it is typically convenient to fabricate them on separate chips, which are connected by aluminium wire-bonds. The resulting circuitry is shown in figure 4.3.1. A short review of the basic working principle of a SQUID is presented in section 4.3.4.

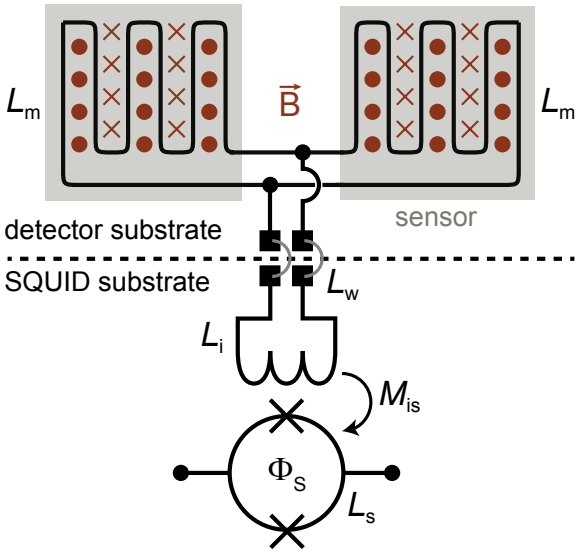

Figure 4.3: Schematic drawing of a gradiometric planar geometry with two detector pixels equipped with temperature sensors and meander-shaped pick-up coils underneath, which are coupled to a SQUID current sensor sitting on a separate substrate.

The magnetic field that is required to align the magnetic moments of the sensor is generated by injecting a persistent current into the superconducting circuit formed by the two meander-shaped pick-up coils. As a result, an inhomogeneous magnetic field is created around the meander of the pick-up coil within the volume of the sensor [Zin04] [Bur04]. The two detectors forming this layout are addressed as *detector pixels* in the following.

There are several advantages related to the implementation of a planar gradiometric geometry. Here we stress three major points.
First of all, in the gradiometric layout both the pick-up coils contribute to the signal,

but with opposite polarities. As a consequence, identical signals occurring simultaneously in both the detector pixels cancel out. This means that changes of flux induced by external magnetic fields and changes of the substrate temperature do not contribute to the signal in the detector, as they affect both the pixels in the same way. Thus, the effects of undesired signals due to external interferences are strongly reduced.
A second important advantage of this geometry is the enhancement of the signal because of the following aspects:

(i) sensor and pick-up coil are very close and, therefore, the coupling between the coil and the magnetic moments of the sensor is improved;

(ii) the indirect coupling between the pick-up coil and the SQUID via a separate coil permits to fabricate the detector and the SQUID on different chips, reducing the effect of the SQUID power dissipation on the detector, which can potentially heat up the sensor and reduce the signal.

As a third point, the employment of a planar geometry is beneficial for the fabrication of large arrays of detectors. On one hand, the magnetic field generated by the supercurrent flowing in the pick-up coils is a multipole of high order and the magnetic crosstalk in an array of detector can be significantly reduced. On the other hand, high-precision microlithographic techniques can be exploited to implement this geometry. Thus, the feasibility for production of large arrays of tightly packed detector pixels is enhanced.

4.3.2 Distribution of the magnetic field

The persistent current injected into the meander-shaped pick-up coil produces a highly inhomogeneous magnetic field. The distribution of the magnetic field lines can be simulated with finite elements methods. The resulting average strength of the field in a plane parallel to the meander drops exponentially with increasing distance between the planes [Fle05].

The magnetic field B at a position $\mathbf{r}$ generated by a persistent current I_0 flowing in a meander formed by superconducting stripes with a pitch (i.e. center-to-center distance) p is given by [Fle05]:

$$B(\mathbf{r}) = \mu_0 G(\mathbf{r}/p)\frac{I_0}{p} \tag{4.14}$$

where $G(\mathbf{r}/p)$ is a local dimensionless geometric factor, which is independent of the overall dimensions of the meander, but it changes with the width to pitch ratio w/p

of the meander stripes. The parameter $G(\mathbf{r}/p)$ also describes the coupling strength between the magnetic moment of a volume element and the magnetic flux in the pick-up coil.

4.3.3 Flux signal in the sensor pick-up coil

The change of magnetic flux in the pick-up coil $\mathrm{d}(\delta\Phi)$ corresponding to the change of magnetisation of a volume element $\mathrm{d}V$, $\delta M = \delta m \cdot \mathrm{d}V$, at the position $\mathbf{r}$ is given by the equivalent of equation 4.12:

$$\mathrm{d}(\delta\Phi) = \mu_0 \frac{G(\mathbf{r}/p)}{p} \delta M(\mathbf{r}) \mathrm{d}V \,. \tag{4.15}$$

To calculate the total flux change $\delta\Phi$ in the meander-shaped pick-up coil caused by an energy input δE, it is required to integrate equation 4.15 and to use equation 4.9:

$$\delta\Phi = \delta T \int_V \mu_0 \frac{G(\mathbf{r}/p)}{p} \frac{\partial M(B(\mathbf{r}), T)}{\partial T} \mathrm{d}V \tag{4.16}$$

where δT is the temperature rise of the sensor and it satisfies:

$$\delta T = \frac{\delta E}{C} = \frac{\delta E}{C_\mathrm{e} + \int_V c_\mathrm{Er}(\mathbf{r}) \mathrm{d}V} \,. \tag{4.17}$$

Here, C is the detector heat capacity, equal to the sum of the electronic contribution C_e of absorber and sensor and the erbium contribution, given by the location-dependent specific heat $c_\mathrm{Er}(\mathbf{r})$.
The resulting integral can be numerically solved with limited computational effort knowing the probability distribution of G, $P(G)$, and defining the weighted average of a parameter x as: $\langle x \rangle_G \coloneqq \int P(G) x(G) \mathrm{d}G$. The final expression that describes the ratio between the change of flux in the meander-shaped pick-up coil $\delta\Phi$ and the energy input δE is given by [Fle05]:

$$\frac{\delta\Phi}{\delta E} = \frac{V}{C_\mathrm{e} + V \langle c_\mathrm{Er} \rangle} \left\langle \mu_0 \frac{G}{p} \frac{\partial M}{\partial T} \right\rangle . \tag{4.18}$$

4.3.4 SQUID-based read-out

The change of flux in the meander-shaped pick-up coil can be read out and converted to a voltage signal using a dc-SQUID. A dc-SQUID consists of a superconducting loop which is interrupted by two Josephson junctions, as illustrated in figure 4.4a.

In order to suppress hysteretic behaviour, the junctions are shunted by a resistor. Small currents can flow without dissipation through the SQUID loop, as the Cooper pairs can tunnel through the weak links between the superconducting paths which are represented by the Josephson junctions. For larger bias currents, quasiparticles partially carry the current through the barrier, leading to a voltage drop V_S across the SQUID, which depends on the bias current I_b and periodically changes with the magnetic flux Φ_S penetrating the SQUID. Figure 4.4b shows the voltage V_S for the two extreme values of the magnetic flux Φ_S in the SQUID and the corresponding periodic voltage-flux characteristics.

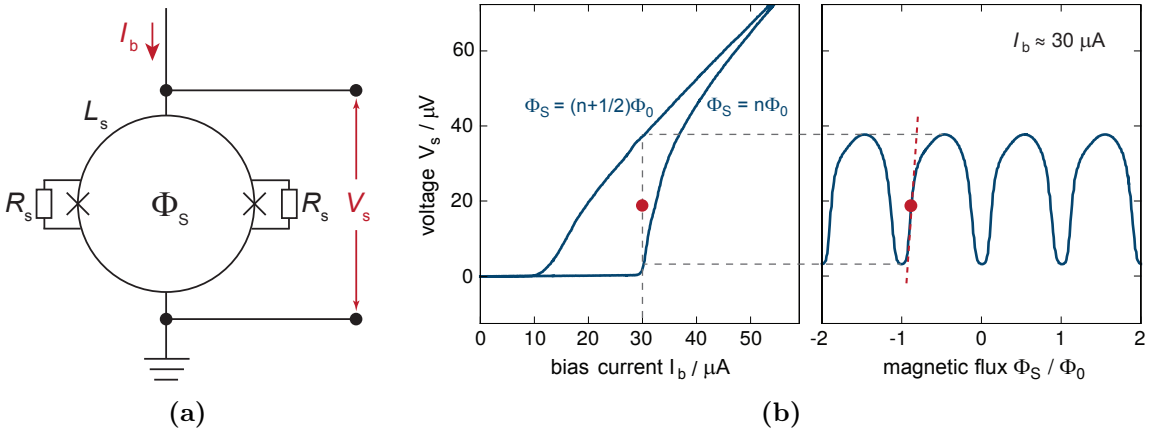

Figure 4.4: **a)** Schematic of a dc-SQUID. The two Josephson junctions are represented by the symbol × and they are shunted with the resistors R_S. The bias current I_b and the voltage drop V_S across the SQUID are indicated. **b)** Current-voltage characteristics (left) of a dc-SQUID and corresponding flux-voltage characteristics (right) for a fixed bias current. The flux is shown in terms of magnetic flux quanta $\Phi_0 = h/2e \approx 2.07 \times 10^{-15}$ Wb. The working point is marked in red.

Hence, a dc-SQUID can be used as a precise flux to voltage converter, which gives a linear response as long as the flux changes within the linear regime of the flux-voltage characteristics, as shown in figure 4.4b. If the flux moves away from the working point by more than $\sim \Phi_0/4$, the voltage response becomes highly non-linear. This inconvenience can be overcome by introducing a feedback mechanism, as described in section 3.1.3.

As mentioned in section 4.3.1, in a planar gradiometric design the two detector pick-up coils are connected in parallel to the input coil of the dc-SQUID, forming a flux transformer. The deposition of energy in one of the two sensors leads to a change of magnetisation, which in turns causes a change of flux in the corresponding pick-up coil, according to equation 4.18. Due to the flux conservation in a superconducting loop, a supercurrent δI is generated negating the initial change of flux $\delta\Phi$ and the a

fraction of this current, δI_{S}, flows in the input coil of the SQUID:

$$\delta I_{\mathrm{S}} = \frac{\delta\Phi}{L_{\mathrm{m}} + 2(L_{\mathrm{i}} + L_{\mathrm{w}})} \tag{4.19}$$

where L_{m}, L_{i} and L_{w} are the inductances of the detector meander-shaped pick-up coil, the input coil of the SQUID and the wires between detector and SQUID, respectively. The corresponding change of flux in the SQUID is $\delta\Phi_{\mathrm{S}} = M_{\mathrm{is}}\delta I_{\mathrm{S}}$, where $M_{\mathrm{is}} = k\sqrt{L_{\mathrm{S}}L_{\mathrm{i}}}$ is the mutual inductance between the SQUID loop and its input coil and L_{S} is the inductance of the SQUID loop. Thus, the transformer coupling f_{c} between the flux in the pick-up coil $\delta\Phi$ and the flux in the SQUID $\delta\Phi_{\mathrm{S}}$ can be derived:

$$f_{\mathrm{c}} = \frac{\delta\Phi}{\delta\Phi_{\mathrm{S}}} = \frac{k\sqrt{L_{\mathrm{S}}L_{\mathrm{i}}}}{L_{\mathrm{m}} + 2(L_{\mathrm{i}} + L_{\mathrm{w}})}\,. \tag{4.20}$$

Assuming $k \approx 1$ and neglecting the inductance of the wires, the best coupling is calculated as $f_{\mathrm{c}}^{*} = 1/(2\sqrt{2})\sqrt{L_{\mathrm{S}}/L_{\mathrm{m}}}$ and it is achieved if the inductance of the input coil equals half of the inductance of the meander-shaped pick-up coil, $L_{\mathrm{i}} = L_{\mathrm{m}}/2$. As an example, considering the illustrative values $L_{\mathrm{m}} = 3.0\,\mathrm{nH}$, $L_{\mathrm{i}} = L_{\mathrm{m}}/2 = 1.5\,\mathrm{nH}$ and $L_{\mathrm{S}} = 0.3\,\mathrm{nH}$, the resulting transformer coupling is $f_{\mathrm{c}}^{*} = 0.043$.

The compensating supercurrent generated in the pick-up coil of one sensor has an opposite sign with respect to the supercurrent generated in the pick-up coil of the other sensor. Thus, the events occurring in the two detector pixels can be distinguished by the polarity of the resulting change of flux in the SQUID. Considering simultaneous energy depositions in the two sensors and, thus, simultaneous flux changes in the two pick-up coils, $\delta\Phi_1$ and $\delta\Phi_2$, the resulting supercurrents δI_1 and δI_2 have an opposite sign and the current in the input coil of the SQUID is given by:

$$\delta I_{\mathrm{S}} = \frac{\delta\Phi_1 - \delta\Phi_2}{L_{\mathrm{m}} + 2(L_{\mathrm{i}} + L_{\mathrm{w}})} \tag{4.21}$$

.

The corresponding measurable flux in the SQUID is:

$$\begin{aligned} \delta\Phi_{\mathrm{S}} &= M_{\mathrm{is}}\delta I_{\mathrm{S}} \\ &= \frac{M_{\mathrm{is}}}{L_{\mathrm{m}} + 2(L_{\mathrm{i}} + L_{\mathrm{w}})}\,(\delta\Phi_1 - \delta\Phi_2) \end{aligned} \tag{4.22}$$

Since the change of flux in each pick-up coil is proportional to the change of temperature of the corresponding sensor, $\delta\Phi_i \propto \delta T_i$ with $i = 1, 2$ for the two detector

pixels, from equation 4.22 it can be observed that the final flux in the SQUID input coil is proportional to the temperature difference between the two sensors, $T_1 - T_2$:

$$\delta\Phi_{\mathrm{S}} \propto \delta T_1 - \delta T_2 \propto T_1 - T_2\,, \tag{4.23}$$

assuming that the two sensors have the same initial temperature prior the energy event. This condition is fulfilled if the two sensors share the same thermal reservoir, which is typically the case in the implementation of the planar gradiometric layout.

4.4 Detector response and energy resolution

The performance of MMC detectors can be ultimately defined by their detector response, in terms of signal shape in the time domain, and their energy resolution, defined as the full width at half maximum (FWHM) of the detector line broadening.

The evolution of the detector response in time can be derived from a simple thermodynamic model of the detector, as shown in section 4.4.1.

The energy resolution depends on two factors: the shape of the signal in the time domain and the time dependent signal-to-noise ratio (SNR). In practice, additional limitations on the detector energy resolution are introduced by external sources that can degrade the detector performance, such as electromagnetic interference, cross-talk between different detector pixels, fluctuations of the detector temperature, etc. However, these effects can be suppressed and they are neglected in the following discussion. The different time-dependent noise contributions are reviewed in section 4.4.2 and the fundamental limit on the achievable energy resolution of MMCs is derived in section 4.4.3.

4.4.1 Detector response

The detector can be modelled as a thermodynamic ensemble consisting of two subsystems, namely the electronic subsystem, which includes the conduction electrons of absorber and sensor, and the spin subsystem, which includes the magnetic moments of the sensor. The resulting layout is depicted in figure 4.5. The two subsystems are characterised by the corresponding heat capacities C_{e} and C_{s}, respectively. The phononic contribution to the heat capacity is neglected for sake of simplicity, as it does not play a significant role at the typical detector operational temperature. The two subsystem are connected by a thermal link with thermal conductivity G_{se}. The electronic subsystem is connected to a thermal bath at temperature T_0 via a weak thermal link with thermal conductivity G_{eb}.

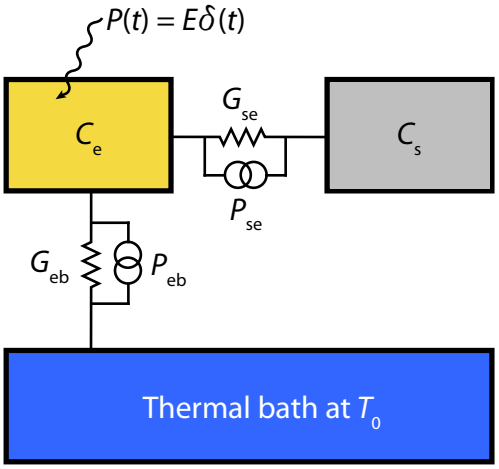

Figure 4.5: Thermodynamic model of the detector consisting of the electronic subsystem, the spin subsystem and the thermal bath at temperature T_0.

In the limit of non-interacting spins[2], the change of magnetic moment δm of the sensor is directly related to the change of energy content of the spin system $\delta E_s = -\delta m \cdot B$, which corresponds to a change of temperature of the subsystem $\delta T_\mathrm{s} = \delta E_s / C_\mathrm{s}$. The magnetic moment δm, in turn, is proportional to the flux in the pick-up coil $\delta\Phi$, which is coupled to the flux in the SQUID $\delta\Phi_\mathrm{S}$. Therefore, the flux in the SQUID is a direct measurement of the temperature change following an energy change of the spin system.

If energy is deposited in the electronic subsystem and it instantly thermalises with the conduction electrons, the resulting time evolution of the energy contents of the two subsystems, E_s and E_e, is given by the coupled differential equations:

$$\dot{E}_\mathrm{e} = C_\mathrm{e}\dot{T}_\mathrm{e} = G_\mathrm{se}(T_\mathrm{s} - T_\mathrm{e}) + G_\mathrm{eb}(T_0 - T_\mathrm{e}) + P(t) \tag{4.24}$$

$$\dot{E}_\mathrm{s} = C_\mathrm{s}\dot{T}_\mathrm{s} = G_\mathrm{se}(T_\mathrm{e} - T_\mathrm{s}) \tag{4.25}$$

where $P(t) = E\delta(t)$ denotes the external power input. Solving the equations for the temperature change of the spin system $\delta T_\mathrm{s} = T_\mathrm{s} - T_0$, the evolution of the detector response measured by the SQUID can be derived:

$$\delta\Phi_\mathrm{S} \propto \delta T_\mathrm{s} = \frac{E}{C_\mathrm{e} + C_\mathrm{s}} \left(-\mathrm{e}^{-t/\tau_r} + \mathrm{e}^{-t/\tau_d}\right) . \tag{4.26}$$

According to equation 4.26, the detector response to an energy input consists of an exponential rise with a time constant τ_r up to the maximum amplitude and a subsequent exponential decay with a time constant τ_d, due to the thermal connection to the thermal bath. The time constants τ_r and τ_d depend in a nontrivial way on

[2]This limit is valid if the interaction between the magnetic moments is much smaller than the Zeeman-splitting in the external magnetic field.

the thermal conductivities G_{se} and G_{eb} as well as on the heat capacities C_{e} and C_{s} [Fle05]. In the simple but realistic case of a detector with a weak thermal bath connection, $G_{\mathrm{eb}} \ll G_{\mathrm{se}}$, and similar heat capacities of the subsystems, $C_{\mathrm{e}} \approx C_{\mathrm{s}}$, the following relation holds:

$$\tau_d = \frac{C_{\mathrm{e}} + C_{\mathrm{s}}}{G_{\mathrm{eb}}} = \frac{C}{G_{\mathrm{eb}}} \tag{4.27}$$

where C denotes the total heat capacity of the detector.

The rise time τ_r depends on the electron-spin coupling in the sensor, as already mentioned in section 4.2.3, via the time constant $\tau_{\mathrm{K}} = K/T$, where K is the Korringa constant:

$$\tau_{\mathrm{r}} = (1-\beta)\tau_{\mathrm{k}}\,. \tag{4.28}$$

Here, $\beta \coloneqq C_{\mathrm{s}}/(C_{\mathrm{e}}+C_{\mathrm{s}})$ represents the fraction of the total heat capacity that belongs to the spin system and it is equal to the the fraction of the initial energy deposition that reaches the spin system, as already introduced in section 4.3. Typically, the resulting rise time is in the order of $\sim 100\,\mathrm{ns}$.

4.4.2 Noise contributions

The intrinsic noise contributions that limit the detector performance arise from different sources that are shortly reviewed in the following.

Energy fluctuations The most fundamental contribution to the noise of MMC detectors is related to the thermodynamic fluctuations of the energy content in the different subsystems of the calorimeter. Using the thermodynamic model presented in the previous section, the resulting thermal noise can be described with the frequency independent spectral power density that is proportional to the thermal conductivity G between the subsystems, $S_{\mathrm{P}} = 4k_{\mathrm{B}}T^2G$. The evolution in time of the system is described by the two coupled differential equations:

$$\dot{E}_{\mathrm{e}} = C_{\mathrm{e}}\dot{T}_{\mathrm{e}} = G_{\mathrm{se}}(T_{\mathrm{s}} - T_{\mathrm{e}}) + G_{\mathrm{eb}}(T_0 - T_{\mathrm{e}}) + P_{\mathrm{eb}} - P_{\mathrm{se}} \tag{4.29}$$

$$\dot{E}_{\mathrm{s}} = C_{\mathrm{s}}\dot{T}_{\mathrm{s}} = G_{\mathrm{se}}(T_{\mathrm{e}} - T_{\mathrm{s}}) + P_{\mathrm{se}} \tag{4.30}$$

where we consider the two noise sources P_{se} and P_{eb} in parallel to the thermal links, as shown in figure 4.5.

Transforming the differential equations into the frequency domain, the spectral power density related to the thermal fluctuations in the spin system is:

$$S_{\mathrm{E_s,th}}(f) = k_{\mathrm{B}} C_{\mathrm{s}} T^2 \left((1-\beta) \frac{4\tau_{\mathrm{r}}}{1+(2\pi\tau_{\mathrm{r}} f)^2} + \beta \frac{4\tau_{\mathrm{d}}}{1+(2\pi\tau_{\mathrm{d}} f)^2} \right) , \tag{4.31}$$

assuming $C_{\mathrm{e}} \approx C_{\mathrm{s}}$ and $\tau_{\mathrm{d}} \gg \tau_{\mathrm{r}}$ [Fle05]. The resulting frequency spectrum is characterised by two plateaus with two cut-off frequency $1/(2\pi\tau_{\mathrm{r}})$ and $1/(2\pi\tau_{\mathrm{d}})$. For typical values of the detector parameters, the equivalent flux noise is $S_\Phi \approx 2 \times 10^4\,(\mu\Phi_0)^2/\mathrm{Hz}$ in the pick-up coil [Hen17].

Magnetic Johnson noise The random electron thermal motions due to the non-zero temperature of the detector generate currents in the metallic components, i.e. sensor and absorber. The Brownian motion of the electrons yields to a changing magnetic field that couples into the pick-up coil or directly into the SQUID. Considering a metallic cube with height h at temperature T with electrical conductivity σ placed at a distance d from a meander-shaped pick-up coil with pitch p and overlap area A, the spectral power density for the magnetic Johnson flux noise is [Pie12][Ens00]:

$$S_{\Phi,\mathrm{J}}(f) = \frac{2.376}{4\pi} \mu_0^2 k_{\mathrm{B}} T \sigma A p \left(e^{-2\pi d/p} - e^{-2\pi(d+h)/p} \right) \tag{4.32}$$

and it is frequency-independent in the relevant frequency range of interest. For a realistic geometry with an absorber close to a pick-up coil at a temperature of 20 mK, the resulting noise density is $S_{\Phi,\mathrm{J}} \approx 0.7\,(\mu\Phi_0)^2/\mathrm{Hz}$.

SQUID noise MMC detectors are typically read out with a two-stage SQUID system, as described in section 3.1.3. The noise contribution from the SQUID is the dominant component in the complete read-out chain. As a matter of fact, the additional noise contributions related to the gain resistor and the room temperature electronics are negligible. The SQUID flux noise spectrum consists of a frequency-independent white noise component $S^{\mathrm{w}}_{\Phi,\mathrm{S}}$ and a $1/f$ component that increases at low frequencies. The white noise component is generated by the shunt resistors R_{s} and the corresponding magnetic flux noise power density for an ideal SQUID with inductance L_{S} is given by [Tes77]:

$$S^{\mathrm{w}}_{\Phi,\mathrm{S}} = \frac{18 k_{\mathrm{B}} T L_{\mathrm{S}}^2}{R_{\mathrm{s}}} . \tag{4.33}$$

In practice, current state-of-the-art SQUIDs show a white noise level independent from the SQUID inductance which is estimated to be $\sqrt{S^{\mathrm{w}}_{\Phi,\mathrm{S}}} \leq 1\,\mu\Phi_0/\sqrt{\mathrm{Hz}}$. The

origin of the $1/f$ component that dominates at low frequencies is not yet fully understood and typical values are in the order of $\sqrt{S_{\Phi,\mathrm{S}}^{1/f}} \approx 5 - 10\,\mu\Phi_0/\sqrt{\mathrm{Hz}}$.

Paramagnetic noise The experimental noise spectra cannot be fully explained including the contributions presented so far, i.e. the thermodynamic fluctuations, the magnetic Johnson noise and the SQUID noise. An excess noise proportional to $1/f^{\xi}$ and surprisingly temperature-independent[3] has been observed and traced back to the erbium ions in the sensor material [Dan05]. Here, ξ is an empirical exponent that depends on the geometry and the properties of the sensor. In particular, it has been demonstrated that this noise source can be described by the imaginary part of the susceptibility of a Au:Er sensor [Hof12] [Wiß13]. Thus, the origin of the noise is related to the different finite response times of the orientation of interacting clusters of magnetic moments. The empirical description of the resulting noise of a Au:Er gold sensor containing N_{Er} erbium ions equipped with a meander-shaped pick-up coil with pitch p and geometrical factor G, as defined in section 4.3.2, is given by the spectral power density:

$$S_{\Phi,\mathrm{Er}}(f) = \frac{\mu_0^2 \langle G^2 \rangle}{p^2} S_{\mathrm{m}}(f) N_{\mathrm{Er}} \tag{4.34}$$

where $S_{\mathrm{m}}(f) \approx 0.12\,\mu_{\mathrm{B}}^2 (f/\mathrm{Hz})^{-\xi}$ describes the fluctuations of the magnetic moment of a single erbium atom. An exemplifying value for this $1/f$ paramagnetic noise, assuming realistic properties of the detector, is $S_{\Phi,\mathrm{Er}}(f = 1\,\mathrm{Hz}) \approx 5 \times 10^4 (\mu\Phi_0)^2/\mathrm{Hz}$.

4.4.3 Energy resolution

The fundamental limit on the achievable energy resolution of MMC detectors can be derived starting from the signal shape discussed in section 4.4.1 and neglecting all the noise contributions previously described besides the thermal noise due to energy fluctuations in the detector subsystems.

Defining the responsivity $p(t)$ of the detector as $p(t) := E_{\mathrm{s}}(t)/E$, where E is the energy deposition in the calorimeter, the noise-equivalent-power NEP can be written as: $\mathrm{NEP} = \sqrt{S_{\mathrm{E_s,th}}(f)}/\tilde{p}(f)$. Within the framework of the optimal filtering approach used to estimate the energy from the recorded detector signal [Fle03], the energy resolution of a detector - defined as the full width at half maximum (FWHM) of the detector line broadening - is related to $\mathrm{NEP}(f)$ by:

[3] The independence upon temperature has been verified in the temperature range between 30 mK and 2 K [Fle05].

$$\Delta E_{\mathrm{FWHM}} = 2\sqrt{2\log(2)} \left(\int_0^{\mathrm{inf}} \frac{4df}{\mathrm{NEP}^2} \right)^{-1/2} \tag{4.35}$$

where log denotes the natural logarithm.

If the model of thermal fluctuations presented before (equation 4.31) is applied, the result is [Fle05]:

$$\Delta E_{\mathrm{FWHM}} = 2\sqrt{2\log(2)}\sqrt{4k_{\mathrm{B}}C_{\mathrm{e}}T^2} \left[\frac{G_{\mathrm{eb}}}{G_{\mathrm{se}}} + \left(\frac{G_{\mathrm{eb}}}{G_{\mathrm{se}}} \right)^2 \right]^{1/4} \tag{4.36}$$

and for $\beta := C_{\mathrm{s}}/(C_{\mathrm{s}} + C_{\mathrm{e}}) \approx 1/2$ and $\tau_{\mathrm{d}} \gg \tau_{\mathrm{r}}$, it approximates to:

$$\Delta E_{\mathrm{FWHM}} \approx 2\sqrt{2\log(2)}\sqrt{4k_{\mathrm{B}}C_{\mathrm{e}}T^2} \left(\frac{1}{\beta(1-\beta)} \frac{\tau_{\mathrm{r}}}{\tau_{\mathrm{d}}} \right)^{1/4} . \tag{4.37}$$

The best energy resolution is achieved for $\beta = 1/2$, i.e. for matching heat capacities of absorber and sensor. According to equation 4.37, in order to further improve the energy resolution of the detector, the working temperature T should be minimised as well as the heat capacity C_{e}. Moreover, a faster signal rise time τ_{r} and a slower decay time τ_{d} also enhance the energy resolution. However, the former is limited by the electron-spin relaxation time, according to the Korringa relation introduced in section 4.4.1, and the latter is proportional to the detector dead time and therefore it cannot be arbitrarily increased.

Assuming an exemplifying microcalorimeter operated at 20 mK with an absorber heat capacity equal to the sensor heat capacity, $C_{\mathrm{e}} = C_{\mathrm{s}} = 1\,\mathrm{pJ/K}$, a rise time $\tau_{\mathrm{r}} = 1\,\mu\mathrm{s}$ and a decay time $\tau_{\mathrm{d}} = 1\,\mathrm{ms}$, the resulting fundamental limit on the energy resolution is $\Delta E_{\mathrm{FWHM}} \leq 1.4\,\mathrm{eV}$.

In the microcalorimeter model used so far, the absorber heat capacity consists only to the electronic contribution due to the conduction electrons of the metal and the phononic contribution. However, as discussed in the previous chapter, in order to optimise MMC detectors for the calorimetric measurement of the ^{163}Ho, the holmium source needs to be embeeded inside the absorber. The implanted ^{163}Ho atoms can lead to a non negligible contribution to the absorber heat capacity, degrading the energy resolution. The expected specific heat of ^{163}Ho is discussed in the following section.

4.5 Effects of ^{163}Ho ions

The ^{163}Ho atoms that are embedded inside the absorbers of the detectors developed for the ECHo experiment inevitably contribute to the heat capacity. According to the ^{163}Ho half-life value of 4570 years reported in literature [Bai83] [Kaw88], the amount of ^{163}Ho atoms corresponding to an activity of 1 Bq is about 2×10^{11}. The amount of holmium source implanted in each detector pixel must be carefully tuned taking into account not only the pile-up fraction, but also the effects on the detector performances due to the corresponding additional heat capacity. The interaction mechanisms that lead to the heat capacity of ^{163}Ho implanted in gold or silver are shortly reviewed in the following from a theoretical point of view.
The specific heat of holmium implanted in gold and silver has been experimentally investigated with relaxation methods and with an experimental approach based on MMC detectors [Her20]. Dedicated heat capacity measurements to evaluate the choice of silver as holmium host material for the next phases of the ECHo experiment have been carried out in the framework of this work, as it will be discussed in chapter 6.

4.5.1 Properties of Ho^{3+} ions implanted in metallic hosts

The expected specific heat of ^{163}Ho implanted in a metallic host, e.g. gold or silver, can be theoretically derived. The system can be treated with the same approach it was used to describe the sensor, where erbium ions are diluted in a metallic host material. Analogously, the holmium atoms occupy regular lattice sites and three electrons of the outer shells delocalise in the conduction band, generating Ho^{3+} ions with the electron configuration $[Kr]4d^{10}4f^{10}5s^25p^6$. As in the case of erbium, the non completely filled 4f orbital leads to a paramagnetic behaviour and the effect of the crystal field is negligible, as the comparably small and deeply located 4f shell is effectively shielded by the fully occupied 5s and 5p shells. Hence, the magnetic moment μ_J can be calculated assuming **LS** coupling and using equation 4.2. According to Hund's rules, the resulting spin, angular momentum and total angular momentum are $S = 2$, $L = 6$ and $J = S + L = 8$, respectively, leading to the Landé factor $g_J = 4/3$.

The seventeen-fold degenerate ground state of independent and isolate Ho^{3+} magnetic moments is the only relevant energy level at low temperatures, as the excited states of the magnetic moments caused by spin-orbit coupling are at energy scales of several thousands Kelvin. However, a more realistic picture should include also the interaction between the Ho^{3+} magnetic moments, the presence of external magnetic fields, the crystal field of the surrounding host material and the hyperfine interac-

tion with the nucleus. These interactions break the degeneracy of the ground state, generating a splitting of the energy levels and, thus, affecting the specific heat.

4.5.2 Contributions to the specific heat of implanted holmium

For temperatures below 1 K, the most relevant contribution to the holmium heat capacity are given by the hyperfine splitting and the crystal field effects. The dipole-dipole interaction and the RKKY interaction, arising from the mutual interaction among magnetic moments, as well as the Zeeman splitting, due to external magnetic fields, are not dominant.

Hyperfine splitting Because of its nuclear spin $I = 7/2$, the nucleus of ^{163}Ho presents a nuclear magnetic dipole moment and, thus, an hyperfine interaction with the 4f electrons. The Hamiltonian of the hyperfine interaction between the magnetic moments of the electrons and the magnetic moment of the nucleus is given by: $H_{\mathrm{hf}} \propto a \cdot \mathbf{I} \cdot \mathbf{J}$, where a is the material dependent hyperfine coupling constant, while $\mathbf{I}$ and $\mathbf{J}$ are the nuclear spin and total angular momentum operators. The hyperfine coupling constant values for Ho^{3+} ions were determined for different host material than gold or silver [Abr70]. Assuming a not critical effect of the crystal field of the surrounding host material ions on the hyperfine interaction and therefore a practically constant factor a, the expected hyperfine energy level splitting is in the range of $0.3\,\mathrm{K}k_{\mathrm{B}}$ [Kru69].

Crystal field The ground state of the Ho^{3+} ions implanted in gold or silver is affected by the crystal field generated by the surrounding host material atoms. The charge distribution of the electronic 4f shell creates an electrostatic potential that can be described by high-order crystal field functions [Ste52]. This approach requires input parameters that define the scale of the energy splitting, which have been estimated theoretically and esperimentally, with inconsistent results [Ble89][Mur70]. Depending on the choice of the input parameters for the definition of the crystal field Hamiltonian, the crystal field influence on the heat capacity of holmium implanted in gold or silver can be significant in the temperature regime of interest, e.g. at about 20 mK. As the hyperfine- and crystal field splitting cannot be separated from each other as they are coupled in J, a single but more complex Schottky peak is expected [Her20], [Kru69].

Interaction between magnetic moments As mentioned in section 4.2.2, if the magnetic moments are not independent, dipole-dipole interaction as well as RKKY interaction arise. Both the corresponding Hamiltonians, reported in equations 4.5

and 4.6 scale with $1/r^3$, where r is the distance between pairs of Ho^{3+} magnetic moments. Since the average distance $\overline{r}$ scales with $x^{-1/3}$, where x is the holmium concentration, the dipole-dipole interaction as well as the RKKY interaction effects depend on the concentration. The holmium concentration that is reached during the detector implantation process is in the range of few percents or below [Gam17] and therefore the interaction between the holmium cannot be completely neglected. Experimental data show that the contribution to the specific heat shift to lower temperatures for samples with lower concentration [Her20].

Zeeman effect External magnetic fields, e.g. the magnetic field created by the persistent current in the detector pick-up coil or the earth magnetic field, cause a Zeeman energy splitting. The corresponding Hamiltonian is $H_{\mathrm{Z}} = g_J \mu_{\mathrm{B}} \mathbf{B} \cdot \mathbf{J}$, where $\mathbf{B}$ is the magnetic field. Considering $\mathbf{B} \parallel J_Z$, the resulting energy eigenvalues are $E_{\mathrm{Z}} = g_J \mu_{\mathrm{B}} |\mathbf{B}| m_J$. Since in the detectors fabricated for the ECHo project the distance between the meander-shaped pick-up coil and the implantation region is $\geq 4\,\mu\mathrm{m}$, the influence of the sensor polarising B-field is negligible. On the other side, the $\approx 60\,\mu\mathrm{T}$ heart field generates a Zeeman splitting that is estimated to be about $50\,\mu\mathrm{K}$ and therefore negligible.

5. ECHo-1k: detector system and high-statistics measurement

The aim of the ECHo-1k experiment, the first phase of the ECHo project, is to improve of one order of magnitude the current best limit on the effective electron neutrino mass of 150 eV 95% C.L. [Vel19a]. For this experiment a new MMC detector array has been developed. In the following the design and fabrication of the ECHo-1k detector are described, as well as the read-out chain that has been used to operate the implanted detectors at millikelvin temperature[1]. The ECHo-1k detector has been fully characterised in the framework of this thesis. Room temperature tests as well as measurements at 4.2 K and at millikelvin temperature have been performed with several chips. The results of the detector characterisation are reported in the following and compared with the expectations based on theoretical calculations. Finally, two selected ECHo-1k detector chips with embedded ^{163}Ho have been used for a high-statistics measurement run over several months. The collected data will allow to reconstruct a ^{163}Ho electron capture spectrum with about 10^8 events, concluding the ECHo-1k phase.

5.1 The ECHo-1k detector

5.1.1 Detector design

The detector designed for the ECHo-1k phase consists of an array of 36 MMC channels, featuring the planar geometry described in section 4.3.1 and thus consisting of two detector pixels. For 34 of these channels both pixels are equipped with sensor and absorber. The input coil of a dc-SQUID is connected in parallel to both the pick-up coils forming a first order gradiometer. Figure 5.1a shows a blow-up picture of a detector channel of the ECHo-1k chip and figure 5.1b shows a photo of the entire chip. The detector pixels are positioned along 4 lines and the orientation of a single channel is indicated in the figure. The chip has a size of 10 mm × 5 mm and is divided into four quarters, each including nine detector channels, i.e. 18 detector pixels.

Two channels, placed at two opposing corners of the array, are dedicated to temperature monitoring. The two temperature monitoring channels are characterised by a non-gradiometric layout, having one of the two pixel not equipped with a sensor.

[1] This chapter contains paragraphs from the author's publications [Man21] and [Man], where the results achieved in the framework of this thesis are presented.

The temperature monitoring channels are not loaded with ^{163}Ho. The temperature fluctuations that are detected using these channels can be exploited to correct the pulse amplitudes acquired with the other channels against temperature drifts.

Two channels at the other two opposing corners have not been implanted and they can be used for diagnostics and characterisation studies, in particular for comparing the performances of the two pixels belonging to the same double meander and, in general, for testing the performances of not implanted MMCs.

The remaining 32 channels in the central area of the chip can be used for the measurement of the ^{163}Ho spectrum and for *in situ* background measurements. For this the implantation mask is designed so that:

- 25 channels have both pixels implanted enclosing ^{163}Ho with activities around 1 Bq;
- the remaining seven channels have only one pixel loaded with ^{163}Ho, so that the empty pixel allows for *in situ* background measurements.

The not implanted pixels dedicated to background studies are crucial to constantly monitor the background level and they allow for a direct comparison of the background data with the simulated background models. The calibration of these not implanted pixels can be achieved exploiting the calibration curve determined for the second pixel implanted with ^{163}Ho belonging to the same channel.

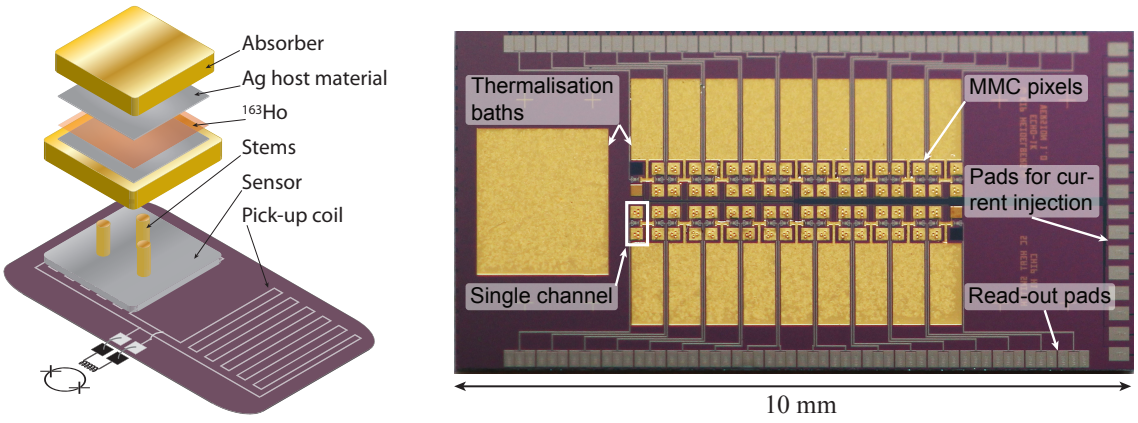

Figure 5.1: **a)** Schematic layout of a single detector channel made of two MMC pixels. **b)** ECHo-1k array chip with 36 MMC channels. Each single detector channel consist of two MMC pixels. The gold thermalisation baths and the read-out pads are highlighted.

The detector heat capacity contains three contributions: the heat capacity of the absorbers C_a, the heat capacity of the sensor C_s and the heat capacity of the ^{163}Ho atoms C_{Ho} [Her20]. The design values, considering the Ag:Er concentration of 445 ppm for the sensor fabrication, are $C_a = 0.46\,\mathrm{pJ/K}$, $C_s = 3.22\,\mathrm{pJ/K}$ and $C_{Ho} = 0.02\,\mathrm{pJ/K}$ at a temperature $T = 20\,\mathrm{mK}$, assuming an activity of 1 Bq.

Each MMC pixel is connected to the thermal bath via a weak thermal link which consists of a gold film with an area of $42.5\,\mu\mathrm{m} \times 5.0\,\mu\mathrm{m}$ and a thickness of $0.3\,\mu\mathrm{m}$. The thermal link connects the sensor to a T-shaped gold area which is then connected to the thermal bath, as visible in figure 5.2.
Each pixel is connected via three gold structures linked in series to the on-chip gold thermalisation baths, as shown in figure 5.2. Specifically, the sensor is connected to a T-shaped gold area via the weak thermal link described above. The T-shaped gold area is in turn connected to the thermal bath with an area of $0.56\,\mathrm{mm}^2$ and a thickness of $5\,\mu\mathrm{m}$. The heat capacity of the thermal bath is $4.0\,\mathrm{pJ/K}$ at a temperature $T = 20\,\mathrm{mK}$. Each thermal bath can be connected via gold wire-bonds to the next one and finally to the larger gold thermsalisation bath (figure 5.1b). The large top thermalisation bath is intended to be connected via gold wire-bonds to the experimental copper holder to guarantee optimal thermalisation.

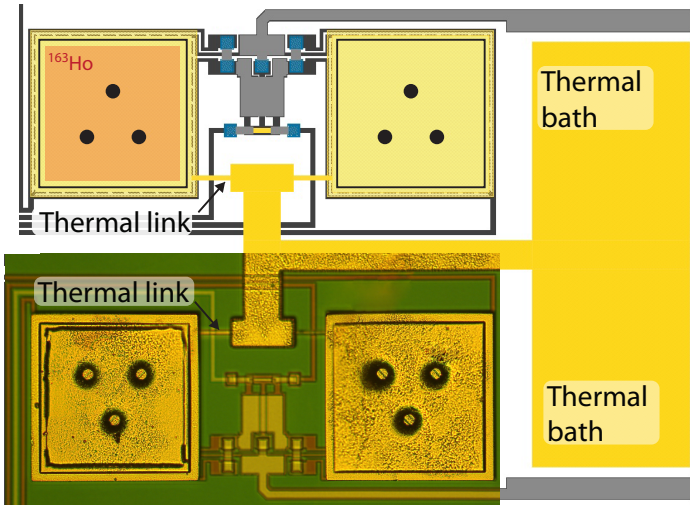

Figure 5.2: Design (pixel pair at the top) and microscope picture (pixel pair at the bottom) of the thermalisation concept in the ECHo-1k design. Four fully fabricated ECHo-1k pixels are shown. The two left pixels are implanted with ^{163}Ho. The weak thermal link and the thermal bath are indicated.

5.1.2 Detector fabrication

The ECHo-1k detectors have been fabricated on 3" silicon wafers in the cleanroom facility of the Kirchhoff-Institute for Physics, Heidelberg University. Each wafers hosts 64 chips. The fabrication is divided into 14 steps (including the ^{163}Ho implantation procedure) which are summarised in table 5.1.

Fabrication steps				
#	Layer	Material	Thickness	Deposition technique
1	Pick-up coils, SQUID lines (layer 1)	Nb	300 nm	Sputtering + etching
2	Isolation	Nb_2O_5	-	Anodisation
3	Isolation	SiO_2	175 nm	Sputtering + lift-off
4	Isolation	SiO_2	175 nm	Sputtering + lift-off
5	Heaters	AuPd	150 nm	Sputtering + lift-off
6	SQUID lines (layer 2)	Nb	600 nm	Sputtering + lift-off
7	Sensor	AgEr	1.3 µm	Sputtering + lift-off
8	Thermalisation	Au	300 nm	Sputtering + lift-off
9	Stems	Au	200 nm	Sputtering
10	Absorber - 1st layer	Au	5 µm	Electroplating + lift-off
11	^{163}Ho host material	Ag	150 nm	Sputtering
12	^{163}Ho implantation	^{163}Ho	-	Ion-implantation
13	^{163}Ho host material	Ag	150 nm	Sputtering + lift-off
14	Absorber - 2nd layer	Au	5 µm	Sputtering + lift-off

Table 5.1: Microfabrication steps of the ECHo-1k detector chip.

The single MMC pixel is depicted in figure 5.1a. The corresponding fabrication process starts with the production of a niobium superconducting meander-shaped pick-up coil, which is used to detect the magnetic response of the sensor and to create the constant magnetic field by means of a persistent current. For this purpose, a 300 nm thick niobium layer is sputter deposited on the full substrate, then photoresist is structured on top covering the areas that are part of the design and finally the rest of the material is removed via reactive-ion etching[2]. The meander-shaped pick-up coil is characterised by 39 stripes with a width of 3 µm and a pitch of 6 µm. The total surface of a single pick-up coil is 172 µm^2. The two pick-up coils belonging to one detector channel are connected to the bonding pads at the rim of the chip (as shown in figure 5.1b). Al:Si bonding wires are used to connect these bonding pads to the corresponding bonding pads leading to the input coil of a front-end dc-SQUID

[2]Etching process performed with ICP Cryogenic Etch System SI 500 C.

located on a SQUID chip. The SQUID chip is positioned as close as possible to the ECHo-1k detector chip to minimise the stray inductance due to the wire-bonds.

For isolation purposes, the niobium structures are anodised and two SiO_2 layers are deposited on top (as reported in Table 5.1). For this, a lift-off technique is employed: photoresist is structured on the substrate leaving open the areas that are part of the design, SiO_2 is then sputter deposited on top and finally the resist is lifted-off.

The next layer contains normal conducting heater elements which are used for the injection of the persistent current in the superconducting niobium pick-up coils (as explained in detail in the subsection 5.1.5). The heaters consist of Au:Pd film with a nominal thickness of 150 nm fabricated via a sputtering and lift-off process.

After that, a second niobium layer is deposited to complete the strip-lines that connects the pick-up coils to the bonding pads. A stripe-line consists of two overlapping connection lines separated by an isolation layer in order to minimise the parasitic inductance between the lines.

On top of the pick-up coil, the Ag:Er sensor layer with an erbium concentration of about 440 ppm and with an area of 168 µm × 168 µm is sputter deposited and lifted-off. The thickness of the sensor is designed to be 1.3 µm, but a gradient over the wafer can occur.

On top of the sensor, a photoresist layer defining three gold stems with a diameter of 10 µm for the support of the first absorber layer above is structured and a 200 nm tick gold layer is sputtered.
A thin sacrificial niobium layer of 50 nm is deposited to protect the gold layer. A second photoresist layer, defining the absorber area of 180 µm × 180 µm, is structured on top. After that, the sacrificial layer is removed via reactive-ion etching. Finally, the stems and the absorber are fabricated simultaneously using the TECHNI-GOLD 25 ES gold plating solution[3] and a current per area of $1 mA/cm^2$. The absorber thickness is designed to be 5 µm.
The purpose of the stems is to minimise the contact area between sensor and absorber. This prevents athermal phonons from travelling through the sensor and releasing the energy in the substrate. This energy would therefore not be detected leading to a low energy asymmetry in the detector response [Has16].

5.1.3 ^{163}Ho implantation

The first attempt of ^{163}Ho on-line ion implantation in MMC detectors was performed at ISOLDE with successful results regarding the detector performance, but radioactive contamination could not be avoided [Gas13]. Off-line ion implantation starting

[3]Produced by Technic Inc., Cranston, Rhode Island.

from a holmium sample which has been chemically purified has been chosen to prevent the presence of radioactive nuclides in the implantation beam other than ^{163}Ho. The production and isolation techniques that are exploited to provide suitable ^{163}Ho samples for the ECHo experiment have been already introduced in section 3.1.2.

The ionisation, mass separation and ion implantation are performed at the RISIKO facility at Mainz University [KT19a]. The working principle of the RISIKO mass separator and its main components are described in section 3.1.2. The 30 keV high quality ^{163}Ho ion-beam is used to perform a direct source implantation in the MMC detectors. The detector chip needs to be adequately prepared, following the microfabrication steps explained in the following.

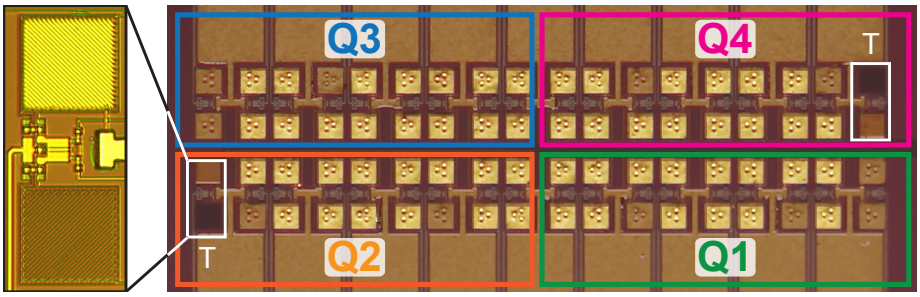

Figure 5.3: The ECHo-1k detector chip covered with a photoresist mask that leaves open only the implantation areas. The four quarters of the chip are highlighted and the two non-gradiometric channels dedicated to temperature monitoring are labelled with the letter T. The inset shows a zoom of one of the non-gradiometric channels.

First, a photoresist mask is applied on a single ECHo-1k chip leaving open only areas of $(150\,\mu\text{m})^2$ on top of each absorber to be implanted, as illustrated in figure 5.3. The reduced area ensures full enclosure of the source.
A thin layer of typically 100 nm of host material of choice is then sputter deposited on the full substrate and it is also exploited to contact to ground and to avoid charging of the sample during implantation. Different host materials - gold, silver and aluminium - have been considered and tested, as explained in the following. The ^{163}Ho implantation depth depends on the selected material and on the ion energy. Assuming the operational ion energy of 30 keV used at RISIKO, a mean longitudinal implantation depth of few nanometers is expected for silver and gold [Gam17].
As next step, the ^{163}Ho is ion-implanted into the host material. To protect the implanted area, a second thin layer of typically 100 nm of the host material is deposited additionally over the sample within a short time after the implantation process.
Finally, the chip undergoes the post-processing phase. The photoresist mask used for implantation is lifted-off and a second photoresist mask is prepared for the structuring of the second part of the absorber. For this a 5 µm gold film is structured on

top of each pixel (including the background pixels) over an area of $(165\,\mu m)^2$. Figure 5.4 shows the post-process steps for the ^{163}Ho implantation and the structuring of the top absorber layer.

The final layouts of an implanted MMC pixel as well as a background not implanted pixel are visible in the microscope image of figure 5.2. The implanted pixel can be distinguished by the presence of three concentric square structures: the inner most one corresponds to the implantation area, the outer most one to the edge of the bottom absorber layer and the one in the middle to the top absorber layer. On the other side, the background pixel does not show the square structure corresponding to the implantation mask, but the top and bottom absorber layers are visible.

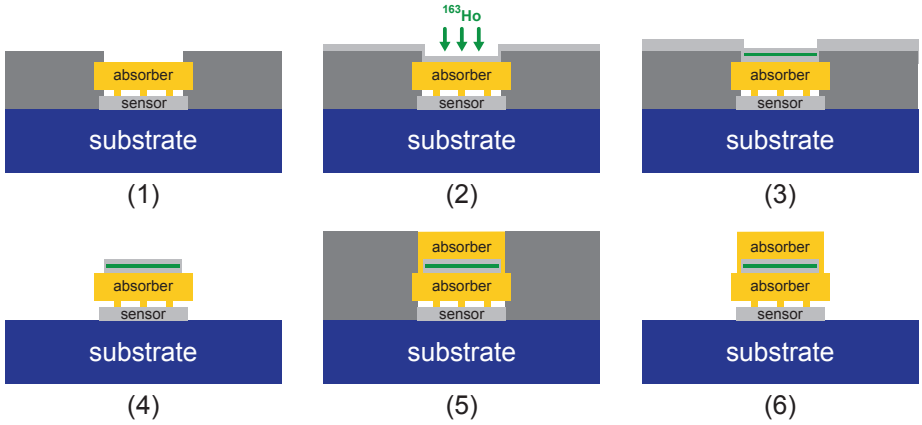

Figure 5.4: The microfabrication steps for implanting ^{163}Ho in the ECHo-1k MMC pixels (corresponding to the layers 11, 12, 13 in table 5.1) are schematically depicted. The photoresist is shown in dark grey; the host-material as well as the sensor are shown in light grey; the ^{163}Ho source is shown in green; the gold absorber is shown in yellow.

5.1.4 ^{163}Ho host material

Different ^{163}Ho host materials have been considered and tested during the ECHo-1k phase: gold, silver and aluminium - as it will be discussed in detail in the next chapter (section 7.2).

Gold is the typical absorber material for MMC detectors and therefore the natural choice and the easiest one from the fabrication point of view. However, gold is characterised by nuclear quadrupole moments which might induce hyperfine splitting, therefore leading to an additional contribution to the heat capacity [Ens00].

On the other hand, silver exhibits a very similar electron shell configuration with respect to gold, but no nuclear quadrupole moment is present and therefore it has

been investigated as host material candidate. Additionally, the heat capacity contribution from the ^{163}Ho ions implanted in silver is lower than for gold in the MMC operational range of about 20 mK [Her20]. The heat capacity of ^{163}Ho in silver has been further studied in the context of this work, as reported in chapter 6.

Finally, aluminium allows a larger penetration depth during the implantation process. According to simulations, the estimated mean longitudinal implantation depth is 19.5 nm, while in the case of gold and silver this value is 1.8 nm and 7.7 nm, respectively [Gam17]. Therefore it should be possible to reach higher ^{163}Ho activities. In order to test this effect, an ECHo-1k chip has been implanted with aluminium as host material. A potential drawback of aluminium is the superconducting nature of this material, which could potentially compromise the detector response.

5.1.5 Detector operation

As already anticipated, the temperature sensor needs to sit in a weak magnetic field, in the order of millitesla. The static magnetic field is created by a persistent current circulating in the closed loop formed by the superconducting meander-shaped pick-up coils. The current can be injected exploiting a normal-conducting element that acts as a heater-switch, driving a small part of the closed superconducting circuit to the normal-conducting state by local Joule heating. The procedure to prepare the supercurrent is schematically shown in figure 5.5:

1. The field generating current ($I_{\mathrm{F}} \sim 30\,\mathrm{mA}$) is injected from +F to −F. Since the flux in a superconducting loop needs to be conserved, the major part of the current flows in the arm having lower inductance;

2. The heater-switch is activated driving a current ($I_{\mathrm{H}} \sim 4.0\,\mathrm{mA}$) through the Au:Pd resistor film, characterised by a resistance of about 10 Ω, as measured at millikelvin temperature. In this way, part of the niobium line is driven to the normal conductive regime, showing a finite resistance. Consequently, the path of the field generating current changes and the current will then flow through the large inductance formed by the meander-shaped pick-up coils in the superconducting state;

3. When the heater-switch is deactivated, all the lines turn superconducting again, leaving the field generating current frozen in the superconducting loop.

The functioning of the heater-switch is fundamental to operate the detectors and therefore the switching point of the heater elements has been tested and carefully characterised.

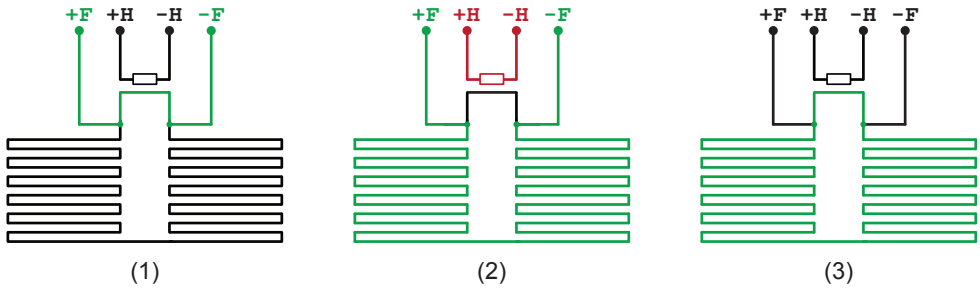

Figure 5.5: Schematic layout showing the procedure to inject persistent super-current into the meander-shaped pick-up coils in order to polarise the sensor. The heater element is connected to the ±H lines. The meandering structures and a shorter path external to the meanders are connected in parallel to the ±F lines. The steps for the current-injection are explained in detail in the text.

All the pick-up coils belonging to one quarter of the chip are connected in series. The same is valid for the heater elements of one quarter. Therefore, the persistent current is injected into all the detectors belonging to one quarter (i.e. 9 detector channels) at a time. The pads connecting the current sources for the heater and the field lines are located in the right periphery of the chip (as shown in figure 5.1b).

5.2 Read-out chain

In order to operate the ECHo-1k detectors at millikelvin temperature, a complete read-out chain has been assembled. The detector module has been designed and built specifically for the ECHo experiment, while the amplification modules, the cabling of the cryogenic platform and the data acquisition hardware and software have been developed within the MMC research group at the Kirchhoff Institute for Physics, Heidelberg University. As a result, a standard scheme for the read-out of 32-channel MMC arrays have been established [Man21]. The full read-out chain is explained in the following, starting from the ECHo-1k detector set-up and ending with the signal read-out and data processing section.

5.2.1 Detector set-up

As described at the beginning of this chapter, the detector chip for the first phase of the ECHo experiment, ECHo-1k, consists of an MMC array by a total of 36 detector channels, i.e. 72 detector pixels. Two of the channels on the chip are devoted to test purposes, namely detector diagnostics and characterisation, two channels are dedicated to temperature monitoring and the remaining 32 channels can be used for measuring the ^{163}Ho spectrum after the source is embedded via ion-implantation.

Each SQUID channel reads out two meander-shaped pick-up coils [Fle05] arranged in a gradiometric configuration allowing for the identification of the detector pixel where a particle event occurred via the polarity of the signal. Moreover, the gradiometric setup makes the MMC channel fairly insensitive to fluctuations of the substrate temperature, as the temperature variations happen simultaneously in both pixels.

The chip is designed to be wire-bonded to external front-end SQUID read-out chips. The detector operational temperature is about 20 mK and is reached by mounting the detector set-up at the mixing chamber plate of a dilution refrigerator. In order to ensure optimal thermalisation, the detector chip is glued on a custom-built T-shaped holder made of annealed OFHC[4] copper with a size of 2.7 cm × 19.3 cm × 0.8 cm, as shown in figure 5.6. Additionally, the on-chip gold thermal baths are connected via gold wire-bonds to the copper holder for a better thermalisation of the detector chip (figure 5.6 inset, A).

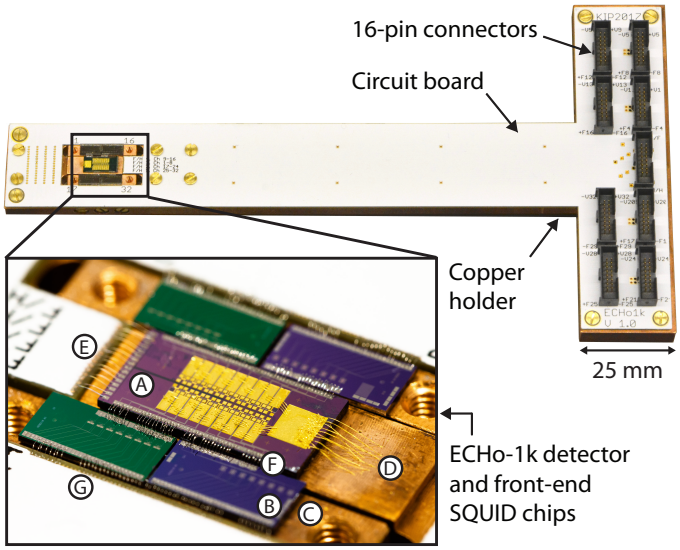

Figure 5.6: ECHo-1k detector sample holder made of copper, mostly covered by a circuit board with white solder mask. In the inset a close-up view on the ECHo-1k detector chip (A) glued onto the holder is shown. The detector chip is wire-bonded to four front-end SQUID chips (B), each one containing 8 SQUID channels, which are glued on separate copper blocks (C). The gold wire-bonds connecting the on-chip thermal baths with the copper holder (D) as well as the aluminium wire-bonds between detector chip and circuit board (E), between detector chip and front-end SQUID chips (F) and between front-end SQUID chips and circuit board (G) are visible.

[4]Oxygen Free High Conductivity.

The front-end SQUID chips are glued onto two separate copper blocks that can be inserted and screwed to the main holder right next to the detector area. This makes the preparation of the detector set-up more flexible, as the SQUID blocks can be easily exchanged allowing for a modular approach, where possibly faulty components can be replaced. The SQUID chips are electrically connected to the detector via aluminium wire-bonds bridging the slits that separate the SQUID copper blocks from the detector holder (figure 5.6, F). The SQUID chips are wire-bonded to the detector on one side and on the other side to a customised double layer circuit board (figure 5.6, G), which is fixed on top of the copper holder. The bond-pads at the bottom periphery of the detector are dedicated to the persistent current injection and they are directly wire-bonded to copper lines on the circuit board (figure 5.6, E).

The T-shaped detector holder can be inserted in an aluminium shield, as shown in figure 5.7. The shield becomes superconducting for temperatures below 1.2 K and therefore, due to the Meißner–Ochsenfeld effect, it shields detector and front-end SQUIDs against changes of external magnetic fields. The ratio between the depth and the longer side length of the opening is about 8.6 and ensures a high shielding level.

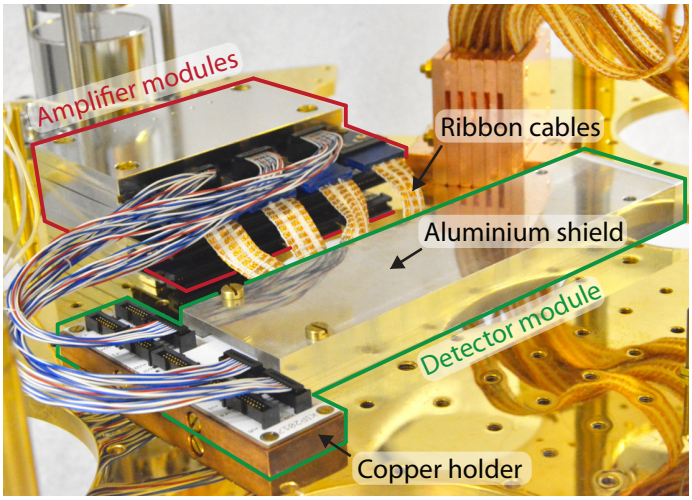

Figure 5.7: The complete cold part of the ECHo-1k set-up placed on the cryostat mixing chamber plate. It includes the shielded detector module and the amplifier stage. Only few cables are connected for illustration purposes.

The circuit board is equipped with nine double-row 16-pin connectors[5]: eight of them are connected to the SQUID lines and one is connected to the lines dedicated to the injection of the persistent current into the pick-up coils. Four wires are necessary

[5]Connector type SHF-108-01-L-D-TH produced by Samtec, 520 Park East Boulevard, New Albany, IN 47150, USA.

to read-out each front-end SQUID channel and therefore each SQUID connector corresponds to four front-end SQUID channels. The front-end SQUID output signals are transferred to second stage SQUIDs via tin-coated copper wires which connect the SQUID connectors on the detector circuit board to the second stage module, as visible in figure 5.7. The wires are commercially available with different wire counts in three different lengths[6]. The second stages consist of 16 SQUID-series arrays and acts as a low temperature amplifier stage. The working principle of a two-stage SQUID read-out and the custom-built amplification module will be described in the following section.

5.2.2 Amplifier modules

The layout of a two-stage SQUID read-out scheme is described in section 3.1.3. It consists of a first stage with front-end SQUIDs directly connected to the detector chip and a second stage with amplifier SQUIDs.
The design and fabrication of front-end and amplifier SQUIDs are tailored to the specific requirements for MMC detectors[7] [Kem15]. In particular, the input coil inductance of the front-end SQUIDs is designed to match the inductance of the detector meander-shaped pick-up coils.

The pick-up coils of the detector and the input coil of the SQUID are connected by superconducting aluminium wires to form a completely superconducting circuit. Changes in external magnetic fields or vibrations of the bonding wires can generate currents in this loop that lead to an increased noise level. An optimised bonding scheme can reduce the additional noise by nearly one to two orders of magnitude [Man21].

While the front-end SQUID chips are glued onto the detector holder and wire-bonded to the detector chip, the second-stage amplifier SQUIDs are placed on separate custom-designed modules to reduce power dissipation to the detector module, operated at about 20 mK. The modules are based on the custom-made circuit boards[8] shown in figure 5.8a. Each circuit board is equipped with:

- six dc-SQUID array chips with a size of 3 mm × 3 mm, each hosting two series arrays of dc-SQUIDs, glued to the circuit board at the end of a 45 mm long circuit board finger and wire-bonded to the copper leads;

[6]Produced by Samtec.

[7]The SQUID chips are designed and fabricated in house at the Kirchhoff-Institute for Physics, Heidelberg University.

[8]Produced by Multi Leiterplatten GmbH, Brunnthaler Straße 2, D-85649 Brunnthal - Hofolding, Germany.

- three double row 16-pin connectors[9] connect to the front-end SQUIDs shown in figure 5.8a;

- four double row 30-pin connectors[10] to which the ribbon type cables that connect the amplifier SQUIDs to the room temperature read-out stage are plugged.

The circuit board is inserted into a tin-plated copper case. This case consists of two copper plates that are coated with about 8 µm thick layer of tin. Due to its high thermal conductivity, copper ensures a reliable thermalisation of the heat produced by the amplifier SQUIDs. On the other hand, tin enters the superconducting regime at 3.7 K and, because of the Meißner–Ochsenfeld effect, provides a shielding against fluctuating external magnetic fields. The bottom plate is equipped with 3 mm deep millings in which the fingers of the circuit board can be inserted. The bottom plate and the upper plate need to be connected forming a long superconducting cup for each amplifier SQUID. In this way, each chip is placed in a separate superconducting compartment and therefore optimally shielded against external magnetic field fluctuations.
To reach this goal, the two tinned copper plates are diffusion welded with indium. Indium enters the superconducting regime at 3.4 K and it forms a eutectic with tin at about 120 °C. Pure indium melts at 157 °C and pure tin at 232 °C. To prepare the diffusion welding both plates are pressed to each other with indium wires of 1 mm diameter placed in between them. The indium wires were positioned as shown in figure 5.8b. In pressed state the plates are baked for three hours at 140 °C in air at normal pressure.

The circuit board is attached to the module case with five screws at the connector side. Therefore, the six fingers of the circuit board can potentially be subjected to vibrations. To prevent that, they are additionally fixed to the module exploiting tinned M 1.6 grub screws inserted into the threads in the upper part of the module, close to the amplifier SQUID chips.

Three amplifier modules, corresponding to 36 read-out channels, can be stacked forming a compact tower, which can be mounted on the mixing chamber plate of a dilution refrigerator, as depicted in figure 5.9a. The amplifier modules are additionally surrounded by a cryoperm shield [11]. This soft magnetic shield allows for a reduced background magnetic field during the transition of the tin parts to the superconducting state.

[9] Connector type SHF-108-01-L-D-TH produced by Samtec.
[10] Connector type TFM-115-01-S-D produced by Samtec.
[11] Produced by Magnetic Shields Ltd, Headcorn Rd, Staplehurst TN12 0DS, UK.

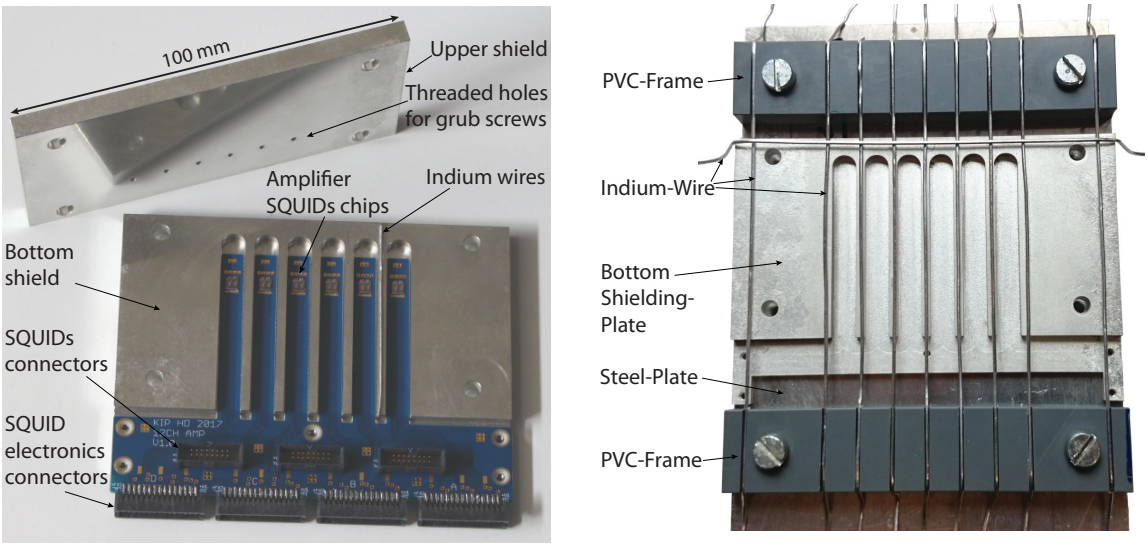

(a) **(b)**

Figure 5.8: **a)** A single array module consisting of the custom made circuit board inserted in the bottom half of the tin plated copper shield. The upper part is placed on top to close the module. **b)** Set-up for the preparation of the superconducting shield. The indium wires are positioned on the bottom plate before pressing the second plate on top of it and proceed with the diffusion welding of the two parts.

5.2.3 Cryogenic unit and parallel cabling

The ECHo detectors are operated in a dedicated dry dilution refrigerator of type BF-XLD[12] that reaches a base temperature below 7 mK. This cryostat has a cooling power of 20 µW at 20 mK at the mixing chamber plate. Along with the capability to host a net load of about 200 kg, the large available experimental space - corresponding to a cylindrical volume with a diameter of 50 cm and a height of 50 cm below the mixing chamber plate - and the continuous operation, the cryostat is suitable for the current and future phases of the ECHo experiment.

Figure 5.9a shows the open cryostat equipped with the cabling described in the following. Two groups of read-out cables are visible, each consisting of 32 parallel SQUID read-out channels and 4 multi-purpose read-out channels for a total of 72 read-out channels that have been installed in the cryostat and exploited to operate two ECHo-1k detector chips in parallel during the ECHo-1k high-statistics measurement campaign.

[12]Produced by BlueFors Cryogenics Oy, Arinatie 10, 00370 Helsinki, Finland.

Two stacks of amplifier modules, each containing 36 read-out channels as described previously, are placed on the mixing chamber plate of the cryostat, as can be seen in figure 5.9a. Altogether, 720 wires (10 wires per read-out channel) connect the amplifier stages to the room temperature electronics. The read-out wires are organised in twisted pairs and twisted triples interwoven in ribbons, each one containing the 30 wires required to read-out three SQUID channels. The ribbons are stably woven with Nomex fibers[13] resulting in 13 mm wide, 0.7 mm thick and 2.2 m long flat ribbons[14]. The two ribbon ends are equipped with connectors: at the room temperature side a 24-pin LEMO connector[15] interfaces a vacuum feedthrough[16] followed by the SQUID electronics. At the low temperature side a double row 30-pin connector[17] matches the connectors of the amplifier modules, as shown in figure 5.9c. The wire material is optimised to reach a compromise between low resistance and low thermal conductance, to minimise the contribution to the heat input. Alloy-30[18], an alloy of 2% nickel in copper, has been chosen. The wires have a diameter of 200 µm and a length of about 2.2 m. The round-trip resistance of a twisted pair of such wires is 6.7 Ω and drops only by about 20% when cooled down. This is low enough that both the voltage noise of the warmer fraction of the wires and the current noise of the input amplifier of the SQUID electronics lead to contributions of the total noise which are marginal.

In order to dump any power that is dissipated in the wires and to reduce the heat load from room temperature to the mixing chamber plate, a good thermal coupling between the ribbons and the different temperature stages of the cryostat is necessary. In-house manufactured OFHC-copper heat sinks have been designed and installed (figure 5.9b) [All17]. They consist of seven 46 mm × 50 mm × 5 mm large copper plates screwed to each other. Six of them feature a milled channel which allows to place two ribbons side by side between each pair of plates, ensuring full surface contact and avoiding mechanical stress of the wires. To maximise the thermal coupling, vacuum grease[19] is distributed on the contact area between ribbon and copper plates and the copper plates. The heat sinks at the two lowest temperature stages have been annealed at 800 °C for 48 hours to remove hydrogen molecules.

[13]Manifactured by DuPont de Nemours GmbH, Hugenottenallee 175, 63263 Neu Isenburg, Germany.

[14]Produced by Tekdata Interconnections Limited, Innovation House, The Glades, Festival Way, Etruria, Stokeon-Trent, Staffordshire, ST1 5SQ, United Kingdom.

[15]Connector EGG.3B.324.ZLL produced by LEMO, Chemin de Champs-Courbes 28, CH-1024 Ecublens, Switzerland.

[16]Coupler SGJ.3B.324.CLLPV produced by LEMO.

[17]Connector type "SFM-115-01-S-D" produced by Samtec.

[18]Purchased from Isabellenhütte, Eibacher Weg 3-5, 35683 Dillenburg, Germany.

[19]Apiezon N, M&I Materials Ltd., Hibernia Way, Trafford Park, Manchester M32 0ZD, United Kingdom

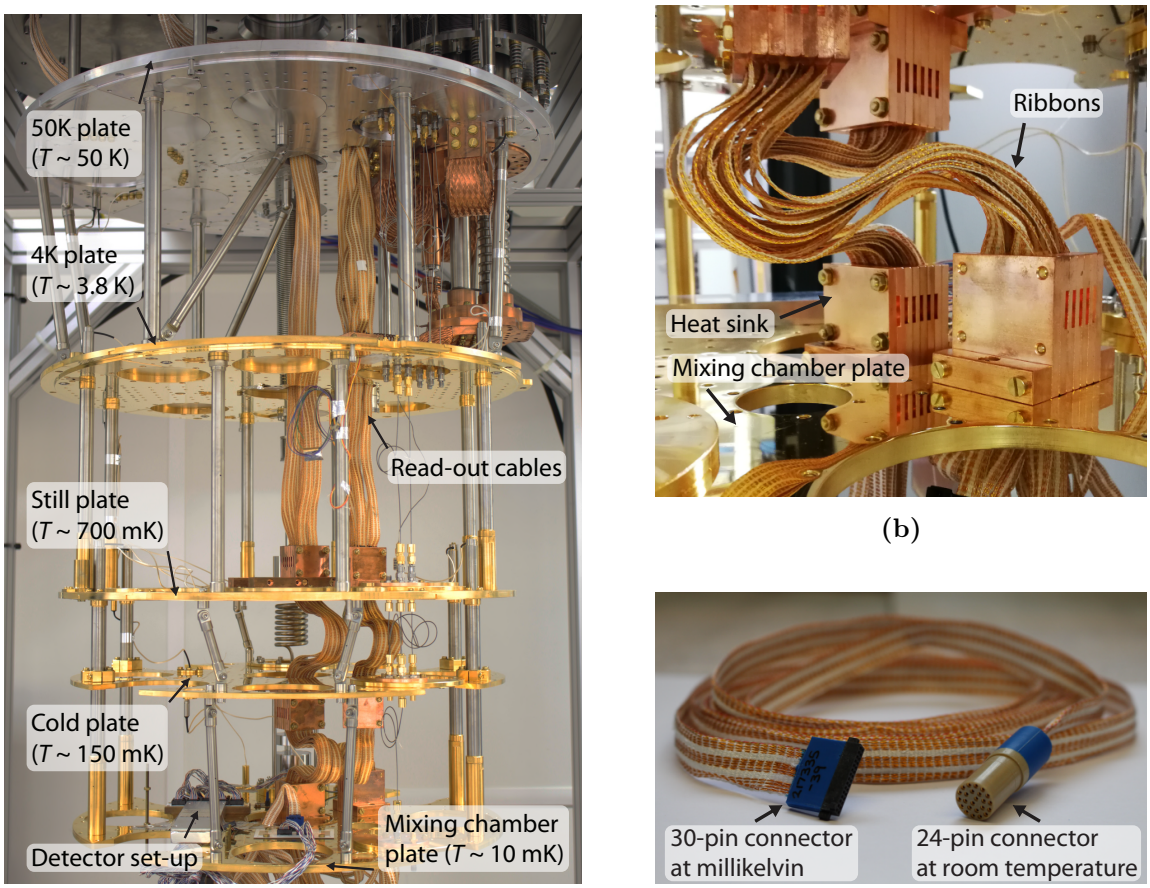

Figure 5.9: **a)** Open dilution refrigerator dedicated to the ECHo experiment. The temperature stages, the detector set-up and the parallel read-out cabling are highlighted. **b)** Copper heat sinks for cable thermalisation trough the cryostat temperature stages. **c)** A single ribbon cable containing 30 wires for three channels.

The ribbons are connected at room temperature to aluminium boxes on top of the cryostat, where 24-pin vacuum feedthroughs connectors[20] are used as interface between the atmospheric pressure outside and the vacuum inside the cryostat and provide the possibility to directly plug in the SQUID electronics used for the ECHo experiment[21]. The SQUID electronics can be connected via LEMO cables to the SQUID connector box, a device which serves as power supply for the SQUID electronics and allows for tuning of the SQUID parameters via software.

[20] Connector type SGJ.3B.324.CLLPV purchased from LEMO Elektronik GmbH, Hanns-Schwindt-Str. 6, 81829 Munich, Germany.

[21] 3XXF-1, Magnicon GmbH, Barkhausenweg 11, 22339 Hamburg, Germany.

5.2.4 Signal read-out and data processing

All the parameters of the programmable two-stage SQUID electronics can be set by software[22]. The output voltage of the linearised SQUID signal is transferred from the SQUID connector box to two ADC modules using coaxial cables equipped with NIM/Camac standard connectors[23]. The digitised signals from the ADC modules are transferred to a computer and acquired by means of a dedicated DAQ software. The complete read-out chain is summarised in the schematic diagram of figure 5.10.

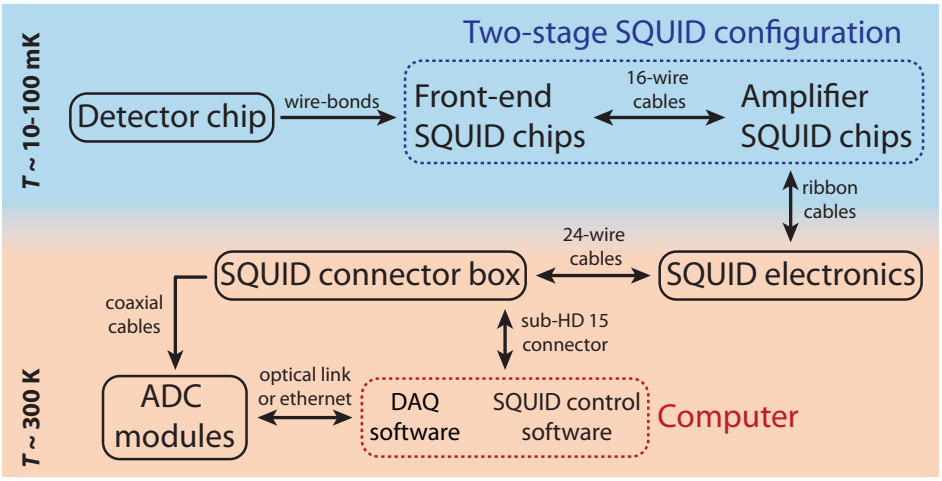

Figure 5.10: Schematic layout of the complete read-out chain for the ECHo experiment. The direction of the arrows refers to the signal and data transfer flow.

Each ADC module is based on a 16-channel digitiser card SIS3316[24]. The cards can either be read-out via ethernet or via a SIS1100/3100[24] connection based on an optical gigabit link. If more than one module is used, theirs clocks can be synchronised, which is essential for coincidence measurements. They feature a maximum sampling rate of 125 MHz per channel and a resolution of 16 bit. Supporting simultaneous acquisition of data and data transfer to the computer as well as individual asynchronous constant fraction trigger engines for each channel, the cards are suitable for high throughput and flexible read-out. Oversampling up to a factor of 256 can be used to acquire larger time windows and to increase the effective resolution of the ADCs from about 13 bit to the full 16 bit. At the same time a high timing precision on the fast clock is available to investigate coincidences.

An in-house developed C++ acquisition software [Hen17] allows to control hardware settings, data transfer, on-line signal processing and data storage. The software offers

[22]SQUID Viewer provided by Magnicon.

[23]Produced by LEMO

[24]Produced by Struck Innovative Systeme GmbH, Harksheider Str. 102, 22399 Hamburg, Germany.

a graphic user interface with a virtual oscilloscope that allows to tune the SQUID parameters before starting the data acquisition and to perform noise measurements to further optimise the SQUID tuning or to characterise the detector properties. When the acquisition is started, for each triggered event the raw signal, typically containing 16384 samples, is saved on disk and relevant information (e.g. signal height, timestamp, polarity, ...) are determined and stored. Subsequently, an individual on-line fitting procedure based on a template fit takes place and the fit results are saved. Additionally, for every triggered signal also a voltage trace of one or several temperature-sensitive channels can be acquired simultaneously to correct for signal height variations due to variations of the detector temperature. Furthermore, the program allows for a software hold-off and a simple on-line rejection of signals, for example based on signal height and shape, is available.

5.3 Detector characterisation

After fabrication, the ECHo-1k detector chips have been tested and fully characterised, in order to proof the functionality, verify the design values and evaluate the operational parameters. The positive outcomes of the first tests at room temperature and at 4 K allowed to proceed with the implantation of the ^{163}Ho source in the detector absorbers. The implanted detectors have been tested at millikelvin temperature, exploiting the read-out chain explained in the previous section. The impact of the implanted ^{163}Ho on the detector performances has been evaluated and the effects of the different implantation materials have been verified. Finally, the ^{163}Ho activity and the energy resolution have been derived for each detector pixel. The experimental methods and the results of the characterisation measurements are presented in the following.

5.3.1 Characterisation at room temperature

Tests at room temperature are relatively fast and easy to be performed, therefore they can be a powerful tool to verify the quality of the single detector channel on a chip or wafer scale.

As first step the chips undergo an optical inspection to exclude evident fabrication issues or damages that can compromise the functionality of the chip. Among others, the continuity of the niobium lines, the stability of the absorbers and the condition of the bond-pads and of the heater elements are important aspects to be verified. After that, the resistances of the niobium lines can be measured at room temperature contacting the corresponding bond-pads with a needle-probe tool, checking for possible shorts. The resistances of the ±F lines connected to the pick-up coils and

the resistances of the ±H lines connected to the heater elements have been measured for 15 ECHo-1k chips belonging to the same wafer and the resulting values are shown in the histograms of figure 5.11. Resistance values in the range of $3 - 5\,\mathrm{k\Omega}$ at room temperature proof the continuity of the corresponding conducting structures. The continuity of the niobium lines that connect the detector pick-up coils to the SQUID pads, to which the SQUID chip will be wire-bonded, is also tested at room temperature and the resistance between all the pads is checked to exclude the presence of shorts on the chip.

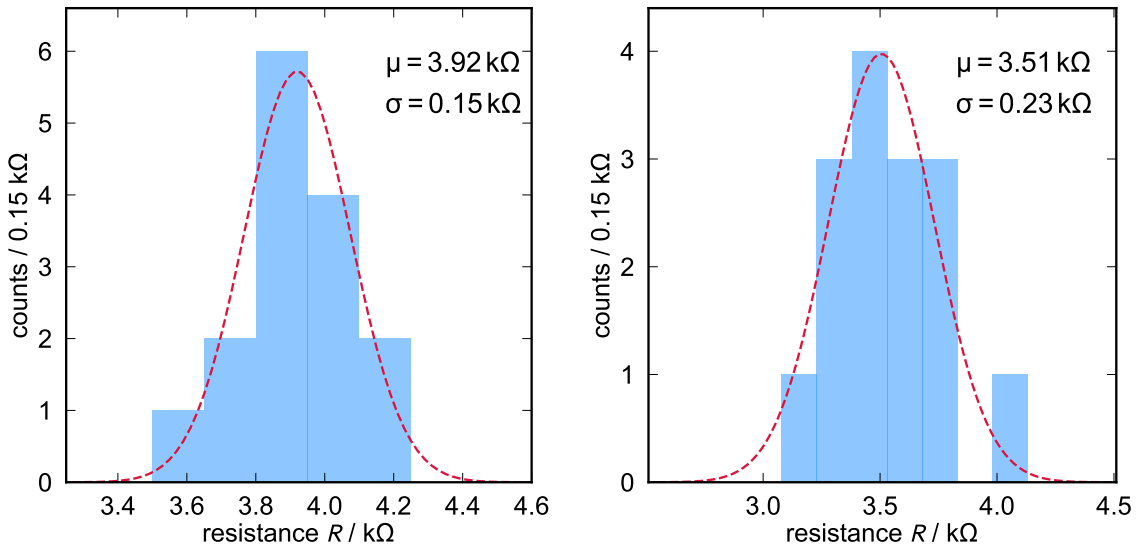

(a) **(b)**

Figure 5.11: Histograms of the resistances at room temperature of the ±F lines **(a)** and ±H lines **(b)** of one quadrant of 15 ECHo-1k chips. The Gaussian fit is shown in red and the corresponding mean μ and standard deviation σ are reported.

5.3.2 Characterisation at 4 K

Several properties of the ECHo-1k detector can be investigated in a temperature range around 4 K. Two experimental approaches can be pursued to reach this temperature, namely immersing the set-up in a liquid helium bath or exploiting the first cooling step of a dry dilution refrigerator based on a two-stage pulse tube cryocooler. Both these methods have been employed for the characterisation measurements that are presented in the following.

Heater switch

In order to probe the chip functionality, it is crucial to check the performance of the heater switch and to determine the current value that activates it. The experimental method is based on the measurement of the resistance of the lines connected to the SQUID read-out pads at a temperature of 4.2 K, which is reached cooling the chip in liquid helium. As depicted in figure 5.12a, the SQUID read-out pads ±S are connected to the pick-up coils, therefore forming a niobium superconducting circuit. Increasing currents are injected through the heater contacts monitoring the resistance between the pads ±S. When the current through the heater generates enough power to locally break the superconductivity, part of the probed circuit enters the normal-conducting regime, creating a non-zero resistance that can be measured. The minimal current leading to the resistance jump is taken as heater switching current.

The heater switching current values have been determined for 15 ECHo-1k chips and they are reported in a histogram in Figure 5.12b. The average heater switching current value is $I_{\mathrm{h,mean}} = 3.92\,\mathrm{mA}$ in a liquid helium bath.

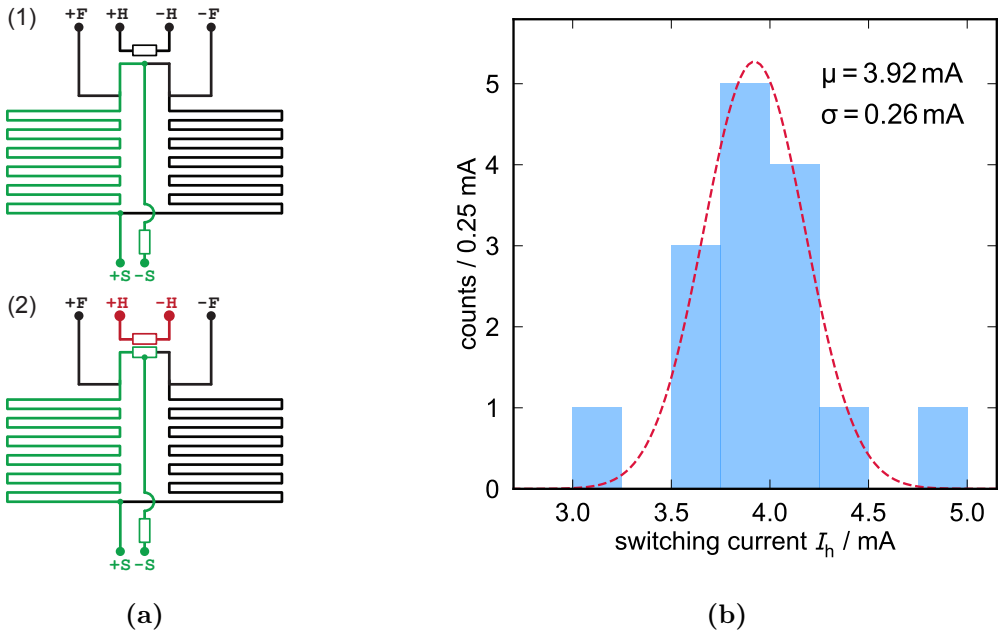

(a) **(b)**

Figure 5.12: **a)** Layout of the measurement method to determine the current to activate the heater switch. **b)** Histogram of the heater switch current values measured for one quadrant of 15 ECHo-1k chip; the distribution is fitted with a Gaussian function and the resulting mean μ and standard deviation σ are reported.

Inductance of the pick-up coil

The inductance of the niobium superconducting meander-shaped pick-up coils is an essential parameter to calculate the flux coupling between detector and SQUID, according to equation 4.20. This value can be determined from a SQUID flux noise measurement performed at $T \approx 4\,\mathrm{K}$. At this temperature the aluminium bonding wires connecting the pick-up coil and the input coil of the SQUID are normal-conducting, while the niobium meander-shaped pick-up coils as well as the input coil of the SQUID are in the superconducting regime. Therefore, the resistance of the bonding wires R_b together with the inductance of the circuit L constitute a low-pass filter with a cut-off frequency $f_\mathrm{c} = R_\mathrm{b}/(2\pi L)$. The corresponding circuit is shown in the inset of figure 5.13. The expected total noise spectral density is given by:

$$S_{\Phi_\mathrm{S}} = M_\mathrm{is}^2 \frac{4k_\mathrm{B}T}{R_\mathrm{b}} \frac{1}{1+(f/f_\mathrm{c})^2} + S_{\Phi_\mathrm{S}}^{\mathrm{S,w}} \tag{5.1}$$

where M_is is the mutual inductance between the pick-up coil and the SQUID and $S_{\Phi_\mathrm{S}}^{\mathrm{S,w}}$ is the white noise of the SQUID. The plateau at low frequency is given by the Johnson noise of the bonding wires.

The spectral flux density measured in the SQUID, with a detector channel connected to it, is shown in figure 5.13 together with a numerical fit performed using equation 5.1, where R_b and L are free parameters. From the value of the total inductance $L = 4.38 \pm 0.01\,\mathrm{nH}$ given by the fit it is possible to estimate the inductance of a single meander-shaped pick-up coil L_m:

$$L_\mathrm{m} = 2 \cdot (L - L_\mathrm{i} - L_\mathrm{b}) \tag{5.2}$$

where L_i is the inductance of the SQUID input coil, which by design is 1.8 nH, and L_b is the inductance of the bonding wires, which can be estimated from the corresponding resistance assuming the relation $L_\mathrm{b} \approx c \cdot R_\mathrm{b}$, with $c = 0.1 \pm 0.02\,\mathrm{nH/m\Omega}$ and $R_\mathrm{b} = 14.66 \pm 0.04\,\mathrm{m\Omega}$ from the fit. The value of c is based on the outcome of noise measurements performed varying the length of the aluminium wire-bonds and its uncertainty is the dominant one in the estimation of the inductance of the meander-shaped pick-up coil. This calculation leads to a pick-up coil inductance value of $L_\mathrm{m} = 2.2 \pm 0.6\,\mathrm{nH}$. The design value of the pick-up coil inductance is $L_\mathrm{m,d} = 2.27\,\mathrm{nH}$, which is consistent with the experimental value[25].

[25] The pick-up coil inductance has been simulated with InductEx, `http://www0.sun.ac.za/ix`.

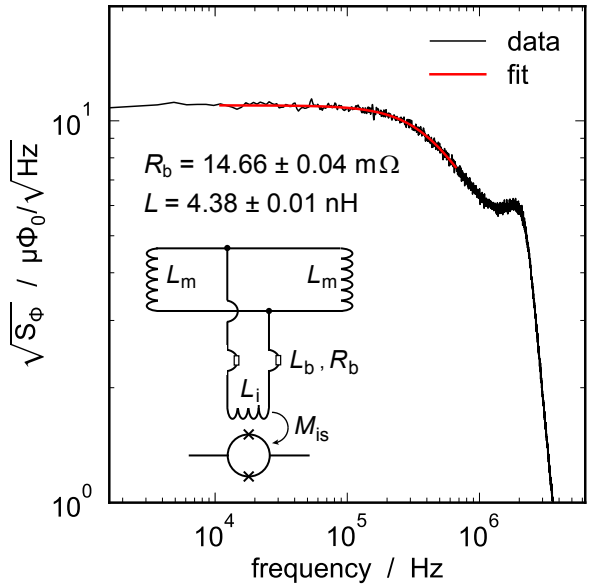

Figure 5.13: Measured spectral flux density in the SQUID for an ECHo-1k detector channel. The data is shown in black while the fit with the parameters R_b and L quoted in the graphic is shown in red. The inset shows the layout of the corresponding circuit.

5.3.3 Characterisation at millikelvin temperature

In order to characterise the ECHo-1k detector at low temperature, the dedicated cryogenic platform and parallel read-out chain that are described in section 5.2 have been used. The detectors have been fully characterised in terms of detector response and pulse shape. Furthermore, it has been demonstrated that resistance values of the ±H lines measured at 4.2 K that lay within three standard deviations from the average value lead to a proper behaviour of the heat switch at millikelvin temperature.
In the following the results for the ECHo-1k detector with ^{163}Ho implanted in silver are presented. The energy resolution as well as the ^{163}Ho activity per pixel have been determined for the two ECHo-1k chips that have been selected for the high statistics measurement.

Magnetisation response

The detector response of MMCs is based on the change of magnetisation in the sensor depending on the detector temperature, as described in section 4.2. The ECHo-1k detector chip is equipped with two non-gradiometric channels - therefore very sensitive to temperature drifts occurring in both the pixels - dedicated to tem-

perature monitoring, as already mentioned in section 5.1.1. Thus, the flux signal from these two detector channels can be used to extract the magnetisation response of the sensor.

Experimentally, the magnetisation response can be measured changing the temperature of the mixing chamber plate (MXC) in steps - so that the temperature of the detector can be reliably estimated - and acquiring the SQUID voltage output of a non-gradiometric channel. Since the voltage range of the ADC is limited, an automatic reset[26] of the SQUID is applied to guarantee that the SQUID voltage output does not exit the ADC range. The output of the MXC thermometer and the voltage output of the SQUID are recorded continuously to be able to correct the voltage jumps of the SQUID output caused by the SQUID resets and to monitor the temperature history. Finally, the data are analysed identifying the temperature plateaus and evaluating the corresponding SQUID voltage level by means of an average over the plateau region. Knowing the mutual inductance M_{fb} between the feedback coil of the two-stage SQUID set-up and the front-end SQUID and the feedback resistance R_{fb} of the feedback loop, the flux in the SQUID Φ_{S} corresponding to a certain voltage V can be calculated:

$$\Phi_{\mathrm{S}} = V \cdot \frac{M_{\mathrm{fb}}}{R_{\mathrm{fb}}} \,. \tag{5.3}$$

The resulting data points for three different values of the persistent current in the pick-up coils, namely 20 mA, 35 mA and 50 mA, are shown in figure 5.14 together with the corresponding numerical simulations[27]. The sensor thickness has been estimated to be about 1 µm measuring the sensor heat capacity. The latter can be extracted from the amplitude of the signals recorded with the detector pixels that are equipped only with the sensor and no absorber. The resulting sensor thickness value has been used as input parameter of the numerical simulations. The simulated magnetisation curves well described the experimental curves, as shown in figure 5.14.
The working principle of the temperature sensor is based on the magnetisation of the spin system of a paramagnetic sample, as explained in section 4.2, and therefore we expect a temperature-dependent susceptibility following approximately the $1/T$ Curie law at high temperatures. The measured curves fulfil the expectation in the temperature range above 80 mK.

[26] When the SQUID output voltage exceeds the threshold value set by the user, the SQUID is set in open loop and then locked back to FLL mode.

[27] For ECHo-10k sensor simualtions a concentration of 440 ppm, as experimentally determined, and a α parameter of 13.5 are used.

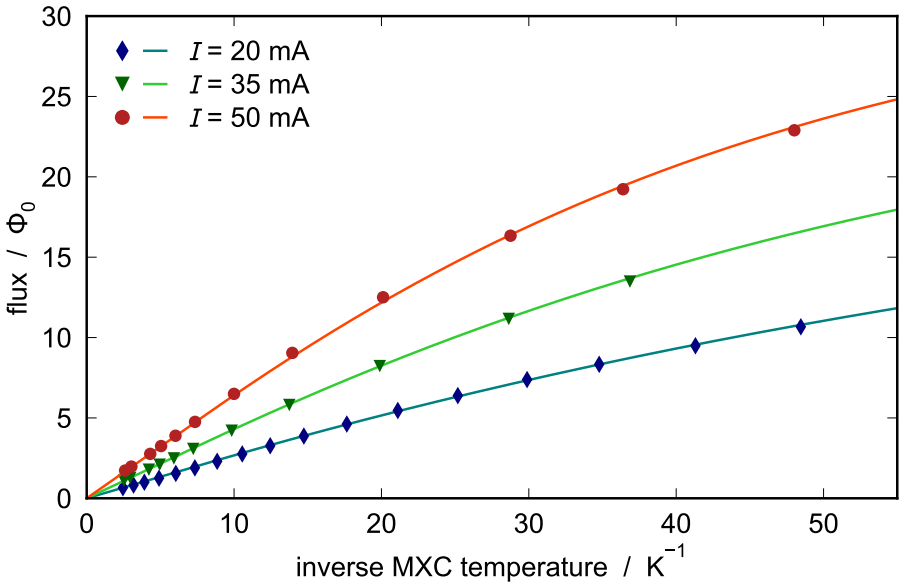

Figure 5.14: Magnetisation response of the ECHo-1k detector for three different persistent current values (20 mA, 35 mA and 50 mA) in the detector pick-up coils. The experimental data points are shown with markers and the theoretical expectations are shown with solid lines.

Pulse shape analysis and thermodynamic properties

As first step after fabrication, the ECHo-1k detectors with only one absorber layer have been tested and shortly characterised with an external sealed ^{55}Fe source. The isotope ^{55}Fe undergoes electron capture emitting de-excitation Auger electrons and X-ray photons. The ^{55}Fe source is equipped with a 200 µm thick beryllium window, which stops the electrons. Therefore, only the K_α and K_β X-rays with energies of about 5.89 keV and 6.49 keV [Hoe97] reach the detector. The positive outcomes of this measurements allowed to proceed with the implantation process, enclosing ^{163}Ho in the first absorber layer and depositing the second absorber layer on top, as explained in section 5.1.3.
Two ECHo-1k detector chips have been fully implanted according to the implantation layout described in section 5.1.1. For each chip 25 pixels have been implanted with ^{163}Ho and a second absorber layer has been deposited on top enclosing the source in the detector, while for the remaining 7 pixels the second absorber layer has been deposited without enclosing any source. The detector response of the chips that underwent the implantation process have been characterised at millikelvin temperatures, adjusting accordingly the MXC temperature T_{MXC}. The detector response has been tested with different currents in the superconducting meander-shaped pick-up coils, namely 20 mA, 35 mA and 50 mA, giving consisting results. Figure 5.15 shows

an overview of the signals from the ^{55}Fe K$_\alpha$ line of a not implanted detector pixel with both the absorber layers. The signals are acquired at different temperatures with a current of 35 mA circulating in the superconducting pick-up coils.

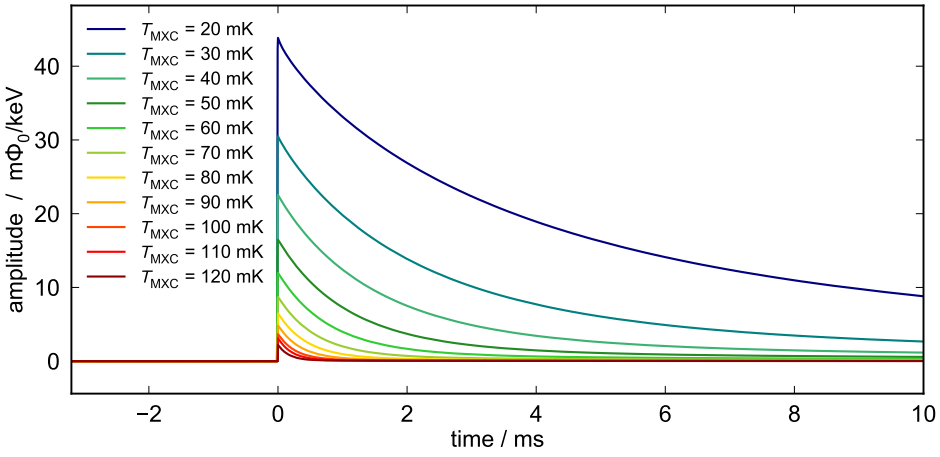

(a)

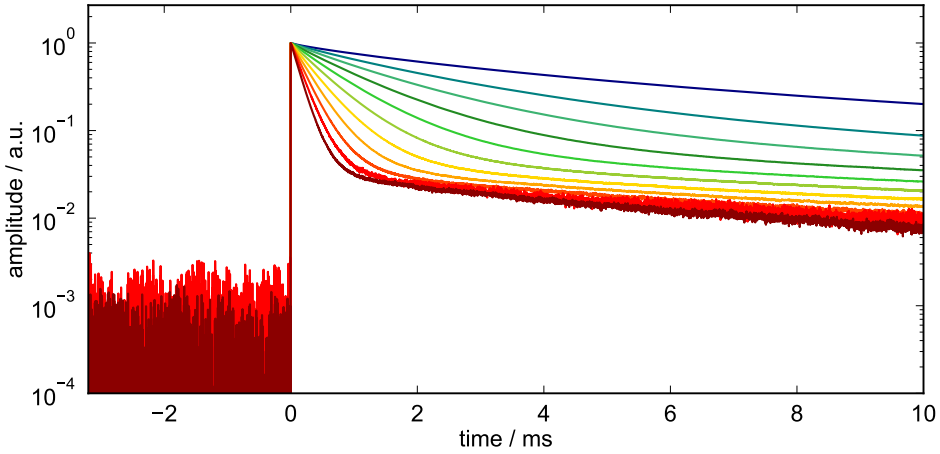

(b)

Figure 5.15: Signals corresponding to the ^{55}Fe K$_\alpha$ line recorded with a not implanted ECHo-1k detector with two absorber layers having a current of 35 mA in the superconducting pick-up coils. In **(a)** the y-axis is shown in linear scale. In **(b)** the pulses are scaled to the same amplitude and the y axis is shown in logarithmic scale. The legend in **(a)** reports the MXC temperature T_{MXC} and is valid also for **(b)**.

As expected, the signal amplitudes are decreasing at higher temperatures due to the increase of the detector heat capacity. The decay time becomes faster at higher temperatures, as visible in 5.15b. This is justified by the increase of the thermal conductance of the thermal link that connects the detector to the thermal reservoir.

Effects of implanted holmium Comparing the detector response before and after the ^{163}Ho implantation, changes in amplitude and in decay time are observed. In figure 5.16 the detector responses in terms of flux change in the pick-up coil[28] for the following detector pixels are compared:

- a detector pixel before implantation, i.e. with only one absorber layer and with no ^{163}Ho;
- a detector pixel after implantation but without source, i.e. with two absorber layers but no ^{163}Ho enclosed in the absorbers;
- a detector pixel after implantation with implanted source, i.e. with two absorber layers and ^{163}Ho enclosed in the absorbers.

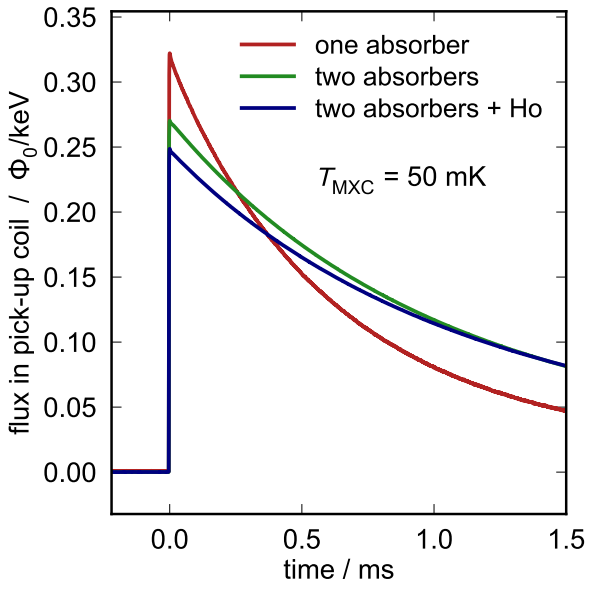

Figure 5.16: Comparison between the detector responses in terms of flux in the pick-up coil after fabrication (with one absorber), after implantation (with two absorbers) with ^{163}Ho and without ^{163}Ho at a MXC temperature of 50 mK. The persistent current in the pick-up coil is 20 mA.

Since additional heat capacity contributions are carried by the second absorber layer and by the ^{163}Ho ions, the amplitude of the detector response becomes smaller and the decay becomes slower, according to equations 4.18 and 4.27. The difference in amplitude between two fully fabricated pixels (i.e. with two absorber layers) with

[28] As the SQUID read-out for the measurements before and after implantation is different, it is not possible to compare the final signal amplitude recorded by the read-out chain and therefore the change of flux in the pick-up coil is used for the comparison.

and without ^{163}Ho can be exploited to estimate the extra heat capacity due to the implanted ^{163}Ho ions and therefore to calculate the heat capacity per ion of ^{163}Ho implanted in silver, as discussed in the chapter 6.

Detector response to different energy inputs In order to verify that the detector response is energy independent, signals from different spectral lines have been compared. Figure 5.17 shows the detector responses acquired at a MXC temperature of 30 mK corresponding to the following energy inputs:

- K_α photons from ^{55}Fe source with an energy of 5.89 keV,
- K_β photons from ^{55}Fe source with an energy of 6.49 keV,
- MI electron capture radiation from ^{163}Ho source with an energy of 2.04 keV,
- NI electron capture radiation from ^{163}Ho source with an energy of 0.41 keV,

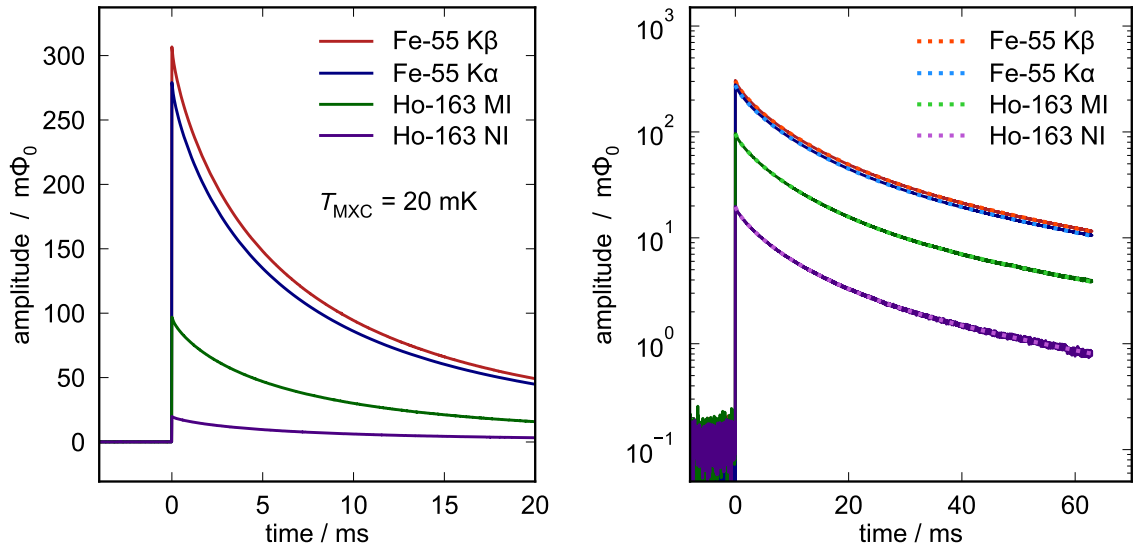

Figure 5.17: Comparison between the detector response for different energy input in linear scale **(a)** and logarithmic scale **(b)**. In (b) a multi-exponential fit is overlaid for each signal. The decay constants returned by the fit are shown in table 5.2.

The detector signals have the same shape independently from the energy at all temperatures.

Figure 5.17b shows the signals in logarithmic scale with a fit performed with a multi-exponential function:

$$f(t) = \sum_{i=1}^{4} a_i \cdot e^{-t/\tau_i} \,. \tag{5.4}$$

The decay constants τ_i returned by the fit shown in figure 5.17b are reported in table 5.2 and they are sorted according to the amplitudes a_i in decreasing order. The decay constants remain fairly unchanged for the different signals, proving that the shape of the decay does not depend on the energy deposition in the detector.

Decay times for different energy inputs					
Spectral line	E / keV	τ_1 / ms	τ_2 / ms	τ_3 / ms	τ_4 / ms
^{55}Fe, K_β	6.49	9.43 ± 0.02	2.77 ± 0.02	43.07 ± 0.07	0.39 ± 0.02
^{55}Fe, K_α	5.89	9.37 ± 0.03	2.75 ± 0.02	42.64 ± 0.08	0.39 ± 0.02
^{163}Ho, MI	2.04	9.40 ± 0.03	2.72 ± 0.03	45.0 ± 0.1	0.38 ± 0.03
^{163}Ho, NI	0.42	9.34 ± 0.05	2.83 ± 0.05	43.0 ± 0.2	0.38 ± 0.03

Table 5.2: Decay constants of signals at different energies extracted from a multi-exponential fit, sorted by the corresponding amplitudes in decreasing order.

From a theoretical point of view, the rise time of the pulses is ultimately limited only by the coupling between the electronic system and the spin system of the sensor, as discussed in 4.2.3. However, in the measurements performed with the ECHo-1k detectors the main limitation is due to the read-out bandwidth, which depends on the gain–bandwidth product (GBP) of the SQUID two-stage set-up. As a result, the typical rise time is estimated to be about 1 µs. Overall, the complete shape of the detector signal is energy independent, allowing to reliably apply a template fit approach, as it will be shown in section 5.4.

Signal decay In section 4.4.1 a basic thermodynamic model of a MMC detector with two sub-systems, namely the spin system of the sensor and the electronic system, is presented. According to this model, the detector signal features an exponential rise and an exponential decay with a time constant $\tau_\mathrm{d} = C/G$, where C is the total detector heat capacity and G is the thermal conductance to the thermal bath. Experimentally, the signal decay of the ECHo-1k detector at different temperatures can be empirically described with a multi-exponential fit (equation 5.4). Figure 5.18 shows an example fit of a signal acquired setting the MXC temperature at 20 mK[29].

[29]The fit excludes the first few microseconds where a fast decay component probably associated to the read-out electronics is observed. Thus, the amplitudes of the exponential terms do not sum exactly to unity.

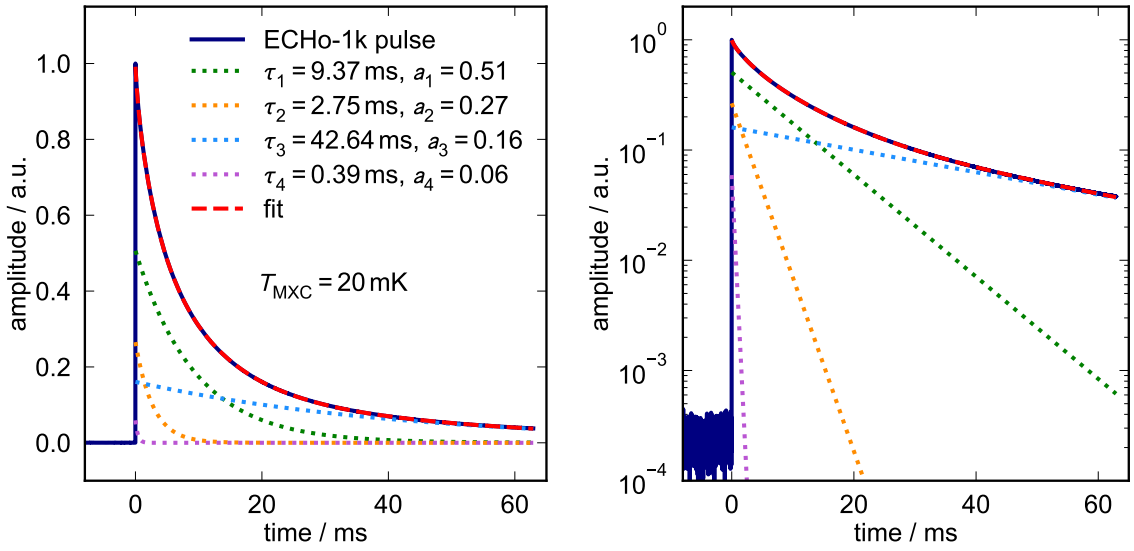

Figure 5.18: Detector signal with amplitude scaled to one, acquired at $T_{MXC} = 20\,\text{mK}$ with an overlaid fit performed using equation 5.4, in linear scale in **(a)** and in logarithmic scale in **(b)**. The four decay components are singularly plotted with dashed lines. The legend of (a) is valid for (b).

The minimum number of decay constants to precisely describe the decay is four, independently from the temperature in the range between 20 mK and 140 mK. This feature points towards the hypothesis that additional thermodynamic sub-systems are present. Therefore, the basic thermodynamical model previously mentioned is not complete. A possible interpretation is that the complex thermalisation design of the ECHo-1k chip (figure 5.2) generates multiple thermalisation channels with different time constants.

^{163}Ho activity

Three ECHo-1k chips have been characterised at millikelvin temperature in terms of ^{163}Ho activity per pixel. The chips differ in the choice of host material employed for the implantation of ^{163}Ho: gold, silver and aluminium. The expected implantation depth profile for aluminium is considerably larger if compared with gold and silver [Gam17] and therefore a higher activity is foreseen in this case.
The ^{163}Ho activity per pixel has been determined with two separate methods, which gave consistent results.

The first method is based on the integral of the ^{163}Ho spectrum histogram in the energy range belonging to the MI peak. The activity cannot be extracted from the

total number of recorded ^{163}Ho events, since the energy threshold prevents to reliably detect events with energy below $\sim 30\,\mathrm{eV}$ for all the implanted pixel.

Using the recent theoretical description of the electron capture (EC) ^{163}Ho spectrum presented in [Bra20], it is possible to calculate the branching ratio of the MI line (i.e. the percentage of events belonging to the MI line), BR_{MI}:

$$BR_{\mathrm{MI}} = \int_{0.99\cdot E_{\mathrm{MI}}}^{1.01\cdot E_{\mathrm{MI}}} S_{\mathrm{N}}(E)\, dE = 0.216 \tag{5.5}$$

where $S_{\mathrm{N}}(E)$ is the normalised spectrum, as shown in figure 5.19a, and $E_{\mathrm{MI}} = 2.04\,\mathrm{keV}$ is the energy of the MI line.

The activity per pixel, a, can be derived as:

$$a = \frac{N_{\mathrm{MI}}}{t} \cdot BR_{\mathrm{MI}} \tag{5.6}$$

where N_{MI} is the number of events in the MI peak and t is the acquisition time.

The dominant error in this method is the systematic uncertainty of the branching ratio of the MI line, since it is based on a not yet perfect theoretical model. This uncertainty is estimated to be below 5%.

The second method exploits the analysis of the ^{163}Ho event rate. Each recorded detector signal is characterised by a time-stamp given by the ADC clock, which corresponds to the time when the pulse is triggered. The distribution of the time-stamp differences between each pulse in one detector pixel and the previous one in the same pixel follows an exponential decay:

$$\frac{\mathrm{d}N(\Delta T)}{\mathrm{d}(\Delta T)} = \frac{N_0}{b} \cdot e^{-\Delta T/\tau} \tag{5.7}$$

where ΔT is the time-stamp difference between two subsequent triggered signals, N_0 is the number of counts in the bin where $\Delta T = 0$, τ is the characteristic decay-time and b is the bin width set at $b = 4\,\mathrm{ms}$.

From a fit of the time-stamp difference histogram, the decay-time τ and N_0 can be extracted.

The ^{163}Ho activity a for each pixel is then given by integrating the fit function and dividing by the acquisition time t:

$$a = \frac{1}{t}\int_0^\infty \frac{\mathrm{d}N(\Delta T)}{\mathrm{d}(\Delta T)}\mathrm{d}(\Delta T) = \frac{N_0 \cdot \tau}{b \cdot t} \tag{5.8}$$

Figure 5.19b shows an example of a time-stamp difference histogram for an ECHo-1k detector pixel with an exponential fit as it has been used to extract the activity.

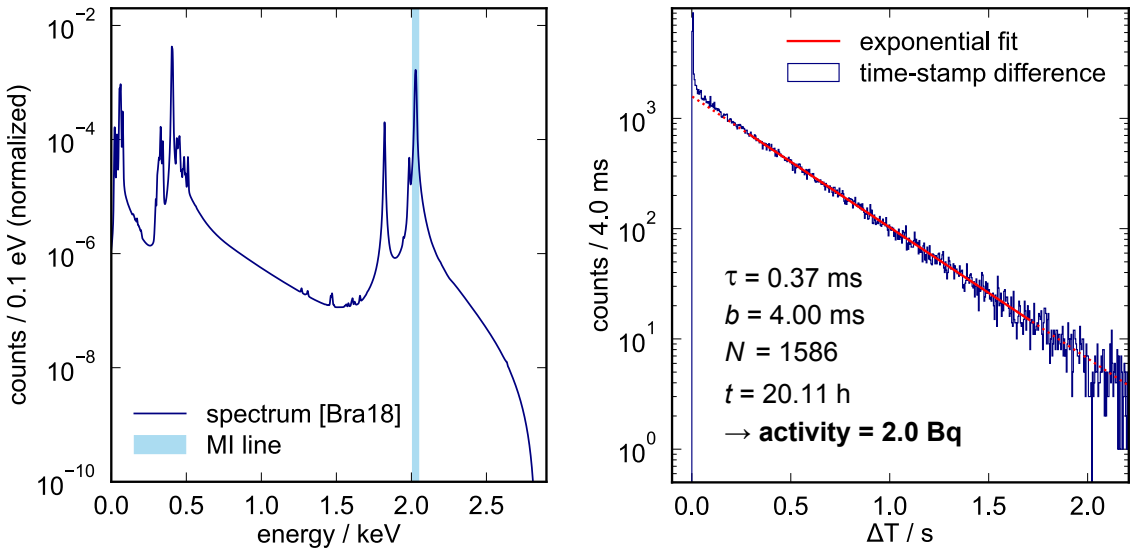

(a) **(b)**

Figure 5.19: **a)** Theoretical spectrum [Bra20] with the energy range of the MI peak marked according to equation 5.5. **b)** Example of the time-stamp difference histogram in a semilogarithmic plot. The exponential fit is overlaid in red and the extracted parameters are reported as well as the estimated activity.

The dominant uncertainties of this method are due to the possible presence of noise traces entering the time-stamp difference histogram and to the finite energy threshold that excludes a fraction of low-energy events from the histogram. The fit range is adapted to take into account only the central part of the histogram, which should not be relevantly affected by noise nor by poor statistics. An uncertainty on the final activity of about 5% has been estimated.

The resulting activity values per pixel of the three ECHo-1k chips are shown in the colour maps of figure 5.20. Not all the MMC pixels could be characterised due to missing connections of the corresponding read-out channels. The average activity and the corresponding standard deviation of each ECHo-1k chip are reported in table 5.3.

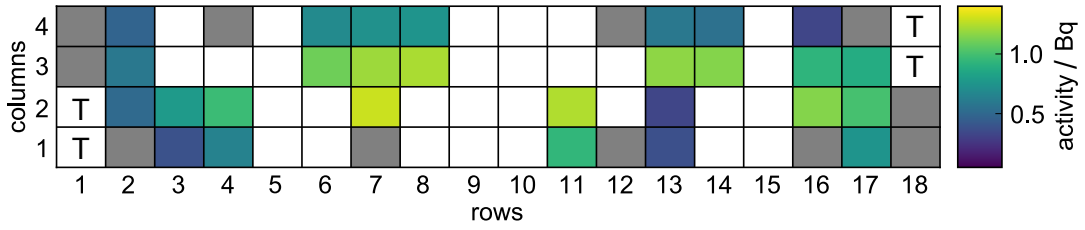

(a) ECHo-1k chip with gold as host-material

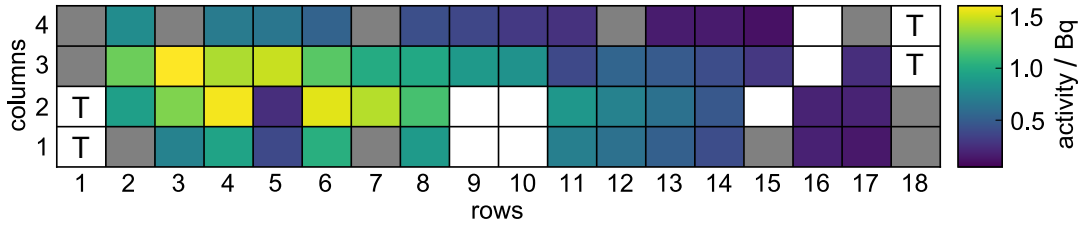

(b) ECHo-1k chip with silver as host-material

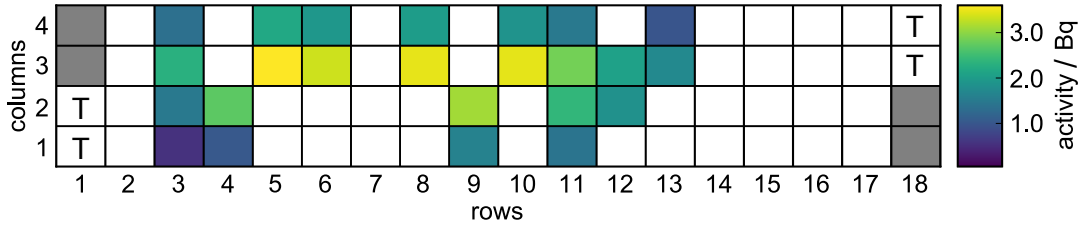

(c) ECHo-1k chip with aluminium as host-material

Figure 5.20: Activity maps of the characterised ECHo-1k chips. The colour code refers to the activity. The pixels marked in grey are not implanted. The pixels in white have not been measured. The temperature pixels are marked with the letter T.

Implantation material	Average activity [Bq]	Standard deviation [Bq]
Gold	0.81	0.30
Silver	0.71	0.44
Aluminium	2.12	0.84

Table 5.3: Summary of the obtained average ^{163}Ho activity values and corresponding standard deviations for the three ECHo-1k chips with different ^{163}Ho host material.

The considerably larger average activity for the ECHo-1k chip where ^{163}Ho has been implanted in aluminium with respect to the other chips matches the expectations. As discussed previously, the larger implantation depth predicted by simulations allows to more easily reach higher activity values.

The large standard deviations show a general lack of homogeneity in the activity

distribution over the absorber pixels. This does not affect the detector performances, since each pixel is operated singularly. However, it would be preferable to gain a precise control on the implanted activity in order to reach exactly the planned activity for each pixel for a more homogeneous detector response. The goal for ECHo is to implant 10 Bq per pixel. For this reason, the implantation system at the Mainz University [KT19a] is being optimised to improve the activity homogeneity.
A clear activity gradient from the centre to the side areas is visible in all the chips. Additionally, the ECHo-1k chip with ^{163}Ho implanted in silver exhibits higher activity in the pixels in the first rows with respect to the pixels in the last rows. The reason for these activity dishomogeneity can be related to the implantation process. In particular, a slight misalignment between collimator and beam bending system could be responsible for this. A new alignment system is presently under development.

Energy resolution

The two ECHo-1k chips with ^{163}Ho implanted in gold and silver, respectively, have been selected to run the high-statistics measurement as conclusion of the ECHo-1k phase.
The detector chips have been operated at about 15 mK and the detector performances could be evaluated during the run, also in terms of energy resolution per pixel.

The energy resolution can be extracted from a fit of the NI line (corresponding to the capture of 4s electrons) at the energy $E_{\mathrm{NI}} = 411\,\mathrm{eV}$ [Ran12]. The fit function is a convolution of a Lorentzian distribution, which is close to the shape of the NI peak, and a Gaussian curve, which takes into account the detector response:

$$f(x) = \frac{\Gamma_i/2\pi}{(x-x_0)^2 + \Gamma_i^2/4} \otimes \frac{1}{\sigma\sqrt{2\pi}} e^{-\frac{(x-x_0)^2}{2\sigma^2}} \,. \tag{5.9}$$

The width parameter Γ of the Lorentzian is fixed to 5.3 eV [Cam01]. The standard deviation σ of the Gaussian is returned by the fit and from that the energy resolution can be determined as full width at half maximum:

$$\Delta E_{\mathrm{FWHM}} = 2\sqrt{2\log(2)}\sigma \tag{5.10}$$

where log denotes the natural logarithm.

Figure 5.21 shows the energy resolution per pixel of the two ECHo-1k chips evaluated for the first data-set acquired for the high-statistics measurement. The data points shown with unfilled markers correspond to the detector pixels with an energy resolution worse than the benchmark for the ECHo-1k phase, i.e. 10 eV FWHM, and

they have been excluded from the histogram in figure 5.21 and from the following average calculations.

The average energy resolution for the chip with gold as host material is $\langle \Delta E_{\mathrm{FWHM}} \rangle = 6.07\,\mathrm{eV}$ with a standard deviation of $\sigma = 1.33\,\mathrm{eV}$. The average energy resolution for the chip with silver as host material is $\langle \Delta E_{\mathrm{FWHM}} \rangle = 5.55\,\mathrm{eV}$ with a standard deviation of $\sigma = 1.70\,\mathrm{eV}$. The relatively small standard deviations show that the energy resolution is fairly similar for all the pixels. This homogeneity ensures a good energy calibration for each single data sample, which in turn guarantees a reliable sum of the corresponding single spectra. Therefore, is it possible to correctly merge all the single ^{163}Ho spectra in order to build the final high-statistic spectrum.

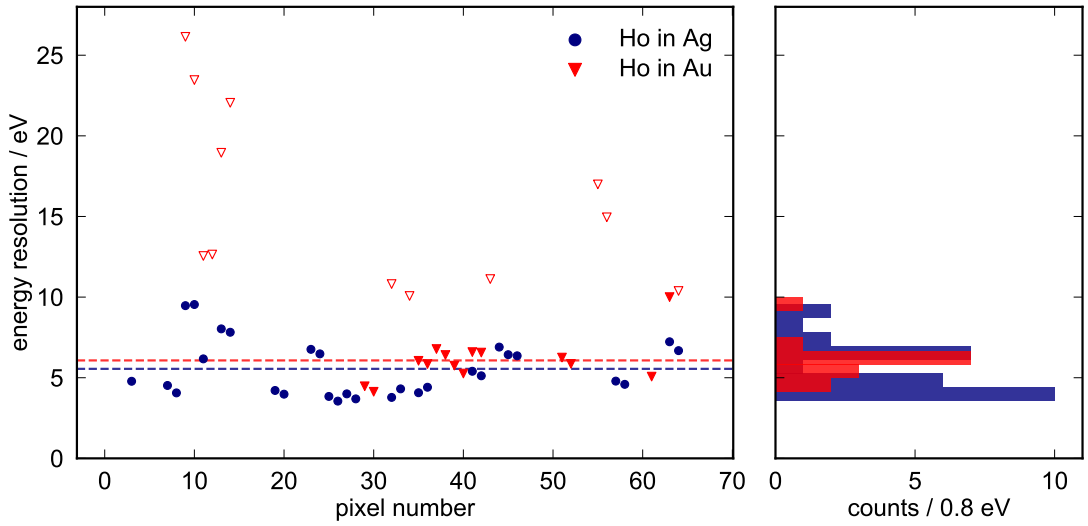

Figure 5.21: Energy resolution ΔE_{FWHM} per pixel of the two ECHo-1k chips under investigation. In red (blue) the data for the chip with gold (silver) as host material are shown. The unfilled markers correspond to the pixels with not sufficient energy resolution. The average energy resolution values for the two set-ups are shown with dashed lines of the corresponding colour.

The estimation of the energy resolution per pixel is the first quality check step in the analysis routine that is implemented for each data-set. In fact, different environmental conditions or noise sources can alter the detector pixel performances during the measurement.

From the theoretical calculation of the detector performances, assuming an implanted ^{163}Ho activity of $a = 1.0\,\mathrm{Bq}$ and the measured read-out noise levels, the expected energy resolution is $\Delta E_{\mathrm{FWHM}} \approx 5.15\,\mathrm{eV}$ at 20 mK. This result is consistent with the experimental observations.

5.4 High-statistics spectrum

Two ECHo-1k detector chips with ^{163}Ho implanted in silver and gold, respectively, have been used for a high-statistics measurement at the end of the ECHo-1k phase. The goal of this measurement campaign was to reach a statistics in the order of 10^8 EC events, which allows for a sensitivity on the effective electron neutrino mass below 20 eV.

5.4.1 Experimental set-up

The experimental set-up consists of two ECHo-1k detector modules surrounded by aluminium shields, as described in section 5.2.1. One detector module is placed horizontally on the mixing chamber plate (figure 5.22a). For the second detector module a dedicated annealed copper arm has been attached vertically to the mixing chamber plate and the second detector module has been fixed on top (figure 5.22b). The vertical arm can host up to two detector modules and it has been previously tested to guarantee that a good thermalisation is reached.

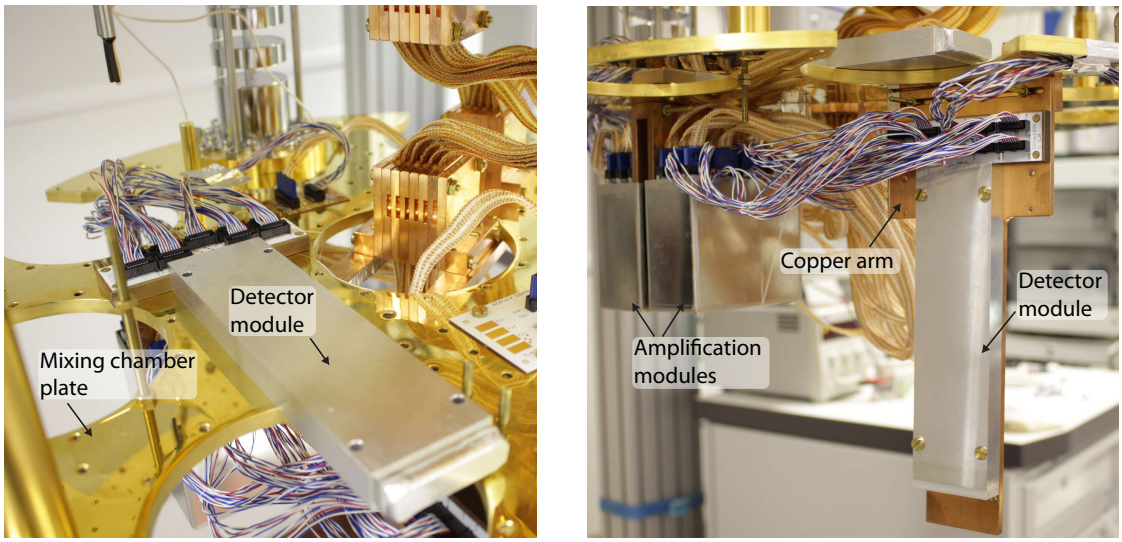

(a) **(b)**

Figure 5.22: **a)** First detector module placed on top of the mixing chamber plate, hosting the ECHo-1k detector with ^{163}Ho implanted in silver. **b)** Vertical copper arm connected to the mixing plate with the second detector module, hosting the ECHo-1k detector with ^{163}Ho implanted in gold.

The read-out chain used for the high-statistics run is described in section 5.2 and its layout consist of 64 SQUID channels and 8 connections dedicated to the injection of the persistent currents in the detector pick-up coils, as described in section 5.1.5.

5.4.2 Towards the final spectrum

The high-statistics measurement started in the end of December 2019 and it ended in May 2020. In total, 71 pixels have been selected to be acquired. For the set-up with ^{163}Ho implanted in silver, 34 implanted pixels, six not-implanted background pixels and two temperature monitoring pixels have been acquired. For the set-up with ^{163}Ho implanted in gold, 24 implanted pixels, four not-implanted background pixels and one temperature monitoring pixel have been acquired. The evolution of the acquired statistics of the raw data over time is represented in figure 5.23. At the end of the run a final statistics of 3.86×10^8 raw events has been reached.

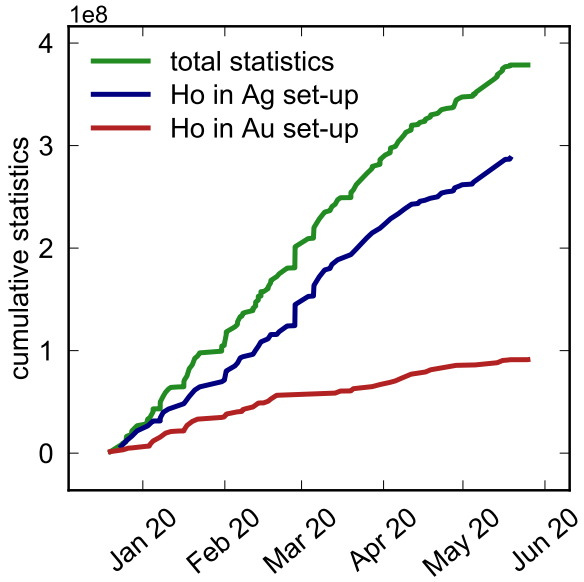

Figure 5.23: Cumulative statistics of the raw data acquired for the two ECHo-1k set-ups as function of time. The green line represents the total statistics, including both the set-ups.

The raw data consist of time traces of the triggered events with an effective sampling rate of 7.81 MHz and a length of 16384 samples of which 4094 are recorded before the trigger. Therefore, the total time window for each signal is 2.08 ms and 0.52 ms are occupied by the baseline before the rise of the pulse. The voltage amplitude of each pulse is proportional to the energy input.

In order to reconstruct the EC ^{163}Ho spectrum starting from the raw data, the following steps are performed [Gri] [Bar]:

- **Data filtering**: The raw data undergo a filtering process based on the trigger time of each signal. The time information can be used to remove very efficiently the noise signals (e.g. GSM noise or electromagnetic noise).
- **Template fit**: A pulse template is created averaging pulses from the MI line and it is used to perform a template fit of all the signals that have passed the previous filter.
- χ^2 **cut**: For each signal a χ^2 parameter is extracted from the fit. The χ^2 is a valid figure of merit to identify and remove background signals (e.g. muon signals) and pile-up events in which a second ^{163}Ho decay occurs after a time shorter than the signal time window of 1.56 ms.
- **Temperature correction**: Possible temperature variations of the thermal bath have an impact on the pulse amplitude, since this latter depends on the detector heat capacity, which in turn depends on the detector temperature. In order to correct for this, the temperature information from the non-gradiometric channels is used.
- **Optimal filter**: In order to extract the energy information from the voltage signals, the optimal (or matched) filter algorithm is implemented [McC05].
- **Energy calibration**: In order to reconstruct the final spectrum, the histograms of the signal amplitudes must be calibrated in energy. For each dataset the central energy of each ^{163}Ho spectral line is derived in arbitrary units (e.g. ADC units or voltage) fitting the corresponding resonance. The resulting central energies of the lines are then fitted against energy values obtained in previous measurements during which a ^{55}Fe source was used as calibration [Ran14]. The fit function is a polynomial of second order, which is finally used to re-calibrate the experimental signal amplitudes.

Figure 5.24 shows a preliminary ^{163}Ho spectrum, including 7.08×10^7 events from 17 detector pixels of the set-up with ^{163}Ho implanted in silver collected over about 23 days of acquisition. The region of interest, i.e. the end-point region of the spectrum is blinded.
The experimental spectrum is compared with the theoretical model currently under development [Bra20]. The theoretical spectrum shown in blue in figure 5.24 is broadened with a Lorentzian with full width at half maximum (FWHM) of 5 eV. Both the theoretical spectra (red line and blue line) are convoluted with a Gaussian of 6 eV FWHM to account for the instrumental energy resolution.

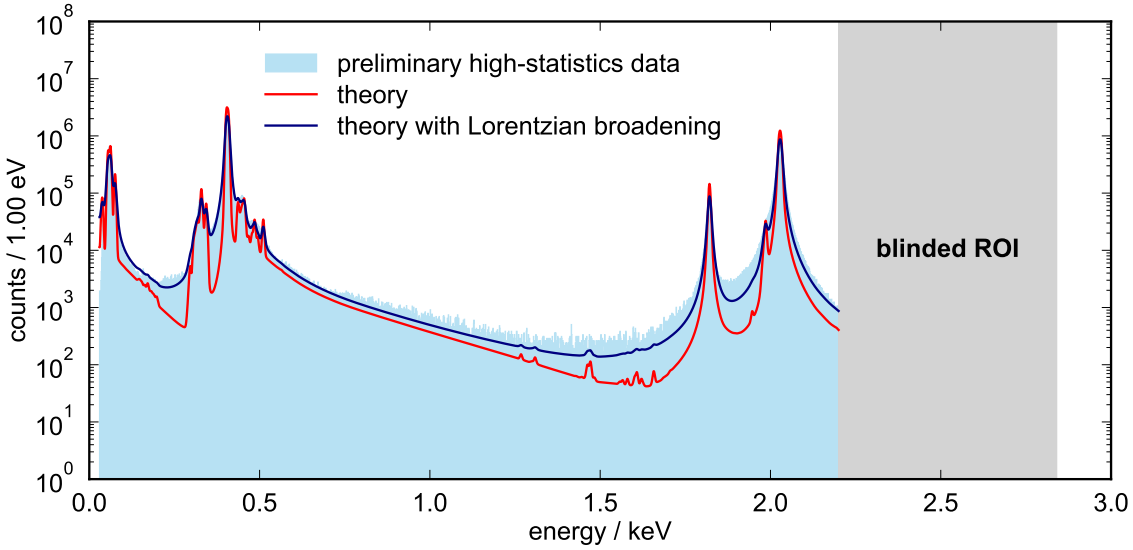

(a)

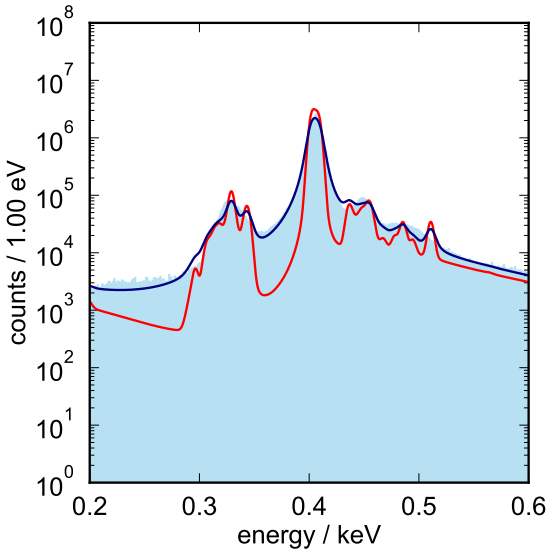

(b)

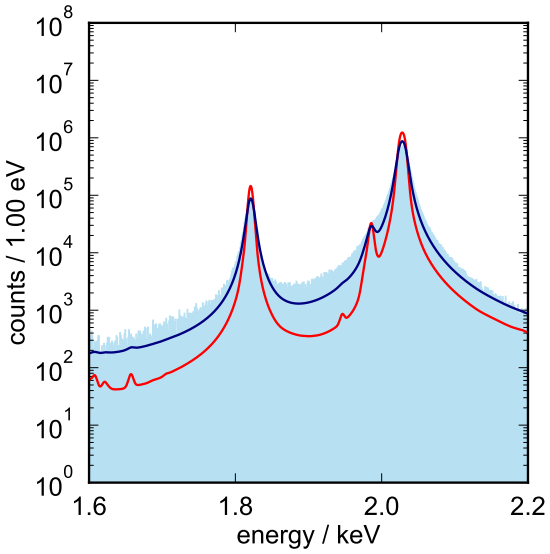

(c)

Figure 5.24: **a)** Preliminary high-statistics spectrum with about 7×10^7 events compared with the theoretical model [Bra20]. The blue line represents the theoretical spectrum broadened by convoluting with a Lorentzian with FWHM of 5 eV. Both the theoretical spectra shown in blue and red are convoluted with a Gaussian with FWHM of 6 eV. **b)** Zoom of the region of the N-edges. **c)** Zoom of the region of the MI line. The legend in **(a)** is also valid for the plots in **(b)** and **(c)** .

Figure 5.24b shows a zoom of the spectrum in the region of the N-edges and figure 5.24c shows a zoom in the region of the MI line. The shoulder on the left side of the MI line and the structures of the N-edges predicted by the theory are already partly resolved by the preliminary experimental spectrum, even if not the full statistics is included yet. The resolving power will be enhanced including the full available statistics, which will increase the counts by one order of magnitude.
The on-going analysis will allow to set a new limit on the effective electron neutrino mass below 20 eV.

6. Specific heat of holmium in silver and investigation of the holmium half-life

The knowledge of the specific heat of ^{163}Ho implanted into the detector absorber is crucial to define the amount of ^{163}Ho that can be enclosed in the detector so that the corresponding heat capacity does not spoil the detector performance, especially in terms of energy resolution. The maximum number of ^{163}Ho ions, in turn, defines the maximum activity per pixel. The specific heat of ^{163}Ho can be estimated exploiting MMC detectors with implanted ^{163}Ho. The very precise MMC-based method we have developed made possible to discover that the value of the ^{163}Ho half-life as currently reported in literature [Bai83] [Kaw88] might be overestimated.

The recently published measurements of the specific heat of ^{163}Ho implanted in gold and silver are reviewed in section 6.1. The general strategy of the heat capacity studies performed with MMC detectors is described in section 6.2. The experimental implementation of the MMC-based measurement of holmium in silver is addressed in section 6.3. The final results and the conclusions which propose a redefinition of the holmium half-life are discussed in section 6.4.

6.1 Previous measurements of the ^{163}Ho specific heat at low temperatures

The specific heat of ^{163}Ho in gold and silver has already been investigated and the corresponding results have been published recently [Her20]. Here, Au:^{165}Ho and Ag:^{165}Ho dilute alloys have been measured in the temperature range between 10 mK and 800 mK exploiting thermal relaxation methods to extract the specific heat. The measurements have been carried out for three different Ag:^{165}Ho samples with holmium concentrations of 0.0162%, 0.184% and 1.66%, respectively.
^{165}Ho is the only stable holmium isotope and it features the same nuclear spin $I = 7/2$ and an almost identical nuclear moment with respect to ^{163}Ho[1]. A Schottky anomaly with a maximum of about $0.9\,k_B$ at about 250 mK has been observed for all samples, independently of the holmium concentration, and it is attributed to hyperfine splitting and crystal field interactions. At temperatures below ~ 130 mK the specific heat of bulk holmium significantly differs from the specific heat of the holmium alloys because of concentration-dependent effects due to dipole-dipole and

[1]The nuclear moment of ^{165}Ho is $4.17\,\mu_N$, while the nuclear moment of ^{163}Ho is $4.23\,\mu_N$, where μ_N is the nuclear magneton.

RKKY interactions [Her20].

The specific heat of holmium implanted in gold or silver at low temperatures can also be experimentally determined exploiting MMC detectors loaded with ^{163}Ho using gold or silver as host material and operated in a dilution refrigerator, as it will be explained in section 6.2. In this case, the number of holmium atoms which is used to calculate the specific heat per ion can be evaluated starting from the ^{163}Ho activity and the ^{163}Ho half-life. Therefore, in this approach the resulting specific heat per ion ultimately depends on the ^{163}Ho half-life.
This method has been used to confirm the results for the Au:^{165}Ho samples obtained with relaxation techniques, showing high congruence [Her20][Vel19a]. However, a new evaluation of the MMC-based results for the specific heat of ^{163}Ho in gold presented in [Her20] and in [Vel19a] has shown the presence of an error in the analysis that leads to an artificially higher specific heat. Thus, the results obtained with relaxation methods are more than a factor of two larger with respect to the corrected results obtained with the MMC-based methodology.

New heat capacity measurements have been performed in the context of this work exploiting MMC detectors with ^{163}Ho implanted in silver. More precise experimental techniques have been used and a larger data-set has been acquired, but the same strategy as the one used in [Her20] has been applied. The resulting specific heat per ^{163}Ho ion implanted in silver, assuming the half-life of about 4570 years as reported in literature [Bai83] [Kaw88], differs from the results obtained with relaxation methods by a comparable factor as the one found in the case of ^{163}Ho in gold.
Therefore, as it will be discussed in detail in section 6.4, our results suggest that the ^{163}Ho half-life might be significantly lower with respect to the value currently reported in literature.

6.2 Methods

In general, the signal produced by calorimeters consists of a rise of temperature ΔT that directly depends on the energy deposition E and on the total detector heat capacity C, which includes the heat capacity of the sensor C_s, the heat capacity of the absorber C_a and the heat capacity of the implanted holmium source C_Ho:

$$\Delta T = \frac{E}{C} = \frac{E}{C_\mathrm{s} + C_\mathrm{a} + C_\mathrm{Ho}} \,. \tag{6.1}$$

Using two identical microcalorimeters which differ only by the presence of ^{163}Ho atoms loaded inside the absorber and comparing their temperature responses ΔT_1 and ΔT_2, following a known energy deposition E, it is possible to extrapolate the

heat capacity contribution from ^{163}Ho:

$$C_{\mathrm{Ho}} = \frac{E}{\Delta T_1} - \frac{E}{\Delta T_2} \tag{6.2}$$

where $\Delta T_{1(2)}$ is the detector response in terms of temperature of the microcalorimeter with (without) implanted ^{163}Ho.

In the case of ECHo, the microcalorimeters are MMC detectors, which are presented in chapter 4. The output signals are in voltage, as discussed in section 4.3.4, and it is necessary to know the magnetisation response of the sensor in order to translate them into the temperature signals ΔT_i, $i = 1, 2$ that enter equation 6.2.

Two important quantities can be determined with this approach, namely the ^{163}Ho relative heat capacity contribution C_{rel} and the specific heat per ^{163}Ho ion $c_{\mathrm{Ho}}^{\mathrm{ion}}$.

The ^{163}Ho relative heat capacity contribution is defined as the ratio between the holmium heat capacity and the detector heat capacity without implanted holmium, i.e. the sum of the sensor heat capacity C_{s} and the absorber heat capacity C_{a}:

$$C_{\mathrm{rel}} = \frac{C_{\mathrm{Ho}}}{C_{\mathrm{s}} + C_{\mathrm{a}}} = \frac{C_{\mathrm{Ho}}}{C - C_{\mathrm{Ho}}} \tag{6.3}$$

where C is the total detector heat capacity, as defined in equation 6.1.

The specific heat per ^{163}Ho ion is evaluated from the number of implanted ions, N_{Ho}:

$$c_{\mathrm{Ho}}^{\mathrm{ion}} = \frac{C_{\mathrm{Ho}}}{N_{\mathrm{Ho}}}\,. \tag{6.4}$$

The number of holmium ions can be estimated from the ^{163}Ho activity of the implanted detector and therefore it depends on the ^{163}Ho half-life. Using the general formula for radioactive decays, $N(t) = N_0 \cdot \exp\big(-t/\tau_{1/2} \cdot \log(2)\big)$, where t is the time, N is the number of radioactive nuclides, $\tau_{1/2}$ is their half-life and log denotes the natural logarithm, the activity can be defined as $a \coloneqq \left|\dot{N}\right| = \mathrm{d}N/\mathrm{d}t$. In the limit of long half-lives, $\tau_{1/2} \gg t$, the activity can be considered constant and the following relation holds:

$$a = \frac{N_0}{\tau_{1/2}} \log(2) \tag{6.5}$$

from which the number of ions N_0 can be derived.

The half-life of ^{163}Ho currently reported in literature is 4570 years [Bai83] [Kaw88]. Using this value, for an activity of $a = 1\,\mathrm{Bq}$, the corresponding number of ions is

$N_{\mathrm{Ho}} = 1/\mathrm{s} \cdot 4570\,\mathrm{y}/\log(2) = 2.08 \times 10^{11}$. A shorter half-life would lower the number of ions for the same ^{163}Ho activity.

6.3 Experimental implementation

The ECHo-1k detector chip used for this study contains seven asymmetrically implanted channels, i.e. with only one pixel loaded with ^{163}Ho, and two non-gradiometric channels - as described in section 5.1.1 - which can be used to measure the magnetisation response of the sensor. In the following the asymmetrically implanted channels are addressed as *asymmetric channels* for the sake of brevity.

The magnetisation response depends on the value of the persistent current flowing in the superconducting pick-up coils. As described in section 5.1.5, the chip is divided into four quarters which are prepared independently for operation, injecting the persistent current into the pick-up coils quarter by quarter. The two non-gradiometric channels are located in two different quarters of the chip and the four asymmetric channels belonging to these two quarters can be taken into consideration in this measurement. In this way, the magnetisation response measured with the non-gradiometric channel of a certain quarter exactly describes the magnetic response of the asymmetric channels of that quarter, since the same persistent current is present in all detector pixels belonging to the quarter. Thus, the magnetisation curve measured for each quarter can be reliably used to translate the voltage signals of the corresponding detector pixels into temperature signals. In fact, even if the nominal value of the injected persistent current is the same in different quarters, it is possible that the actual current flowing in the meander-shaped pick-up coils is different to some extent, due to potential bottlenecks in the superconducting circuit or slight variations in the experimental procedure during the current injection[2].

The four ECHo-1k asymmetric detector channels placed in the quarters where the non-gradiometric channels are also present are "SQ11", "SQ16", "SQ1" and "SQ6"[3]. The first two detector channels belong to quarter 4, where the non-gradiometric channel "SQT2" is present, while the other two belong to quarter 2, where the non-gradiometric channel "SQT1" is present. For the sake of simplicity, the four asymmetric channels and the two non-gradiometric channels mentioned above are addressed in the following with a simplified notation, "<K>Q<N>-<M>", where the first letter <K> indicates the kind of channel ("A" for asymmetric and "T" for non-gradiometric temperature monitoring channel), the number <N> indicates the quarter of the chip and the number <M> is a unique number assigned to the channel in case more than one channel of that type is present in the same quarter.

[2]Recently an automatic procedure for the injection of the persistent current has been developed.

[3]Here the on-chip channel labels of the ECHo-1k design are used.

Detector channel	Quarter	Simplified notation	^{163}Ho activity
SQ1	2	AQ2-1	0.99 Bq
SQ6	2	AQ2-2	1.23 Bq
SQ11	4	AQ4-1	0.49 Bq
SQ16	4	AQ4-2	0.20 Bq
SQT1	2	TQ2	0.00 Bq
SQT2	4	TQ4	0.00 Bq

Table 6.1: The detector channels of the ECHo-1k detector chip that play an important role in this study are listed, together with the chip quarter they belong to as well as with the simplified notation used in the text and the implanted ^{163}Ho activity.

The simplified notation used for each channel is reported in table 6.1. In the same table also the ^{163}Ho activity of each channel is indicated.

The selected asymmetric detector channels have been measured in a temperature range between 20 mK and 150 mK. For the detector channels AQ2-1 and AQ2-2 three different nominal values of persistent current have been used, namely 20 mA, 35 mA and 50 mA. For the detector channels AQ4-1 and AQ4-2 two different nominal values of persistent current have been used, namely 20 mA and 50 mA.

The asymmetric channels have been irradiated with an external ^{55}Fe source and the voltage signals of the two pixels corresponding to the same spectral line K_α, with energy $E = 5.89\,\text{keV}$, have been measured and compared. This measurement has been repeated stabilising the detector temperature at 13 different points between 20 mK and 150 mK. As expected, the amplitude of pulses belonging to the pixel with implanted ^{163}Ho shows a smaller amplitude and a longer decay time because of the higher heat capacity, as visible in the example plot of figure 6.1a. The signal amplitude decreases with higher temperatures since the total detector heat capacity increases, but for each temperature the MMC pixel loaded with ^{163}Ho always shows lower signals with respect to the pixel without ^{163}Ho, as shown in 6.1b[4].

The signal amplitude in voltage is proportional to the signal amplitude in temperature with the same proportionality factor for both the pixels belonging to one channel. From the difference between the signal amplitude ΔV_1 of the pixel with ^{163}Ho and the signal amplitude ΔV_2 of the pixel without ^{163}Ho it is possible to extract the ^{163}Ho relative contribution C_{rel} to the detector heat capacity, as defined in equation 6.3:

$$C_{\text{rel}} = \frac{\Delta V_2 - \Delta V_1}{\Delta V_1}\,. \tag{6.6}$$

Figure 6.1c[4] shows the relative contribution calculated for the asymmetric channel AQ4-2. The complete results for all the analysed channels including the corresponding uncertainties are presented and discussed in the next section.

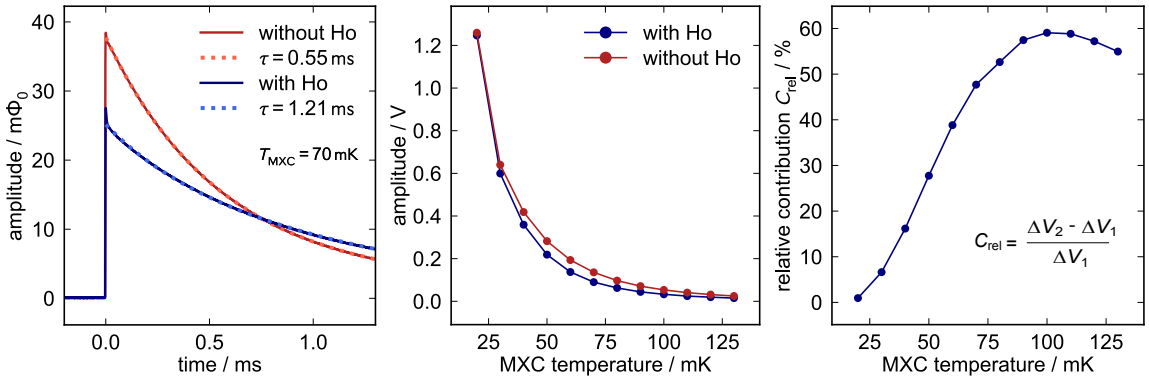

(a) **(b)** **(c)**

Figure 6.1: **a)** Pulses from the two pixels belonging to an asymmetric channel at a temperature of 70 mK. The dominant decay constant extracted from the multi-exponential fit is shown in the legend. **b)** Signal amplitudes of the two pixels of the same asymmetric channel as a function of temperature. **c)** Relative heat capacity contribution from ^{163}Ho for the same asymmetric channel.

The magnetisation responses have been measured for both the non-gradiometric channels of the ECHo-1k chip and they can be well described by the sensor simulations, as shown in section 5.3.3. The magnetisation curves have been acquired using a NI DAQ ADC[5] with high input impedance, while the detector signals have been acquired with the DAQ system presented in section 5.2.4 with ADC modules with a lower input impedance. In order to account for this difference, a correction factor $k = 0.97 \pm 0.01$ has been experimentally measured and used to correct the voltage amplitudes of the recorded detector signals. The local derivative $\mathrm{d}V/\mathrm{d}T|_{T^*}$ of the magnetisation curve at a certain temperature T^* is used as transfer coefficient to calculate the change of temperature ΔT associated to a certain change of voltage ΔV at the temperature T^*:

$$\Delta T|_{T^*} = \Delta V|_{T^*} \frac{1}{\mathrm{d}V/\mathrm{d}T|_{T^*}} \,. \tag{6.7}$$

Here, ΔV indicates the voltage amplitudes already corrected, $\Delta V = \Delta V_{\mathrm{meas}}/k$, where

[4]This exemplary plot does not yet include the uncertainties on the data points, which are introduced and discussed in the next section.

[5]National Instruments USB-6351.

ΔV_{meas} stands for the measured voltage amplitude. The transfer coefficient $\mathrm{d}V/\mathrm{d}T|_{T^*}$ can be assumed constant for small change of temperatures.

Finally, from the comparison of the temperature signals ΔT of the two pixels belonging to the asymmetric channel, the ^{163}Ho contribution to the detector heat capacity C_{Ho} can be calculated as:

$$C_{\mathrm{Ho}} = E \cdot \left.\frac{\mathrm{d}V}{\mathrm{d}T}\right|_{\mathrm{T}^*} \cdot \left(\frac{1}{\Delta V_1} - \frac{1}{\Delta V_2}\right) \tag{6.8}$$

and the ^{163}Ho specific heat per ion can be evaluated:

$$c_{\mathrm{Ho}}^{\mathrm{ion}} = \frac{C_{\mathrm{Ho}}}{N_{\mathrm{Ho}}} = E \cdot \left.\frac{\mathrm{d}V}{\mathrm{d}T}\right|_{\mathrm{T}^*} \cdot \left(\frac{1}{\Delta V_1} - \frac{1}{\Delta V_2}\right) \cdot \frac{\log(2)}{a \cdot \tau_{1/2}} \tag{6.9}$$

where $N_{\mathrm{Ho}} = (a \cdot \tau_{1/2})/\log(2)$ is the number of implanted ^{163}Ho ions, a is the ^{163}Ho activity and $\tau_{1/2}$ is the ^{163}Ho half-life.

The experimental method that has been explained so far is based on the assumption that the two pixels belonging to the asymmetric channels are identical except for the presence of ^{163}Ho in one of the two pixel. However, due to limitations in the fabrication precision, the ECHo-1k pixels can be slightly different. This is demonstrated by two observations:

- the not implanted pixels produce signals with slightly different amplitude and decay time as response to the same energy input, meaning that the heat capacities of the detectors are very similar but not identical;
- the magnetisation response to a common change of temperature of the two pixels belonging to a gradiometric channel is in general not flat, meaning that the two sensors do not have equal geometry and properties.

Comparing the amplitude of the signals in the not implanted detector pixels at different temperatures, it appears that the difference is larger between detector pixels belonging to different quadrants. This can be interpreted as a gradient in the thickness of the absorber or sensor layers along the chip, which does not affect the accuracy of the estimation of the ^{163}Ho specific heat, as pairs of pixels belonging to the same channels - which are therefore located very close by each other - are used for this analysis.
Comparing the amplitudes of the not implanted pixels of channels belonging to the same quarter, a difference up to $\sim 3\%$ ($\sim 8\%$) is observed for channels AQ2-1 and AQ2-2 (AQ4-1 and AQ4-2). This difference is used to estimate the systematic error

on the relative heat capacity, the total ^{163}Ho heat capacity and the specific heat per ^{163}Ho ion, as discussed in section 6.4.

In order to correct for the difference in the sensors, the magnetisation response as function of the detector temperature has been measured for the asymmetric channels used in the study, according to the procedure explained in section 5.3.3. The derivative of the magnetisation curve at a given temperature can be used to correct for the difference in the detector response introduced by unequal sensors in the two pixels. However, the magnetisation curve for the channels used for this analysis show a very small deviation from a perfectly gradiometric behaviour, with a total magnetisation signal being about three orders of magnitude smaller than for a non-gradiometric channel. Thus, the geometries and properties of the sensors of the two pixels can be considered identical. As a consequence, the difference in the signal amplitude of the not implanted pixels previously discussed is attributed mainly to a difference in the electronic heat capacity.

6.4 Results and discussion

In the following the results obtained with the experimental methods previously described are discussed.

6.4.1 Relative heat capacity contribution of holmium

Figure 6.2 shows the relative heat capacity contribution due to ^{163}Ho, calculated with the formula reported in equation 6.6 for each detector channel and for each persistent current value.

The uncertainty on this calculation is given by the statistical error on the signal amplitudes and by the systematic error due to the possible differences in the electronic heat capacity of the two pixels, beside the ^{163}Ho contribution, which is derived from the amplitude difference of not implanted pixels, as discussed in detail in the appendix A. The asymmetric channels AQ4-1 and AQ4-2 are characterised by higher systematic uncertainties. On one hand, the activities of these channels are smaller if compared to those of the other channels, leading to a less pronounced effect of the implanted ^{163}Ho on the detector heat capacity. On the other hand, these two channels are characterised by a not negligible difference in the electronic heat capacity, as pointed out in section 6.3.
The relative error on the temperature measured with the thermometer of the mixing chamber plate of the cryostat is estimated to be 3% in the temperature range below 40 mK, 1% in the temperature range above 70 mK and 2% elsewhere.

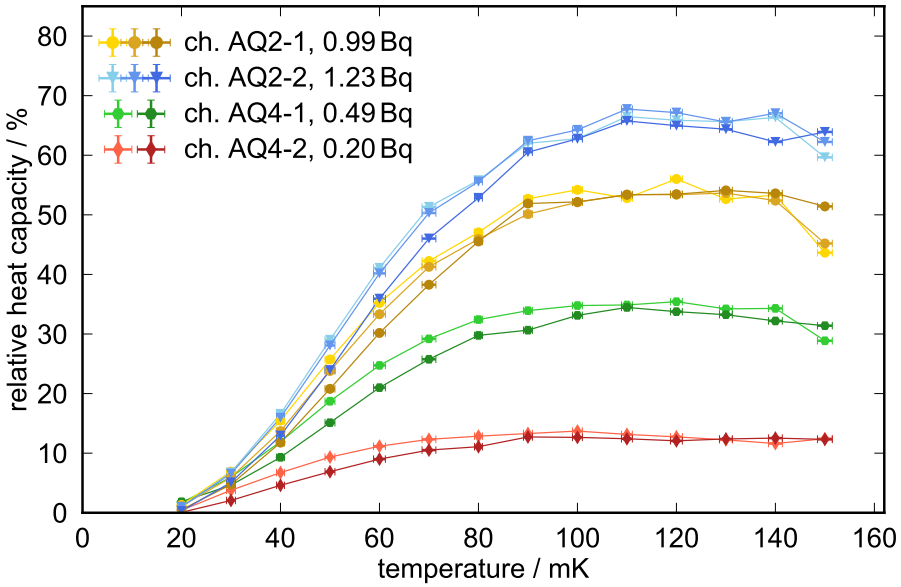

Figure 6.2: Relative contribution of ^{163}Ho to the detector heat capacity with statistical uncertainties included in the error bars. The different colours for each channel correspond to the different values of the persistent current (nominally 20, 35, 50 mA) with darker shades for higher current values. The ^{163}Ho activity of each detector channel is reported in the legend.

As expected, the relative contribution scales with the number of implanted ^{163}Ho ions, i.e. with the ^{163}Ho activity. Higher values of the persistent current lead to larger magnetic fields, thus increasing the heat capacity of the Ag:Er sensor. Therefore, the relative contribution of the holmium ions to the total heat capacity is expected to be higher for smaller values of the persistent current.

Overall, at the typical detector operational temperature of about 20 mK, the relative contribution to the detector heat capacity due to the ^{163}Ho implanted in silver is well below 2% for an activity of about 1 Bq. For the next phase of the ECHo experiment, ECHo-100k, an activity of about 10 Bq is planned. Therefore, the impact of the implanted source on the detector heat capacity will be below 20%, assuming the same total detector heat capacity and, in first approximation, a linear scaling of the relative heat capacity with the activity.

6.4.2 Total heat capacity of holmium

The total heat capacity due to the implanted ^{163}Ho is calculated according to equation 6.8 for each temperature point. The resulting curves for the asymmetric channels AQ2-1 and AQ2-2 and for each persistent current value are shown in figure 6.3. The

asymmetric channels AQ4-1 and AQ4-2 are excluded from this part of the analysis because of the more sever systematic uncertainties discussed in section 6.4.1.
The statistical uncertainty of this calculation is given by the statistical errors that affect the parameters that enter equation 6.8. As in the case of the relative heat capacity estimation, the systematic error accounts for the not identical electronic heat capacity of the two pixels, besides the ^{163}Ho contribution. More details on the treatment of the uncertainties on the total heat capacity calculation are given in the appendix A.

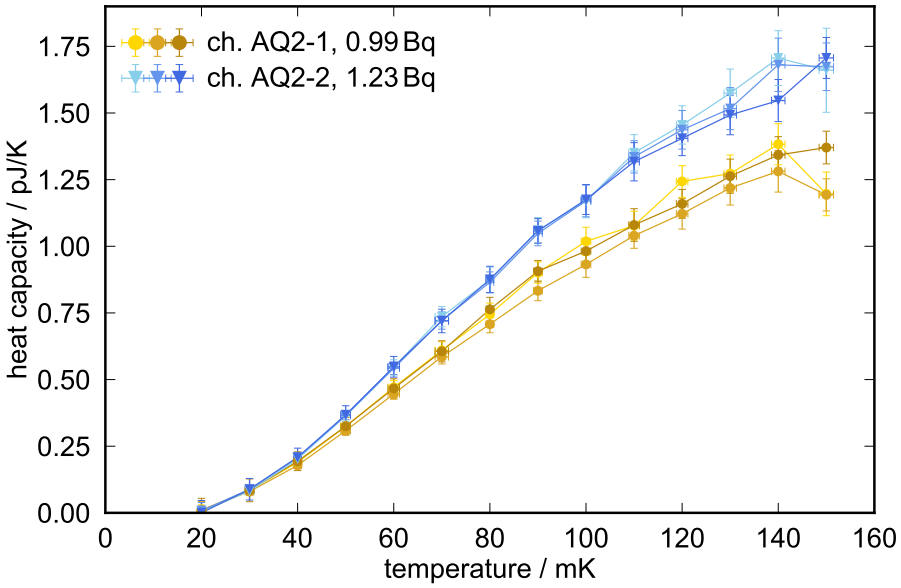

Figure 6.3: Total specific heat due to ^{163}Ho as function of temperature with statistical and systematic uncertainties included in the error bars. The different colours for each channel correspond to the different values of persistent current (nominally 20, 35, 50 mA), with darker shades for higher current values. The ^{163}Ho activity of each detector channel is reported in the legend.

Higher ^{163}Ho activities correspond to larger amount of ^{163}Ho and therefore to higher heat capacities. However, this effect is not linear for two main reasons. On one side the concentration does not scale linearly with the activity. In fact, the concentration of ^{163}Ho in the implantation volume is not uniform and it is affected by the fact that each impinging ^{163}Ho ion removes several surface atoms [Gam17]. On the other side, the specific heat per ion depends non-linearly on the concentration and at low temperatures it is higher for smaller concentrations [Her20].

6.4.3 Specific heat per holmium ion

The specific heat per ion is calculated from the total ^{163}Ho heat capacity divided by the number of ^{163}Ho, according to equation 6.9. The first has been determined with good precision, as shown in section 6.4.2, while the second can be calculated from the ^{163}Ho activity, which is also accurately measured.
Using the ^{163}Ho half-life from literature [Bai83] [Kaw88], the resulting specific heat as a function of temperature is determined for the asymmetric channels AQ2-1 and AQ2-2 for the different persistent current values, as shown in figure 6.4. The asymmetric channels AQ4-1 and AQ4-2 are excluded for the same reasons discussed above.

As expected, the specific heat is increasing with temperature in the range under analysis between 20 mK and 150 mK. The maximum of the Schottky anomaly is expected at about 250 mK.
The specific heat of holmium does not depend on the magnetic field produced by the persistent current in the pick-up coil. In fact, the plot of figure 6.4 shows that the data-sets with different persistent current values for each detector channel give the same results, within the corresponding uncertainty.

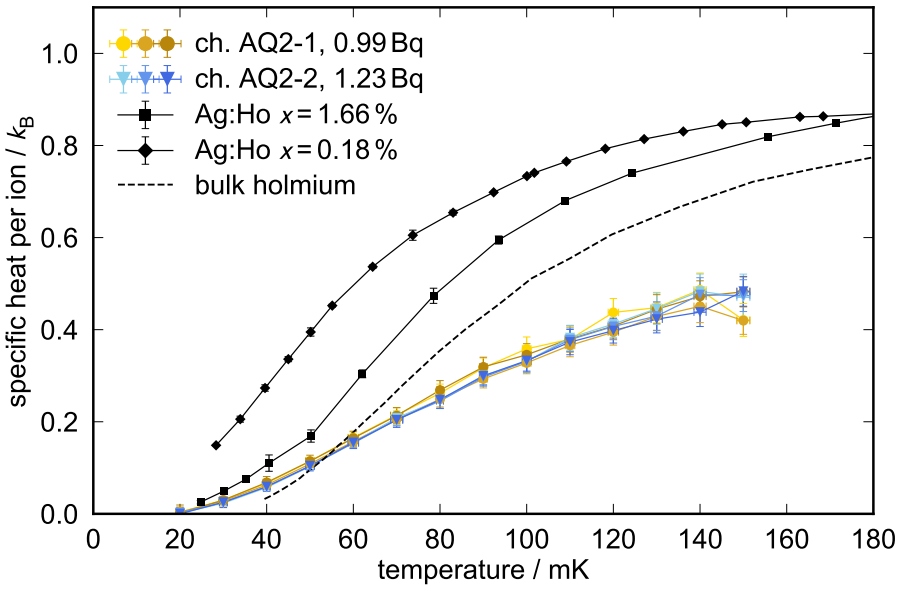

Figure 6.4: The specific heat per holmium ion obtained with the detector channels AQ2-1 and AQ2-2 is shown. The statistical and systematic uncertainties are included in the error bars. The different colours for each channel correspond to the different values of the persistent current (nominally 20, 35, 50 mA), with darker shades for higher current values. As comparison, the specific heat of a Ag:Ho sample with concentration $x = 0.18\%$ and $x = 1.66\%$ [Her20] and the specific heat of bulk holmium [Kru69] are shown in black.

The resulting specific heat per ^{163}Ho ion can be compared with the available results obtained with thermal relaxation methods applied to Ag:Ho samples with concentrations of 0.0162%, 0.184% and 1.2%, respectively [Her20]. Lower concentrations correspond to higher specific heat at low temperatures. Figure 6.4 shows the comparison with the results to Ag:Ho samples with concentration of 0.18% and 1.66%, respectively. The specific heat obtained with the experimental approach based on MMC detectors is significantly lower than the results achieved with thermal relaxation methods. As reference, also the specific heat of bulk holmium reported in [Kru69] is shown in the figure.

This mismatch could be explained either by assuming a totally different specific heat of the implanted holmium if compared to the homogeneous sample used for the relaxation-based measurements or by questioning the ^{163}Ho half-life value reported in literature [Bai83] [Kaw88]. The first explanation is unlikely, since towards high temperatures the specific heat is dominated by the hyperfine splitting effects, which are not affected by the concentration or by the environment that surrounds the holmium atoms. On the other hand, the second explanation is acceptable, as discussed in detail in section 6.4.4.

6.4.4 Redefinition of the ^{163}Ho half-life

The quantities that enter equation 6.9 for the calculation of the specific heat per ion are all experimentally determined, except for the K_α energy and the ^{163}Ho half-life. While the K_α energy is a well known parameter reported in several publications [Hoe97] [Sch00], the ^{163}Ho half-life has been determined with sufficient precision only in [Bai83] and in [Kaw88].

In [Bai83] the ^{163}Ho half-life is estimated to be 4570 ± 50 y using isotope-dilution mass spectrometry. The ^{163}Ho source was produced by neutron activation of a ^{162}Er enriched target and holmium was then chemically separated. A known amount of ^{164}Dy spike solution was added to the parent ^{163}Ho fraction to reduce the uncertainties associated to the yield of dysprosium in the separation procedure. From the change in the ^{163}Dy/^{164}Dy ratio as a function of time, the rate of in-growth of the daughter atom ^{163}Dy is determined, from which the half-life of ^{163}Ho is calculated. This measurement is affected by inaccuracies due to several aspects, as for example the small expected in-growth of ^{163}Dy due to the rather modest sample mass of about 0.7 mg and the short measurement times, the intrinsic precision limitations of the chromatographic ion exchange technique employed to separate holmium and dysprosium and the non-trivial blank contributions to the mass spectrometer signal.

The work presented in [Kaw88] is based on the same approach used in [Bai83], but some differences must be mentioned. The ^{163}Ho source is produced by means of the

^{164}Dy(p, 2n) reaction via irradiation of an enriched ^{164}Dy metal target. The amount of ^{163}Ho in the parent fraction is 1.56 µg, i.e. about 1/400 of the amount used in [Bai83]. On the other side, the measurement time is about 1.3 y, while in [Bai83] it is only about 0.6 y. Similarly to the measurement present in [Bai83], also in this case blank contributions are present in the mass spectrometer signal. Moreover, a small amount of target dysprosium was found in the parent ^{163}Ho fraction. The estimated half-life is 4570 ± 38 y.

As conclusion, the observed mismatch among the specific heat obtained with thermal relaxation methods and the results obtained using MMC detectors loaded with ^{163}Ho seems to be linked to the value of the ^{163}Ho half-life.

In order to determine a new value of the ^{163}Ho half-life, the total ^{163}Ho heat capacity curve obtained in this analysis can be fitted against a known specific heat curve obtained with methods that are independent of the ^{163}Ho half-life, using equation 6.9 and leaving the half-life as free parameter. For that, the reference specific heat curve should correspond to a sample with a comparable concentration with respect to the asymmetric channels used in this analysis, as the concentration affects the absolute scale of the specific heat per ion as well as the shape of the corresponding curve as a function of temperature.
As previously mentioned, three specific heat curves with concentrations of 0.0162%, 0.184% and 1.66% are available [Her20]. The shape of the specific heat curves of channels AQ2-1 and AQ2-2 fits very well the shape of the curve with a concentration of 1.66%, while it fits neither the shapes of the other curves nor the shape of the bulk holmium curve [Kru69]. In fact, a concentration of 1.66% is a plausible value for the implanted detectors, as it will be discussed later.

The six specific heat curves for channels AQ2-1 and AQ2-2 and for the three different persistent current values are fitted against the specific heat curve with concentration of 1.66%. Averaging the six values of the ^{163}Ho half-life returned by the fits, propagating the statistical error accordingly and estimating the systematic uncertainty as described below, the following value of half-life is found:

$$\tau_{1/2} = 2542 \pm 23(\text{stat})^{+531}_{-793}(\text{sys})\,\text{y}\,. \tag{6.10}$$

Figure 6.5 shows the specific heat per ^{163}Ho ion as a function of temperature for the two channels under analysis, using the obtained ^{163}Ho half-life value.

The statistical uncertainty includes all the statistical errors that affect the parameters that enter equation 6.9. The systematic uncertainty is dominated by the unavailability of relaxation-based measurements of samples with larger concentration than 1.66% and by the unknown holmium concentration of the asymmetric channels AQ2-1 and AQ2-2. In fact, this method assumes that a concentration of 1.66% is a

reasonable estimation of the holmium concentration in the implantation layer of the detector pixels used in this study.

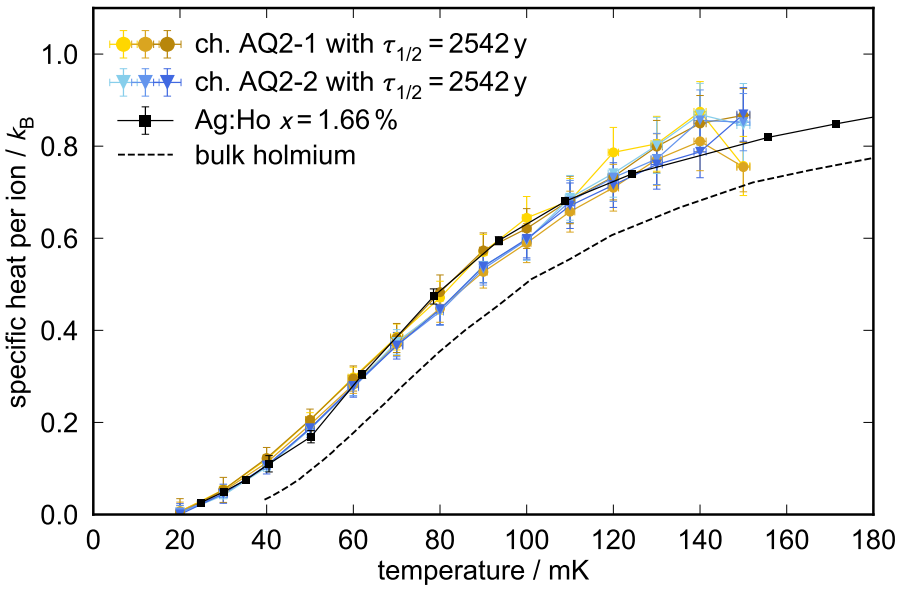

Figure 6.5: The specific heat per ion obtained with the data-set under analysis using the value of ^{163}Ho half-life obtained in this analysis is shown in colour and it matches the specific heat curve reported in [Her20], which is shown in black. The error bars include both statistical and systematic uncertainties.

In first approximation, the holmium concentration can be determined from the number of implanted ^{163}Ho atoms, N_{Ho}, which depends on the measured activity a and on the half-life $\tau_{1/2}$. However, as the ^{163}Ho half-life enters this calculation, it is not useful in this case. It is possible - but rather difficult - to estimate the number of atoms and the concentration from indirect sources of information, as the simulated depth profiles of implantation targets [Gam17], according to which a concentration between 1.15% and 2% is expected. An important observation is that channels AQ2-1 and AQ2-2 are characterised by an activity of 0.99 Bq and 1.23 Bq, respectively, which would correspond to a somewhat different concentration, but the resulting specific heat curves are comparable within the corresponding uncertainty. Therefore, small differences in concentration in this concentration range seem not to affect in a macroscopic way the specific heat curve.

Overall, the ^{163}Ho half-life obtained with this kind of analysis is affected by a severe systematic error due to the unknown number of implanted holmium ions in the detectors that have been used and to the lack of reference specific heat curves obtained with independent methods for samples with different concentrations in the range between 1% and 3%.

More technical details about the treatment of the statistical and systematic uncertainties of this analysis are given in the appendix A.

6.4.5 Summary and outlook

The specific heat of holmium at low temperatures has been investigated exploiting MMC detectors implanted with ^{163}Ho using silver as host material. In particular, two asymmetrically implanted detector channels of the ECHo-1k detector, where one pixel is implanted and the other one is not, have been used. In this calculation, the input energy, the derivative of the magnetisation response of the detector, the amplitudes of the detector signals, the implanted ^{163}Ho activity and the ^{163}Ho half-life enter. All these parameters are experimentally accessible and directly measured in this study, except for the input energy - corresponding to the ^{55}Fe K_α line - and the ^{163}Ho half-life.

The obtained specific heat as a function of temperature follows the expected trend, but it is significantly smaller with respect to the results obtained with thermal relaxation techniques. In particular, the measurement of a Ag:Ho sample with a concentration of 1.66% is taken as reference [Her20]. In order to match the two results, the ^{163}Ho half-life must be shorter than the value reported in [Bai83] and in [Kaw88]. With this method the ^{163}Ho half-life is estimated to be $\tau_{1/2} = 2542 \pm 23(\text{stat}) \,^{+531}_{-793}(\text{sys})$ y.
The achieved statistical uncertainty is remarkably small, but the systematic uncertainty is very large. The main limitation of the applied strategy, which is responsible for the large systematic uncertainty, is the unknown number of implanted holmium atoms in the detectors that are used for this study and the lack of reference curves with concentrations higher than 1.66%. The systematic uncertainty can be significantly reduced performing further measurements of homogeneous Ag:Ho samples with different concentrations by means of thermal relaxation methods, in order to be able to compare the MMC-based results with a wider set of reference specific heat curves.

7. Detector optimisation towards ECHo-100k

The ECHo-100k phase aims to reach a sensitivity below 2 eV on the effective electron neutrino mass, exploiting a total ^{163}Ho activity of 100 kBq. The new challenging requirements - not only in terms of activity, but also of energy resolution and read-out technology - are presented in section 7.1. The results from the ECHo-1k phase already discussed in chapter 5 have paved the way towards a new detector design for the ECHo-100k experiment. The optimisation studies that have been performed to improve the detector design and performances are described in section 7.2. The final ECHo-100k design and the fabrication process are described in section 7.3 and 7.4, respectively. The ECHo-100k detector has been characterised and the outcomes fully match the expectations, thus fulfilling the detector requirements for the ECHo-100k phase. The results of the detector characterisation at room temperature, at 4 K and at millikelvin temperature are shown in section 7.5.

7.1 Detector requirements for the ECHo-100k experiment

The total statistics that is required to reach a sensitivity below 3 eV on the effective electron neutrino mass is about 10^{13} electron capture (EC) events, assuming an energy resolution below 5 eV FWHM. The planned total ^{163}Ho activity to achieve this goal is 100 kBq.

The maximum activity per pixel can be determined considering on one side the maximum level of unresolved pile-up in the end-point region and on the other side the contribution to the detector heat capacity from the implanted ^{163}Ho atoms, which has a direct impact on the detector performances, as described in section 4.5. The unresolved pile-up fraction must be kept below 10^{-5}, as discussed in section 3.1. Therefore, a rise time below 0.5 µs implies a maximum activity of 20 Bq per detector channel, i.e. 10 Bq per pixel. Assuming this value, in order to reach a total activity of 100 kBq, as planned for the ECHo-100k experimental phase, at lest 10000 pixels are needed. This poses the challenge to simultaneously read-out a large number of detector channels. A low-noise microwave SQUID multiplexing technique is currently under development to tackle this challenge [Weg18b] [San19].
Table 7.1 summarises the requirements of the ECHo-100k phase and compares them with the experimental conditions for the previous phase, ECHo-1k.

	ECHo-1k	**ECHo-100k**
Activity	$a \approx 1\,\mathrm{Bq/pixel}$	$a \approx 10\,\mathrm{Bq/pixel}$
Detector energy resolution	$\Delta E_{\mathrm{FWHM}} \leq 10\,\mathrm{eV}$	$\Delta E_{\mathrm{FWHM}} \leq 5\,\mathrm{eV}$
Number of pixels	$N = 57$	$N = 12000$
Read-out technology	Parallel SQUID read-out	μMUXing[a]

Table 7.1: Overview of the experimental requirements for the ECHo-100k phase in comparison with the ECHo-1k phase.

[a]Microwave SQUID multiplexing.

The experimental requirements for the ECHo-100k phase translate into necessary upgrades in terms of detector design.

The maximum activity value of 10 Bq/pixel deriving from the previous considerations on the allowed pile-up fraction needs to be confirmed by dedicated investigations on the corresponding heat capacity contribution. The studies presented in chapter 6 show that the specific heat per holmium ion implanted in silver is below $0.02\,k_{\mathrm{B}}$, which corresponds to a heat capacity of $\sim 0.3\,\mathrm{pJ/K}$ for 10 Bq of ^{163}Ho source[1]. The detector performances will be inevitably affected by a larger amount of implanted ^{163}Ho ions with respect to the ECHo-1k phase, even if not in a substantial way. Futhermore, the required energy resolution for the ECHo-100k is a factor of two higher with respect to the previous experimental phase.
Therefore, the detector response needs to be optimised to reach optimal energy resolution and signal shape as starting condition before implantation. The effects of the larger activity need to be precisely evaluated and taken into account in the optimisation studies for the final design. As described in section 5.1.3, the ^{163}Ho ions are implanted into the detector absorber by means of an ion beam scan over the detector array. In order to allow for an efficient implantation from the geometrical point of view, the position of the detector pixels on the chip needs to be optimised. Such a large number of detectors requires a multiplexed read-out, as already mentioned, and therefore the detector design should also be compatible to the new read-out system.

Summarising, the ECHo-100k requirements in terms of detector design are:

- definition of maximum ^{163}Ho activity per pixel;
- improved detector performances, especially in terms of signal shape and energy resolution;
- pixel layout for high implantation geometrical efficiency;
- compatibility to multiplexed read-out.

[1]For this calculation the new value of the ^{163}Ho half-life presented in chapter 6 is used.

7.2 Optimisation studies

In order to fulfill the detector requirements previously presented, dedicated studies and simulations have been performed. The specific heat contribution from the implanted ^{163}Ho ions plays a crucial role in the final detector performance and the corresponding studies have already been discussed in chapter 6. In the following the remaining optimisation studies are described. In section 7.2.1 the optimisation of the absorber thickness on the basis of Montecarlo simulations is presented. In section 7.2.2 the choice of the host material for the ^{163}Ho implantation is discussed, according to the results obtained with the different materials tested during the ECHo-1k phase, as described in section 5.3.3.

7.2.1 Absorber thickness

The final goal of the ECHo experiment is to determine the effective electron neutrino mass by means of the analysis of the end-point region of the ^{163}Ho EC spectrum. Therefore, possibly undetected events in the spectrum represent a potentially dangerous issue. For this reason it is crucial that the quantum efficiency of the detector is as close as possible to 100%. On the other hand, the heat capacity of the gold absorber contributes to the total detector heat capacity, which should be minimised to improve the detector response. As both the quantum efficiency and the heat capacity increase with the volume of the absorber, the optimum is defined by the minimum volume that guarantees a sufficient stopping power.

The absorber area cannot be arbitrarily small because of the alignment of the implantation area and the second absorber layer. Moreover, co-deposition of silver is planned during the implantation process in order to avoid saturation effects [Gam17] and the smaller the implantation area is, the larger becomes the amount of co-deposited material, increasing the absorber volume. Thus, the size of the absorber area is set to $180\,\mu \times 180\,\mu$, as in the ECHo-1k design. The thickness of the absorber is the only parameter that can be tuned to define the absorber volume. In order to find the optimal absorber thickness, dedicated Montecarlo simulations have been set up. Only the photonic contribution to the EC de-excitation energy is taken into account, since electrons have a negligible penetration depth in gold.

For each event in the simulation, the following steps are implemented:

1. The implantation layer is defined as a square within the x-y coordinate plane[2], as shown in the schematics in figure 7.1. A photon is created at a random x-y position in the implantation layer.

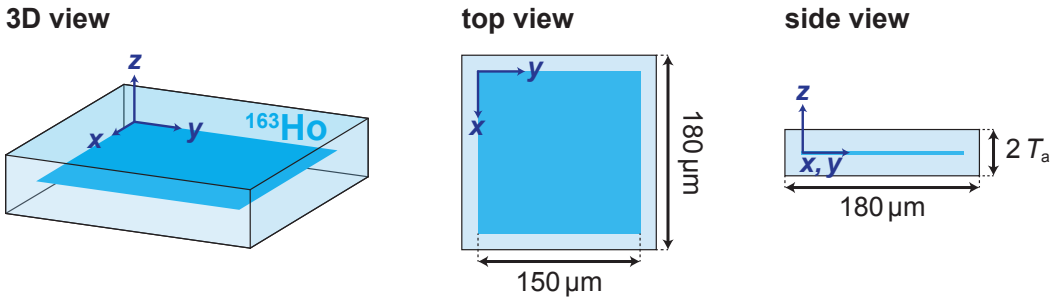

Figure 7.1: Schematic drawings (3D, top view and side view) of the geometry used for the Montecarlo simulations. The dimensions are not on scale.

2. A random energy E^* is assigned to the photon, according to the energy probability distribution defined by the ^{163}Ho EC spectrum. For that, a random number r is generated in the range of the function $f(E)$ that describes the EC spectrum[3] and the energy E^* is calculated as:

$$E^* = \mathscr{F}^{-1}(r) \tag{7.1}$$

where $\mathscr{F}$ is the integral function of the spectrum function f: $\mathscr{F} = \int f(E)\mathrm{d}E$. The integral function $\mathscr{F}$ is numerically calculated.

3. A random direction vector in the 4π sphere is assigned to the photon.

4. The intersection between the photon trajectory and the outer surface of the absorbers is found. The intersection point can be situated on the top/bottom surfaces or on the side surfaces. The travelled distance x is calculated accordingly.

5. The interaction probability can be estimated assuming that the photoelectric effect is the the dominant interaction mechanism. As the maximum photon energy - given by the Q-value of the ^{163}Ho EC decay - is below 3 keV, Compton effect and pair production mechanism are energetically forbidden. The energy

[2]This assumption is legitimate as the penetration depth of the ^{163}Ho ions during implantation is few nanometers and therefore negligible with respect to the implantation area of 150 µm × 150µm.

[3]For this purpose the simplest model from equation 2.22 is used.

dependent survival probability $p_s(E)$ (i.e. the probability that the photon is not absorbed) is then given by:

$$p_s(E) = e^{-\mu(E)x} \tag{7.2}$$

where $\mu(E)$ is the linear attenuation coefficient, which can be calculated as:

$$\mu(E) = \mu_m(E) \cdot \rho_{Au} \tag{7.3}$$

where $\mu_m(E)$ is the mass attenuation coefficient and ρ_{Au} is the density of gold. The mass attenuation coefficient depends on the energy E and it is estimated from a linear interpolation of the values reported in [NIS19].

Each simulation is run for a total of 10^9 events and the absorber thickness T_a of a single absorber layer[4] is varied between 2.0 µm and 5.0 µm with a step of 0.5 µm.

The total survival probability P_s for a certain absorber thickness is given by the integral of the survival probability in the energy range under consideration:

$$P_s = \int_{E_{min}}^{E_{max}} p_s(E) \mathrm{d}E \,. \tag{7.4}$$

The absorption probability or stopping power S is equivalent to:

$$S = 1 - P_s \,. \tag{7.5}$$

The final output of the simulation is a normalised histogram of the survival probability versus the photon energy, as shown in figure 7.2 for the case of an absorber thickness of 3 µm.

Two different energy ranges have been considered for the simulations. The first energy range is set between 1.800 keV and $Q_{EC} = 2.833$ keV to gain an overview on the survival probability of events belonging to the region where the MI and MII lines are present as well as on the end-point region, as shown in figure 7.2a. Even if the final analysis for the determination of the effective electron neutrino mass will be focused on the end-point, it is relevant to obtain a reliable experimental shape of the MI and MII lines to be compared with the theoretical models currently under development [Bra20]. The second energy range is set between 2.600 keV and $Q_{EC} = 2.833$ keV to precisely estimate the probability of undetected events in the region of interest for the determination of the neutrino mass, as shown in figure 7.2b.

[4] As discussed in the section 5.1.1 for the ECHo-1k detector, the complete geometry includes two absorber layers embedding the ^{163}Ho source.

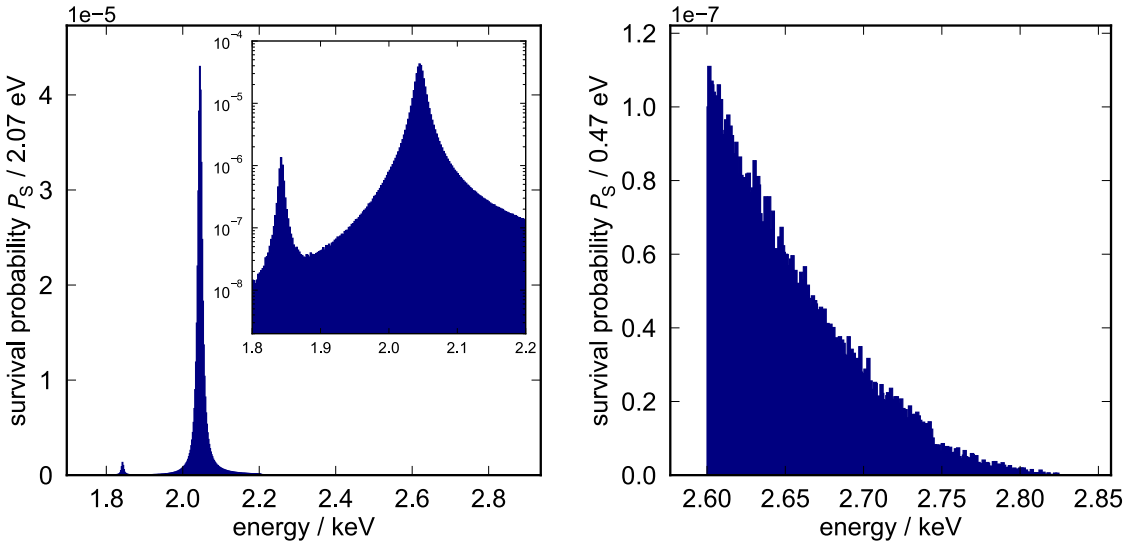

(a) **(b)**

Figure 7.2: Survival probability histograms calculated with Montecarlo simulations with 10^9 events assuming an absorber thickness of 3.0 µm. In **a)** the energy range is between 1.800 keV and $Q_{\mathrm{EC}} = 2.833$ keV and in the inset a magnification in the energy region of the MI and MII resonances is shown in logarithmic scale. In **b)** the energy range is between 2.600 keV and $Q_{\mathrm{EC}} = 2.833$ keV. The discontinuity visible at 2.75 keV is due to the absorption edge corresponding to the binding energy of the M3-shell.

Table 7.2 shows the total survival probability and the corresponding stopping power for different absorber thickness values and for the two energy ranges taken into consideration. The resulting stopping power for the two energy ranges taken into account is plotted in figure 7.3 as function of the absorber thickness T_{a}.

	$\boldsymbol{E = 1.800 - 2.833\,\mathrm{keV}}$		$\boldsymbol{E = 2.600 - 2.833\,\mathrm{keV}}$	
T_{a} / µm	P_{S}	$S = 1 - P_{\mathrm{S}}$	P_{S}	$S = 1 - P_{\mathrm{S}}$
2.0	3.763×10^{-3}	0.996237	4.280×10^{-5}	0.999957
2.5	1.225×10^{-3}	0.998775	1.751×10^{-5}	0.999982
3.0	4.348×10^{-4}	0.999565	1.497×10^{-5}	0.999985
3.5	1.833×10^{-4}	0.999817	1.471×10^{-5}	0.999985
4.0	1.020×10^{-4}	0.999898	1.469×10^{-5}	0.999985
4.5	7.542×10^{-5}	0.999925	1.468×10^{-5}	0.999985
5.0	6.635×10^{-5}	0.999934	1.466×10^{-5}	0.999985

Table 7.2: Survival probability P_{S} and stopping power S for different absorber thickness values T_{a} and for the two energy ranges taken into consideration.

Overall, an absorber thickness of 2.5 µm already guarantees enough stopping power. In fact, considering the events belonging to the MI line (i.e. an energy range between 2.02 keV and 2.06 keV), the survival probability is 9.86×10^{-4}. Assuming a total statistics of 10^{13} events, as planned for ECHo-100k, the number of events falling in the MI line region is about 2.2×10^{12} and only 2.1×10^{9} would be undetected, not significantly affecting the line shape. On the other side, looking at the region of interest for the final analysis, i.e. the last 50 eV at the end-point, the survival probability is estimated to be about 1.65×10^{-8}. In absolute numbers, for a total statistics of 10^{13} events, about 8.3×10^{5} are present in this range and no events are expected to be undetected.

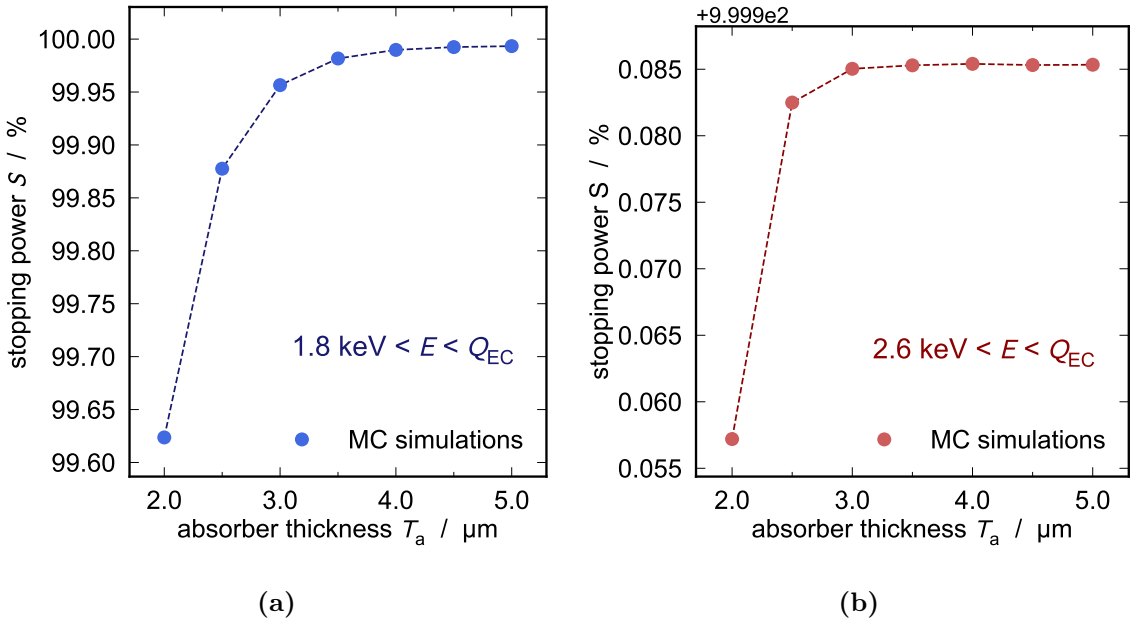

Figure 7.3: Stopping power S resulting from the Montecarlo simulations as a function of the absorber thickness T_a, for the energy range 1.800 keV $- Q_{EC}$ in **(a)** and for the energy range 2.600 keV $- Q_{EC}$ in **(b)**.

A drawback of a very thin absorber is the potential instability during the microfabrication processes and during the delicate implantation post-processing (described in section 5.1.3). Therefore, in order to avoid instability issues, the final absorber thickness value chosen for the design of the ECHo-100k detector is 3.0 µm, which on one hand guarantees enough stopping power and on the other hand does not endanger the detector stability, as demonstrated with the stability tests described in section 7.4.

7.2.2 Selection of the ^{163}Ho host material

The choice of the metal to employ as ^{163}Ho host material is an important point of the detector optimisation towards the final ECHo-100k design. As anticipated in section 5.1.4, different ^{163}Ho host materials have been considered and tested during the ECHo-1k phase: gold, silver and aluminium. The advantage of silver with respect to gold is the absence of quadrupole moments, which might increase the detector heat capacity if ^{163}Ho is implanted in gold due to the consequent hyperfine splitting. Aluminium is an interesting metal to test as host material since a considerably higher implantation depth is expected according to simulation results [Gam17]. A possible disadvantage of aluminium is its superconducting behaviour below 1.2 K, which possibly can lead to long relaxation times due to long-living quasiparticle excitations [Cos93][Per04].

Three ECHo-1k detector chips with these three different ^{163}Ho host material - gold, silver an aluminium - have been characterised at millikelvin temperature, comparing the detector responses at different temperatures and for different persistent currents in the detector pick-up coils. Figure 7.4 shows the signals of the ECHo-1k detectors with gold[5], silver and aluminium as host materials and the corresponding ^{163}Ho activity is about 0.9 Bq, 0.99 Bq and 3.7 Bq, respectively. The detector with gold as host material exhibit smaller flux amplitudes at lower temperatures, which can be correlated with a thermal decoupling between detector and mixing chamber plate, possibly due to a not optimal thermalisation, heating due to power input from the SQUID or not optimal SQUID working point. Due to the higher heat capacity that comes along with the higher activity, the detector signals of the pixel with ^{163}Ho implanted in aluminium shows a smaller amplitude with respect to the pixel with silver as host material. This is due to the fact that the signal amplitude scales with $1/C$, where C is the detector heat capacity.

[5]The data of the ECHo-1k detector with ^{163}Ho implanted in gold have already been presented in [Vel19a].

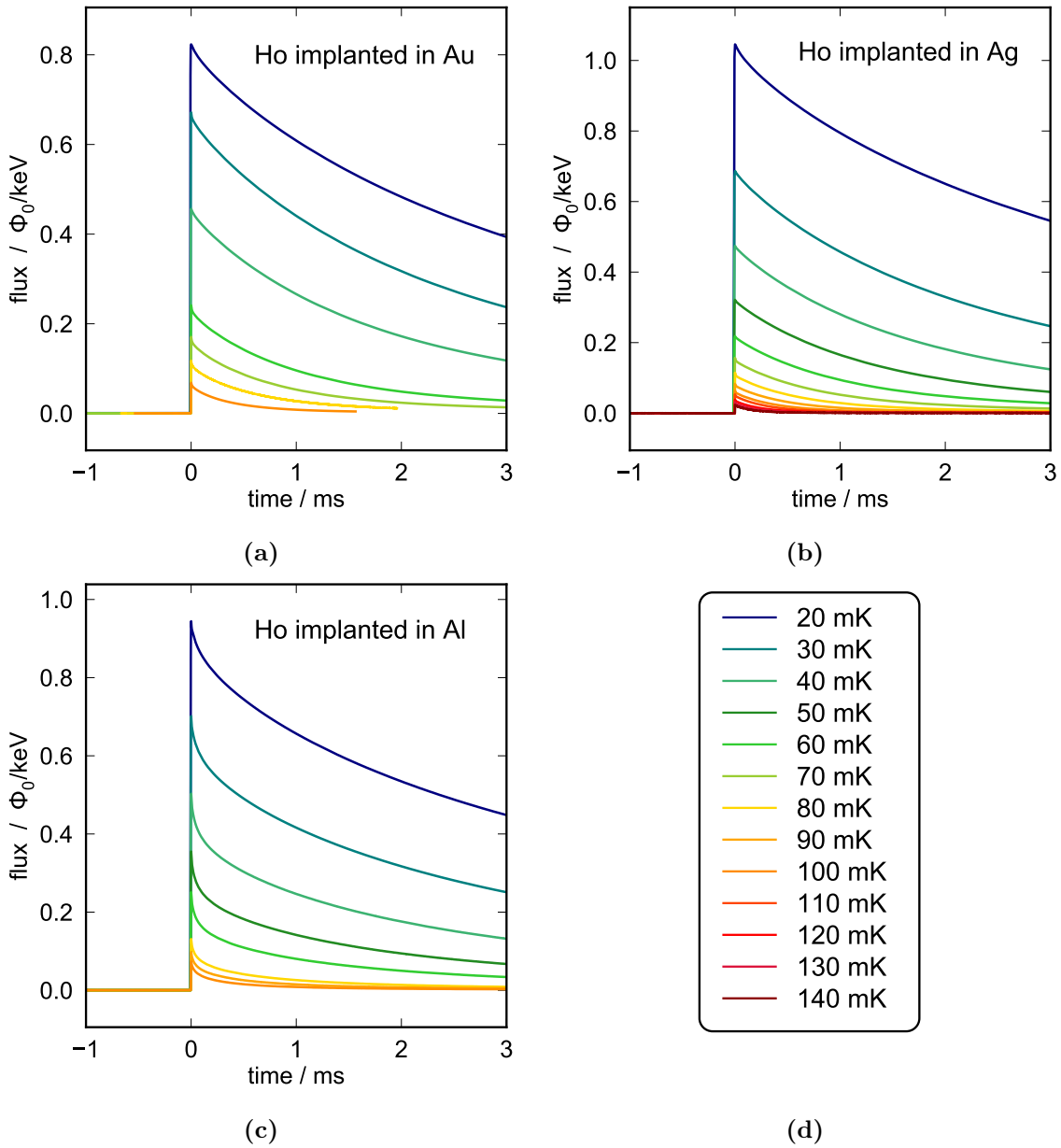

Figure 7.4: Signals of implanted ECHo-1k detectors with gold **(a)**, silver **(b)** and aluminium **(c)** as ^{163}Ho host material acquired with a persistent current of 35 mA and at different temperatures of the cryostat mixing chamber plate reported in the legend in **(d)**. The amplitude is expressed as flux in the pick-up coil per keV, in order to compare detectors with different coupling to the SQUID.

In order to investigate the signal shape of the detectors with the three different host materials, an acquisition with a long time window that includes the signal tails has been performed at base temperature $T_{\mathrm{MXC}} \approx 10\,\mathrm{mK}$ and ensuring sufficient thermalisation for all set-ups. Figure 7.5 shows a direct comparison of the detector responses. The signal amplitudes are scaled to unity in order to compare the pulse shape. No substantial difference in the pulse shapes is visible.

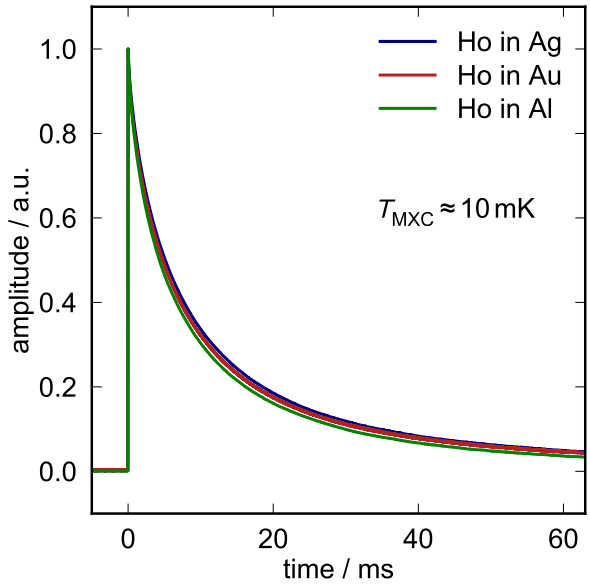

Figure 7.5: Detector responses from three detectors with different host materials acquired at $T_{\mathrm{MXC}} \approx 10\,\mathrm{mK}$ and with amplitude scaled to unity. The ^{163}Ho activities are 0.74 Bq (Ho in Ag), 0.78 Bq (Ho in Au) and 0.99 Bq (Ho in Al).

Even if no significant differences in the pulse shapes have been experimentally found for the three tested host materials, silver seems to be the best choice, being free from quadrupole moments and superconducting effects. Moreover, the energy resolution achieved with the ECHo-1k set-up with ^{163}Ho implanted in silver is higher if compared to the set-up with ^{163}Ho implanted in gold, as shown in section 5.3.3.
One more crucial point needs to be taken into account, namely the contribution to the detector heat capacity from the ^{163}Ho ions, which is expected to depend on temperature and ^{163}Ho concentration as well as on the host material itself. As reported in [Her20], at low temperatures $T \lesssim 30\,\mathrm{mK}$ the specific heat of silver alloys is lower than that of gold alloys with the same concentration. Thus, silver is considered the most suitable host material and it will be employed for the ^{163}Ho implantation of the ECHo-100k detectors.

7.3 Detector design

On the basis of the discussed optimisation studies, a new detector design has been developed in the context of this work, to meet the experimental requirements of the ECHo-100k phase.
The ECHo-100k detector chip is a MMC detector array with 64 MMC pixels. Each pair of pixels share the same read-out channel and therefore the chip can be read-out by 32 SQUID channels. The read-out can be performed both via parallel dc-SQUIDs, in the fashion of the ECHo-1k phase, or via multiplexed read-out [Weg18b] [San19].

Two detector channels (i.e. two pairs of pixels), placed at two opposing corners of the array, are characterised by a completely non-gradiometric layout and they are dedicate to temperature monitoring. Specifically, one of the two pixel consists only of the superconducting pick-up coil, while the other pixel is completely fabricated and equipped with sensor and absorber. These channels are not meant to be implanted with ^{163}Ho. Temperature fluctuations affect the detector heat capacity and therefore the signal amplitudes. Thus, it is crucial to precisely monitor any change of temperature and to correct for it. The remaining 60 pixels form 30 gradiometric channels which are insensitive to common change of temperature. Similarly to the ECHo-1k design presented in section 5.1.1, 23 channels will have both pixels implanted with ^{163}Ho and seven channels will have only one pixel enclosing the ^{163}Ho source, allowing for in situ background measurements. Figure 7.6 shows the ECHo-100k chip after fabrication.

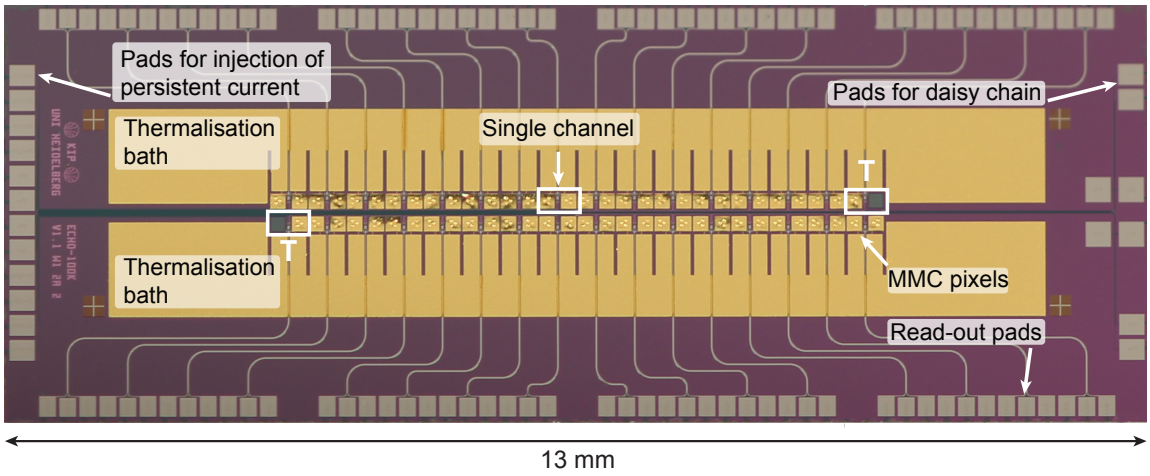

Figure 7.6: ECHo-100k chip with 32 detector channels, each one consisting of two MMC pixels. The gold thermalisation baths as well as the read-out pads, the pads dedicated to the injection of the persistent current and the pads for daisy chain connections are highlighted. The two non-gradiometric detector channels for temperature monitoring are labelled with the letter T.

The MMC pixels are positioned along two lines and the orientation of a single channel is 90° rotated with respect to the ECHo-1k design, featuring a more compact geometry. The chip size is 10 mm × 13 mm, allowing to conveniently connect the read-out chips via wire-bonding.
The main features and innovative aspects of the ECHo-100k detector design are presented in the next sections, starting from the description of the geometry of the single detector pixel, followed by the description of the chip layout and of the available options for detector operation and read-out.

7.3.1 Single pixel geometry

As described in section 3.1.1, each MMC pixel consists of three main elements: absorber, paramagnetic sensor and superconducting pick-up coil. The general layout of the single pixel is equivalent to the case of the ECHo-1k detector, as shown in figure 5.1a.

In order to optimise the detector performances, the total detector heat capacity C should be minimised, considering that the signal amplitude is inversely proportional to C and the energy resolution ΔE_{FWHM} is proportional to $\sqrt{C}$ (equations 4.37 and 4.26). Sufficiently large amplitudes of the detector signals are also important to guarantee an efficient multiplexed read-out. The heat capacity of absorber and sensor depends on material and volume. The material employed for absorber and sensor are gold and Ag:Er, respectively, and they are chosen on the basis of the considerations presented in sections 4.1.1 and 4.2.1.

The absorber thickness has been optimised on the basis of the Montecarlo simulations and calculations presented in section 7.2.1. The chosen design value for the thickness of each absorber layer is 3.0 µm. Therefore, the final absorber layout of each detector pixel includes from bottom to top:

- first absorber layer with a thickness of 3.0 µm;
- first silver host material layer with a thickness of 100 nm [6];
- implanted ^{163}Ho source (with co-deposition of silver);
- second host material (silver) layer with the same thickness as the first one to fully embed the source;
- second absorber layer with a thickness of 3.0 µm.

[6] The thickness of the host material is chosen as small as possible to minimise the contribution to the detector heat capacity, but large enough to be reliably microfabricated.

The implantation area is 150 µm × 150 µm and the photoresist mask is designed such that no ^{163}Ho ions are implanted in correspondence of the stem structures, minimising the probability that phonons travel to the sensor trough the stems, causing a loss of signal.

At the operational temperature of 20 mK, the total heat capacity of both the absorber layers is 0.26 pJ/K. Considering the half-life of ^{163}Ho as currently reported in literature [Bai83] [Kaw88] and assuming a ^{163}Ho activity of 10 Bq, the heat capacity from the implanted ions in silver is estimated to be about 0.73 pJ/K.
The volume of the sensor is adjusted such that the heat capacity of the sensor matches the heat capacity of the absorber (including the contribution from the implanted ^{163}Ho) in order to achieve the optimal detector performances, as discussed in section 4.4.3. Thus, the sensor thickness is designed to be 0.48 µm, while the area needs to be smaller than the absorber area and is set to 170 µm × 170 µm. Considering this sensor volume, an expected erbium concentration of about 410 ppm and a persistent current of 35 mA, the sensor heat capacity is estimated to be about 1.04 pJ/K, which matches the heat capacity of the implanted absorber layers.

The meander-shaped pick-up coil covers the area that corresponds to the sensor. The width of the niobium lines is 3 µm and the pitch[7] is 6 µm. Each meander consists of 39 diagonal niobium lines connected via rounded corners.

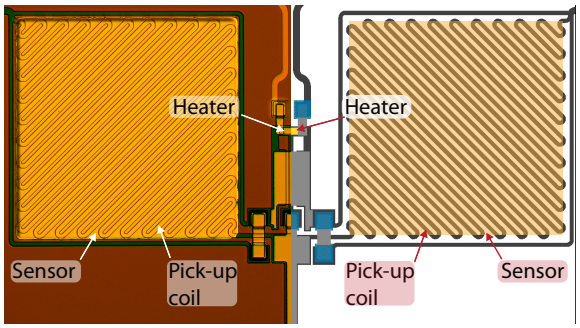

Figure 7.7: Microscope picture (left half) and schematic design (right half) of an ECHo-100k detector channel consisting of two MMC pixels. The meander-shaped pick-up coil and the sensor are present, while the absorber layers are not deposited yet.

Figure 7.7 shows a detector channel consisting of two identical MMC pixels, where sensor and meander-shaped pick-up coils are visible, as the absorber layers are still missing. For the right pixel the schematic design is shown, while for the left pixel a microscope picture is shown. The microfabricated structures precisely match the design. The pick-up coil is visible trough the sensor layer due to the thinness of the latter.

[7]The pitch is defined as the distance between the centre of two consequent niobium stripes.

7.3.2 On-chip thermalisation

In order to improve the detector thermalisation, two main aspects have been modified with respect to the ECHo-1k design: the layout of the connection between sensor and thermal bath and the thermal connection between the different thermal baths.

In the case of ECHo-1k, the geometry of the connection between sensor and on-chip thermal bath could be responsible for the multiple components in the signal decay, as discussed in section 5.3.3. In order to improve this aspect, the ECHo-100k detector design includes a direct connection between the sensor and the gold area that serves as thermal bath through the weak thermal link, as shown in figure 7.8.

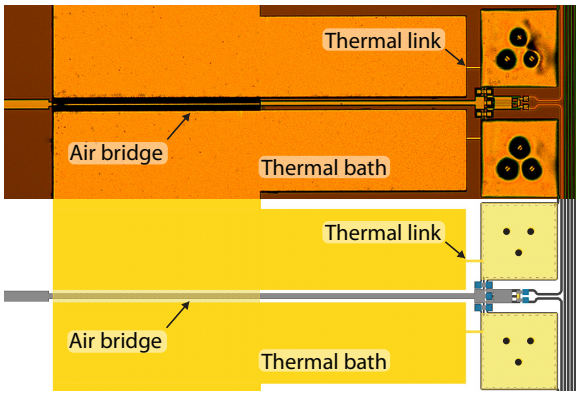

Figure 7.8: Microscope picture (top half) and schematic design (bottom half) of the thermalisation layout of the ECHo-100k detector. The sensors are not visible, being placed underneath the absorbers. The thermal links and thermal baths as well as the air bridges to connect consecutive thermal baths are indicated.

In the ECHo-1k design each group of four MMC pixels, corresponding to two detector channels, are connected to one gold area that serves as thermal bath, as shown in figure 5.2. Each gold area is separated from the next one because of niobium connection lines passing in between. Therefore, each gold area must be connected to the next one via gold bond-wires and the final one in the series is connected to a large squared-shaped gold area at the edge of the chip. The large gold area is in turn connected to the copper holder to which the chip is glued. The holder is in direct contact with the mixing chamber plate of the cryostat. This layout brings two drawbacks: on one hand, the gold bond-wires could be instable and easily detach during the handling of the set-up and, on the other hand, placing the gold bond-wires is a delicate and time consuming extra-step in the preparation of the detector set-up.

An innovative solution for the thermal connection between the thermal baths has been developed and successfully implemented for the ECHo-100k design. Here, each pair of MMC pixels is connected to a gold area that is linked to the consecutive

one via gold air bridges that are structured during the microfabrication process, as explained in the section 7.4. Figure 7.8 shows the air bridges in a microscope picture as well as in the design scheme. A schematic top view and side view of the air bridge structure are depicted in figure 7.9.

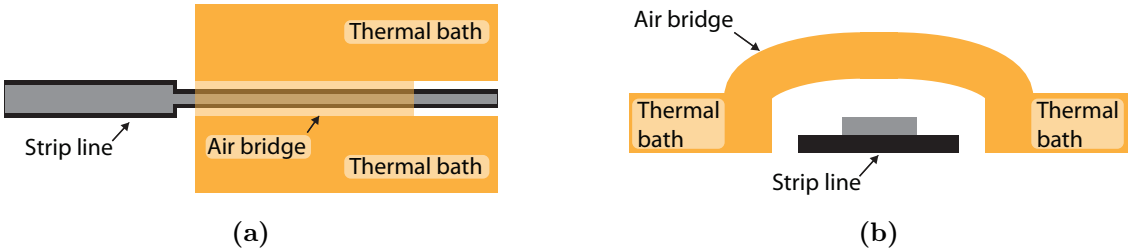

Figure 7.9: Top **(a)** and side **(b)** views of the air bridge structure to connect consecutive thermal baths in the ECHo-100k design. The thermal baths are separated by niobium strip-lines (consisting of two overlapping niobium lines with isolation in between). The air bridges look dark in the microscope photo because of the shadow on the tilted areas.

7.3.3 Rounded superconducting lines

The ECHo-100k design contains niobium connection lines that serve for two different purposes:

- to inject the persistent current into the meander-shaped pick-up coils, in order to create the magnetic field that polarises the spins in the sensor, according to the operation concept explained in section 5.1.5;
- to carry the flux signal from the pick-up coil to the read-out pads that are in turn connected to the read-out stage.

The lines that carry the current to be injected into the meander-shaped pick-up coil are labelled ±F and they connect the pick-up coils to the dedicated bond-pads. The corresponding line width is 5 µm and it is reduced to 3 µm in the meander-shaped pick-up coil. The lines that carry the current to activate the heater switch are labelled ±H and they connect the gold-palladium resistor to the dedicated bond-pads (figure 7.10). The corresponding line width is 5 µm. The connection layout for the injection of the persistent current is explained in section 7.3.5.

The connection lines that carry the signal consist of strip-lines with two overlapping niobium layers with isolation in between, as indicated in the scheme of figure 7.10. The width of the first (second) niobium layer is 24 µm (22 µm) and it reduces to 12 µm (10 µm) in the parts of the paths that pass underneath the thermalisation air

bridges (figure 7.9a), as the width of the air bridges must be minimised to guarantee the highest stability.

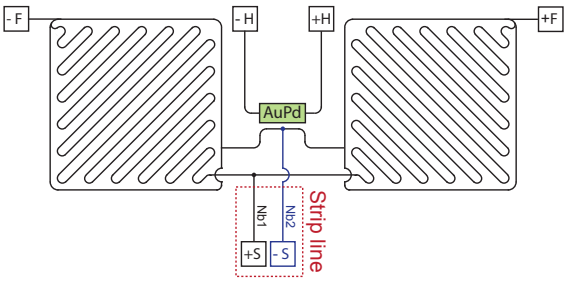

Figure 7.10: Schematic drawing of the connections for the injection of the persistent current and for the signal read-out.

All the connections lines as well as the meander-shaped pick-up coils are rounded at their corners, as shown in figure 7.7 to avoid current crowding that could lead to potential singularity points in the distribution of the magnetic field lines [Hag63].

7.3.4 Pixel arrangement for highly efficient implantation

The ^{163}Ho implantation is performed at the RISIKO facility at Mainz University [KT19a] [KT19b]. The detector chip (or wafer, in case the implantation occurs on wafer scale) is covered with a photoresist mask and a thin metallic layer that serves as host material. Only the implantation areas are left open, as described in section 5.1.3 for the ECHo-1k detector. The area of interest on the chip, in correspondence of the absorber array, is scanned with an ion-beam with a size of about 0.7 mm, thanks to the post-focusing. The ^{163}Ho ions are directly implanted into the whole scanned area. Thus, after implantation, ^{163}Ho is present also in the host material layer that covers the regions in between the implantation areas. A dedicated process to recover the ^{163}Ho from the photoresist after the latter has been lifted off is currently under development at the Institute for Nuclear Chemistry at Mainz University. However, in order to reduce the amount of ^{163}Ho that is wasted in first place during the implantation process, the space between the implantation areas should be minimised. Hence, the ECHo-100k design features a compact pixel arrangement, as visible in figure 7.6. The total area that needs to undergo the implantation scan is $0.43 \times 7.40\,\mathrm{mm}^2$, while for ECHo-1k it is $1.14 \times 4.24\,\mathrm{mm}^2$. Considering that in the ECHo-100k (ECHo-1k) detector chip 53 (57) MMC pixels are implanted, the total useful implantation area is $1.193\,\mathrm{mm}^2$ ($1.282\,\mathrm{mm}^2$) and the space between the implantation areas where the ^{163}Ho is implanted in the mask layer is $1.989\,\mathrm{mm}^2$ ($3.552\,\mathrm{mm}^2$). Thus, the amount of ^{163}Ho per pixel that is lost in first place during the implantation procedure is reduced by 40% in the new detector design.

7.3.5 Operation flexibility

As described in section 5.1.5, the ECHo-1k design is divided into four quarters, each one including nine detector channels (i.e. 18 pixels) for a total of 36 detector channels. Similarly, the ECHo-100k design consists of four quarters, each one containing eight detector channels (i.e. 16 pixels) for a total of 32 detector channels. The procedure to inject persistent currents into the pick-up coils is discussed in section 5.1.5 and it is necessarily performed quarter by quarter in the ECHo-1k detector. This aspect can represent a limitation in the homogeneity of the detector response in different pixels, as the injection procedure could potentially differ for each quarter. For this reason, the ECHo-100k detector chip is designed to allow the injection of the persistent current into all the superconducting pick-up coils at once, without sacrificing the flexibility of the injection quarter by quarter. The connection layout of the ±F and ±H lines dedicated to this purpose is depicted in the schematic drawing of figure 7.11.

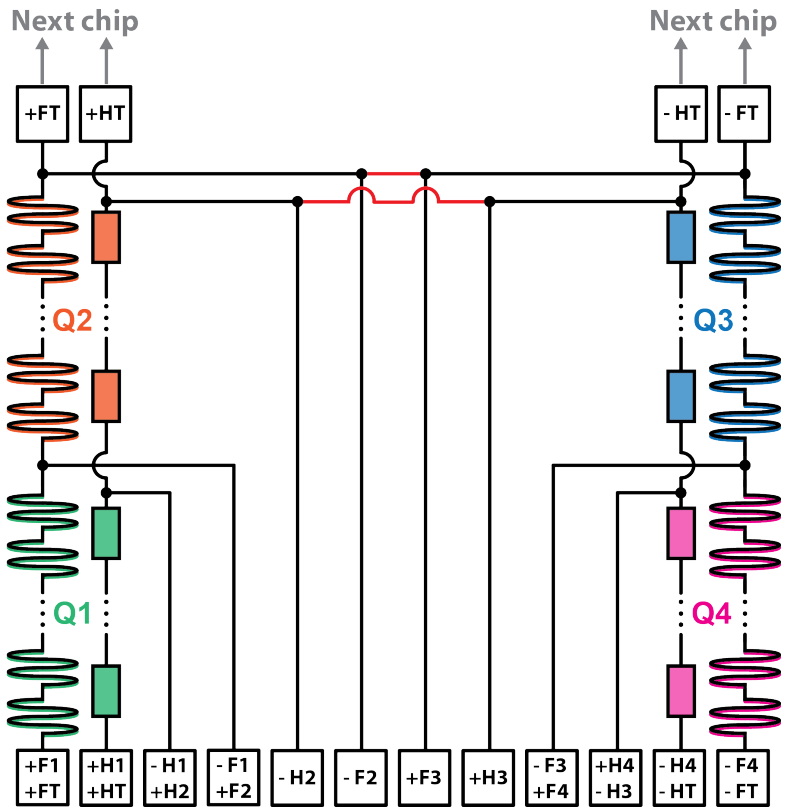

Figure 7.11: Layout of the ±F and ±H lines which connect the meander-shaped pick-up coils and the heat-switches of the ECHo-100k chip, respectively. The four quarters of the chip are marked with different colours. The pick-up coils are depicted as meandering lines, while the heaters are represented as boxes.

The following modi operandi are available with this layout:

1. injection of the persistent current quarter by quarter into one detector chip;
2. injection of the persistent current into all the pixels of the detector chip at once;
3. injection of the persistent current into all the pixels of multiple detector chips at once.

The first option is particularly useful during the characterisation measurements, since it allows to have different values of persistent current in different pixels, so that the corresponding detector responses can be efficiently acquired in parallel and compared. To apply this option the bond-pads labelled with the corresponding quarter number need to be used (e.g. $\pm F_2$ and $\pm H_2$ to inject current into the second quarter).

The second option guarantees a homogeneous preparation of the persistent current in the complete detector chip and it can be exploited during standard operation of a single ECHo-100k chip. In this case, the bond-pads $\pm F_T$ and $\pm H_T$ are used and the wire-bonds to close the circuit - indicated in red in the scheme of figure 7.11 - need to be placed.

Finally, the third option can be implemented if many detector chips are daisy chained in series in a multiplexing set-up, as explained in the next section. The persistent current in all the detector chips can be homogeneously inserted in a single operation. An arbitrarily large number of detector chips can be connected placing aluminium wire-bonds from each chip to the consecutive one, as shown with grey arrows in figure 7.11. The last chip of the series needs to be equipped with the wire-bonds to close the circuit, as in the previous case. The bond-pads $\pm F_T$ and $\pm H_T$ of the first chip of the series are used for the injection of the persistent current.

Overall, the layout for the persistent current injection of the ECHo-100k detector offers flexibility and it is adapted to the daisy chain configuration planned for the multiplexing read-out scheme.

7.3.6 Read-out flexibility

As pointed out at the beginning of this chapter, the ECHo-100k experiment requires a multiplexed read-out to deal with thousands of MMC detectors operated in parallel. The microwave SQUID multiplexing system currently under development has been shortly presented in section 3.1.3 [Weg18b] [San19].

During the transition phase from parallel read-out - where each detector channel is read out by a dc-SQUID, as it has been implemented for ECHo-1k - to multiplexed read-out, it is beneficial to be able to switch from one to the other read-out layout

with the same detector chip. For this reason, the ECHo-100k detector is designed to be conveniently connected via wire-bonds to both dc-SQUID front-end read-out chips and microwave SQUID multiplexing read-out chips.

The front-end dc-SQUID read-out chips are produced in house (cleanroom facility at the Kirchhoff Institute for Physics, Heidelberg University) and their standard layout consists of a chip size of 3 mm × 3 mm containing four dc-SQUID channels. Therefore, in order to read-out a complete ECHo-100k detector chip, eight front-end chips are needed. Four front-end SQUID chips are placed on each side of the ECHo-100k detector chip and wire-bonded to the dedicated read-out pads, as shown in figure 7.6.

On other side, the current design of the μMUXing read-out chip has a length of 15 mm. The width of the chip will depend on the chosen microwave resonator geometry. Currently coplanar waveguide resonators and lumped element resonators are possible candidates. Each μMUXing read-out chip contains 16 channels and, therefore, two μMUX chips are used to read out every ECHo-100k chip. As already mentioned in the previous section, the ECHo-100k detector can be operated as single chip (with parallel or multiplexed read-out) or multiple detector chips can be daisy chained and read out by a single μMUX set-up.

For the final measurement of the ECHo-100k phase, groups of ten ECHo-100k detector chips will be daisy chained and read out by one μMUX set-up. Therefore, to read out 12000 MMC detector pixels, about 200 ECHo-100k chips will be used and about 15 μMUX set-ups will be operated in parallel.

7.4 Detector fabrication

The fabrication of the ECHo-100k detectors has been performed as part of this thesis in the cleanroom facility of the Kirchhoff-Institute for Physics. The complete list of fabrication steps is reported in table 7.3 and the corresponding microscope pictures are shown in figure 7.12[8]. The newly produced ECHo-100k chips with only the first absorber layer deposited (layer 10) are fully characterised before proceeding with the ^{163}Ho implantation and the deposition of the second absorber layer (layers 11-14), as shown in the next section.

The fabrication steps and the micro-lithography techniques employed for each layer are equivalent to the ones used for the production of the ECHo-1k detectors and they have been described in detail in section 5.1.2. However, the design and the detector geometry are substantially different, as discussed in the previous section. Nonetheless, particular care has to be taken for the fabrication of the thermalisation air bridges (layer 8) and of the absorbers (layer 10-14).

Fabrication steps				
#	Layer	Material	Thickness	Deposition technique
1	Pick-up coils, SQUID lines (layer 1)	Nb	250 nm	Sputtering + etching
2	Isolation	Nb_2O_5	-	Anodisation
3	Isolation	SiO_2	175 nm	Sputtering + lift-off
4	Isolation	SiO_2	175 nm	Sputtering + lift-off
5	Heaters	AuPd	150 nm	Sputtering + lift-off
6	SQUID lines (layer 2)	Nb	600 nm	Sputtering + lift-off
7	Sensor	AgEr	480 nm	Sputtering + lift-off
8	Thermalisation	Au	300 nm	Sputtering + lift-off
9	Stems	Au	100 nm	Sputtering
10	Absorber - 1st layer	Au	3 µm	Electroplating + lift-off
11	^{163}Ho host material	Ag	100 nm	Sputtering
12	^{163}Ho implantation	^{163}Ho	-	Ion-implantation
13	^{163}Ho host material	Ag	100 nm	Sputtering + lift-off
14	Absorber - 2nd layer	Au	3 µm	Sputtering + lift-off

Table 7.3: Microfabrication steps of the ECHo-100k detector chip.

[8]The colours change from layer 1 to layer 2 due to the isolation deposition and the anodisation process. The colours of the remaining layers are affected by the illumination and the presence of photoresist.

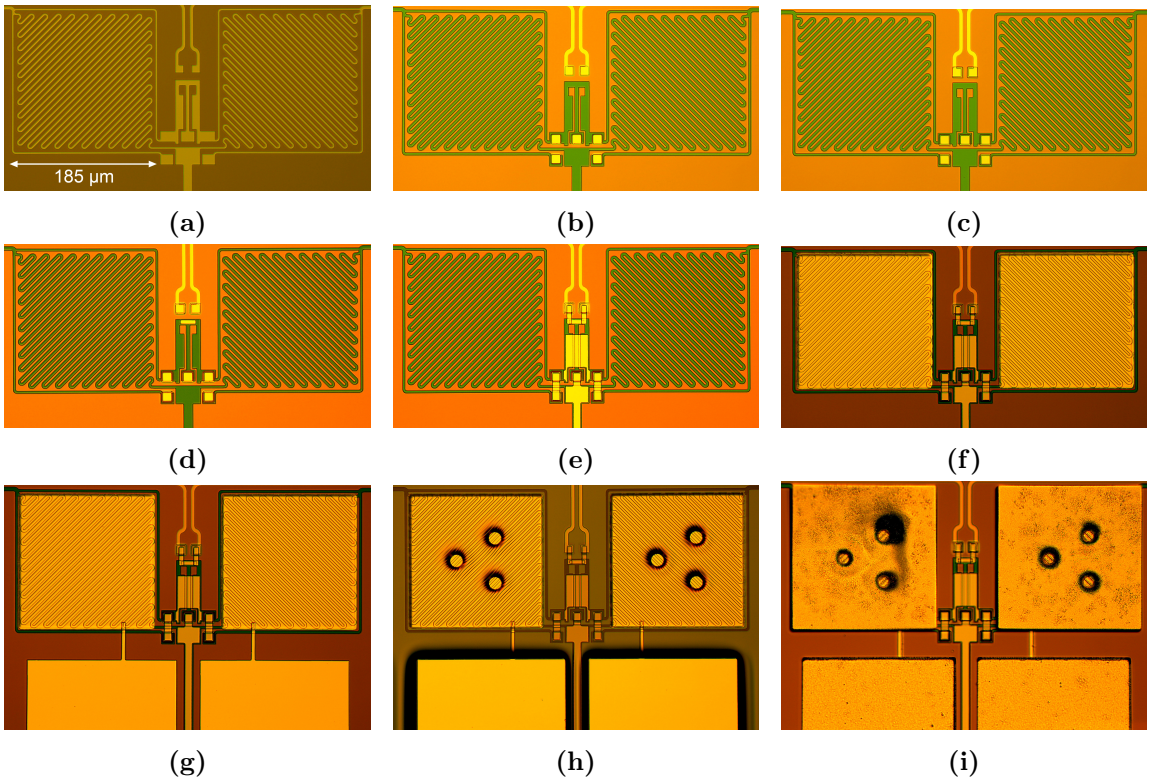

Figure 7.12: Microscope pictures of the fabrication steps of the ECHo-100k detector. **(a)** #1: first niobium layer, **(b)** #2-3: anodisation + first silicon dioxide isolation, **(c)** #4: second silicon dioxide isolation, **(d)** #5: gold-palladium heaters, **(e)** #6: second niobium layer, **(f)** #7: silver-erbium sensor, **(g)** #8: gold thermalisation layer, **(h)** #9: gold stems, **(i)** #10: gold first absorber layer.

The innovative on-chip thermalisation with gold air bridges could pose potential problems during the fabrication, e.g. photoresist residual underneath the bridges after the lift-off process or damages due to possible instabilities of the final structures.

Each absorber layer is designed to be 3 µm thick, according to the optimisation studies presented in section 7.2.1. Thus, the absorbers of the ECHo-100k detector are significantly thinner if compared to the ECHo-1k design and therefore potentially prone to instability issues.

For these reasons, after the fabrication was completed up to layer 10, a group of three ECHo-100k detector chips underwent stability tests to check the endurance of the most fragile structures, as air bridges and absorbers, and to verify the feasibility of the following microfabrication processes for the ^{163}Ho implantation. Two methods are implemented to test the structures' stability:

1. placing the detector chip in a container filled with N,N-Dimethylformamide

(DMF), which is immersed in an ultrasonic bath and exposed to different ultrasonic powers at different immersion times, with the aim to test the cleaning procedure to remove the protective photoresist layer that is deposited over the wafer before the sawing procedure to obtain the the single chips;

2. deposition of a thick layer of photoresist[9] on top of the single ECHo-100k chip and spreading the photoresist using a spin coater at 3000 rpm, followed by lift-off with DMF in an ultrasonic bath with the parameters that provide sufficient cleaning without damaging the chips, with the aim to test the feasibility of the post-process procedure to fabricate the second absorber layer.

The best results of the first test are achieved using an ultrasonic power percentage of 10% with the SONOREX DIGITAL DK 512 P device and performing the ultrasonic cleaning with a series of about five to seven immersions, each one with a duration of 5 s and followed by a break of about the same duration. With these parameters, the tested ECHo-100k chips were successfully cleaned without suffering any damage. A detailed optical inspection after the ultrasonic cleaning and photoresist spinning tests confirmed the integrity of the air bridges and the absorber structures. Power percentages of 20% or above become critical for the stability of the thin absorbers.

7.5 Detector characterisation

The newly fabricated ECHo-100k detectors underwent a full characterisation process. The main goals of the characterisation measurements are to test the detector functionality, to compare the measured parameters with the design values, to verify the match between detector response and corresponding simulations and, finally, to demonstrate that the changes in the ECHo-100k detector design with respect to the ECHo-1k design lead to an improved performance. In the following the experimental methods and the results of the characterisation measurements at room temperature, at 4 K and at millikelvin temperature are presented.
Based on the outcomes of these measurements, the suitability of the new ECHo-100k design for the corresponding experimental phase will be evaluated. In case of a positive result, it will be possible to proceed with the ^{163} implantation procedure.

[9] AZ nLof 2070 distributed by MicroChemicals GmbH, Nicolaus-Otto-Str. 39, D-89079 Ulm, Germany.

7.5.1 Characterisation at room temperature

After fabrication, the complete ECHo-100k wafer[10], containing 40 detector chips, underwent a detailed optical inspection to check the continuity of the niobium lines as well as the conditions of the main structures. As next step, the resistances of the niobium lines of a bunch of four ECHo-100k chips have been tested at room temperature, contacting the corresponding bond-pads with a needle-prober tool. Both the connections dedicated to the read-out and the ones dedicated to the injection of the persistent currents into the pick-up coils showed the expected resistances and no shorts, for all the tested detector chips. The read-out connections (labelled as $\pm\mathrm{SQ}N$, where $N \in [1, 32]$ is the detector channel number) feature resistances in the range between $915\,\Omega$ and $1060\,\Omega$, depending on the length of the niobium lines and therefore on the position of the detector channel in the array. The connections for the injection of persistent currents (labelled as $\pm\mathrm{F}_i$ and $\pm\mathrm{H}_i$, where $i \in [1, 4]$ is the quarter number) feature larger resistances in the range between $2.87\,\mathrm{k}\Omega$ and $4.41\,\mathrm{k}\Omega$, due to the long paths through the meander-shaped pick-up coils.

7.5.2 Characterisation at 4 K

The characterisation of the ECHo-100k detectors at a temperature of about 4 K includes resistance and critical current measurements, heater switch tests and evaluation of the inductance of the pick-up coil. The detector chips are cooled down to 4 K by means of a liquid helium bath or of a pulse tube cryocooler.

Resistances

To proof the superconductivity of the read-out niobium connections and of the lines connecting the detector meander-shaped pick-up coils ($\pm\mathrm{F}_i$, $i \in [1, 4]$) as well as to measure the resistances of the gold-palladium heaters ($\pm\mathrm{H}_i$, $i \in [1, 4]$), four-wire measurements are performed at a temperature $T = 4.2\,\mathrm{K}$. Each ECHo-100k chip to be tested is glued on a holder and immersed in a liquid helium Dewar. The average measurement results are summarised in table 7.4. Since each quarter of the ECHo-100k chip contains eight heaters and the complete chip contains 32 heaters, from the values reported in the table it is possible to estimate the resistance of a single heater element, $R_\mathrm{H}(T = 4.2\,\mathrm{K}) = 6.3 \pm 0.4\,\mathrm{Ohm}$, which is compatible with the expectations based on the material and the geometry of the heaters.

[10] ECHo-100k design version v1.1, #w1.

Average resistance values measured at $T = 4.2\,\mathrm{K}$	
Connection	R_{mean}/Ω
$\pm\mathrm{F}_i$, $i \in [1,4]$	≤ 0.01
$\pm\mathrm{F_T}$	≤ 0.01
$\pm\mathrm{H}_i$, $i \in [1,4]$	50.03 ± 1.6
$\pm\mathrm{H_T}$	200 ± 6

Table 7.4: Average resistances of the lines connecting the meander-shaped pick-up coils ($\pm$F) and of the lines connecting the heaters ($\pm$H) measured at $T = 4.2\,\mathrm{K}$.

Critical currents

The geometry of the niobium connections of the ECHo-100k design has been upgraded, introducing rounded corners, as described in section 7.3.3.

The critical current[11] of the niobium structures that form the meander-shaped pick-up coils can be measured running a current through the $\pm$F connections that link all the pick-up coils and monitoring the corresponding resistance via a four-wire measurement. Initially a very small current of few milliampere is used and the measured resistance is vanishing due to the superconductivity of the niobium lines. The current is gradually increased until the superconductive regime is broken and a finite resistance is measured. During this measurement the heater switch must be activated, so that the current flows inside the meander-shaped pick-up coils, according to the schematics in figure 5.5.
The average critical current of the $\pm$F connections is estimated to be $\bar{I}_{\mathrm{c}}(T = 4.2\,\mathrm{K}) = 102.8 \pm 4.4\,\mathrm{mA}$ in a liquid helium bath. The typical persistent current values that are used to operate the detector are below 50 mA and therefore more than a factor of two smaller than the measured critical current, which is more than sufficient.

The $\pm$F connections are fabricated in the first niobium layer, while the $\pm$H connections and the SQUID read-out lines are partly fabricated in the first niobium layer and partly in the second niobium layer. Therefore, the $\pm$H connections contain vias, i.e. connections through the isolation layers in between the two niobium layers. The vias represent the bottleneck for the achievement of high current flows and for this reason they are used only for the $\pm$H connections and the read-out lines, as both are meant to carry comparably low currents.

The critical current through vias has been determined with the same method explained above applied to a connection containing a via. The average critical current through vias is $\bar{I}_{\mathrm{c,vias}}(T = 4.2\,\mathrm{K}) = 38\,\mathrm{mA}$ with a standard deviation of 1.4 mA. The

[11] The critical current of a superconductive structure is defined as the maximum current that does not cause the superconductivity to break down.

lowest measured critical current through vias is 37 mA. As the typical current values that are needed in the ±H connections to activate the heater switches are in the order of few milliampere and the read-out currents are in the order of microampare, the results satisfy the requirements.

Heater switch

The area of the heater switch in the ECHo-100k design is reduced with respect to the ECHo-1k design and its position is closer to the surrounding niobium circuit. Therefore, the minimum current value that activates the heater switch is expected to be different from the case of the ECHo-1k detector. This parameter can be determined via a four-wire measurement of the heater circuit running different currents trough it, as explained in detail in section 5.3.2 and illustrated in figure 5.12a. The average minimum current that activates the heater switch has been measured in a liquid helium bath and the result is $\bar{I}_{\mathrm{h,min}} \approx 2.0\,\mathrm{mA}$ with a standard deviation of 0.9 mA.

Inductance of the pick-up coil

As reported in equation 4.20 in section 4.3.4, the coupling between detector and SQUID depends on the inductance of the meander-shaped pick up coil. This parameter can be derived from the analysis of a SQUID flux noise spectrum measured at a temperature $T \approx 4\,\mathrm{K}$, as it is described in section 5.3.2 in the case of the ECHo-1k detector chip. At this temperature the aluminium wire-bonds that connect the detector chip to the SQUID front-end chip are normal conducting and their resistance R_{b} together with the inductance L of the superconducting circuit formed by the pick-up coils and the SQUID input coil create a low-pass filter, as shown in the inset of figure 7.13.

The expected noise spectral density of such a set-up is described by equation 5.1 in the frequency domain. The spectral flux density measured in the SQUID, with a ECHo-100k detector channel connected to it, is shown in figure 7.13, with the corresponding numerical fit.
The inductance of a single meander-shaped pick-up coil is given by $L_{\mathrm{m}} = 2 \cdot (L - L_{\mathrm{i}} - L_{\mathrm{b}})$, where $L = 2.83 \pm 0.03\,\mathrm{nH}$ is the resulting total inductance given by the fit, $L_{\mathrm{i}} = 1.24\,\mathrm{nH}$ is the inductance of the SQUID input coil, $L_{\mathrm{b}} \approx c \cdot R_{\mathrm{b}}$ is the inductance of the bonding wires, with $c = 0.1 \pm 0.02\,\mathrm{nH/m\Omega}$ and $R_{\mathrm{b}} = 5.35 \pm 0.03\,\mathrm{m\Omega}$ from the fit. The derived value for the pick-up coil inductance $L_{\mathrm{m}} = 2.1 \pm 0.2\,\mathrm{nH}$ is consistent with the expected value of $L_{\mathrm{m,sim}} = 2.27\,\mathrm{nH}$, obtained from simulations[12].

[12]The pick-up coil inductance has been simulated with InductEx, `http://www0.sun.ac.za/ix`.

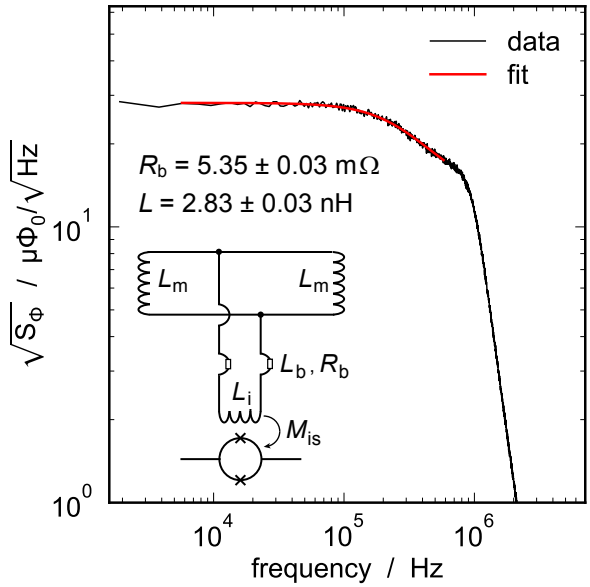

Figure 7.13: Measured spectral flux density in the SQUID for an ECHo-100k detector channel. The data is shown in black while the fit with the parameters R_b and L quoted in the graphic is shown in red. The inset shows the layout of the corresponding circuit.

7.5.3 Characterisation at millikelvin temperature

The positive outcome of the first measurements of the ECHo-100k detector performed at room temperature and at 4 K allowed to proceed with the characterisation of the ECHo-100k detector at millikelvin temperature, exploiting the cryogenic platform and the read-out chain presented in section 5.2. The ECHo-100k detectors do not contain any ^{163}Ho source inside the absorber yet and the characterisation in the cryogenic unit has been performed with the same external ^{55}Fe source used for the ECHo-1k detector. The main properties of the ^{55}Fe source have already been shortly described in section 5.3.3. The detector module developed for the ECHo-1k phase and described in section 5.2.1 has been used and an aluminium shield with a slit in correspondence of the MMC array has been employed, so that the ^{55}Fe X-rays could reach the detector pixels. The different connection layout of the ECHo-100k design with respect to the ECHo-1k design required a newly designed circuit board that matches the circuitry for the injection of the persistent current and the geometry of the bond pads [Wic20].

Functionality tests

The ECHo-100k design offers more flexibility both for the read-out scheme and the injection of the persistent current into the meander-shaped pick-up coils. Because of that, the layout of the niobium connections on the chip has been heavily modified with respect to the ECHo-1k design, as shown in figure 7.11. For this reason, the first tests at millikelvin temperature are dedicated to demonstrate the full functionality of the chip. The injection of the persistent current into each quarter and in all the detector pixels has been successfully tested and it was possible to observe a response in every single pixel. The current used to activate the heater switch were chosen between 2.5 mA and 4.5 mA, in order to be sufficiently high to break the superconductivity regime in the area of interest and sufficiently low to avoid a quench. These values are higher than the switching value determined by the tests at 4 K presented in section 7.5.2. The difference could be partly justified by the resistance values of the Au:Pd heater elements at millikelvin temperature, which are few ohm lower with respect to the resistance values at 4 K.

Magnetisation response

The magnetisation response of the Ag:Er sensor depends on the volume and on the erbium concentration, which is estimated to be about 400 ppm. The magnetisation response of the ECHo-100k detector has been reconstructed using the experimental method explained in section 5.3.3. The expected magnetisation response can be calculated exploiting dedicated sensor simulations[13], as mentioned in section 4.2.2. Figure 7.14 shows the experimental data points compared with the simulated curve as a function of the inverse mixing chamber (MXC) temperature for two different persistent current values, namely 35 mA and 50 mA. The experimental data are well described by the simulated curve in the high temperature range, but at low temperatures the agreement is not satisfying. This can be interpreted as the consequence of a local heating caused by the front-end SQUID connected to the detector channel or of a thermal decoupling between the MXC plate and the detector, the latter exhibiting a higher temperature.

[13]For ECHo-100k sensor simualtions a concentration of 445 ppm, as experimentally determined, and a α parameter of 13.5 are used.

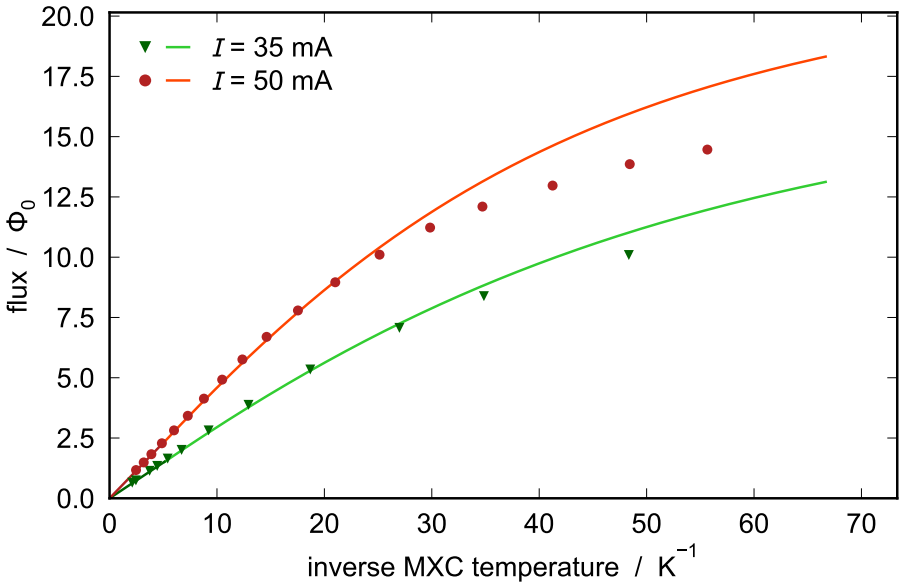

Figure 7.14: Magnetisation response recorded with a non-gradiometric MMC channel of the ECHo-100k detector for two different values of persistent current, 35 mA and 50 mA. The experimental data are compared with the simulations based on the detector properties.

Pulse shape analysis and thermodynamic properties

In order to verify the impact of the new design on the detector response, the ECHo-100k detector has been irradiated with an external ^{55}Fe source and the signals corresponding to the K_α line [Hoe97] have been recorded at different temperatures and with two different persistent current values, 35 mA and 50 mA. The time window has been set between 1.3 ms and 83.9 ms to include the complete tail of the pulses. Figure 7.15 shows an overview of the ECHo-100k signals at different MXC temperatures for the persistent current value of 35 mA. As expected, the signal amplitudes decrease and the signal decays become faster with increasing temperatures, due to the higher heat capacity of the detector. As a direct consequence, the signal to noise ratio is worse at higher temperatures, as clearly visible in the logarithmic plot of figure 7.15b, where the signals are scaled to the same amplitude.

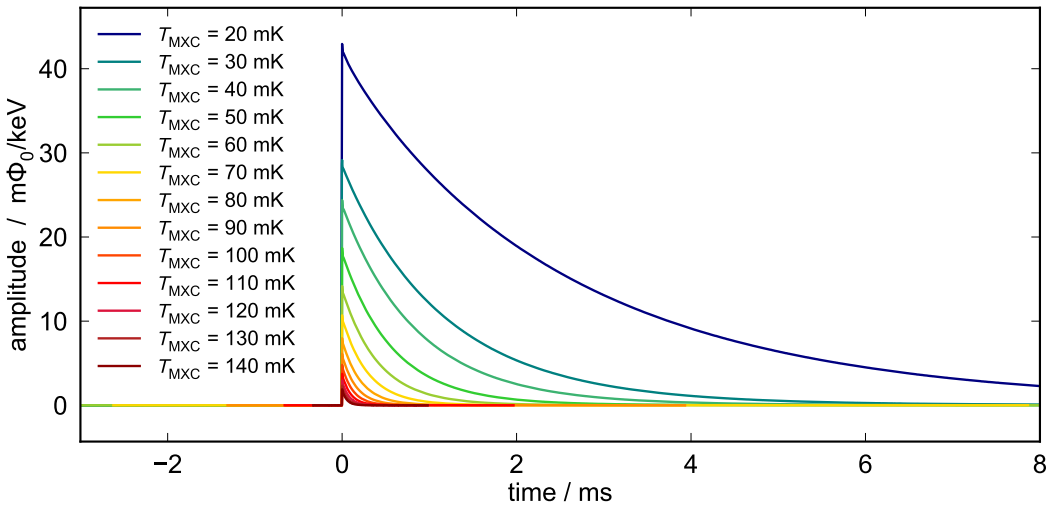

(a)

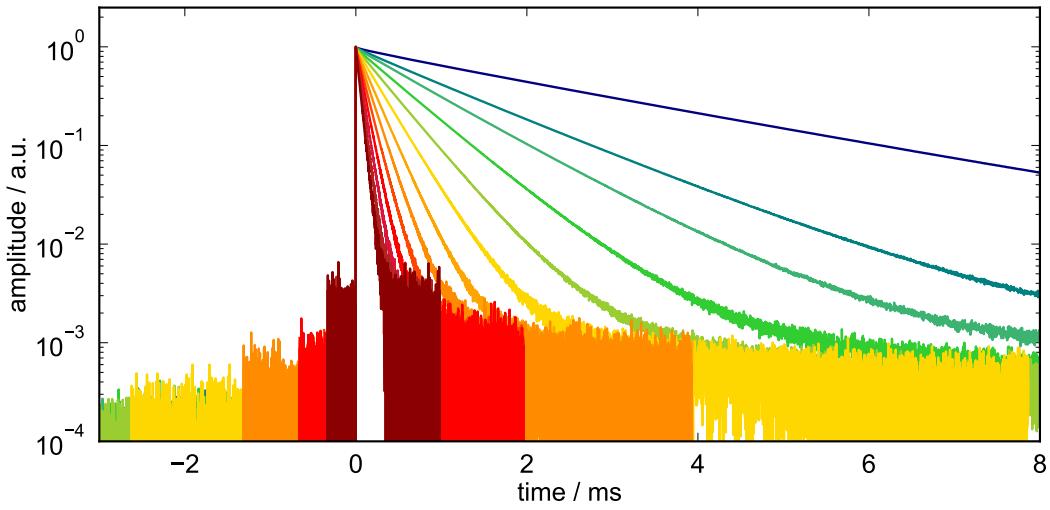

(b)

Figure 7.15: ECHo-100k detector response corresponding to the ^{55}Fe K_α line with a persistent current of 35 mA in the superconducting pick-up coils. In **(a)** the y-axis is shown in linear scale. In **(b)** the pulses are scaled to the same amplitude and the y axis is shown in logarithmic scale. The legend in **(a)** reports the MXC temperature T_{MXC} and it is valid also for **(b)**.

Signal amplitude The amplitudes of the detector response in terms of flux in the SQUID per unit of energy have been estimated from the available data at different temperatures and for different persistent current values. The same considerations presented in the discussion of the signal amplitude of the ECHo-1k detector in section 5.3.3 are valid here. Thus, also for the ECHo-100k detector an overall decrease

of the signal height with increasing temperatures is expected. The theoretical amplitudes, calculated from numerical simulations (see section 4.2.2), are compared with the experimental results in figure 7.16 for two different values of the persistent current in the pick-up coils, namely 35 mA and 50 mA. The amplitudes are larger in the first case, as expected. The value of the persistent current that maximises the signal amplitudes is an optimum between too small currents, which yield to a flatter magnetisation response of the sensor, as visible in figure 7.14, and too large currents, which increase the heat capacity of the sensor, decreasing the temperature response of the calorimeter.

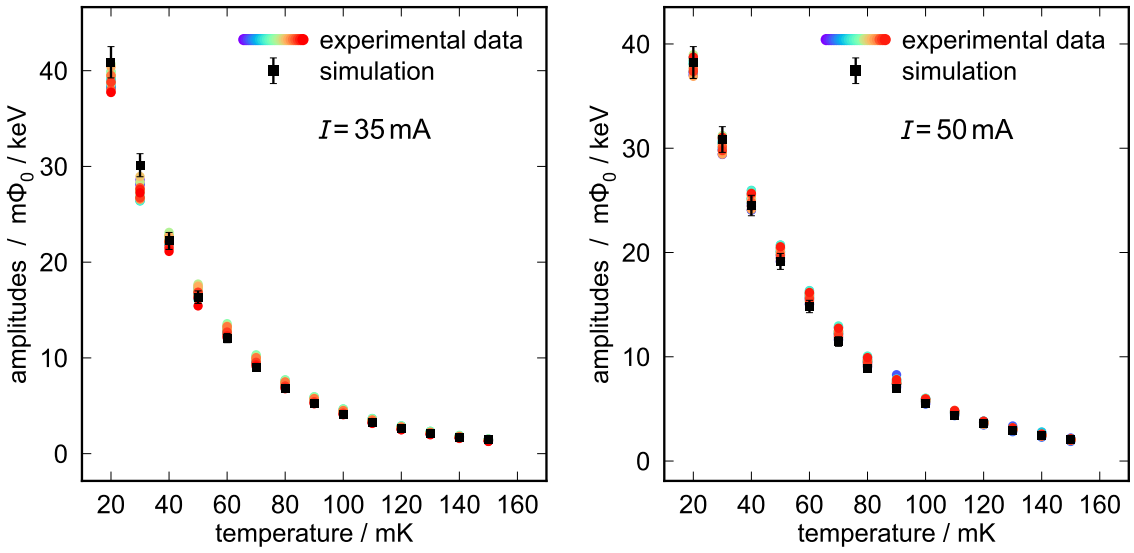

Figure 7.16: The experimentally measured signal amplitudes of the ECHo-100k detector in terms of flux in the SQUID per unit of energy (coloured marks) are compared with the theoretical expectation based on numerical simulations (black marks) for a persistent current of 35 mA **(a)** and 50 mA **(b)**.

The uncertainty on the theoretical value is dominated by the uncertainty in the estimation of the transformer coupling, which depends on the inductance of the wire-bonds and on additional parasitic inductances of the circuits that are difficult to evaluate precisely. The variation of the wire-bond inductances over the detector chip is estimated from a fit of the noise spectra recorded at a temperature $T \approx 4\,\mathrm{K}$ for each channel, according to equation 5.1. From the wire-bond resistance values extracted from the fits, the corresponding wire-bond inductances can be calculated. The resulting average wire-bond inductance and the corresponding standard deviation bring information on the variation of the transformer coupling from channel to channel. Additionally, the uncertainty on the conversion factor from wire-bond resistance to

wire-bond inductance, which depends on the geometry of the aluminium bondings, and the supplementary parasitic inductance add further uncertainties. Overall, the relative error on the flux transformer coupling is estimated to be about 4%. The resulting theoretical predictions show high congruence with the experimental measurements, as visible in the plots of figure 7.16.

The spread of the signal amplitude values over the different channels can be interpreted as the consequence of the variation of the flux transformer coupling, which depends on the wire-bond inductance as well as on the parasitic inductances, both channel-dependent. Additionally, small discrepancies in the geometry of the microfabricated structures (e.g. sensor and absorber volumes) can lead to slightly different heat capacity values for different pixels and thus to not identical signal sizes.

Detector heat capacity The heat capacity of the detector plays a crucial role in the detector response and performances, as both the signal size and the energy resolution are affected by it. The optimisation process to define the new ECHo-100k design was based on theoretical calculations which assumed a reliable prediction of the single heat capacity contributions, i.e. heat capacity of absorber, sensor and implanted holmium.

In order to verify the model, the theoretical heat capacity must be compared with the experimental observations. The heat capacity of the detector is experimentally accessible from the signal amplitude in temperature $\Delta T = E/C$, where E is the known energy input and C is the total heat capacity of the microcalorimeter. The derivative of the magnetisation response measured as flux in the SQUID as a function of temperature (figure 7.14), $\mathrm{d}\Phi_\mathrm{S}/\mathrm{d}T$, can be used as translation factor to calculate the temperature increase ΔT corresponding to a certain flux signal in the SQUID $\Delta\Phi_\mathrm{S}$:

$$\Delta T = \Delta\Phi_\mathrm{S} \cdot \frac{1}{\mathrm{d}\Phi_\mathrm{S}/\mathrm{d}T}\,. \tag{7.6}$$

Figure 7.17 shows the comparison between the calculated detector heat capacity C_tot, as sum of the heat capacity contribution from the absorber C_a and from the sensor C_s, and the detector heat capacity extracted from the experimental data. The absorber contribution C_a is linearly increasing with temperature, since it is dominated by the electronic term, $C_\mathrm{a} \approx C_\mathrm{a,e} = \gamma T$, where γ is the Sommerfeld coefficient. On the other hand, the sensor contribution C_s exhibit a $1/T^2$ dependency at temperatures above the Schottky anomaly, as discussed in section 4.2.2. The error bars on the experimental heat capacity values are due to the uncertainty on the flux transformer coupling, which enters in the estimation of the translation factor $\mathrm{d}\Phi_\mathrm{S}/\mathrm{d}T$. As previously discussed, the relative error on the flux transformer coupling is estimated to be

about 4% and therefore the same relative error affects the calculation of the detector heat capacity. The theoretical expectations match with the experimental values, demonstrating the reliability of the detector model used for the optimisation process. The heat capacity values show a spread for different channels that goes beyond the error bar ranges. This can be due to small variations in the microfabricated structures or to an underestimated variation of the flux transformer coupling.

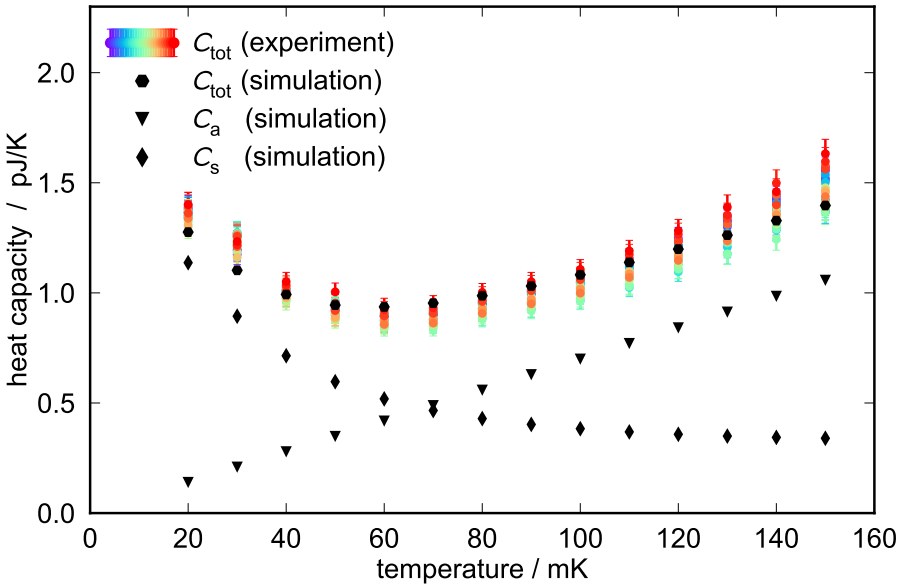

Figure 7.17: The heat capacity of the single detector pixels deduced from experimental data with persistent current of 35 mA (coloured marks) is compared with the heat capacity based on simulations (black hexagons). The single theoretical contributions of absorber, C_s, and sensor, C_a, are also plotted separately.

Signal decay The improved thermalisation layout implemented in the design of the ECHo-100k detector and the lower detector heat capacity allow for a faster signal decay that can be empirically well described by a multi-exponential fit function, $f(t) = \sum_i a_i \cdot e^{-t/\tau_i}$, where three terms are enough to represent accurately the signal shape, as shown in figures 7.18a and 7.18b. For temperatures above 90 mK two terms are sufficient to fit the detector response, as shown in figures 7.18c and 7.18d. This shows an improvement with respect to the ECHo-1k detector, for which a multi-exponential function with four terms was necessary to fit the decay signal, as reported in section 5.3.3. In particular, the long tail in the detector signal shape that was visible in the case of the ECHo-1k detector (figure 5.15) is not present any more, probably because of the better thermalisation layout.

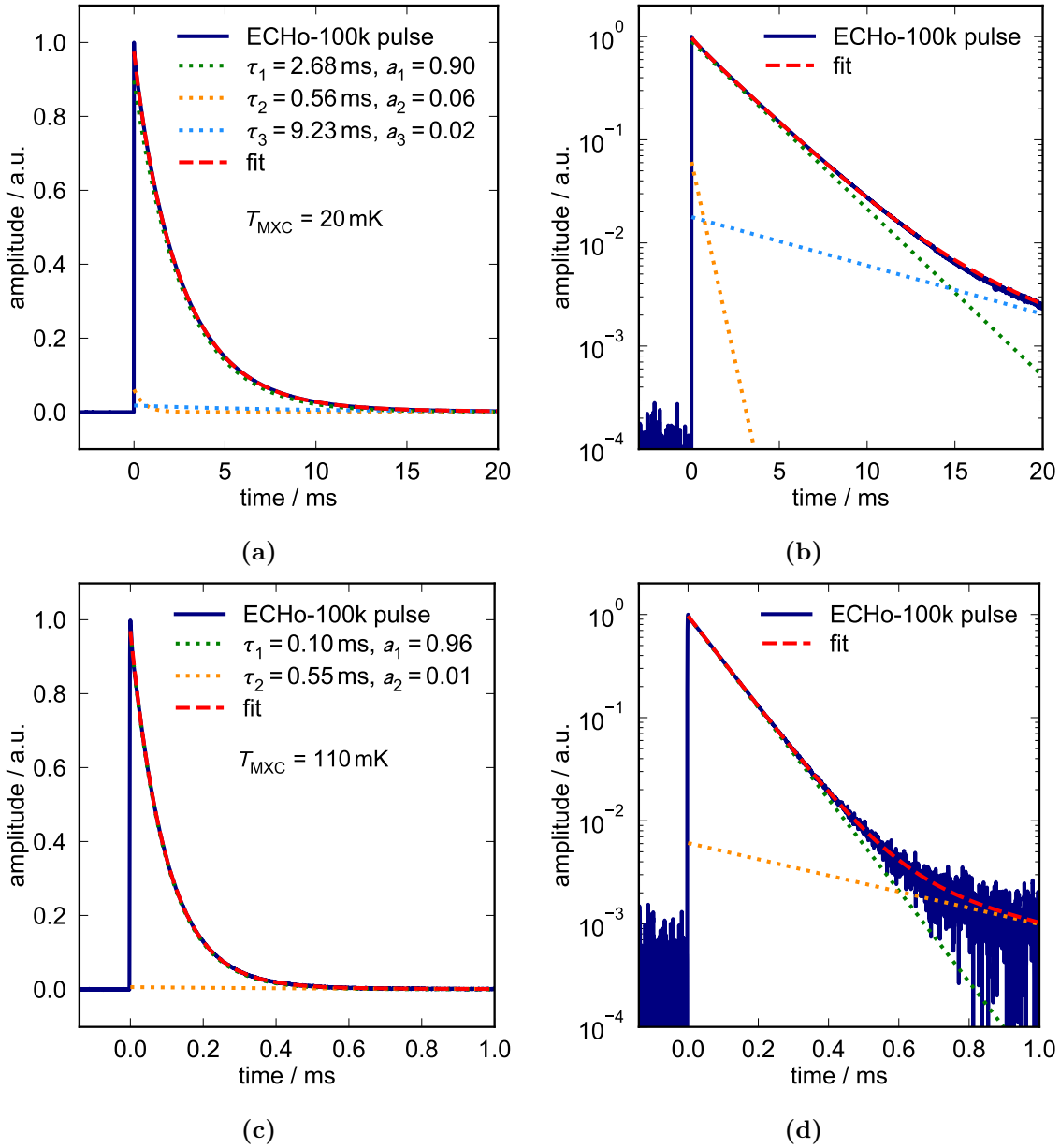

Figure 7.18: ECHo-100k signals corresponding to the ^{55}Fe K_α line recorded with a current of 35 mA in the superconducting pick-up coils. The mixing chamber temperature is 20 mK in **(a)**, **(b)** and 110 mK in **(c)**, **(d)**. The signals are fitted with three (**(a)**, **(b)**) and two exponential terms (**(c)**, **(d)**) and shown in linear and logarithmic scale, respectively. The fit parameters are shown in the legend of the plots in linear scale.

Thermal conductance of the thermal link to the bath The time characteristics of the dominant exponential decay is shown in figure 7.19a as a function of temperature. The thermal conductance G associated with the weak thermal link between sensor and thermal bath depends on the decay constant τ_1 via the simple relation $G \approx C/\tau_1$, where C is the total heat capacity of the detector, which can be extracted from the signal amplitude, as mentioned above. The resulting thermal conductance G as a function of temperature is well described by the fit function $G(T) = A_e \cdot T + A_{ph} \cdot T^3$, which includes an electronic term proportional to T and a phononic term proportional to T^3, as shown in figure 7.19b. This reveals that at high temperature the phononic contribution to the thermal conductance becomes important.

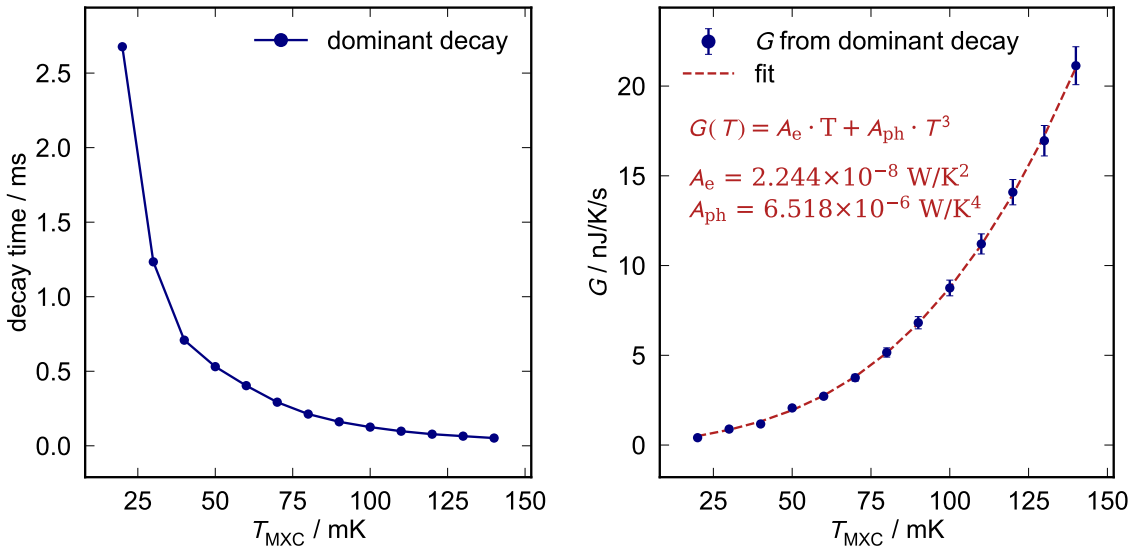

(a) **(b)**

Figure 7.19: **(a)** Decay time of the dominant exponential term as a function of temperature for the data-set with persistent current of 35 mA. The uncertainties are negligible. **(b)** Thermal conductance calculated from the dominant decay time and the detector heat capacity as a function of temperature. The fit is overlaid in red and the fit function as well as the function parameters returned by the fit are reported.

According to the Wiedemann-Franz law, the ratio between thermal conductivity k and electrical conductivity σ is given by the Lorenz number $\mathcal{L}$:

$$\frac{k}{\sigma} = \frac{G \cdot l}{T \cdot S} \cdot \rho_{\mathrm{Au}}^{10\,\mathrm{mK}} = \mathcal{L} \tag{7.7}$$

where G is the thermal conductance of the thermal link, T is the temperature, l and S are the length and the cross section of the weak thermal link connecting the sensor

to the bath, respectively, and $\rho_{\mathrm{Au}}^{10\,\mathrm{mK}}$ is the resistivity of gold at low temperature.

The relation 7.7 can be written highlighting the linear dependence of the thermal conductance G with the temperature T:

$$G = \left(\frac{\mathcal{L}}{\rho_{\mathrm{Au}}^{10\,\mathrm{mK}}} \cdot \frac{S}{l} \right) \cdot T = A_{\mathrm{e}} \cdot T \tag{7.8}$$

where A_{e} corresponds to the electronic term that is also returned from the fit. Inserting in equation 7.8 the value of the parameter A_{e} and the parameters $S = 300\,\mathrm{nm} \times 5\,\mu\mathrm{m}$ and $l = 42.5\,\mu\mathrm{m}$ from the design geometry of the thermal link, it is possible to extract the resistivity of the thermal link at millikelvin temperature: $\rho_{\mathrm{Au}}^{10\,\mathrm{mK}} = 3.84 \times 10^{-8}\,\Omega\mathrm{m}$.

Energy resolution

The ECHo-100k design has been conceived with the aim of improving the detector performances and of reaching higher energy resolution with respect to the predecessor ECHo-1k. The benchmark energy resolution for the ECHo-100k experimental phase is 5 eV FWHM and the planned ^{163}Ho activity is in the order of 10 Bq, as discussed in section 7.1. These requirements have guided the optimisation process of the ECHo-100k detector. According to theoretical calculations, the expected energy resolution of the ECHo-100k detector without implanted holmium is between 3.0 eV and 3.5 eV, considering the expected SQUID noise level. The fundamental limit on the energy resolution given by the energy fluctuations between the spin system and the electron system and with the substrate is below 1 eV at 20 mK. Therefore, improvements on the read-out side could lead to a substantial enhancement on the energy resolution achievable with this design.

The detector response corresponding to the ^{55}Fe K_α line has been measured for each detector pixel and the corresponding energy resolution per pixel has been evaluated. The K_α line exhibits a hyperfine splitting of 12 eV that can be resolved by high energy resolution detectors. The energy resolution is determined by means of a fit of the ^{55}Fe K_α doublet. The fit function is based on the convolution of two contributions. The first contribution reflects the natural line-shape and it is mathematically modelled as a sum of Lorentzians [Hoe97]. The second contribution accounts for the detector response due to the instrumental finite energy resolution and it is modelled by a Gaussian function. The FWHM (full width half maxmimum) of the Gaussian function is left as free parameter in the fit and it corresponds to the detector energy resolution. Figure 7.20 shows an example fit for two detector pixels belonging to the same channel.

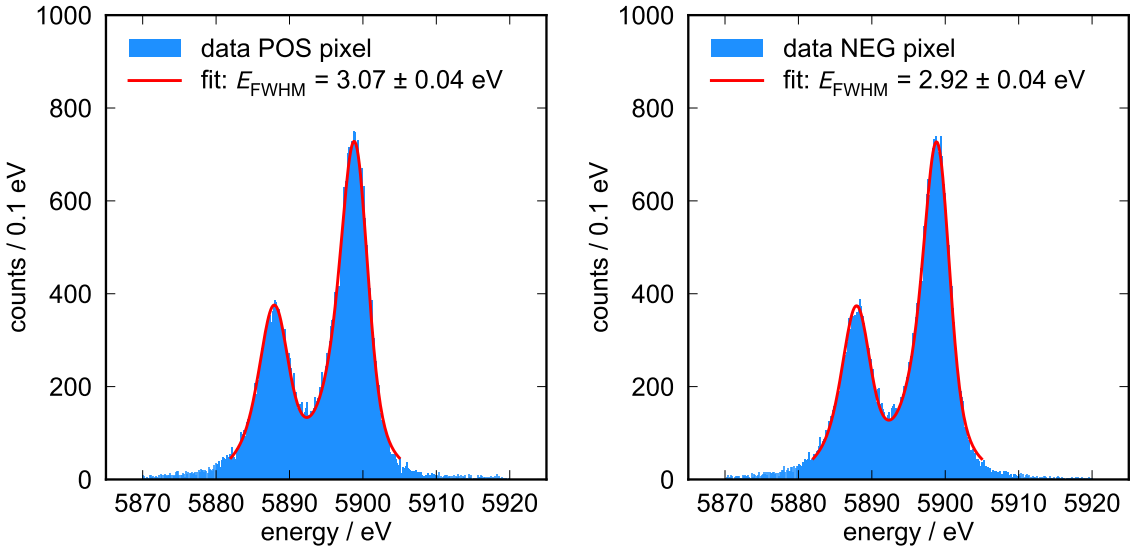

(a) (b)

Figure 7.20: ^{55}Fe spectrum with a zoom on the K_α doublet for the detector pixel with positive polarity signals labelled as "POS" **(a)** and for the detector pixel with negative polarity signals labelled as "NEG" **(b)** belonging to the same detector channel (on-chip label SQ17). The fit is shown in red and the resulting energy resolution is reported in the legend.

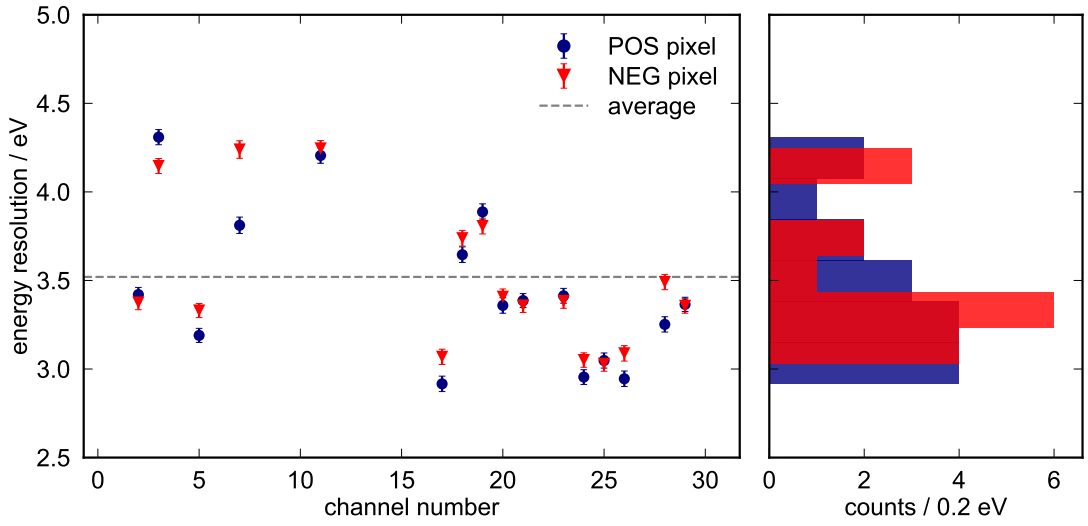

Figure 7.21: The energy resolution ΔE_{FWHM} from the fit of the K_α doublet for each measured detector pixel is shown. The average value is indicated with a grey dashed line. The channel number on the x-axis correspond to the on-chip channel label.

The resulting energy resolution values per pixel are summarised in figure 7.21[14]. The achieved energy resolution depends on the noise level of the single read-out channel and on the accuracy of the applied correction for temperature drifts. As explained in section 7.3, the detector channels that will be implanted with ^{163}Ho are characterised by a gradiometric layout, where two detector pixels are read out by the same SQUID and they give rise to signals with opposite polarities. Therefore, the read-out noise that affects two pixels belonging to the same gradiometric channel is the same. However, the energy resolution of two pixels belonging to one channel is not always equal, as shown in figure 7.21. This observation can be explained as the consequence of the presence of spurious signals in the ^{55}Fe spectrum (e.g. sensor hits caused by a damage in the absorber layer) or of a slightly different heat capacity of the two pixels because of not identical sensor and absorber volumes.
The average energy resolution is 3.52 eV FWHM with a standard deviation of 0.41 eV, which is consistent with the expectations. The best energy resolution achieved in this measurement is 2.92 ± 0.04 eV FWHM.

7.5.4 Outlook

Based on the performance obtained with the ECHo-1k detector and on the stronger requirements for the detector performance foreseen for the second phase of the ECHo experiment, ECHo-100k, a new detector chip has been developed. The single pixel design as well as the on-chip thermalisation layout have been optimised. Moreover, the new design offers high flexibility for the injection of the persistent current into the pick-up coils and is compatible both with dc-SQUID parallel read-out and multiplexed read-out.

The optimisation calculations have been performed assuming a ^{163}Ho half-life of 4570 y, as currently reported in literature [Bai83] [Kaw88]. However, the studies on the specific heat of holmium in silver presented in chapter 6 suggest a redefinition of the half-life, reducing the current literature value. At the light of the redefinition of the ^{163}Ho half-life, the amount of holmium ions corresponding to an activity of 10 Bq is about 10^{12} atoms. Therefore the ^{163}Ho implanted source in the ECHo-100k detector will increase the detector heat capacity by only about 24%, without spoiling the detector performances and at the same time guaranteeing sufficient count rate.

The newly fabricated ECHo-100k detector underwent functionality tests at 4 K and at millikelvin temperatures, ensuring the correct operation of the detector. Furthermore, the detector has been fully characterised in terms of magnetisation response, signal size, thermodynamic properties, signal shape and energy resolution. The de-

[14]Only the detector channels that have been measured are shown. Some channels could not be measured because of not working front-end SQUIDs or because of high noise level.

tector properties deduced from the experimental data match the expectations based on theoretical calculations and simulations. The detector performances in terms of detector response and energy resolution fully satisfy the requisites for the ECHo-100k phase.

In conclusion, the ECHo-100k detector is ready for the implantation of ^{163}Ho and for the measurement of a high-statistics and high-resolution ^{163}Ho spectrum with multiplexed read-out.

8. Summary and conclusion

The ECHo experiment aims to determine the effective electron neutrino mass by analysing the end-point region of the ^{163}Ho electron capture spectrum. In order to achieve this goal, it is necessary to acquire a high-statistics and high-energy resolution ^{163}Ho calorimetric spectrum with reduced background.

The detector technology employed in the ECHo experiment is based on metallic magnetic calorimeters with embedded ^{163}Ho operated at millikelvin temperatures. Each microcalorimeter pixel consists of a gold absorber, enclosing the ^{163}Ho source, in good thermal contact with a paramagnetic sensor which is immersed in a weak static magnetic field and is weakly connected to a thermal reservoir. The magnetisation signal is read out by a superconducting pick-up coil which is placed underneath the sensor and is coupled to a Superconducting Quantum Interference Device (SQUID). This work is focused on the development, fabrication, characterisation and operation of suitable detectors matching the challenging requirements of the ECHo experiment.

For the first experimental phase, ECHo-1k, 72-pixel microcalorimeter array prototypes with implanted ^{163}Ho ions have been fully characterised. In particular, the detector properties in terms of magnetisation response, signal amplitude and pulse shape have been compared with theoretical calculations and different ^{163}Ho host materials have been tested. The ^{163}Ho activity per pixel has been evaluated exploiting two independent methods which give consistent results. The average activities per pixel of the ECHo-1k detector arrays with ^{163}Ho implanted in gold, silver and aluminium are 0.81 Bq, 0.71 Bq and 2.12 Bq, respectively. The higher activity achieved with aluminium as host material is expected due to the deeper penetration of the implanted ions. The energy resolution per pixel has been determined for the two ECHo-1k detector arrays with ^{163}Ho implanted in gold and silver, yielding to average values of 6.07 eV FWHM and 5.55 eV FWHM, respectively, in the energy range of interest of the ECHo experiment.

A dedicated read-out chain has been installed in the cryogenic platform, in order to simultaneously operate two ECHo-1k detectors with ^{163}Ho implanted in gold and silver for the final high-statistics campaign of the ECHo-1k experimental phase. The data acquisition has run from December 2019 until May 2020. The resulting ^{163}Ho spectrum with more than 10^8 electron capture events is currently being analysed and it will allow to improve the current best limit on the effective electron neutrino mass of about one order of magnitude, achieving a sensitivity of 20 eV.

The precise knowledge of the specific heat of the implanted ^{163}Ho is essential to

define the ^{163}Ho activity per pixel and to evaluate the corresponding impact on the detector performances. The ECHo-1k detector chip with ^{163}Ho implanted in silver has been used to carry out a dedicated specific heat study. Comparing the temperature amplitudes corresponding to the detector signals of two detector pixels that differ only in presence of ^{163}Ho, the total heat capacity contribution from the ^{163}Ho source in the temperature range between 20 mK and 150 mK has been precisely measured.

Thanks to the very accurate measurements and analysis of the thermodynamic properties of the ECHo-1k detector and in particular of the heat capacity of the implanted ^{163}Ho source, it was possible to discover that the ^{163}Ho half-life seems to be a factor of 1.8 shorter than the value of 4570 y reported in literature [Bai83] [Kaw88].

For the second phase of the ECHo experiment, ECHo-100k, the number of detectors to be operated in parallel will be increased to about 12000 pixels and the ^{163}Ho activity per pixel will reach 10 Bq. Furthermore, the detector energy resolution is required to be below 5 eV FWHM. In order to reach this goal, dedicated Montecarlo simulations and optimisation studies have been carried out to upgrade the detector design and fulfil the requirements of the ECHo-100k phase. The new design of the single detector pixel features a thinner absorber which nevertheless ensures optimal quantum efficiency. The pixel geometry is optimised so that the heat capacity of the sensor and absorber layers with implanted ^{163}Ho match in order to reach the best detector performance.

The achieved energy resolution of the detector before ^{163}Ho implantation is about 3 eV at 6 keV. Thus, after the implantation of the planned activity of 10 Bq, the energy resolution of the detector is expected to be still well below 5 eV FWHM, fulfilling the requirements for the ECHo-100k experimental phase. The layout of the pixels arrangement has been modified to make the detector array as compact as possible, improving the geometrical efficiency of the ^{163}Ho implantation procedure. The on-chip thermalisation has been improved introducing gold air-bridges that connect the on-chip gold thermalisation islands. The on-chip circuitry dedicated to the read-out and to the detector operation has been reorganised. The new layout allows for high-flexibility in the detector operation, on one side, and for daisy chain operation and read-out, on the other side, compatibly with the microwave SQUID multiplexing read-out system currently under development.

The newly designed ECHo-100k detector array has been successfully fabricated exploiting microlitrographic techniques. After preliminary tests at room temperature and at 4 K, the detector has been fully characterised at millikelvin temperature by means of an external ^{55}Fe source irradiating the detector pixels. The detector response has been investigated in terms of magnetisation response, signal amplitude and pulse shape. From the signal amplitudes it was possible to extract the detector

heat capacity as a function of temperature. The results precisely match the design values, which are calculated on the basis of the single pixel geometry, the materials properties and the static magnetic field.
Overall, the ECHo-100k detector array has shown improved detector performances, with a response signal that can be understood from a thermodynamic point of view and an excellent energy resolution. Therefore, it can be concluded that the ECHo-100k detector array is suitable for the ECHo-100k phase and it is ready for the ^{163}Ho implantation.

The plans for the next future will be to verify the detector response with the embedded ^{163}Ho source and to proceed with the production and implantation of about 12000 detector pixels, i.e. about 200 detector chips, which will be simultaneously operated by means of a microwave SQUID multiplexing read-out system. The resulting high-resolution ^{163}Ho spectrum with about 10^{13} electron capture events will allow to set a limit below 2 eV on the effective electron neutrino mass, improving by one order of magnitude the goal limit of the ECHo-1k phase.

A. Uncertainties in the holmium specific heat and half-life studies

The error bars shown in the plots with the relative contribution to the heat capacity from holmium in figure 6.2, with the total holmium heat capacity in figure 6.3 and with the specific heat per holmium ion in figure 6.4 contain both the statistical and the systematic uncertainties on the data points.

Uncertainty on holmium relative heat capacity The statistical error in the calculation of the relative holmium heat capacity from equation 6.6 is dominated by the uncertainties on the determination of the signal amplitudes, $\delta(\Delta V_i)_{i=1,2}$. The amplitude of the signals are evaluated fitting the signal with a multi-exponential function. The fit range is selected in order to exclude the first part of the decay, where in some cases a fast decay component with a yet unknown but not thermodynamic origin is observed. The statistical error on the amplitude includes two contributions. The first contribution is the uncertainty on the pretrigger level, i.e. the voltage level before the signal rise, that is evaluated for each signal. This effect becomes more important at high temperatures, where the signal-to-noise ratio becomes lower. The second contribution is the uncertainty on the amplitude extracted from the fit. Each amplitude term of the multi-exponential function returned by the fit carries an error and the uncertainty on the total amplitude is calculated taking into account the correlation among the fit parameters.

The error propagation gives the following expression for the uncertainty on the relative heat capacity contribution δC_{rel}:

$$\delta C_{\mathrm{rel}} = \sqrt{\left(\frac{1}{\Delta V_1}\right)^2 \cdot \delta(\Delta V_2)^2 + \left(\frac{\Delta V_2}{\Delta V_1^2}\right)^2 \cdot \delta(\Delta V_1)^2}\,. \tag{A.1}$$

The systematic error on the relative holmium heat capacity is due to the possible differences in the heat capacity of the two pixels belonging to one asymmetric channel, besides the contribution from the implanted ^{163}Ho. This uncertainty can be quantified comparing the signal amplitudes of not-implanted pixels belonging to the same quadrant, as explained in section 6.3. The statistical error σ_{stat} and the systematic error σ_{sys} are combined according to the formula: $\sigma = \sqrt{\sigma_{\mathrm{stat}}^2 + \sigma_{\mathrm{sys}}^2}$.

Uncertainty on holmium heat capacity The statistical uncertainties affecting the calculation of the holmium heat capacity are the following: uncertainty on the derivative of the magnetisation curve $\mathrm{d}V/\mathrm{d}T$, uncertainty on the amplitudes of the signals ΔV_i (discussed above) and uncertainty on the correction factor k due to impedance mismatch.

The derivative of the magnetisation curve is calculated using dedicated sensor simulations that return the sensor magnetisation response in terms of flux in the pick-up coil. In order to convert this quantity to voltage, two factors are needed, namely the transformer coupling f_c to convert from flux in the pick-up coil to flux in the SQUID and the conversion factor from flux in the SQUID to voltage.
The dominant uncertainty is on the transformer coupling f_c, which depends on the inductance of the aluminium wire-bonds and on stray inductances (equation 4.20), which can vary for different detector channels. The corresponding statistical uncertainty has been experimentally determined comparing different noise spectral densities acquired at a temperature of $T \approx 4\,\mathrm{K}$ for different detector channels. As discussed in section 5.3.2, the resulting experimental data can be fitted and the inductance of the circuit, which depends also on the inductance of the wire-bonds, can be extracted. The statistical variation on the transformer coupling of different channels is estimated to be about 4%.
The error on the conversion factor from flux in the SQUID to voltage is experimentally estimated for each dataset and is about 1%.

The measured amplitude must be corrected to take into account the impedance mismatch of the two ADC devices used to acquire the detector signal and the magnetisation response, as mentioned above. The correction factor k is experimentally measured and therefore also affected by a statistical uncertainty of 1%.

The statistical uncertainty on the holmium heat capacity is given by the following formula:

$$\begin{aligned}\delta C_\mathrm{Ho} = E \Bigg[&\left(\frac{\mathrm{d}V}{\mathrm{d}T} \, \frac{1}{\Delta V_{12}} \delta k \right)^2 + \\ &\left(k \, \frac{1}{\Delta V_{12}} \delta \left(\frac{\mathrm{d}V}{\mathrm{d}T} \right) \right)^2 + \left(k \, \frac{\mathrm{d}V}{\mathrm{d}T} \frac{1}{\Delta V_1^2} \delta(\Delta V_1) \right)^2 + \left(k \frac{\mathrm{d}V}{\mathrm{d}T} \frac{1}{\Delta V_2^2} \delta(\Delta V_2) \right)^2 \Bigg]^{1/2}\end{aligned} \tag{A.2}$$

where $1/\Delta V_{12} = 1/\Delta V_2 - 1/\Delta V_1$ and the symbol δx denotes the uncertainty on the parameter x.

Uncertainty on specific heat per holmium ion The specific heat per holmium ion is calculated as the total holmium heat capacity C_{Ho} divided by the number of holmium ions $N_{\mathrm{Ho}} = a \cdot \tau_{1/2}/\log(2)$. In the analysis presented here the half-life is left as free parameter. Therefore the statistical error on the specific heat per ion is affected by the same contributions already discussed for the holmium heat capacity and one further contribution, namely the uncertainty on the ^{163}Ho activity. The latter is determined exploiting the two methods described in section 5.3.3 and the corresponding uncertainty is about 5%, as already mentioned.

The statistical uncertainty on the specific heat per ion is given by the following formula:

$$\begin{aligned}\delta c_{\mathrm{Ho}}^{\mathrm{ion}} =& \frac{E}{\tau}\,\frac{\log(2)}{a}\,\left[\left(\frac{k}{a}\,\frac{\mathrm{d}V}{\mathrm{d}T}\,\frac{1}{\Delta V_{12}}\delta a\right)^2 + \left(\frac{\mathrm{d}V}{\mathrm{d}T}\,\frac{1}{\Delta V_{12}}\delta k\right)^2 + \right.\\ &\left.\left(k\,\frac{1}{\Delta V_{12}}\delta\left(\frac{\mathrm{d}V}{\mathrm{d}T}\right)\right)^2 + \left(k\,\frac{\mathrm{d}V}{\mathrm{d}T}\frac{1}{\Delta V_1^2}\delta(\Delta V_1)\right)^2 + \left(k\frac{\mathrm{d}V}{\mathrm{d}T}\frac{1}{\Delta V_2^2}\delta(\Delta V_2)\right)^2\right]^{1/2}\end{aligned} \tag{A.3}$$

Uncertainty on holmium half-life The proposed new value of the ^{163}Ho half-life is obtained by fitting the holmium heat capacity curve to the specific heat curve previously obtained with relaxation techniques applied to a Ag:Ho sample with a concentration of 1.66% [Her20] and leaving the ^{163}Ho half-life as free parameter. This estimation is affected by a statistical uncertainty given by the fit and by a systematic uncertainty due to the unknown number of implanted holmium ions and corresponding concentration, as discussed in section 6.4.3.

With the currently available information, it is not possible to precisely determine the systematic uncertainty on the obtained ^{163}Ho half-life. A rough estimation of the systematic uncertainty can be performed with some strong assumption which deviates from the real situation. In first approximation, the number of implanted holmium atoms is related to the holmium concentration through the following expression:

$$x = \frac{N_{\mathrm{Ho}}}{N_{\mathrm{Ho}} + N_{\mathrm{Ag}}} = \frac{1}{1 + \frac{N_{\mathrm{Ag}} \cdot \log(2)}{a \cdot \tau_{1/2}}} \tag{A.4}$$

where N_{Ag} is the number of silver atoms in the volume of the implantation layer, $N_{\mathrm{Ho}} = a \cdot \tau_{1/2}/\log(2)$ is the number of holmium atoms, a is the measured activity and $\tau_{1/2}$ is the ^{163}Ho half-life.
The number of silver atoms N_{Ag} is calculated from the volume of the implantation layer, assuming that in first approximation it is completely occupied by silver atoms.

The implantation volume is given by the implantation area defined by the photoresist mask of 150 µm × 150 µm, as explained in section 5.1.3, and by the penetration depth of the implanted ^{163}Ho ions, the average of which is estimated to be about 7.7 nm for holmium in silver [Gam17].
Equation A.4 assumes a linear dependence of the concentration with respect to the activity, which is not entirely correct for the reasons discussed in section 6.4.2. Another necessary assumption is that the number of silver atoms stays constant for different concentrations. An equation system with N equations of the form of equation A.4 for N different concentrations can be written and solved for N values of the ^{163}Ho half-life, each one corresponding to a different concentration. Assuming a range of concentrations between 1.15% and 2% the corresponding systematic error can be inferred, leading to an upper bound for the ^{163}Ho half-life of 3073 y and a lower bound of 1749 y.

Bibliography

[Aal16] J. Aalbers and the DARWIN Collaboration, DARWIN: towards the ultimate dark matter detector, *JCAP*, **11**, 2016.

[Abd09] J. N. Abdurashitov, V. N. Gavrin, V. V. Gorbachev, et al., Measurement of the solar neutrino capture rate with gallium metal. III. Results for the 2002–2007 data-taking period, *Phys. Rev. C*, **80**, 2009.

[Abe11] K. Abe, Y. Hayato, T. Iida, and the Super-Kamiokande Collaboration, Solar neutrino results in Super-Kamiokande-III, *Phys. Rev. D*, **83**, 2011.

[Abg17] N. Abgrall and the LEGEND Collaboration, Probing Majorana neutrinos with double-β decay, *AIP Conference Proceedings*, **1894**, 2017.

[Abr70] A. Abragam and B. Bleaney, Electron Paramagnetic Resonance of Transition Ions, 1970.

[Agh20] N. Aghanim and the Planck Collaboration, Planck 2018 results. vi. cosmological parameters, *AA*, **641**, 2020.

[Ago20] M. Agostini and the GERDA Collaboration, Final Results of GERDA on the Search for Neutrinoless Double-βDecay, *Phys. Rev. Lett.*, **125**, 2020.

[Ahm02] Q. R. Ahmad, R. C. Allen, T. C. Andersen, and the SNO Collaboration, Direct Evidence for Neutrino Flavor Transformation from Neutral-Current Interactions in the Sudbury Neutrino Observatory, *Phys Rev Lett*, **89**, 2002.

[Ake19] M. Aker and the KATRIN Collaboration, An improved upper limit on the neutrino mass from a direct kinematic method by KATRIN, *Phys. Rev. Lett.*, **123**, 2019.

[Ake21] M. Aker and the KATRIN Collaboration, The Design, Construction, and Commissioning of the KATRIN Experiment, prepared for submission to *JINST*, 2021.

[Alb18] J. Albert and the EXO-200 Collaboration, Search for Neutrinoless Double-Beta Decay with the Upgraded EXO-200 Detector, *Physical Review Letters*, **120**, 2018.

[Ald18] C. Alduino and the CUORE Collaboration, First Results from CUORE: A Search for Lepton Number Violation via $0\nu\beta\beta$ Decay of 130Te, *Phys. Rev. Lett.*, **120**, 2018.

[Ale19] V. Alenkov, H. W. Bae, J. Beyer, R. S. Boiko, K. Boonin, O. Buzanov, N. Chanthima, M. K. Cheoun, D. M. Chernyak, J. S. Choe, S. Choi, F. A. Danevich, M. Djamal, D. Drung, C. Enss, A. Fleischmann, A. M. Gangapshev, L. Gastaldo, et al., First results from the AMoRE-Pilot neutrinoless double beta decay experiment, *Eur. Phys. J. C*, **79**, 791, 2019.

[All17] S. Allgeier, Entwicklung einer modularen 36-Kanal-Auslesekette mit rauscharmen SQUID-basierten Vorverstärkern für die 4k-Pixel-Molekülkamera MOCCA, Masters thesis, Kirchhoff-Institut für Physik, Universität Heidelberg, 2017.

[Alp15] B. Alpert and at al. (HOLMES Collaboration), The electron capture decay of ^{163}Ho to measure the electron neutrino mass with sub-eV sensitivity, *Eur. Phys. J. C*, **75**, 2015.

[Alt05] M. Altmann, M. Balata, P. Belli, et al., Complete results for five years of gno solar neutrino observations, *Physics Letters B*, **616**, 174–190, 2005.

[Alv19] S. I. Alvis and the Majorana Collaboration, Search for neutrinoless double-β decay in ^{76}Ge with 26 kg yr of exposure from the Majorana Demonstrator, *Phys. Rev. C*, **100**, 2019.

[Asn13] D. M. Asner and the Project 8 Collaboration, Project 8: Determining neutrino mass from tritium beta decayusing a frequency-based method, in *Proceedings, 2013 Community Summer Study on the Future of U.S. Particle Physics: Snowmass on the Mississippi (CSS2013)*, 2013.

[Bai83] P. A. Baisden, D. H. Sisson, S. Niemeyer, B. Hudson, C. L. Bennett, and R. A. Naumann, Measurement of the half-life of ^{163}Ho, *Phys. Rev. C*, **28**, 337–341, 1983.

[Ban93] S. R. Bandler, C. Enss, R. E. Lanou, H. J. Maris, T. More, F. S. Porter, and G. M. Seidel, Metallic magnetic bolometers for particle detection, *J. Low Temp. Phys.*, **93**, 709–714, 1993.

[Bar] A. Barth, in preparation, Phd thesis, Kirchhoff-Institut für Physik, Universität Heidelberg.

[Bla13] K. Blaum, J. Dilling, and W. Noörtershäuse, Precision atomic physics techniques fornuclear physics with radioactive beams, *Phys. Scr.*, **T152**, 2013.

[Ble89] B. Bleaney, Lanthanide ions in metallic gold - II. Terbium and holmium, *Proc. R. Soc. Lond. A*, **424**, 299–306, 1989.

[Blo07] M. Block, D. Ackermann, K. Blaum, et al., Towards direct mass measurements of nobelium at SHIPTRAP, *Eur. Phys. J. D*, **45**, 39–45, 2007.

[Bra18] M. Brass, C. Enss, L. Gastaldo, M. Haverkort, and R. Green, Ab initio calculation of the calorimetric electron capture spectrum of ^{163}Ho: Intra-atomic decay into bound-states, *Phys. Rev. C*, **97**, 1623–1694, 2018.

[Bra20] M. Brass and M. Haverkort, Ab initio calculation of the electron capture spectrum of ^{163}Ho: Auger-Meitner decay into continuum states, *New J. Phys.*, **22**, 2020.

[Bro81] L. Brown and G. Gabrielse, Precision spectroscopy of a charged particle in an imperfect Penning trap, *Phys. Rev. A*, **25**, 1981.

[Bro86] L. S. Brown and G. Gabrielse, Geonium theory: Physics of a single electron or ion in a penning trap, *Rev. Mod. Phys.*, **58**, 233, 1986.

[Bro19] C. Brofferio, O. Cremonesi, and S. Dell'Oro, Neutrinoless Double Beta Decay Experiments With TeO_2 Low-Temperature Detectors, *Front. Phys.*, **86**, 2019.

[Bur04] A. Burck, Entwicklung großflächiger magnetischer Kalorimeter zur energieaufgelösten Detektion von Röntgenquanten und hochenergetischen Teilchen, Diplomarbeit, Kirchhoff-Institut für Physik, Universität Heidelberg, 2004.

[Bur08] A. Burck, Entwicklung großflächiger mikrostrukturierter magnetischer Kalorimeter mit Au:Er- und Ag:Er-Sensoren für den energieaufgelösten Nachweis von Röntgenquanten und hochenergetischen Teilchen, PhD Thesis, Kirchhoff-Institut für Physik, Universität Heidelberg, 2008.

[Cam01] J. Campbell and T. Papp, Widths of the atomic K–N7 levels, *Atomic Data and Nuclear Data Tables*, **77**, 2001.

[Cla04] J. Clarke and A. I. Braginski (Ed.), The SQUID Handbook, WILEY-VCH, 2004.

[Cle98] B. T. Cleveland, T. Daily, J. Raymond Davis, et al., Measurement of the solar electron neutrino flux with the homestake chlorine detector, *The Astrophysical Journal*, **496**, 1998.

[Cos93] E. Cosulich, F. Gatti, and S. Vitale, Further results on μ-calorimeters with superconducting absorber, *J Low Temp Phys*, **93**, 263–268, 1993.

[Cro16] M. Croce, M. Rabin, V. Mocko, and the NuMECS Collaboration, Development of Holmium-163 Electron-Capture Spectroscopy with Transition-Edge Sensors, *J. Low Temp. Phys.*, **184**, 958, 2016.

[DA87] W. David Arnett and J. L. Rosner, Neutrino mass limits from SN1987A, *Phys. Rev. Lett.*, **58**, 1906, 1987.

[Dan05] T. Daniyarov, Metallische magnetische Kalorimeter zum hochauflösenden Nachweis von Röntgenquanten und hochenergetischen Molekülen, PhD Thesis, Kirchhoff-Institut für Physik, Universität Heidelberg, 2005.

[Dor18] H. Dorrer, K. Chrysalidis, T. Goodacre, C. E. Düllmann, K. Eberhardt, C. Enss, L. Gastaldo, R. Haas, J. Harding, C. Hassel, K. Johnston, T. Kieck, U. Köster, B. Marsh, C. Mokry, S. Rothe, J. Runke, F. Schneider, T. Stora, A. Türler, et al., Production, isolation and characterization of radiochemically pure ^{163}Ho samples for the ECHo-project, *Radiochim. Acta*, **106**, 2018.

[DR82] A. De Rújula and M. Lusignoli, Calorimetric measurements of Holmium-163 decay as tools to determine the electron neutrino mass, *Phys. Lett. B*, **118**, 429–434, 1982.

[Dre13] G. Drexlin, V. Hannen, S. Mertens, and C. Weinheimer, Current direct neutrino mass experiments, *Advances in High Energy Physics*, **2013**, 2013.

[DS18] S. De Salas, P.F. abd Gariazzo, O. Mena, C. Temes, and M. Tortola, Neutrino mass ordering from oscillations and beyond: 2018 status and future prospects, *Front. Astron. Space Sci.*, **5**, 2018.

[Eli13a] S. Eliseev, K. Blaum, M. Block, A. Dörr, C. Droese, T. Eronen, M. Goncharov, M. Höcker, J. Ketter, E. Minaya Ramirez, D. A. Nesterenko, Y. N. Novikov, and L. Schweikhard, A phase-imaging technique for cyclotron-frequency measurements, *Appl. Phys. B*, **114**, 107–128, 2013.

[Eli13b] S. Eliseev, K. Blaum, M. Block, C. Droese, M. Goncharov, E. Minaya Ramirez, D. A. Nesterenko, Y. N. Novikov, and L. Schweikhard, Phase-imaging ion-cyclotron-resonance measurements for short-lived nuclides, *Phys. Rev. Lett.*, **110**, 2013.

[Eli15] S. Eliseev, K. Blaum, M. Block, S. Chenmarev, H. Dorrer, C. E. Düllmann, C. Enss, P. Filianin, L. Gastaldo, M. Goncharov, U. Köster, F. Lautenschläger, Y. Novikov, A. Rischka, R. X. Schüssler, L. Schweikhard, and A. Türler, Direct Measurement of the Mass Difference of ^{163}Ho and ^{163}Dy Solves the Q-Value Puzzle for the Neutrino Mass Determination, *Phys. Rev. Lett.*, **115**, 1623–1694, 2015.

[Ens00] C. Enss, A. Fleischmann, K. Horst, J. Schönefeld, J. Sollner, Y. C. P. Huang, Y. Kim, J. Adams, and G. Seidel, Metallic magnetic calorimeters for particle detection, *J. Low Temp. Phys.*, **121**, 137–176, 2000.

[Ens05] C. Enss and S. Hunklinger, Low-Temperature Physics, SpringerLink: Springer e-Books, Springer Berlin Heidelberg, 2005.

[Est20] I. Esteban, M. Gonzalez-Garcia, M. Maltoni, T. Schwetz, and A. Zhou, The fate of hints: updated global analysis of three-flavor neutrino oscillations, *JHEP*, **09**, 2020.

[Fal65] K. Faler, Determination of the half-life of the longer-lived ^{166}Ho isomer, *J. Inorg. Nucl. Chem.*, **27**, 25–27, 1965.

[Fle00] A. Fleischmann, J. Schönefeld, J. Sollner, C. Enss, J. Adams, S. Bandler, and G. Seidel, Low temperature properties of erbium in gold, *J. Low Temp. Phys.*, **118**, 7–21, 2000.

[Fle03] A. Fleischmann, Magnetische Mikrokalorimeter: Hochauflösende Röntgenspektroskopie mit energiedispersiven Detektoren, PhD Thesis, Kirchhoff-Institut für Physik, Universität Heidelberg, 2003.

[Fle05] A. Fleischmann, C. Enss, and G. Seidel, Metallic magnetic calorimeters, in C. Enss (Ed.), *Cryogenic Particle Detection, Topics in Applied Physics*, Volume 99, 151–216, Springer-Verlag, Berlin, Heidelberg, New York, 2005.

[Fle09] A. Fleischmann, L. Gastaldo, J. Porst, S. Kempf, A. Kirsch, A. Pabinger, C. Pies, P. Ranitzsch, S. Schäfer, F. Seggern, T. Wolf, C. Enss, and G. Seidel, Metallic magnetic calorimeters, *AIP Conf. Proc.*, **1185**, 2009.

[Fuk98] Y. Fukuda and the Super-Kamiokande Collaboration, Evidence for oscillation of atmospheric neutrinos, *Phys. Rev. Lett.*, **81**, 1562, 1998.

[Gam16] L. Gamer, D. Schulz, C. Enss, A. Fleischmann, L. Gastaldo, S. Kempf, C. Krantz, O. Novotny, D. Schwalm, and A. Wolf, MOCCA: A 4k-Pixel Molecule Camera for the Position and Energy-Resolving Detection of Neutral Molecule Fragments at CSR, *J. Low Temp. Phys.*, **184**, 839, 2016.

[Gam17] L. Gamer, C. E. Düllmann, C. Enss, A. Fleischmann, L. Gastaldo, C. Hassel, S. Kempf, T. Kieck, and K. Wendt, Simulation and optimization of the implantation of holmium atoms into metallic magnetic microcalorimeters for neutrino mass determination experiments, *Nucl. Instr. Meth. Phys. Res. A*, **854**, 139–148, 2017.

[Gan16] A. Gando and the KamLAND-Zen Collaboration, Search for Majorana Neutrinos Near the Inverted Mass HierarchyRegion with KamLAND-Zen, *Physical Review Letters*, **117**, 2016.

[Gas13] L. Gastaldo, P. Ranitzsch, F. von Seggern, J.-P. Porst, S. Schäfer, C. Pies, S. Kempf, T. Wolf, A. Fleischmann, C. Enss, A. Herlert, and K. Johnston, Characterization of low temperature metallic magnetic calorimeters having gold absorbers with implanted ^{163}Ho ions Determination, *Nucl. Inst. Meth. A*, **711**, 2013.

[Gas17] L. Gastaldo and the ECHo Collaboration, The electron capture in ^{163}Ho experiment - ECHo, *Eur. Phys. J. Special Topics*, **226**, 1623–1694, 2017.

[Gat97] F. Gatti, P. Meunier, C. Salvo, and S. Vitale, Calorimetric measurement of the ^{163}Ho spectrum by means of a cryogenic detector, *Phys. Lett. B*, **398**, 415–419, 1997.

[Giu07] C. Giunti and C. W. Kim, Fundamentals of Neutrino Physics and Astrophysics, 2007.

[Giu12] A. Giuliani and A. Poves, Neutrinoless double-beta decay, *Advances in High Energy Physics*, **2012**, 2012.

[Goe20] A. Goeggelmann, J. Jochum, L. Gastaldo, C. Velte, and F. Mantegazzini, Study of muon-induced background in MMC detector arrays for the ECHo experiment, *accepted by EPJ C*, 2020.

[Gri] M. Griedel, in preparation.

[Gru05] C. Grupen, Astroparticle Physics, 2005.

[Hag63] F. B. Hagedorn and P. M. Hall, Right-angle bends in thin strip conductors, *J. Appl. Phys.*, **34**, 128–133, 1963.

[Hah92] W. Hahn, M. Löwenhaupt, and B. Frick, Crystal field excitation in dilute rare earths noble metal alloys, *Phys. B*, **180**, 176/178, 1992.

[Ham99] W. Hampel, J. Handt, G. Heusser, et al., Gallex solar neutrino observations: results for gallex iv, *Physics Letters B*, **447**, 127–133, 1999.

[Has16] C. Hassel, K. Blaum, T. Goodacre, H. Dorrer, C. E. Düllmann, K. Eberhardt, S. Eliseev, C. Enss, P. Filianin, A. Faessler, A. Fleischmann, L. Gastaldo, et al., Recent Results for the ECHo Experiment, *J. Low Temp. Phys.*, **184**, 2016.

[Hen15] D. Hengstler, M. Keller, C. Schötz, J. Geist, M. Krantz, S. Kempf, L. Gastaldo, A. Fleischmann, T. Gassner, G. Weber, R. Maertin, T. Stoehlker, and C. Enss, Towards FAIR: first measurements of metallic magnetic calorimeters for high-resolution x-ray spectroscopy at GSI, *Physica Spripta*, **T166**, 2015.

[Hen17] D. Hengstler, Development and characterization of two-dimensional metallic magnetic calorimeter arrays for the high-resolution X-ray spectroscopy, Phd thesis, Kirchhoff-Institut für Physik, Universität Heidelberg, 2017.

[Her00] T. Herrmannsdörfer, R. Königa, and C. Enss, Properties of Er-doped Au at ultralow temperatures, *Phys. B*, **284-288**, 1698–1699, 2000.

[Her20] M. Herbst, A. Reifenberger, Velte, H. Dorrer, C. E. Düllmann, C. Enss, A. Fleischmann, L. Gastaldo, S. Kempf, T. Kieck, U. Köster, F. Mantegazzini, and K. Wendt, Specific heat of holmium in gold and silver at low temperatures, *J.Low Temp. Phys.*, 2020.

[Hoe97] G. Hoelzer, M. Fritsch, M. Deutsch, J. Haertwig, and E. Foerster, K$\alpha_{1,2}$ and K$\beta_{1,3}$ x-ray emission lines of the 3d transition metals, *Phys. Rev. A*, **56**, 4554, 1997.

[Hof12] V. Hoffmann, Messung der AC-Suszeptibilität von paramagnetischem Au:Er bei Temperaturen oberhalb des Spinglasübergangs, B.sc. thesis, Kirchhoff-Institut für Physik, Universität Heidelberg, 2012.

[Kaw88] O. Kawakami, A. Masuda, M. Fujioka, T. Omori, and S. Yasumi, Measurement of the halflife of Ho-163 by isotope dilution mass spectrometry, in *16th INS International Symposium on Neutrino Mass and Related Topics*, 274–277, 1988.

[Kem15] S. Kempf, A. Ferring, A. Fleischmann, and C. Enss, Direct-current superconducting quantum interference devices for the readout of metallic magnetic calorimeters, *Supercond. Sci. Technol.*, **28**, 045008, 2015.

[Kem18] S. Kempf, A. Fleischmann, L. Gastaldo, and C. Enss, Physics and applications of metallic magnetic calorimeters, *J. Low Temp. Phys.*, **193**, 2018.

[Kor88] J. Korkisch, CRC Handbook of Ion Exchange Resins, CRC Press, Boca Raton, FL, USA, 1988.

[Kru69] M. Krusius, A. C. Anderson, and B. Holmström, Calorimetric Investigation of Hyperfine Interactions in Metallic Ho and Tb, *Phys. Rev.*, **177**, 910, 1969.

[KT19a] H. Kieck T., Dorrer, E. Düllmann, V. Gadelshin, F. Schneider, and K. Wendt, Highly efficient isotope separation and ion implantation of ^{163}Ho for the ECHo project, *Nucl. Inst. Meth. A*, **945**, 2019.

[KT19b] S. Kieck T., Biebricher, Düllmann, and K. Wendt, Optimization of a laser ion source for ^{163}Ho isotope separation, *Review of Scientific Instruments*, **90**, 2019.

[Man] F. Mantegazzini et al., Metallic magnetic calorimeter arrays for the first phase of the ECHo experiment, to be submitted.

[Man21] F. Mantegazzini, B. A. Allgeier, S., C. Enss, A. Ferring-Siebert, A. Fleischmann, L. Gastaldo, R. Hammann, D. Hengstler, S. Kempf, D. Richter, D. Schulz, D. Unger, C. Velte, and M. Wegner, Multichannel read-out for arrays of metallic magnetic calorimeters, accepted by *JINST*, 2021.

[Mat12] J. Mates, K. Irwin, L. Vale, et al., Flux-Ramp Modulation for SQUID Multiplexing, *J Low Temp Phys*, **167**, 707–712, 2012.

[McC93] D. McCammon, M. Cui, W. Juda, J. Morgenthaler, J. Zhang, R. Kelley, S. Holt, G. Madejski, S. Moseley, and A. Szymkowiak, Thermal calorimeters for high resolution X-ray spectroscopy, *Nucl. Instr. Meth. Phys. Res. A*, **326**, 157–165, 1993.

[McC05] D. McCammon, Semiconductor Thermistors, in C. Enss (Ed.), *Cryogenic Particle Detection, Topics in Applied Physics*, Volume 99, Springer-Verlag, Berlin, Heidelberg, New York, 2005.

[Mer13] S. Mertens, Direct neutrino mass experiments, *J. Phys. Conf. Ser.*, **718**, 2013.

[Moc15] V. Mocko, W. A. Taylor, F. Nortier, E. J. W., T. E. Barnhart, R. J. Nickles, A. D. Pollington, G. J. Kunde, M. W. Rabin, and E. R. Birnbaum, Isolation of ^{163}ho from dysprosium target material by hplc forneutrino mass measurements, *Radiochimica Acta*, **103**, 577–585, 2015.

[Mon09] B. Monreal and J. A. Formaggio, Relativistic cyclotron radiation detection of tritium decay electrons as a new technique for measuring the neutrino mass, *Phys. Rev. D*, **80**, 2009.

[Mur70] A. P. Murani, Magnetic susceptibility and electrical resistivity of some gold-rare-earth alloys, *J. Phys. C: Solid State Phys.*, **3**, S153, 1970.

[NIS19] NIST, X-Ray Mass Attenuation Coefficients, checked in 2019.

[NuF] NuFIT 5.0 (2020), www.nu-fit.org.

[Par16] H. K. Park and the AMoRE collaboration, The AMoRE: Search for Neutrinoless Double Beta Decay in ^{100}Mo, *Nucl. Part. Phys. Proc.*, **273–275**, 2630–2632, 2016.

[Per04] E. Perinati, M. Barbera, A. Collura, S. Serio, and E. Silver, Spectral broadening by incomplete thermalization of the energy in x-ray microcalorimeters with superconducting absorber and ntd-ge thermal sensor, *Nucl. Inst. Meth. A*, **531**, 459–466, 2004.

[Pie12] C. Pies, S. Schäfer, S. Heuser, S. Kempf, A. Pabinger, J.-P. Porst, P. Ranitsch, N. Foerster, D. Hengstler, A. Kampkötter, T. Wolf, L. Gastaldo, A. Fleischmann, and C. Enss, maXs: Microcalorimeter Arrays for High-Resolution X-Ray Spectroscopy at GSI/FAIR, *J. Low Temp. Phys.*, **167**, 2012.

[Pon68] B. Pontecorvo, Neutrino experiments and the problem of conservation of leptonic charge, *Sov. Phys. JETP*, **26**, 984–988, 1968.

[Pow74] R. Powers, P. Martin, G. Miller, R. Welsh, and D. Jenkins, Muonic ^{197}Au: A test of the weak-coupling model, *Nucl. Phys. A*, **230**, 413–444, 1974.

[Rac16] G. D. Racca, R. Laureijs, L. Stagnaro, J.-C. Salvignol, J. L. Alvarez, G. S. Criado, L. G. Venancio, A. Short, P. Strada, T. Bönke, C. Colombo, A. Calvi, E. Maiorano, O. Piersanti, S. Prezelus, P. Rosato, J. Pinel, H. Rozemeijer, V. Lesna, P. Musi, et al., The Euclid mission design, in H. A. MacEwen, G. G. Fazio, M. Lystrup, N. Batalha, N. Siegler, and E. C. Tong (Ed.), *Space Telescopes and Instrumentation 2016: Optical, Infrared, and Millimeter Wave*, Volume 9904, 235 – 257, International Society for Optics and Photonics, SPIE, 2016.

[Ran12] P. C.-O. Ranitzsch, J.-P. Porst, S. Kempf, C. Pies, S. Schäfer, A. Hengstler, D. Fleischmann, C. Enss, L. Gastaldo, and H. A., Development of Metallic Magnetic Calorimeters for High Precision Measurements of Calorimetric ^{187}Re and ^{163}Ho Spectra, *J. Low Temp. Phys.*, **167**, 2012.

[Ran14] P.-O. Ranitzsch, Development and characterization of metallic magnetic calorimeters for the calorimetric measurement of the electron capture spectrum of ^{163}Ho for the purpose of neutrino mass determination, Phd thesis, Kirchhoff-Institut für Physik, Universität Heidelberg, 2014.

[Rot11] S. Rothe, B. A. Marsh, C. Mattolat, V. N. Fedosseev, and K. Wendt, A complementary laser system for isolde rilis, *J. Phys.: Conf. Ser.*, **312**, 2011.

[Rou12] C. Roux, C. Böhm, A. Dörr, S. Eliseev, S. George, M. Goncharov, Y. N. Novikov, J. Repp, S. Sturm, U. S., and K. Blaum, The trap design of PENTATRAP, *Appl. Phys. B*, **107**, 997–1005, 2012.

[San19] O. Sander, N. Karcher, O. Krömer, M. Kempf, S. an Wegner, C. Enss, and M. Weber, Software-Defined Radio Readout System for the ECHo Experiment, *IEEE TRANSACTIONS ON NUCLEAR SCIENCE*, **66**, 2019.

[Sav91] G. Savard, S. Becker, G. Bollen, K. H.-J., M. R.B., T. Otto, L. Schweikhard, H. Stolzenberg, and U. Wiess, A new cooling technique for heavy ions in a penning trap, *Phys. Lett. A*, **158**, 247–252, 1991.

[Sch00] U. Schoetzig, Half-life and X-ray emission probabilities of ^{55}Fe, *Appl. Radiat. Isot.*, **53**, 469–472, 2000.

[Sik20] T. Sikorsky, J. Geist, D. Hengstler, S. Kempf, L. Gastaldo, C. Enss, C. Mokry, J. Runke, C. Düllmann, P. Wobrauschek, K. Beeks, V. Rosecker, J. Sterba, G. Kazakov, T. Schumm, and A. Fleischmann, Measurement of the ^{229}Th Isomer Energy with a Magnetic Microcalorimeter, *Phys. Rev. Lett.*, **125**, 2020.

[Sim20] A. Simon and the NEXT collaboration, The NEXT experiment for neutrinoless double beta decay searches, *J. Phys.: Conf. Ser.*, **1342**, 2020.

[Son15] V. Sonnenschein1, I. D. Moore1, I. Pohjalainen, M. Reponen, S. Rothe, and K. Wendt, Intracavity frequency doubling and difference frequency mixing for pulsed ns ti:sapphire laser systems at on-line radioactive ion beam facilities, *JPS Conf. Proc.*, **6**, 1–6, 2015.

[Spr87] P. Springer, C. Bennett, and P. Baisden, Measurement of the neutrino mass using the inner bremsstrahlung emitted in the electron-capture decay of ^{163}Ho, *Phys. Rev. A*, **35**, 679–689, 1987.

[Ste52] K. W. H. Stevens, Matrix elements and operator equivalents connected with the magnetic properties of rare earth ions, *Proc. Phys. Soc. A*, **65**, 209, 1952.

[Tes77] C. D. Tesche and J. Clarke, dc SQUID: Noise and optimization, *J. Low Temp. Phys.*, **29**, 301–331, 1977.

[Tre02] V. Tretyak and Y. Zdesenko, Tables of double beta decay data: an update., *At Data Nucl Data Tables*, **80**, 83–116, 2002.

[Uml92] E. Umlauf and M. Buehler, *Proc. Int. Workshop Low Temperature Detectors for Neutrinos and Dark Matter (LTD4)*, 229, 1992.

[Vel19a] C. Velte, Measurement of a high energy resolution and high statistics ^{163}Ho spectrum for the ECHo experiment, Phd thesis, Kirchhoff-Institut für Physik, Universität Heidelberg, 2019.

[Vel19b] C. Velte et al., High-resolution and low-background ^{163}Ho spectrum: interpretation of the resonance tails, *Eur. Phys. J. C*, **79**, 1623–1694, 2019.

[Wal77] L. R. Walker and R. E. Walstedt, Computer model of metallic spin-glasses, *Phys. Rev. Lett.*, **38**, 514, 1977.

[Wan12] M. Wang, G. Audi, A. Wapstra, F. Kondev, M. MacCormick, X. Xu, and B. Pfeiffer, The Ame2012 atomic mass evaluation, *Chinese Phys. C*, **36**, 2012.

[Wan17] M. Wang, G. Audi, F. Kondev, W. Huang, S. Naimi, and X. Xu, The Ame2016 atomic mass evaluation, *Chinese Phys. C*, **41**, 2017.

[Wat17] D. Waters, for the NEMO-3, and the SuperNEMO Collaborations, Latest Results from NEMO-3 Status of theSuperNEMO Experiment, *J. Phys.:Conf. Ser.*, **888**, 2017.

[Weg18a] M. Wegner, Entwicklung, Herstellung und Charakterisierung eines auf metallischen magnetischen Kalorimetern basierenden Detektorarrays mit 64 Pixeln und integriertem Mikrowellen-SQUID-Multiplexer, Phd thesis, Kirchhoff-Institut für Physik, Universität Heidelberg, 2018.

[Weg18b] M. Wegner, N. Karcher, O. Krömer, D. Richter, F. Ahrens, O. Sander, S. Kempf, M. Weber, and C. Enss, Microwave SQUID Multiplexing of Metallic Magnetic Calorimeters: Status of Multiplexer Performance and Room-Temperature Readout Electronics Development, *J. Low Temp. Phys.*, **193**, 2018.

[Wic20] T. Wickenhäuser, Characterization of an optimized MMC detector array for the ECHo-100k experiment, Masters thesis, Kirchhoff-Institut für Physik, Universität Heidelberg, 2020.

[Wil69] G. Williams and L. L. Hirst, Crystal-field effects in solid solutions of rare earths in noble metals, *Phys. Rev.*, **185**, 407, 1969.

[Wiß13] V. Wißdorf, Magnetisches 1/f-Rauschen und Imaginärteil der magnetischen Suszeptibilität von Erbium dotiertem Gold bei Millikelvin Temperaturen, B.sc. thesis, Kirchhoff-Institut für Physik, Universität Heidelberg, 2013.

[Won11] Y. Y. Wong, Neutrino mass in cosmology: status and prospects, *Ann.Rev.Nucl.Part.Sci.*, **61**, 69–98, 2011.

[Zin04] B. Zink, K. Irwin, G. Hilton, D. Pappas, J. Ullom, and M. Huber, Lithographically patterned magnetic calorimeter X-ray detectors with integrated SQUID readout, *Nucl. Instr. Meth. B*, **520**, 52–55, 2004.